International
Progress Report

IPR-06-19

Äspö Hard Rock Laboratory

Äspö Task Force on modelling of groundwater flow and transport of solutes

Modelling of Task 6D, 6E and 6F, using CHAN3D

James Crawford
Luis Moreno

Department of Chemical Engineering
and Technology
Royal Institute of Technology,
Stockholm Sweden

June 2006

Svensk Kärnbränslehantering AB
Swedish Nuclear Fuel
and Waste Management Co
Box 5864
SE-102 40 Stockholm Sweden
Tel 08-459 84 00
+46 8 459 84 00
Fax 08-661 57 19
+46 8 661 57 19

Report no.
IPR-06-19
No.
F65K
Author
James Crawford
Luis Moreno
Date
June 2006
Checked by
Jan-Olof Selroos
Date
December 2006
Approved
Anders Sjöland
Date
2006-12-19

Äspö Hard Rock Laboratory

Äspö Task Force on modelling of groundwater flow and transport of solutes

Modelling of Task 6D, 6E and 6F, using CHAN3D

James Crawford
Luis Moreno

Department of Chemical Engineering
and Technology
Royal Institute of Technology,
Stockholm Sweden

June 2006

Keywords: Fractures, Rock matrix, Channel network, Modelling

This report concerns a study which was conducted for SKB. The conclusions and viewpoints presented in the report are those of the author(s) and do not necessarily coincide with those of the client.

Abstract

This report details the subtasks 6D, 6E, and 6F of the Task 6 modelling project. Tasks 6D and 6E involve modelling of the tracer test C2 performed within the TRUE Block Scale Project. The simulation model is based upon the semi-synthetic hydrostructural model developed earlier within Task 6C. For this propose, in both tasks, the Channel Network model incorporated in the CHAN3D program has been used.

In Task 6D and Task 6E, the 200 m scale, semi-synthetic hydrostructural model created within the Task 6C subproject (Dershowitz et al., 2003) is used as a common reference basis for the modelling work. The breakthrough of the tracers ^{129}I, ^{47}Ca, ^{137}Cs, ^{226}Ra, ^{99}Tc and ^{241}Am have been simulated in these tasks. Task 6E extends the Task 6D transport calculations to a reference set of PA time scales and boundary conditions.

In Task 6F, two features in 100 m scale (1S and 4S) were modelled. The tracers were injected along a 3m line in the feature plane and were collected at a line located 20 m downstream. The CHAN3D program was used for these calculations, in its original version, i.e., diffusion into an infinite matrix.

In Task 6F2, some additional sets of calculations were performed. In the first set, the results obtained with the original version of CHAN3D are compared with those obtained with a new version that can handle diffusion into a matrix formed by several layers (skins) and the matrix proper. From this comparison, the need of a model that can handle diffusion into a complex matrix is demonstrated. In the second set, the components of the total residence time are discussed. Here, it is concluded that the residence time is determined by different mechanisms in SC and PA.

Sammanfattning

Den här rapporten behandlar deluppgifterna Task 6D, 6E och 6F inom modelleringsprojektet Task 6. Task 6D och 6E innefattar modellering av spårämnesförsöken C2 som genomförs inom TRUE Block Scale projektet. Simuleringsmodellen baseras på den semi-syntetiska hydrostrukturmodellen som utvecklats tidigare inom Task 6C. I båda deluppgifterna har kanalnätverksmodellen i programmet CHAN3D använts.

I Task 6D och 6E, används den semi-syntetiska hydrostrukturmodellen i 200 meters skala som skapades inom Task 6C (Dershowitz et al., 2003) som en gemensam referens för modellarbetet. Genombrottskurvorna för spårämnena ^{129}I, ^{47}Ca, ^{137}Cs, ^{226}Ra, ^{99}Tc och ^{241}Am har simulerats i dessa deluppgifter. Task 6E förlänger transportberäkningarna i 6D till en referensuppsättning av tidsskalor och randvillkor relevanta för säkerhetsanalyser.

I Task 6F modellerades två sprickenheter i 100 metersskala (1S och 4S). Spårämnena injicerades längs en 3 meter lång linje i sprickenhetens plan och samlades upp längs en linje 20 meter nerströms. För dessa beräkningar användes programmet CHAN3D i sin originalversion, dvs med diffusion in i en oändlig matris.

I Task 6F2, genomfördes ytterligare beräkningar. I den första jämfördes resultat erhållna med originalversionen av CHAN3D med de som erhållits med en ny version som kan hantera diffusion in i en matris uppbyggd av flera lager inklusive den egentliga bergmatrisen. Baserad på denna jämförelse visas att det finns behov av en modell som kan hantera diffusion in i en komplex matris. I den andra beräkningen diskuteras de olika komponenter som bidrar till den totala uppehållstiden. Det konstateras att uppehållstiden styrs av olika mekanismer i platsbeskrivnings- och säkerhetsanalysskala.

Executive summary

The tracer test C2 performed within the TRUE Block Scale Project has been modelled using the Channel Network model incorporated in the CHAN3D program (Moreno and Neretnieks, 1993; Gylling, 1997). This work comprised the subprojects Task 6D, Task 6E, Task 6F, and Task 6F2 of the Äspö Task 6 modelling project.

Task 6 seeks to provide a bridge between Site Characterisation (SC) and Performance Assessment (PA) approaches to solute transport in fractured rock. In Tasks 6D and 6E, the 200 m scale, semi-synthetic hydrostructural model created within the Task 6C subproject (Dershowitz et al., 2003) is used as a common reference basis for the modelling work. The model is based on the network of major conductive features identified in the Äspö TRUE Block Scale experiment and the Äspö site-scale characterisation programs. In addition to the identified features, the model also contains synthetic features that have been generated based on geostatistical analysis of information from the TRUE Block Scale program.

In Tasks 6D and 6E, the breakthrough of the tracers ^{129}I, ^{47}Ca, ^{137}Cs, ^{226}Ra, ^{99}Tc and ^{241}Am have been simulated, although not all of these tracers were used in the C2 test (Andersson et al., 2002b). The tracers selected for the actual tracer experiment were chosen upon the basis of their utility in an SC scheme, where the focus was upon discerning the transport properties and connectivity of the fracture system. In Task 6D the purpose of including other tracers was to include radionuclides relevant for PA and, in the case of Technetium and Americium, also to study how the retardation of more sorbing radionuclides can be extrapolated in time.

A channel network analogue was created of the discrete fracture network (DFN). The Block Scale DFN consisted of 5648 fracture polygons. It was found to be unnecessary to simulate the entire 200 m Block Scale volume and a smaller 75 m sub volume was found to be satisfactory for modelling of tracer test C2.

For the Task 6D, tracer transport was found to occur along two principal flowpaths in the channel network with fracture features 20D, 21D, 22D, 23D and 1925B being implicated in solute transport from the injection well to the recovery borehole. Task 6E extends the Task 6D transport calculations to a reference set of PA time scales and boundary conditions. Tracer transport was found to occur along two principal flowpaths in the channel network with fracture features 20D-23D, 17S, as well as background features 1925B and 2292B being implicated in solute transport from the injection well to the Western boundary recovery plane at Easting = 1800.

The Tasks 6F and 6F2 of the Äspö Task 6 modelling project have been modelled using the Channel Network model incorporated in the CHAN3D program. Two synthetic features of Geological Type 1 (Feature 1S) and Type 2 (Feature 4S) taken from the discrete features specified in the Task 6C, were used in the modelling.

Solute transport along a 20 meter long part of the fractures was modelled. The boundary conditions as defined to have an estimated groundwater travel time through the 20 meter section of the features of 0.1, 1 and 10 years, respectively. The tracer source section is assumed to be an intersecting fracture with a linear extension of 3 meters, which was modelled as several point sources on a line. The recovery section is assumed to be an intersecting fracture located at a distance of 20 meters from the tracer source section. Tracers I-129, Cs-137 and Am-241 were simulated and simulations were performed for a Dirac pulse input (unit input).

Since the original version of CHAN3D considers diffusion into an infinite matrix composed of only one geological material some assumptions were needed. In the fracture, it is assumed that instantaneous equilibrium is reached between the radionuclides dissolved in the water in the fracture and those sorbed onto the material in the fracture (coating and gouge material). For the cases with a small hydraulic head difference (long travel time), it is assumed that instantaneous equilibrium is reached with some of the layers forming the matrix (e.g., cataclasite or altered rock).

In Task 6F2, the Channel Network model was improved to handle diffusion into a matrix composed of several layers and a semi-infinite matrix. The differential equation for the fracture, the layers, and the semi-infinite matrix are solved by using Laplace Transforms. The breakthrough curves in the time-domain are then obtained by numerical inversion of the solution in the Laplace-domain. Solutions obtained using a complex matrix are compared with those obtained using CHAN3D. It is also studied as the different components of the residence time vary with the water flow rate and the sorption coefficient. The main conclusions are:

- The residence time is determined by different mechanisms in SC and PA. The process that is dominanting in SC have little or not at all influence on the travel time under PA conditions

- When the solute transport is modelled assuming instantaneous equilibrium with the material in the fracture (coating, gouge, and cataclasite) the resultant residence time may be not conservative.

Contents

List of Tables

List of Figures

1 Introduction

1.1 Background

The Swedish concept for the disposal of high-level nuclear waste (the KBS-3 system) involves encapsulation of spent fuel rods in corrosion-resistant, iron-copper canisters surrounded by a bentonite clay buffer at a depth of approximately 500 metres in crystalline bedrock. The canisters are to be located in deposition holes that will be bored in the floors of a system of tunnels comprising the repository. Central to the successful implementation of the KBS-3 system is a meticulous characterisation of potential sites as a starting point for determining an appropriate repository location. In addition to this, a comprehensive performance assessment is also required to give an indication of whether the repository will behave as intended over the geological time scales appropriate for risk analysis.

The goal of Site Characterisation (SC) is to obtain input data that can later be used in performance assessment (PA) calculations. This input data generally takes the form of parameter values describing the physical and geochemical properties of the studied rock volume. Performance assessment calculations are based upon the premise that there may be one or more initially defective canisters that can leak radionuclides to the surrounding rock (even though the structural integrity of the canister is designed to remain intact for some 100 000 years). The properties of the surrounding rock volume that comprises the natural barrier for radionuclide migration are therefore of overwhelming importance for the operational safety of the repository after closure.

Frequently, the parameter values necessary for PA are obtained from interpretation of field tests and experiments using theoretical models that attempt to capture the essential physics of the flow and transport system. Processes that may be important in a PA setting may not necessarily be dominating processes or may not even be observable in the SC phase. There is therefore a continuing need to bridge the conceptual gaps between the models used to interpret field data during SC and the models used to make PA predictions, and more specifically, how the parameter values derived from SC may be expected to be different in a PA setting.

To provide a methodological basis for this work, an exhaustive program of experimental and theoretical analysis has been undertaken at the Äspö Hard Rock Laboratory (HRL) in the municipality of Oskarshamn, Sweden. The Äspö HRL constitutes an important component of SKB's work to design, construct, and implement a deep geological repository for spent nuclear fuel, as well as to develop and test methods for characterisation of selected repository sites (SKB, 2001).

Radionuclides that are released to the rock volume are transported by the groundwater flowing in fractures within the rock. From the fractures, they may diffuse into and interact with the micro-surfaces within the rock matrix. Diffusion into the rock matrix and retention within the rock mass are important retardation mechanisms for the transport of radionuclides. The retention effect of the rock at Äspö HRL has been studied by tracer tests in the TRUE experimental programme (Tracer Retention Understanding Experiments).

Laboratory investigations have difficulties in simulating representative natural conditions that may exist within a repository environment and require supplementary field studies for corroboration. Theoretical models also require in-data from both laboratory and field investigations, and need to be validated against field observations. For this reason, a programme of modelling tasks has been undertaken as an adjunct to the experimental field studies carried out within TRUE.

The present report concerns the modelling sub-tasks Task 6D, Task 6E, Task 6F, and Task 6F2 within the Äspö Modelling Taskforce programme. In Task 6D, the TRUE Block Scale tracer test C2 with sorbing and non-sorbing tracers was to be modelled using the block-scale, semi synthetic hydrostructural model developed within Task 6C. This task provides a common reference platform for all SC-type and PA-type modelling in the considered scale (200 m) and ensures a common basis for Task 6E.

In Task 6E, the transport of a number of sorbing and non-sorbing tracers was to be modelled under PA-type conditions using the block-scale, semi synthetic hydrostructural model developed within Task 6C.

Finally in Task 6F, the transport of sorbing and non-sorbing tracers was modelled in a simple 2-D fracture. The hydraulic conditions used are those characteristic for Site Characterisation (SC) and Performance Assessment (PA).

1.2 Objectives

The purpose of Task 6D and Task 6E is to provide a common reference platform for SC and PA modelling to be carried out in subsequent tasks with the aim to provide a basis for future comparison. In a broader perspective, the objectives of Task 6 are (Benabderrahmane et al., 2000):

1) To assess simplifications used in PA models including:
   a) identifying the key assumptions and the less important assumptions for long-term PA predictions.
   b) identifying the most significant PA model components of a site.
   c) prioritisation of PA modelling assumptions and demonstration of a rationale for simplification of PA models by parallel application of several PA models of varying degrees of simplification.
   d) provision of a benchmark for comparison of PA and SC models in terms of PA measures for radionuclide transport at PA temporal and spatial scales.
   e) establishment of a methodology for transforming SC models using Site Characterisation data into PA models in a consistent manner.
2) To determine how, and to what extent, experimental tracer and flow experiments can constrain the range of parameters used in PA models.
3) To support the design of Site Characterisation programmes to ensure that the results have optimal value for performance assessment calculations.
4) To improve the understanding of site-specific flow and transport behaviour at different scales using Site Characterisation models.

The purpose of Task 6F is to study the behaviour of radionuclides under SC and PA conditions in a simple geometry, i.e., a single feature of Geological Structure Type 1 or Type 2.

2 Modelling Tasks

Task 6 seeks to provide a bridge between Site Characterisation (SC) and performance assessment (PA) approaches to solute transport in fractured rock. In Task 6, both PA-type and SC-type models are applied to tracer experiments considering both the experimental boundary conditions and boundary conditions for a PA scale.

In the first tasks (Task 6A, 6B and 6B2), solute transport on a 5-10 meter scale in a single feature was modelled. These tasks were based upon the TRUE-1 tracer test STT-1b performed between packed off borehole sections containing a water-conducting geological feature with an interpreted "simple" planar structure (Feature A). The tracer test STT-1b in Task 6A (previously modelled in Task 4E) was revisited with the purpose to provide a common basis for future comparison of the modelling carried out within Task 6. Similarly, in Task 6B the injection and withdrawal of tracer were assumed to occur in the same borehole sections as in the STT-1b test, but with a flow rate that was only 1/1000 of that in Task 6A in order to mimic PA time scales. In Task 6B2, the boundary conditions were modified to produce flow and transport over a larger area of Feature A. The input boundary was in this case a line source and the tracers were assumed to be collected in a hypothetical fracture, intersecting Feature A.

In Tasks 6D and 6E solute transport over longer distances including several geological features are modelled. The basis for the modelling is the block scale semi-synthetic hydrostructural model developed within Task 6C (Dershowitz et al., 2003) at two different scales, 200 m and 2000 m. In this task a semi-synthetic hydrostructural model was developed based on the conditions at the TRUE Block scale site in the southwest of the Äspö Hard Rock Laboratory. The model was built through a combination of deterministic and stochastic analyses of hydraulically significant structural features at scales from millimetres to kilometres. At each scale the geometric, hydraulic and transport properties of the structures are described.

2.1 Task 6C semi-synthetic hydro-structural model

In the modelling of Task 6D, the 200 m scale hydrostructural model developed within Task 6C has been used (Dershowitz et al, 2003). The model is based on the network of major conductive features identified in the Äspö TRUE Block Scale experiment and the Äspö site-scale characterisation programs. In addition to the identified features, the model also contains synthetic features that have been generated based on geostatistical analysis of information from the TRUE Block Scale program.

The implementation of the Task 6C, 200 m scale Semi-synthetic hydrostructural model is presented in Section 5.1 of the Task 6C report. The model is primarily based on the deterministic structures of the TRUE Block Scale hydrostructural model (Andersson et al., 2002a) with the addition of synthetic 100 m scale structures and background fractures. The model contains 11 deterministic structures, 25 synthetic 100 m scale structures and 5660 synthetic background fractures (see section 3.2, Figure 3).

The properties of the deterministic features are based on measurements (see Chapter 3 of Task 6C report). For the synthetic structures, the properties are assigned depending on their size. A stepwise procedure is used to derive the properties from stochastic correlation relationships as described in Chapter 4 of the Task 6C report (see Figure 4-2 in the Task 6C report). In the hydrostructural model the geological structures are divided into two basic Geologic Structure Types, Type 1 "Fault" and Type 2 "Non-fault", see Figure 1 and Figure 2 below:

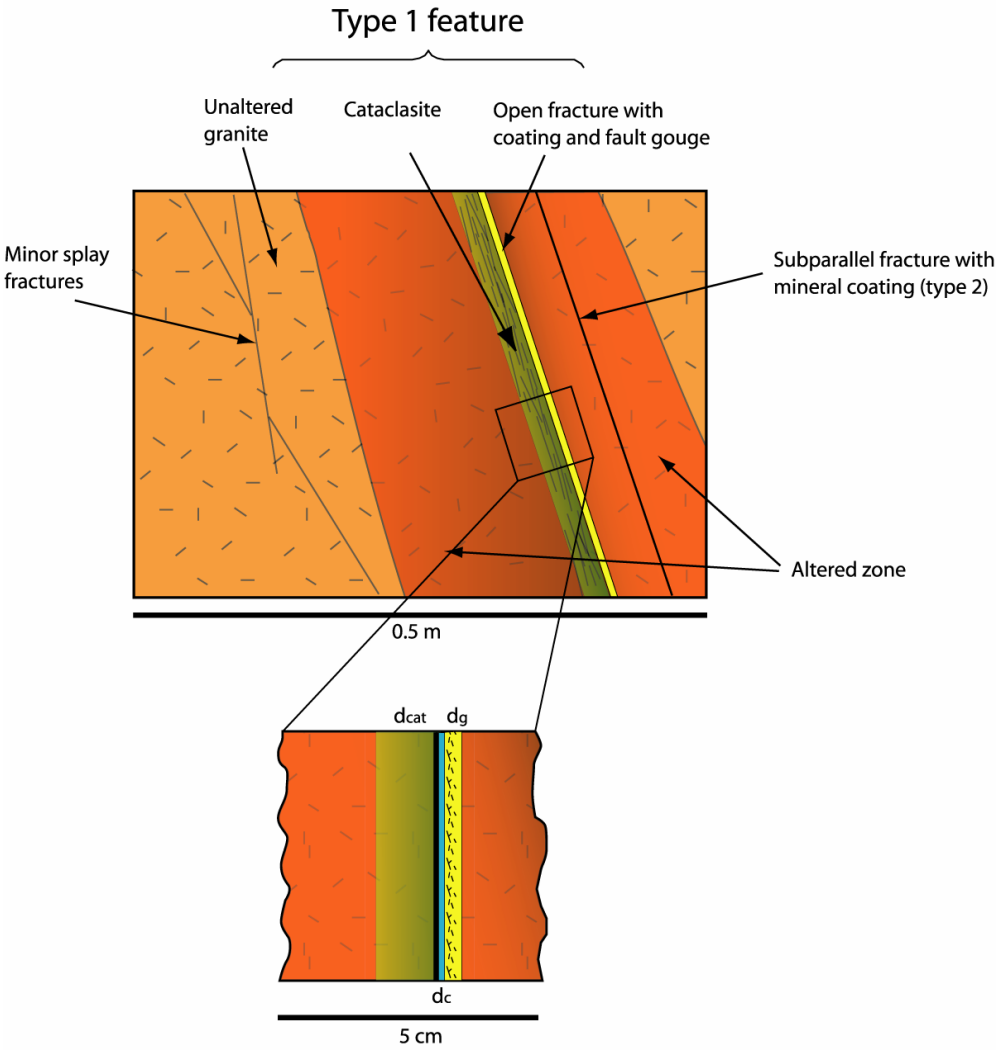

Figure 1. *Illustration of the Geological Structure Type 1 (Fault). From Task 6C report (Dershowitz et al., 2003).*

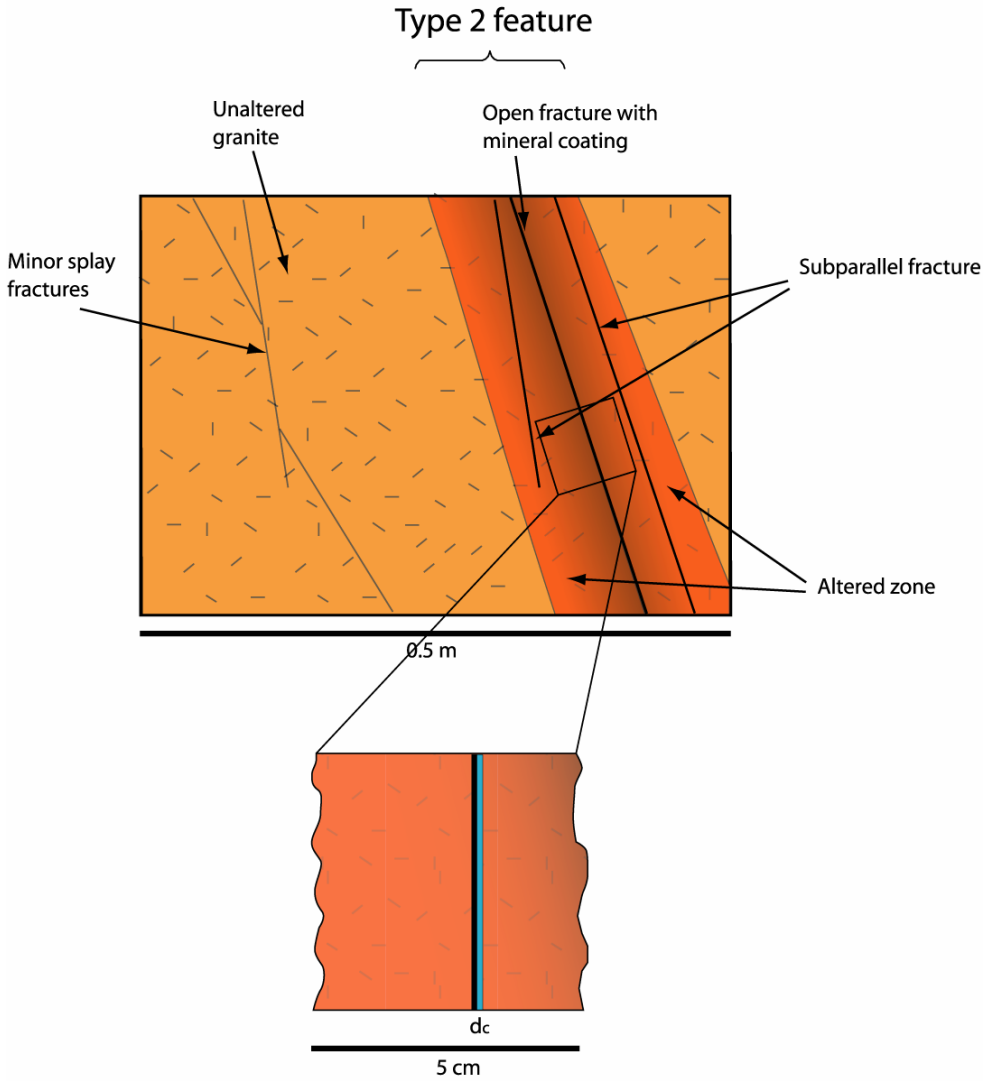

Figure 2. *Illustration of the Geological Structure Type 2 (Non-fault). From Task 6C report (Dershowitz et al., 2003).*

Investigations at Äspö have shown that many structures are made up of several conductive features and the number of sub-parallel features may vary over the extent of the structure. Thus, a structure may at one location consist of a single fracture of Geological Structure Type 1, while at another location it may consist of two fractures of Geological Structure Type 1 and 2, respectively. Larger scale structures may consist of tens, or more of sub-parallel and hydraulically conductive fracture splays and similar features. As the possible combination of fracture-features within a structure is immense, a simplified classification scheme is introduced. A Complexity Factor ranging from 1 to 5 is defined. The Complexity Factor 1 represents structures consisting of a single feature while Complexity Factor 5 represents structures consisting of more than 10 features (see Table 4-5 in the Task 6C report).

In the data delivery used as the basis for defining the model used in the Task 6D calculations, the full geometrical description of the features, the transmissivity, the aperture, the Geological Structure Type and the Complexity Factor of the features are provided.

2.2 Task 6D. Block scale transport on a tracer test time scale

Task 6D focuses upon the simulation of TRUE Block Scale tracer test C2 using the hydrostructural model developed in Task 6C as a basis. The time scale for the simulation is the "*tracer test time scale*" corresponding to a few months to a few years. In the Task 6D specification, some additional tracers, not used in the actual tracer tests have been included. As some of these tracers are more sorbing than the actual tracers used, the time scale of the simulation extends over a longer time scale than the actual time for the tracer experiment.

The spatial scale for the simulation is the "block" spatial scale considering transport from a single, TRUE-1 type fracture through a network of fractures and structures similar to those defined by the TRUE Block Scale Project.

The simulations of solute transport in Task 6D were to be performed under experimental conditions. It was therefore necessary to take into account the underground openings of the Äspö HRL. In order to avoid construction of complex 3D models, boundary conditions that embed the underground openings without including them explicitly in the models were supplied as part of the Task 6D data distribution to the various modelling groups involved. The boundary conditions for the Block Scale model were obtained by interpolation from head measurements in the TRUE Block Scale rock volume.

In Task 6D, the breakthrough of the tracers ^{129}I, ^{47}Ca, ^{137}Cs, ^{226}Ra, ^{99}Tc and ^{241}Am were to be simulated, although not all of these tracers were used in the C2 test. The tracers selected for the actual tracer experiment were chosen upon the basis of their utility in an SC scheme, where the focus was upon discerning the transport properties and connectivity of the fracture system. In Task 6D the purpose of including other tracers was to include radionuclides relevant for PA and, in the case of Technetium and Americium, also to study how the retardation of more sorbing radionuclides can be extrapolated in time.

In the short time perspective of the C2 test the perrhenate anion (ReO_4^-) was expected to be non-sorbing with very similar behaviour to iodide (I^-) (see, for example, Byegård et al., 1992 and Holmqvist et al., 2000). The injection time history of ^{129}I is therefore assumed to be identical to that of ^{186}Re and it is furthermore assumed that the breakthrough of ^{186}Re can be used as a proxy for ^{129}I, thus allowing direct comparison of the simulated breakthrough of ^{129}I with the experimental breakthrough of ^{186}Re.

The injection time histories of ^{226}Ra, ^{99}Tc and ^{241}Am were assumed to be identical to that of ^{137}Cs. In this case, however, no comparison could be made with experimental data.

In addition to the measured injection curves, simulations were also requested for a Dirac pulse input (unit input).

The experimental breakthrough data supplied as part of the data distribution to the modelling groups were corrected for radioactive decay and, in order to improve result transparency, it was requested that radioactive decay not be considered in the modelling of solute transport.

2.2.1 TRUE Block Scale tracer test

The tracer tests performed at the TRUE Block Scale site are summarised by Andersson et al. (2002b). The tracer Test Stage was made up of three phases. The last of these phases (Phase C) included injections of radioactive sorbing tracers in three different source locations (Andersson et al, 2001).

Tracer test C2 involves transport from borehole KI0025F03:P7 to KI0023B:P6 along a pathway through Structures 23, 22, 20, and 21 (Andersson et al, 2002b). Table 1 below, details parameters of importance for tracer test C2.

Table 1. Data for source and sink sections used in tracer test C2. Coordinates given in the ÄSPÖ96 system.

Parameter	Source section KI0025F03:P7	Sink section KI0023B:P6
Northing	**7194.840**	**7186.294**
Easting	**1929.741**	**1914.628**
Elevation	**-476.100**	**-473.065**
Injection rate	**1.67×10^{-7} m^3/s(10 ml/min)**	
Pumping rate		**3.25×10^{-5} m^3/s (1.95 l/min)**
Cartesian distance	**17.6m**	
DFN Path Length	**66m**	
Structures involved	**23, 22, 20, 21**	

The tracers used in the C2 test covered a range of sorption properties: non-sorbing (^{186}Re as perrhenate), slightly sorbing (^{47}Ca), moderately sorbing (^{131}Ba) and strongly sorbing (^{137}Cs). The injection time history curves for these tracers were supplied in the Task 6D data distribution.

2.3 Task 6E – Block scale transport on a PA time scale

Task 6E focuses upon the simulation of radionuclide transport under conditions representative for PA. The time scale for the simulation is the "*performance assessment time scale*" which extends to many thousands of years.

The spatial scale for the simulation is the "block" spatial scale considering transport from a single, TRUE-1 type fracture through a network of fractures and structures similar to those defined by the TRUE Block Scale Project.

The simulations of solute transport in Task 6E were to be performed under PA relevant boundary conditions. It was not therefore necessary to take into account the underground openings of the Äspö HRL. The boundary conditions for the Block Scale model consist of a simple linear gradient of 0.5% across the TRUE Block Scale rock volume extending from East (1 m head) to West (0 m head), with no-flow boundary conditions on all other bounding planes.

In Task 6E, the breakthrough of the tracers ^{129}I, ^{47}Ca, ^{137}Cs, ^{226}Ra, ^{99}Tc and ^{241}Am were to be simulated. The tracers were selected to include radionuclides relevant for PA and, in the case of Technetium and Americium, also to study how the retardation of more sorbing radionuclides can be extrapolated in time.

Simulations were requested for a Dirac pulse input (unit input) as well as for an extended pulse of 1 MBq/year with a duration of 1000 years. In order to improve result transparency, it was requested that radioactive decay not be considered in the modelling of solute transport.

2.4 Task 6F – Test bench

Task 6 seeks to provide a bridge between Site Characterisation (SC) and performance assessment (PA) approaches to solute transport in fractured rock. In Task 6, both PA-type and SC-type models are applied to tracer experiments considering both the experimental boundary conditions and boundary conditions for a PA scale.

In the first tasks (Task 6A, 6B and 6B2), solute transport on a 5-10 meter scale in a single feature was modelled. These tasks were based upon the TRUE-1 tracer test STT-1b performed between packed off borehole sections containing a water-conducting geological feature with an interpreted "simple" planar structure (Feature A). The tracer test STT-1b in Task 6A (previously modelled in Task 4E) was revisited with the purpose to provide a common basis for future comparison of the modelling carried out within Task 6. Similarly, in Task 6B the injection and withdrawal of tracer were assumed to occur in the same borehole sections as in the STT-1b test, but with a flow rate that was only 1/1000 of that in Task 6A in order to mimic PA time scales. In Task 6B2, the boundary conditions were modified to produce flow and transport over a larger area of Feature A. The input boundary was in this case a line source and the tracers were assumed to be collected in a hypothetical fracture, intersecting Feature A.

In Tasks 6D and 6E solute transport over longer distances including several geological features are modelled. The basis for the modelling is the block scale semi-synthetic hydrostructural model developed within Task 6C (Dershowitz et al., 2003) at two different scales, 200 m and 2000 m. In this task a semi-synthetic hydrostructural model was developed based on the conditions at the TRUE Block scale site in the southwest of the Äspö Hard Rock Laboratory. The model was built through a combination of deterministic and stochastic analyses of hydraulically significant structural features at scales from millimetres to kilometres. At each scale the geometric, hydraulic and transport properties of the structures are described.

This subtask Task 6F is proposed due to the high level of complexity in Task 6E, with large networks of fractures of different type being conceptually and mathematically modelled in different ways by the various Modelling Groups, makes comparison and analysis of reasons for differences tremendously difficult. Thus, a series of "benchmark" runs on a simplified system were proposed.

The task consists of simulating flow and transport in a single Type 1 and a Type 2 feature, respectively. The features will follow the geometrical description from Task 6C. However, the implementation of the Task 6C hydrogeostructural model in a flow and transport model may be done in several ways. An important step in this subtask is to describe how the Task 6C model is implemented and what assumptions are made in the process.

Hydrological properties of the features (Transmissivity, aperture, storativity) are taken from distinct features of the Task 6C model. Tracers Iodide (I-129), Caesium (Cs-137, and Americium (Am-241) selected from Task 6E will be used. The transport and sorption data for these tracers should be as prescribed for Task 6E.

The source term is a Dirac pulse from a spatially extended source as in Task 6E. Breakthrough over a "collection line" at a distance of 20 meters will be used for the performance measures. A prescribed hydraulic head giving water transit times of roughly 0.1, 1 and 10 years.

2.5 Task 6F2 - Sensitivity study

Two aspects are studied and discussed in this Task, namely:

- Comparison of the results obtained with CHAN3D and those obtained with a model handling a matrix composed of several layers. In order to do this, the Channel Network model was improved to handle diffusion into a matrix composed of several layers and a semi-infinite matrix. The differential equation for the fracture, the layers, and the semi-infinite matrix are solved by using Laplace Transforms. For the case where the properties of the matrix are kept constant in the modelled volume, the breakthrough curves in the time-domain may be obtained by numerical inversion of the solution in the Laplace-domain.

- Factors determining the residence time. Here, it is studied as the different components of the residence time vary with the water flow rate and the sorption coefficient. Three components are distinguished. One is the water residence time in the channel/fracture, which is determined by the channel volume and the water flow rate. The second one is the residence due to instantaneous equilibrium between the solute dissolved in the water in the fracture and that sorbed onto the material in the fracture (coating, gouge). The third one is the residence time due to diffusion/sorption within the rock matrix.

3 Model description

The simulations were made using the CHAN3D computer program (Gylling, 1997), which is based on the Channel Network model (Moreno and Neretnieks, 1993). The model takes into account the uneven flow distribution observed in fractured rock and the stochastic nature of hydraulic features as well as solute transport retarding processes such as diffusion and sorption within the rock matrix.

The code CHAN3D is actually two separate programs; the CHAN3D-flow program that computes the flow field in the rock fracture system, and the CHAN3D-transport program that computes the transport of solutes once the flow field is established using CHAN3D-flow.

The following sections detail how the Task 6D modelling exercise was carried out within the framework of the CHAN3D program and how the discrete fracture network (DFN) model provided in the data distribution was converted into the channel network analogue required for the CHAN3D simulations.

3.1 Implementation of the Task 6C semi-synthetic hydrostructural model

The information contained in the Task 6C report, IPR-03-13 (Dershowitz et al., 2003) was used as a basis for generating the geological and hydrostructural features incorporated in the CHAN3D simulation model. In the initial stages of the modelling work, the entire 200 m×200 m×200 m rock volume as described in the Task 6C hydrostructural model was employed. The channel length used was 2 m, thereby giving a channel network containing 101^3 nodes.

In later stages of the work, it was found that much of the rock volume was computationally superfluous and a smaller rock volume of 75 m×75 m×75 m was used instead. This was done largely for reasons of numerical expediency as simulations could then be made with more detailed resolution of fracture features within the tracer transport zone. In the smaller model, a channel length of 1m was chosen, thus giving a channel network containing 76^3 nodes. The smaller overall network dimensions in the 75 m×75 m×75 m model gave considerable improvements in computational performance when solving the hydrological problem and also lowered memory usage for the subsequent transport simulations.

The following sections detail how the hydrostructural features were translated to a channel network description for incorporation within the CHAN3D simulation program.

3.2 Geometrical description

3.2.1 Fracture network

The fractures defined in the hydrostructural model were distributed to the modelling groups in the Microsoft Excel file, "Features_200_ver2.xls". The fractures were defined as rectangular polygons with four given vertex coordinates. Each fracture was defined with a transmissivity, nominal fracture aperture, storativity, as well as a geological structure type and complexity class. The geological structure type was deemed to be either of type 1 (fault), or type 2 (non-fault). Type 1 structures contained tectonically and hydrothermally altered rocks, typically characterised by the presence of reactivated mylonite, cataclasite and fault gouge. Type 2 structures, on the other hand, were deemed to be fractures with no significant tectonic or hydrothermal alteration. The altered zone around the type 2 structures was conceptualised to have been altered by supergene processes and not through hydrothermal (hypogene) activity. The complexity class refers to the effective number of subparallel fractures or splays associated with the fracture. A more detailed description of how the complexity factor was defined can be found in the Task 6C report, section 4.4.2.

The distributed data set consisted of 4 different subsets of fractures (D, S, B, C) defined in the fashion described above. The subset D consisted of 11 "deterministic" fractures interpreted directly from borehole data with sizes (lengths) ranging from roughly 25m up to 500 m in extent with a typical L/W aspect ratio ranging from 0.5-1.5. Subset S consisted of 19 "synthetic" fractures with similar dimensions, although generated stochastically (i.e., they do not represent known or interpreted fractures in the TRUE Block Scale rock volume). In addition, there were two separate subsets of background features containing 3111 (B) and 2537 (C) fractures, respectively. The background features were square polygons with sizes ranging from roughly 3.5 m to 70 m. The median size of a typical background fracture was on the order of 5.6 m in extent. The main difference between subset B and subset C was purported to be the orientation of the fractures, with the subset B fractures being oriented predominantly in a NNW direction.

The rock volume modelled was centred on the 200 m Block Scale anchor point as defined in the Task 6C report. The ÄSPÖ96 coordinates of the anchor point were given as:

Northing	7170
Easting	1900
Elevation	-450

The various features comprising the 200 m TRUE Block Scale rock volume are shown below in Figure 3:

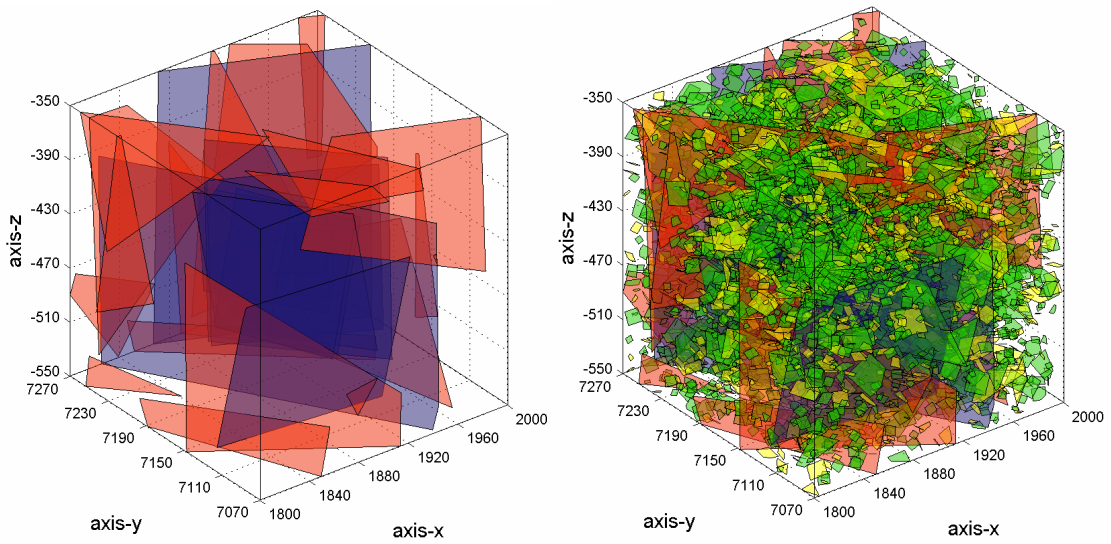

Figure 3. *Visualisation of fractures within the TRUE Block Scale 200 m rock volume. The left-hand image shows the D (blue) and S (red) fracture subsets only. The image on the right shows the entire complement of fractures including subset B (green) and C (yellow). The axis-x corresponds to the Northerly directional vector, axis-y is the Easterly directional vector, and axis-z is the elevation (metres above sea level).*

The 75 m rock volume used in later simulations was defined with an anchor point midway between the injection and recovery boreholes used in the C2 tracer test. Based upon the coordinates of the tracer injection and recovery locations as given in the Task 6D specification, the coordinates of the new anchor point were calculated to be:

Northing	7190.6
Easting	1922.2
Elevation	-474.58

The location of the smaller 75 m rock volume relative to the 200 m TRUE Block Scale cube is indicated in Figure 4 below:

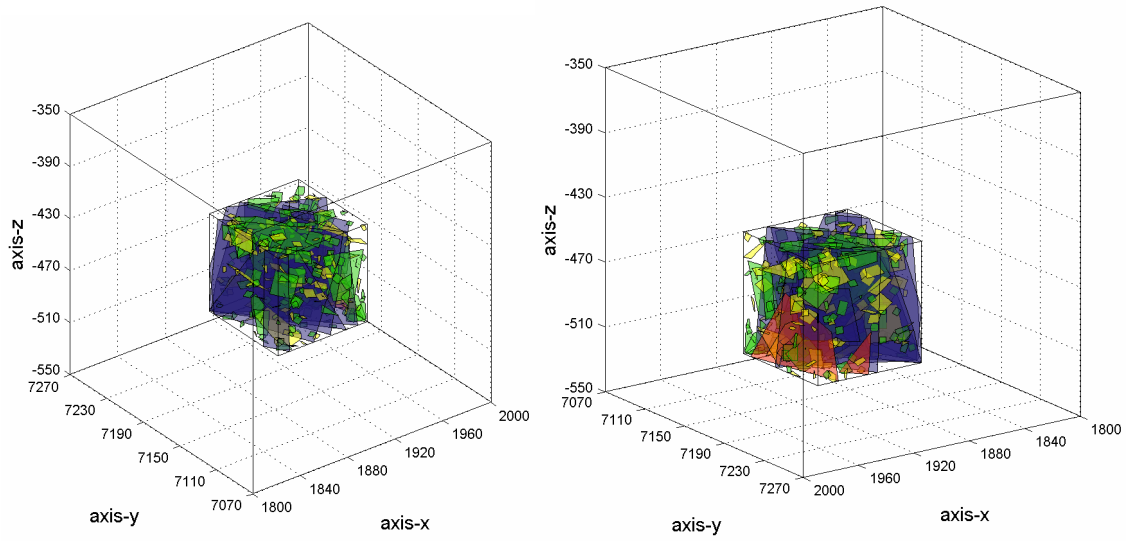

Figure 4. *Visualisation from two different perspectives of the 75 m rock volume relative to the original TRUE Block Scale 200 m cube.*

The various features comprising the 75 m rock volume are shown in Figure 5 below from both a forward and reverse angle directions:

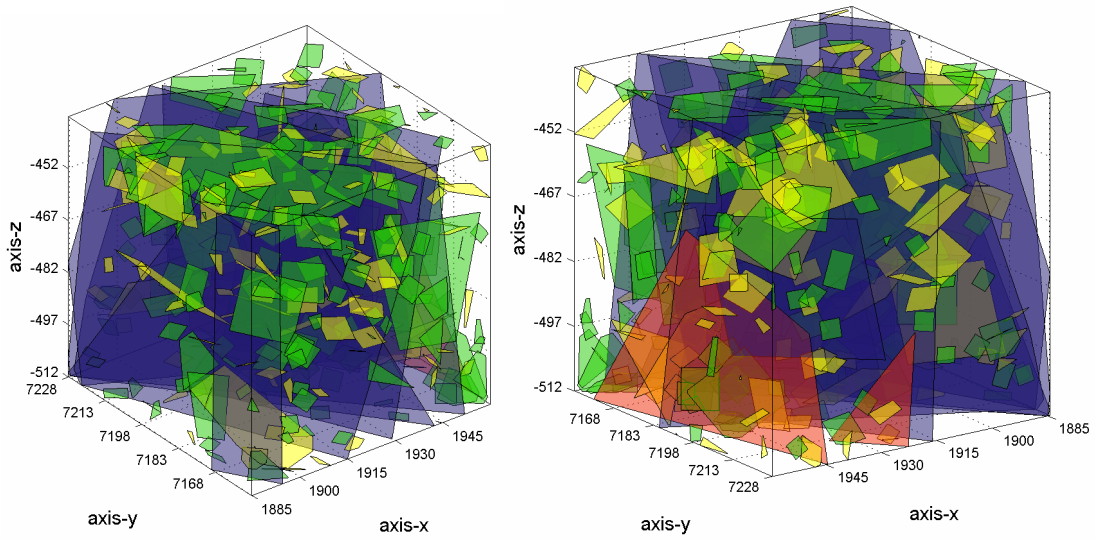

Figure 5. *Visualisation of the 75 m rock volume from a forward and reverse angle perspective.*

Of the 5678 fractures in the data set, a total of 418 are either internal to (or, at least partially contained within) the 75 m rock volume.

3.2.2 Pore space

In the CHAN3D simulation program, the flow of water and transport of solutes is conceptualised to occur in a regular orthogonal network of interconnected nodes and channels (i.e., a rectangular grid). To be able to simulate the C2 tracer test in the TRUE Block Scale rock volume, it was therefore necessary to translate the fracture polygons as defined in the data distribution to an equivalent set of channels with appropriately scaled hydrological and material properties. Figure 6 below, shows schematically the arrangement of mixing nodes and interconnected channels making up a typical channel network:

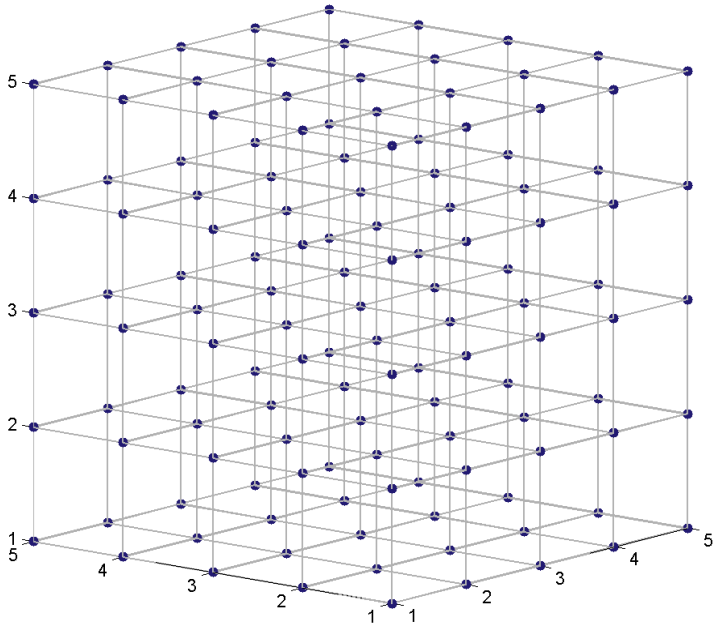

Figure 6. *Schematic showing the arrangement of mixing nodes and interconnected channels making up the orthogonal channel network employed in the CHAN3D simulation program.*

All network channels were initially given arbitrarily low conductances (in this case, 10^{-12} m^2/y). Channels lying within the zone of influence of particular fractures were then assigned appropriate conductances depending upon the transmissivity of the fracture. These were calculated on the basis of the given transmissivity of the individual fracture in the DFN and a theoretically derived conversion factor to convert transmissivity to an equivalent channel conductance (see Appendix A1). The zone of influence (or "fracture depth") was defined arbitrarily as one channel length perpendicular distance on each side of the defined fracture polygon. It was found that a fracture depth of about two channel lengths was the minimum required to give good channel network connectivity in 3D space for randomly oriented fracture polygons. If a fracture depth of less than two channel lengths is used, there is some risk that the channel network representation will be poorly connected or even disconnected in 3D space. A typical channel network used to represent a fracture is shown in Figure 7 below:

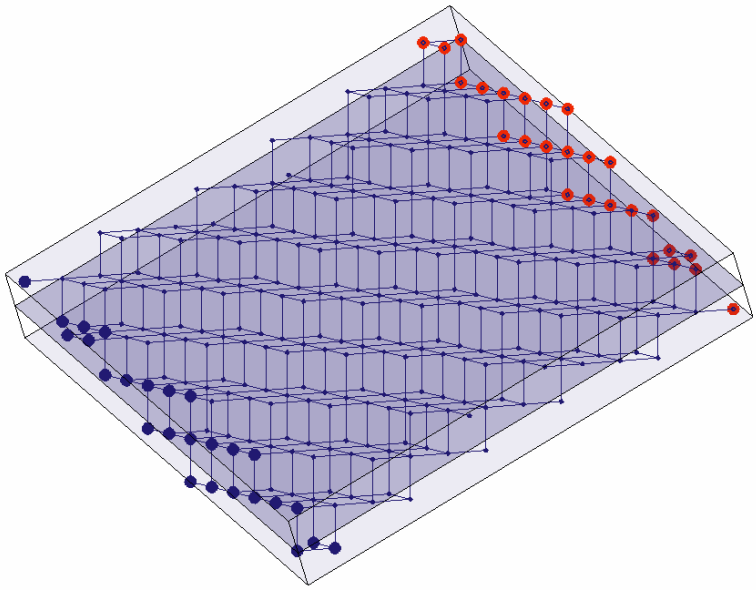

Figure 7. *Typical channel network used to represent a discrete fracture plane. The volume surrounding the shaded plane corresponds to the "zone of influence" of the fracture, which in this case is two channel lengths in depth. All channels lying outside the zone of influence are assigned arbitrarily low conductances. Boundary nodes that could be used for a simple flow simulation are visualised as red and blue markers in the figure.*

In order to allow the possibility of flow channelling within individual fractures, channel conductances were assigned randomly from a lognormal distribution specific to each fracture. As there were no additional data available relating to channelling effects, a standard deviation of unity ($\log_{10}$ units) was assumed for channels residing in all fractures. The conductance of channels at fracture intersections was calculated on the basis of the mean transmissivity of the fractures involved.

In this way a set of conductive channels was defined, embedded in a background network of essentially non-conductive channels. The mean $\log_{10}$-conductance [m^2/y] of channels in the active network varied from -1.9 to 2.2 (i.e., mean conductance of channels belonging to specific individual fractures). Inactive background channels, on the other hand, were all assigned $\log_{10}$-conductances of -12.

3.3 Flow model

3.3.1 Processes considered

The Channel Network model upon which the CHAN3D program is based, assumes that fluid flow takes place within a network of interconnected flow channels in the rock. Channels are conceptualised in the model as being purely hydrological entities representing paths of preferential flow within individual fractures and therefore do not necessarily correspond to entire fractures. Thus, there may be many separate channels comprising any given fracture. Flows in individual channels may diverge along separate flowpaths or converge and mix. Channels contained within a given fracture may also interconnect with channels belonging to intersecting fractures thereby giving rise to three-dimensional connectivity in the channel network.

Although the true geometry of intersecting flow channels in fractured rock may be irregular or random, the Channel Network model considers a regular, rectangular grid of orthogonal channels as indicated in Figure 6. The hydraulic properties of individual channels are influenced by the channel length, fracture geometry, fracture transmissivity, as well as the specifics of how channels are used to represent fractures in the Channel Network model. Details of this are given in Appendix A1. Steady state flow in CHAN3D is calculated by way of Darcy's law where the flowrate in an individual channel is assumed to be proportional to the hydraulic head difference across the end nodes of the channel.

3.3.2 Mathematical description

Each member of the channel network is assigned a hydraulic conductance. This is the only entity required to calculate the flow, if the head field is known. The conductance is defined by analogy with electrical networks where it is the reciprocal of resistance. Here, the flow may be expressed as the channel conductance multiplied by the hydraulic head difference between its ends. In the current model, we assume that the conductances of the channel members are log-normally distributed (with a characteristic mean, μ_c, and standard deviation, σ_c) and not correlated in space. Using a random normal deviate taken from a random number generator, the conductance is assigned from the equation:

$$\log_{10} C_{ij} = \mu_c + (randn) \times \sigma_c \qquad (1)$$

The variable C_{ij} is the channel conductance connecting the nodes i and j. The corresponding flow, q_{ij} is then given by:

$$q_{ij} = C_{ij} \left(H_i - H_j \right) \qquad (2)$$

H_i and H_j are the hydraulic heads at the nodes i and j. Furthermore, at each node i, we have the hydraulic analogy of Kirchoff's current law:

$$\sum_j q_{ij} = 0 \qquad (3)$$

This is simply a mass balance stating that the net flow of water into a node should also equal the flow out of the node under steady state conditions.

The solution of this system of equations gives the hydraulic head at each node. For a network of nodes interconnected in this way, we must solve a sparse system of linear equations. The CHAN3D-flow program solves this equation system using an iterative, sparse linear equation solver. Once the hydraulic head at each node is known, the flow between adjacent channels may be calculated using equation 2.

The properties of individual channels may differ considerably if a large standard deviation is used for the conductance distribution. This leads to a sparse flow system where there will be a few channels with relatively large flowrates and some with almost no flow at all. This is similar to what is observed in fractured rock when hydraulic tests are carried out.

3.3.3 Numerical implementation

To solve for the unknown heads in the channel network, the mass balances for all network nodes are combined to form a matrix of coupled linear equations. Each row in the mass balance matrix represents the mass balance for a node in the channel network. The row consists of a central element on the diagonal (the conductance sum), and up to six other conductances corresponding to the channels connected to the node. The mass balance is obtained by combining equation 2 and 3 thus giving:

$$H_i \sum_{j=1}^{6} C_{ij} - C_{i1}H_1 - C_{i2}H_2 - C_{i3}H_3 - C_{i4}H_4 - C_{i5}H_5 - C_{i6}H_6 = b_i \qquad (4)$$

The term, b_i on the right hand side of the equation represents a boundary condition for that node. For nodes that have no associated boundary condition, the following applies:

$$b_i = 0 \qquad (5)$$

For nodes that are assigned a constant head boundary condition, an additional channel with arbitrarily high conductance is added to equation 4:

$$H_i \left(C_b + \sum_{j=1}^{6} C_{ij} \right) - C_{i1}H_1 - C_{i2}H_2 - C_{i3}H_3 - C_{i4}H_4 - C_{i5}H_5 - C_{i6}H_6 = b_i \qquad (6)$$

$$b_i = C_b H_b \qquad (7)$$

For a constant flow boundary condition (i.e., a flow injection or extraction point), we have instead:

$$H_i \sum_{j=1}^{6} C_{ij} - C_{i1}H_1 - C_{i2}H_2 - C_{i3}H_3 - C_{i4}H_4 - C_{i5}H_5 - C_{i6}H_6 = b_i \qquad (8)$$

$$b_i = \pm Q_b \qquad (9)$$

For an injection point or "source", the flow is set to a positive value; for an extraction point or "sink", the flow is set to a negative value.

The total number of network nodes is $n = ni \times nj \times nk$ for a channel network volume with dimensions of *ni*, *nj*, and *nk* nodes along the x-, y-, and z-axes, respectively. The system of equations can then be written in the form:

$$Ax = b \qquad (10)$$

where, A (henceforth referred to as the "A-matrix") is an n×n square matrix representing the coupled set of mass balances, x is the vector of unknown head values for all nodes, and b (the "b-vector") is the vector of boundary conditions. Each row of the A-matrix contains no more than seven, non-zero elements giving a sparse band-diagonal matrix that is symmetrical about the diagonal.

The number of equations to be solved in the system can be very large. For a domain containing 101×101×101 nodes (the 200 m Block Scale model), for example, the A-matrix has dimensions ≈ $10^6 \times 10^6$ (i.e., 10^{12} matrix elements). For a domain with dimensions 76×76×76 (the reduced 75 m Block Scale model), on the other hand, the A-matrix is about one fifth the size. Even for very modest systems, an efficient numerical method must be chosen to obtain a solution within a reasonable amount of time.

CHAN3D-flow employs an iterative solver using the biconjugate gradient method (BiCG) with incomplete LU-preconditioning. The algorithm used was that contained in the public domain SLATEC package obtainable from the Netlib numerical software repository[1].

3.3.4 Parameters

Parameters of importance for formulating the CHAN3D-flow simulation include the DFN fracture definitions and fracture transmissivities as provided in the Task 6D data distribution. Equivalent channel conductances are determined using purpose-written computational geometry routines developed within MATLAB. Fixed head boundary conditions for the faces of the cube defining the simulation volume as well as flow injection and pumping rates are also required in order to define the numerical problem.

3.4 Transport model

3.4.1 Processes considered

Solute transport is simulated using a particle following technique in the CHAN3D-transport program (Robinson, 1984; Moreno et al., 1988). Many particles are introduced, one at a time, into the known flow field at the tracer injection location. Particles arriving at an intersection are distributed in the outlet channel members with a probability proportional to their flow rates. This is equivalent to assuming total mixing at the intersections. Each individual particle is followed through the network until it arrives at either the recovery borehole or a system boundary. Only tracer particles reaching recovery nodes are included, however, in the breakthrough data. The residence time for water (or a non-interacting solute) in a given channel is determined by the flow through the channel member and by its volume. For sorbing tracers, the residence time is obtained from an analytical solution for solute transport where infinite matrix diffusion and sorption are considered.

The channel volume is estimated by assuming that the conductance of a channel is proportional to the cube of the channel aperture. It is, however, possible to alter the flow exponent in the input data to simulate different flow-aperture relations. The proportionality constant is determined, based upon the estimated flow porosity of the system. The flow porosity can be determined from the experimental residence time distribution (RTD) of a non-sorbing (conservative) tracer.

The residence time of an individual particle along the whole path is determined as the sum of residence times in every channel member that the particle has traversed. The residence time distribution (RTD) is then obtained from the residence times of a multitude of individual particle runs representing different flowpaths through the system. Hydrodynamic dispersion in individual channels is considered to be negligible. Dispersion arises instead as a result of the varying transit times for particles taking alternative routes through the channel network.

---

[1] http://www.netlib.org/slatec/index.html

For a Dirac pulse tracer injection it is assumed that all particles are released simultaneously into the channel network. For non-ideal tracer experiments where a cumulative mass injection-time curve is available, each particle is released into the network with a time delay relating to the fraction of tracer released into the system at different times.

3.4.2 Mathematical description

Within an individual channel, the tracer is transported by advective flow. At the same time, the tracer may diffuse from the channel into the rock matrix. For an instantaneous step change in inlet concentration, the penetration of tracer substance into the rock matrix may appear as shown schematically in Figure 8 below:

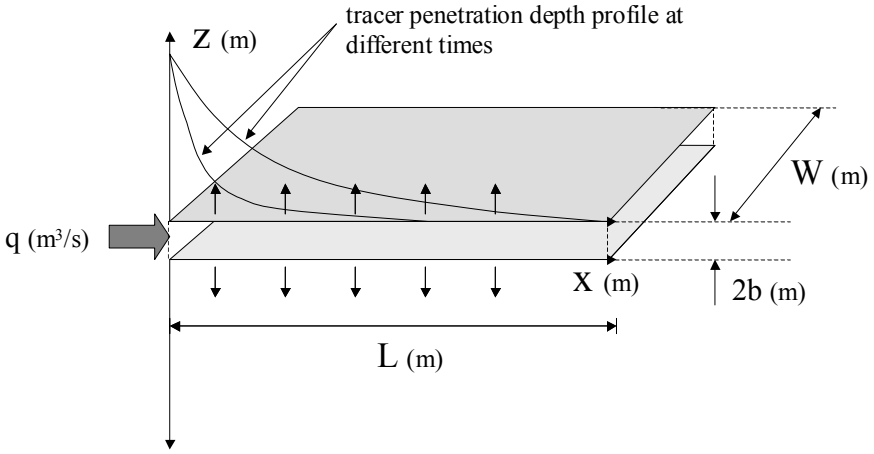

Figure 8. *Conceptual illustration of tracer transport within a channel combined with diffusion within the rock matrix. Advective flow occurs in the channel along the x-axis, while matrix diffusion is outwards into the rock volume perpendicular to the fracture plane.*

A transient, differential mass balance is used to describe the advective transport of the tracer, linear sorption on the fracture surface, and diffusion from an individual channel into the rock matrix (assumed to be infinite in extent). In the absence of radioactive decay, this mass balance is:

$$\left(1+\frac{K_a}{b}\right)\frac{\partial C_f}{\partial t} = -\frac{q}{2Wb}\frac{\partial C_f}{\partial x} + \frac{D_e}{b}\frac{\partial C_p}{\partial z}\bigg|_{z=0} \tag{11}$$

Here, C_f is the aqueous concentration in the fracture, C_p is the porewater concentration, K_a is the surface sorption coefficient, b is the fracture half-aperture, W is the channel width, D_e is the effective diffusivity, and q is the advective flowrate in the channel. The term on the left-hand side of the equation is the accumulation term describing the rate of change of concentration in the fracture water, where sorption of tracer on the fracture surface is accounted for. On the right-hand side of the equation the advective flux term and the matrix diffusive flux term are represented. The flow-wetted surface (FWS) of the channel is defined as:

$$FWS = 2WL \tag{12}$$

The multiplier on the left-hand side of the mass balance is frequently referred to as the retardation factor, R_*:

$$R_* = 1 + \frac{K_a}{b} \tag{13}$$

A similar mass balance is used to describe the diffusive transport and linear sorption of a tracer within the rock matrix:

$$K_d \rho_b \frac{\partial C_p}{\partial t} = D_e \frac{\partial^2 C_p}{\partial z^2} \tag{14}$$

where,

$$K_d \rho_b = \varepsilon_p + \left(1 - \varepsilon_p\right) \cdot K_d' \rho_s \tag{15}$$

K_d and K_d' are the matrix sorption coefficients based upon the bulk (ρ_b) and solid densities (ρ_s), respectively; ε_p is the matrix porosity. The relation between the bulk and solid density is:

$$\rho_b = \left(1 - \varepsilon_p\right) \rho_s \tag{16}$$

As the matrix porosity is very low in igneous rocks, the bulk and solid densities are for all practical purposes the same.

In the rock matrix differential mass balance, the accumulation term on the left-hand side of the equation gives the rate of change of the pore water concentration within the rock matrix, where the sorbed concentration of tracer is simultaneously accounted for. The term on the right-hand side of the equation is the diffusive flux term for the tracer.

For an instantaneous "step" change in concentration at the mouth of the channel, the coupled mass balances can be solved to give an analytical solution for the tracer concentration at the channel outlet. This is the breakthrough curve, or BTC for the channel. In terms of the flow-wetted surface to flow ratio, this is:

$$\frac{C(t)}{C_0} = \begin{cases} 0 & \text{for } t \le R_* t_w \\ \operatorname{erfc}\left[\frac{1}{2}\left(\frac{D_e K_d \rho_b}{t - R_* t_w}\right)^{\frac{1}{2}} \cdot \frac{FWS}{q}\right] & \text{for } t > R_* t_w \end{cases} \tag{17}$$

The strength of matrix interaction for a tracer is determined by the materials property group (MPG), which is defined as:

$$MPG = \sqrt{D_e K_d \rho_b} \tag{18}$$

The water residence time, t_w is equal to the volume of the channel divided by the flowrate through the channel. As the volume of the channel is equal to the channel half-aperture multiplied by the flow-wetted surface (FWS), the water residence time is given by the relation:

$$t_w = \frac{FWS}{q} \times b \tag{19}$$

The BTC for a channel is actually the cumulative residence time distribution (RTD) curve for the tracer residence times in the channel.

3.4.3 Numerical implementation

The CHAN3D-transport program uses the flow-field data generated by CHAN3D-flow to calculate the movement of solutes in the channel network. The generalised relation between channel flow, channel aperture, and conductance (Neretnieks, 2002) can be written as:

$$q = C\Delta H = k\delta^n \tag{20}$$

Where k is a constant of proportionality (not the hydraulic conductivity), and n is the generalised flow condition exponent. For laminar flow in a fracture of constant aperture, the exponent n can be shown to be equal to 3 (Hagen-Poiseuille flow). This is the so-called "cubic" law case for flow. If the fracture is filled with particles, it behaves as a packed bed and the flow is proportional to the aperture width (n = 1). For the case where resistance arises due to constrictions along the flow path, the flow rate is constant (n = 0) and independent of the non-constricted aperture.

Using equation 20 we can show that for a given channel length and width, the volume of the channel is related to the conductance by:

$$V_c = a\, C^{1/n} \tag{21}$$

Where the variable a is a constant. To calculate the proportionality constant, a, we need to first determine the relation between the total channel volume and the flow porosity (ϕ) of the rock. For a simulation volume of dimensions $ni \times nj \times nk$ (x-, y-, and z-axes, respectively), the relation between the flow porosity and the total channel volume is:

$$(ni-1)(nj-1)(nk-1)L^3\phi = a\sum_{r=1}^{s} C_r^{1/n} \tag{22}$$

Where, s is the total number of channels in the network. By rearranging equation 22, the constant a can be calculated as:

$$a = \frac{(ni-1)(nj-1)(nk-1)}{\sum_{r=1}^{s} C_r^{1/n}} L^3\phi \tag{23}$$

The channel volume divided by the flowrate gives the residence time for water in an individual channel:

$$t_w = \frac{V_r}{q_r} = \frac{a\, C_r^{1/n}}{\Delta H_r C_r} \tag{24}$$

Where, ΔH_r is the hydraulic head difference between adjacent nodes in the network.

When a particle arrives at a node during particle tracking, it chooses an exit flowpath from among the six possible exit channels with a probability dependent upon the flow in the channels. From the flowrate in the channel and its conductance, the water residence time is then obtained directly. The residence time of a particle along a flowpath is calculated to be the sum of residence times in the individual channels comprising the flowpath. After many particles are followed from a specified release point to a recovery location, the cumulative residence time distribution is then obtained as the ensemble of particle travel times for a given network realisation.

After calculating the water residence time in an individual channel, equation 17 can be used to estimate the travel time for a solute retarded by matrix interaction and surface sorption.

For each node where tracer release occurs, the particles are tracked through the channel network until the particles leave the boundaries of the system or reach a node flagged as a tracer recovery location. Only tracer particles reaching recovery nodes are included in the breakthrough data. The FWS/Q ratio encountered by each particle is recorded as the sum of FWS/Q values in each channel along the pathway. The breakthrough curve can then be calculated as an ensemble average over those calculated for each individual flowpath.

For a Dirac pulse injection it is assumed that all particles are released simultaneously into the network. If a cumulative mass injection-time curve is available, on the other hand, each particle released into the channel network is given a time delay relating to the fraction of particles released into the system at different times.

3.4.4 Parameters

Parameters of importance for formulating the CHAN3D-transport simulation include the flow field calculated using CHAN3D-flow, the individual channel conductances, the flow porosity, as well as matrix interaction parameters (i.e., the material properties group, MPG and surface sorption parameter, K_a) for individual tracers. For the simulation of the C2 tracer test a cumulative injection-time curve giving the injected activity fraction as a function of time was also required.

In the Task 6C semi synthetic model matrix interaction and sorption data are given for a number of radionuclide tracers in various rock types making up the TRUE Block Scale rock volume. These data consist of tabulated porosities (ε_p), effective diffusivities (D_e), and volumetric distribution coefficients (K'_d). The surface sorption coefficient (K_a) was estimated by assuming equilibrium with the first 0.5 mm (d_p) of the rock matrix:

$$K_a = K_d \rho_b d_p = \left(\varepsilon_p + \left(1-\varepsilon_p\right) K'_d \rho_s\right) d_p \qquad (25)$$

The porosity, ε_p of the fracture coating was assumed to be 0.05 for all rock types.

The materials property group, *MPG* and surface sorption parameter, K_a have been calculated based upon the recommended data given in the Task 6C report and are plotted in Figure 9 below in the form of a parameter space diagram:

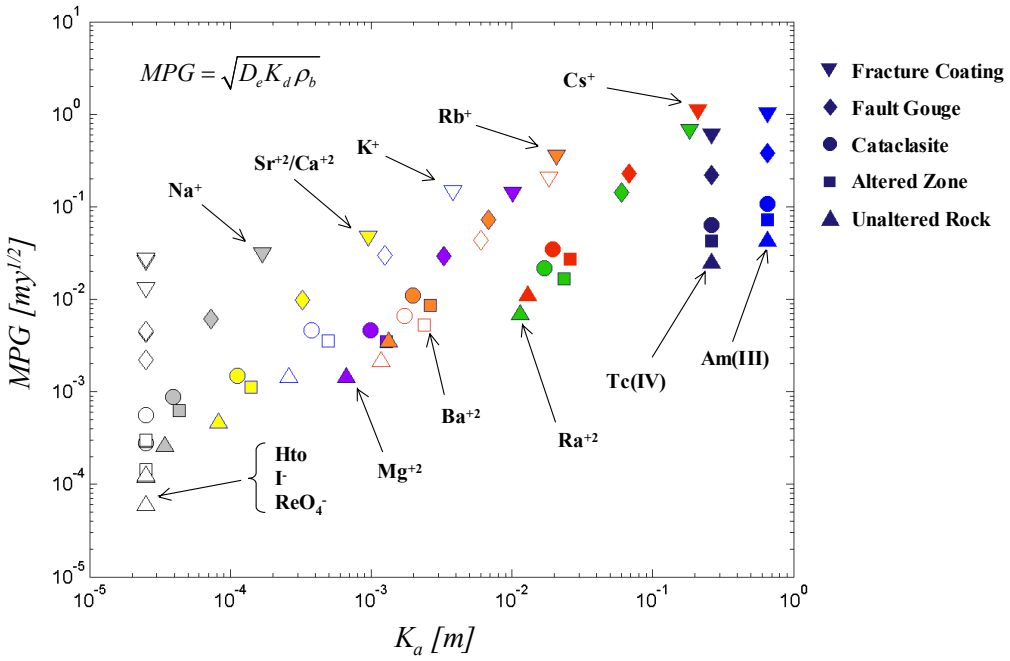

Figure 9. *Parameter space diagram for various tracers showing materials property group (MPG) plotted against estimated K_a. Symbols indicate data for different rock types.*

4 Task 6D

4.1 Modelling strategy

The DFN definitions given in the data distribution were used to generate an equivalent channel network representation in CHAN3D. Initially, the entire 200 m Block Scale volume was simulated for the purpose of obtaining new boundary conditions. The 200 m Block Scale volume was discretised into a cube with dimensions of 101×101×101 nodes. The individual channel members making up the channel network were 2 m in length for these initial simulations.

After these initial hydraulic simulations were performed, the average values of the head field for 20 realisations were used to estimate new fixed head boundary conditions at the faces of the 75 m reduced simulation volume. The 75 m simulation cube had dimensions of 76×76×76 nodes with a channel length of 1 m.

In all hydraulic simulations, flow injection and pumping (recovery) were performed at single nodes. The injection and recovery nodes (resident in conductive fractures) were selected on the basis of closest proximity to the given injection and recovery coordinates specified in the Task 6D specification. The coordinates of the injection source and recovery sink and associated flowrates were:

Table 2. Data for source and sink sections in tracer test C2 as defined in Task 6D data distribution.

	Source Section	Sink Section
Northing	7194.840	7186.294
Easting	1929.741	1914.628
Elevation	-476.100	-473.065
Flow	5.27 m^3/y (10 ml/min)	1024.3 m^3/y (1.95 l/min)

For channels identified as belonging to multiple fractures, the fault-type geological class was given precedence over non-fault geological class when assigning material properties. Channels resident in fault-type fractures were assigned properties for Cataclasite; Non-fault type channels were assigned material properties for unaltered rock. Surface sorption, K_a parameters were identically assumed to be for fracture coating material in both fault and non-fault fracture types. Similarly, the highest complexity factor was assumed to take precedence where there were conflicting fracture complexity definitions for channels shared between multiple fractures.

The flow-wetted surface of channels was normalised to give a total flow wetted surface corresponding to twice the DFN polygon surface area resident within the simulation volume (i.e., the polygon vertices were truncated to the simulation volume extents). The flow-wetted surface of individual channels was then multiplied by a scaling factor dependent upon the assigned complexity as defined in the data distribution (see Table 3 below).

Table 3. FWS-multiplier used to scale flow wetted surface of individual channels based upon complexity factor assigned in the Task 6D data distribution.

Complexity Factor	FWS-multiplier
1	1
2	2
3	3
4	5
5	10

Using the tracer injection data and recovery breakthrough curve for the non-sorbing tracer ReO_4^-, the flow porosity of the system was adjusted to give an approximate match between the simulated tracer recovery curve and the experimental data for the TRUE Block Scale tracer test C2. Calculations were then performed for the tracers, ^{129}I (assumed to have the same retention properties as ReO_4^-), ^{47}Ca, ^{137}Cs, ^{226}Ra, ^{99}Tc, and ^{241}Am. Although not actually used in the C2 tracer test, the injection time histories of ^{226}Ra, ^{99}Tc, and ^{241}Am were assumed to be the same as for ^{137}Cs.

In line with the Task 6D specifications, simulations were performed for both a Dirac pulse and also for the cumulative mass injection-time curves given for each tracer.

4.2 Model calibration

Boundary conditions were supplied in the form of six, 10×10 arrays of hydraulic head values corresponding to each of the six faces of the 200 m Block Scale volume. For the initial CHAN3D-flow simulations these were extrapolated to six, 101×101 arrays using bicubic 2D interpolation. The original boundary conditions in the data distribution are plotted in Figure 10 below:

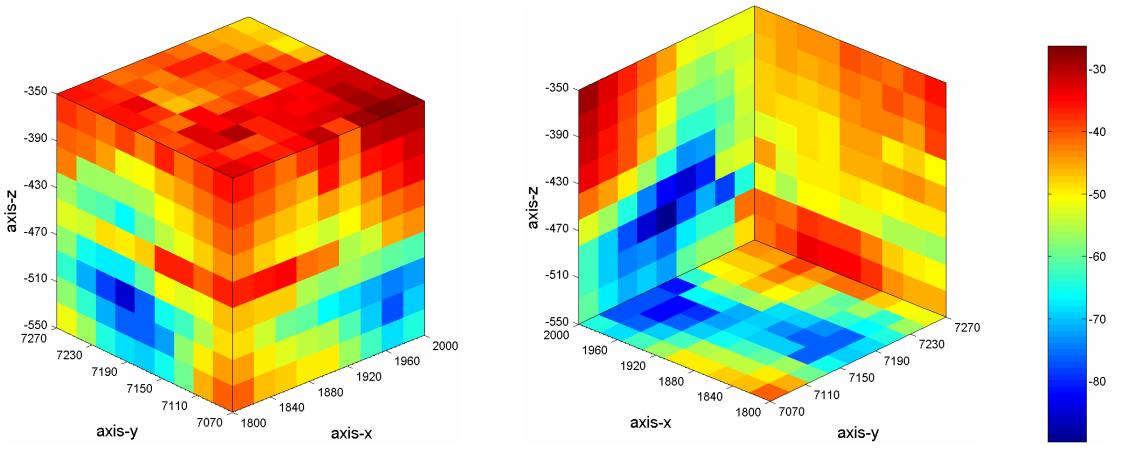

Figure 10 *Visualisation of original hydraulic head boundary conditions specified in the data distribution. Left-hand image shows forward perspective from above; Right-hand image shows a reverse angle image with view from below. All six boundary planes are visible in the images.*

The derived boundary conditions, interpolated to fit the 101×101 arrays needed for the 200 m simulations are shown below in Figure 11:

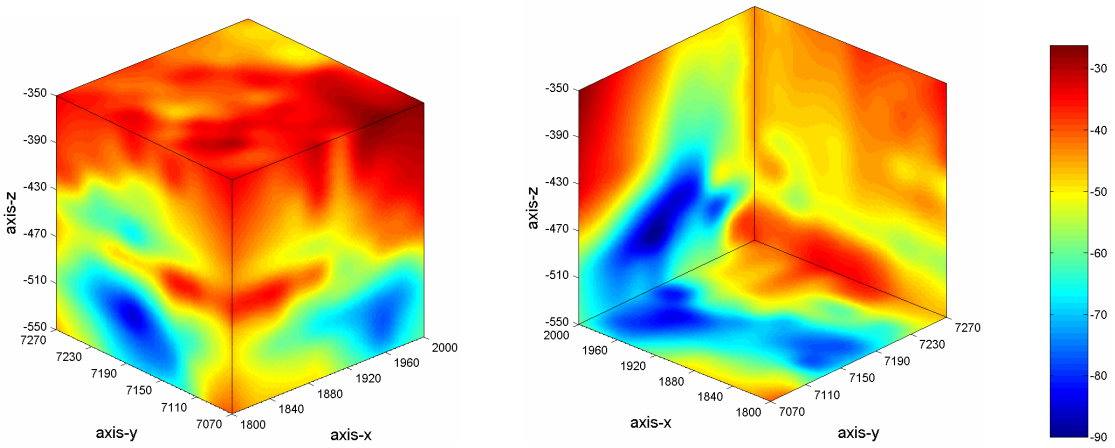

Figure 11. *Visualisation of interpolated hydraulic head boundary conditions for the 200 m Block Scale simulations. Left-hand image shows forward perspective from above; Right-hand image shows a reverse angle image with view from below. All six boundary planes are visible in the images.*

In subsequent simulations for the reduced 75 m-simulation cube, a new set of boundary conditions were interpolated from the results of the initial 200 m simulations. The new boundary conditions (i.e., six sets of 76×76 arrays) for the 75 m cube are shown in Figure 12 below:

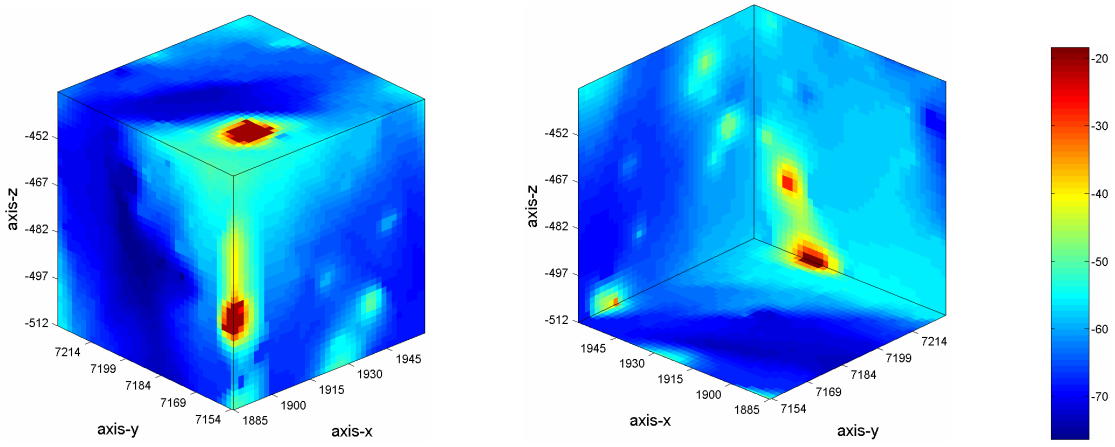

Figure 12. *Visualisation of interpolated hydraulic head boundary conditions for the 75m reduced volume simulations. Left-hand image shows forward perspective from above; Right-hand image shows a reverse angle image with view from below. All six boundary planes are visible in the images.*

In order to estimate the flow porosity of the system, a number of simulations were carried out with porosities varying in the range 1.0×10^{-5} – 1.75×10^{-4}. The appropriate flow-porosity for the simulations was then estimated by visual curve matching of the experimental breakthrough data for the non-sorbing tracer ReO_4^- (as a proxy for ^{129}I) with the simulated results using the injection-time history curve for the tracer test C2.

As the experimental and simulated breakthrough curves have a somewhat different overall shape, it was arbitrarily decided to match the breakthrough curves on the basis of t_{50} values (i.e., the time required to recover 50% of the total recovered tracer activity).

In the C2 tracer experiment roughly 80% of the injected tracer was recovered. It is uncertain whether this tracer was delayed along slow flowpaths to such an extent that it didn't show up in the breakthrough data (owing to the short half-life of the tracer), or whether a fraction of the tracer was lost along flowpaths that didn't eventually end up at the recovery borehole.

We feel that the former is more likely, although we cannot say for certain as the recorded tracer activity ends after about 500 hours for the ReO_4^- recovery. If we assume that the limit of detection is roughly equal to that of the first recovered activity at 38 hours, the tracer activity at 500 hours is about 20 times higher than this value. However, the recovery data have been corrected for radioactive decay and given that ^{186}Re has a half-life of 90 hours, we would therefore expect the "corrected" activity corresponding to the limit of detection at 500 hours to be about 35 times higher than the corrected limit of detection at 38 hours (the period from 38 h to 500 h is approximately 5 half-lives of ^{186}Re). The final recovered activity in the experimental recovery data set is roughly 18 times higher than that observed at 38 hours.

If the tracer was delayed, we should expect some of it to appear at times later than 500 hours as the recovery of other injected tracers extends to as long as 18 000 hours. It seems, however, that this may not be possible to achieve using this tracer at times much later than about 500 hours owing to the short half-life of ^{186}Re.

The meaning of 50% recovery of the injected tracer therefore represents a conceptual problem when attempting to match breakthrough times owing to that 100% of the injected tracer ends up at the recovery borehole in the numerical simulations. For the purposes of Task 6D, however, we have chosen to base the flow-porosity calibration procedure upon the time corresponding to 50% of the recovered activity rather than 50% of the injected activity. Therefore, 5%, 50% and 95% of the recovered tracer actually correspond to 4%, 40%, and 76% of the injected tracer. Figure 13 below shows the results of a number of CHAN3D simulations where the flow porosity was varied in order to find the best fit with the experimental data.

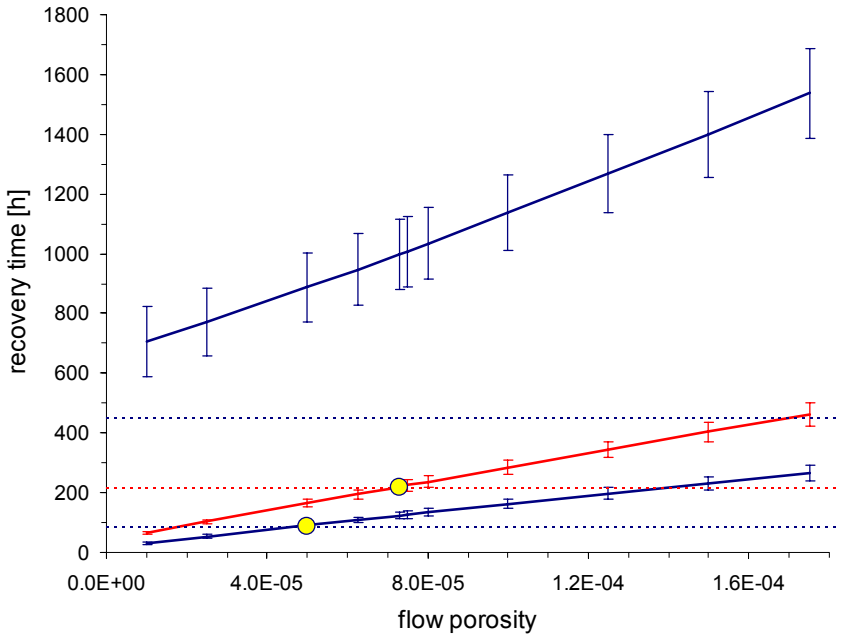

Figure 13. *Calibration data for the estimation of the flow porosity. Broken lines indicate times for 5%, 50%, and 95% (t_{05}, t_{50}, and t_{95}) of the recovered tracer. Solid curves show simulation results for mean t_{05}, t_{50}, and t_{95} obtained from 20 CHAN3D realisations where error bars correspond to one standard deviation of the mean values. Yellow symbols indicate flow porosities where experimental and simulated t_{05} and t_{50} times coincide.*

The best fit of the recovery data based upon recovery t_{50} values was obtained with a flow porosity, $\varepsilon_f = 7.3\times10^{-5}$.

Figure 14 below shows the activity-time breakthrough curve for this calibration simulation:

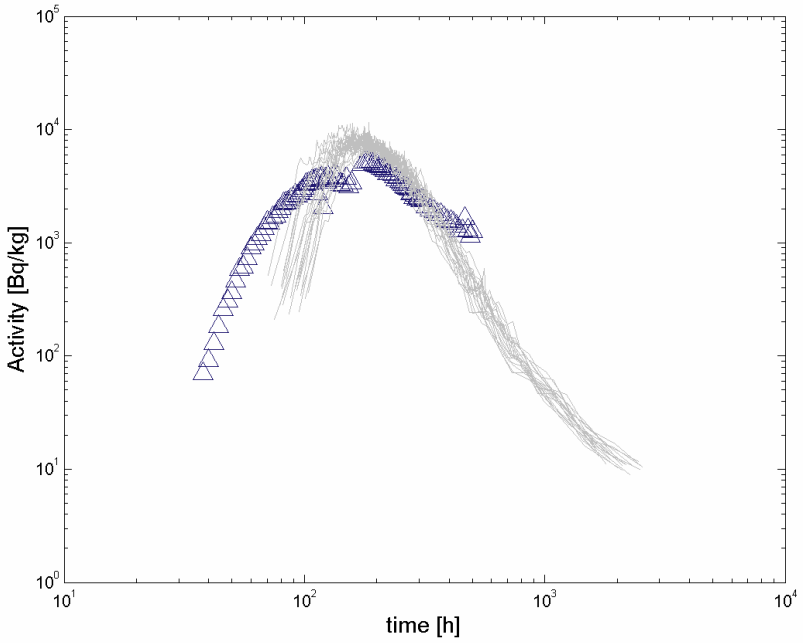

Figure 14. *Typical breakthrough data for CHAN3D simulations (grey curves) shown against experimental data (symbols) for a flow porosity of $\varepsilon_f = 7.3\times10^{-5}$. The simulation data represent 20 CHAN3D flow and transport realisations.*

As can be seen in Figure 14, the best fit CHAN3D simulation based upon the experimental t_{50} recovery time for the injected tracer does not give a good match for the early tracer breakthrough. If, instead, the calibration was based upon the experimental t_{05} recovery time (i.e., the time corresponding to 5% of the recovered tracer), the best-fit flow porosity is, $\varepsilon_f = 5\times10^{-5}$. The activity-time breakthrough curve for this case is given in Figure 15 below:

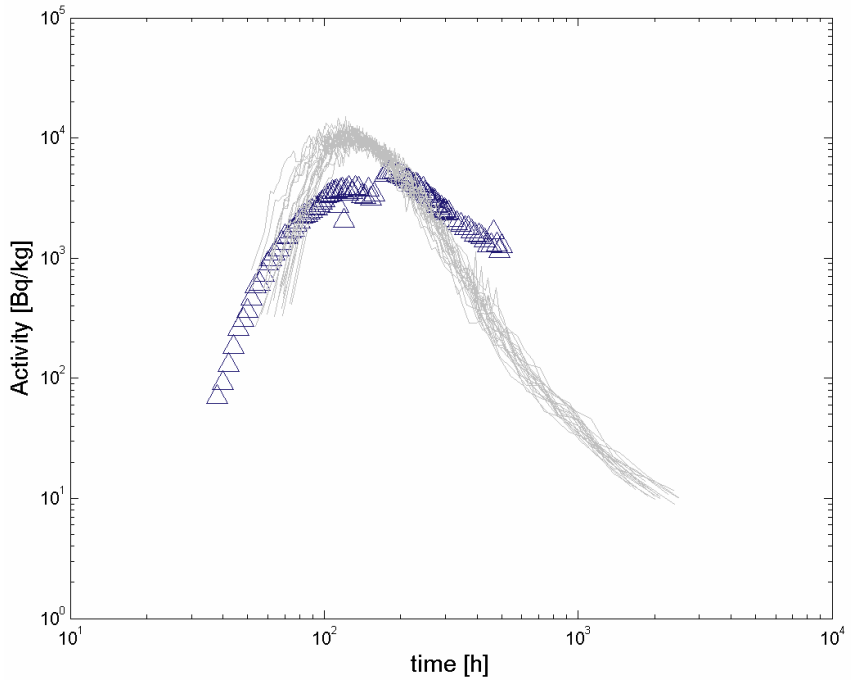

Figure 15. *Typical breakthrough data for CHAN3D simulations (grey curves) shown against experimental data (symbols) for a flow porosity of $\varepsilon_f = 5\times10^{-5}$. The simulation data represent 20 CHAN3D flow and transport realisations.*

It is apparent from the data that dispersion in the actual fracture system is greater than that obtained in the simulations owing to the broad peak of the experimental tracer recovery curve and the fast breakthrough of tracer at early times. Although the peak tracer breakthrough times are approximately equal for a flow-porosity $\varepsilon_f = 7.3\times10^{-5}$, it is not possible to simultaneously reproduce the early tracer breakthrough of the experimental results. This would appear to indicate a significant degree of flowpath channelling in the experimental system that is not fully captured in the channel network representation of the Task 6C DFN model using the conductance distribution assumed for the base case simulations (i.e. log-normally distributed channel conductances with $\sigma_c = 1$).

For the base-case simulations given in the rest of this report, a flow-porosity of $\varepsilon_f = 7.3\times10^{-5}$ has been assumed as a basis for the transport calculations.

4.3 Results

4.3.1 Flow

Using CHAN3D, 20 flow and transport realisations were performed for the 75 m simulation of the tracer test C2. Owing to the large contrast in conductance between the active channels comprising the fracture system and the background network channels (see Section 3.2.2), there was some difficulty in obtaining a completely convergent solution to the groundwater flow problem. For a conductance standard deviation of $\sigma_c = 1$, however, the numerical non-convergence was largely restricted to non-active background channels in the network and therefore not significant for the flow mass balance along the main flowpaths. If there is significant non-convergence of the hydrological mass balance along major transport pathways, there is a strong tendency for non-physical "looping" effects to occur during the transport simulation particle tracking. There was no evidence of such looping effects occurring during any of the transport simulations carried out.

Description of flow paths

Tracer transport was found to occur along two principal flowpaths in the channel network (henceforth referred to as the upper- and the lower flowpath as indicated in Figure 16). The proportion of tracer following each flowpath varies from run to run, although with a mean split of 46/54 (i.e., upper flowpath/lower flowpath) over 20 realisations. Figure 16 below shows the tracer particle trajectory for a typical transport realisation:

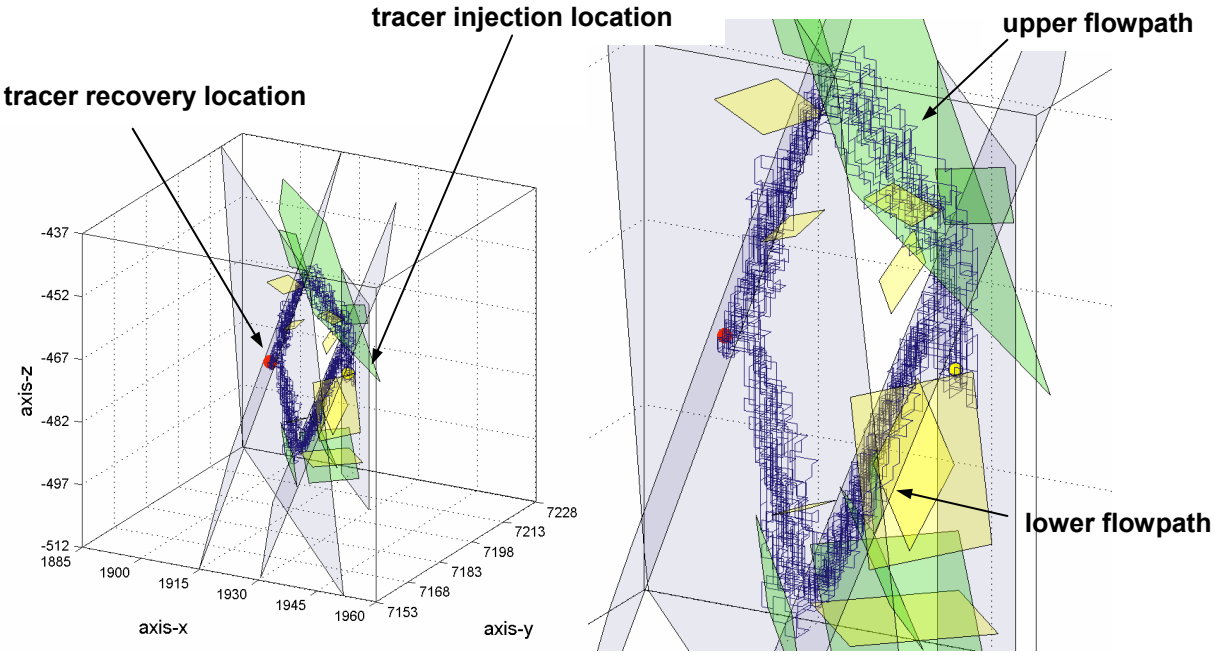

Figure 16. *Visualisation of tracer flowpaths for a typical CHAN3D-transport realisation. Particle tracks are shown in the context of DFN fracture planes within which tracer transport occurs. The data represents the trajectory of 100 particles randomly chosen from 10 000 actually used in the transport simulation. Tracer injection location is indicated with a yellow marker while tracer recovery location is shown with a red marker.*

The tracer particles were observed to travel predominantly in "deterministic" fractures 20D, 21D, 22D, and 23D as well as a number of minor background fractures (i.e., B and C type fractures) associated with these larger features. The background fracture, 1925B was particularly important for transport along the upper flowpath as can be seen from Figure 16 (large green shaded polygon in top right hand section of the upper flowpath).

Drawdown in injection and pumping borehole

Based on the results of 20 CHAN3D-flow realisations, the mean drawdown was found to be -66 m at the injection location and -343 m at the recovery borehole. Owing to the high pumping flowrate and given that a single network node was used to represent the recovery borehole, it is likely that the drawdown at the recovery location is unrealistically low. The mean drawdown in the 26 surrounding nodes lying one channel length distant from the recovery borehole is -173 m, or roughly half of the value at the recovery borehole node. The flowrate at the injection node, however, is relatively low and the mean drawdown in the surrounding nodes is roughly the same. The large change in drawdown occurs at the recovery borehole because of network connectivity issues (i.e., there are a maximum of six active channels connecting this node with the rest of the network) coupled with the high pumping flowrate used.

Water residence time distribution

Figure 17 below shows the water residence time distribution obtained for the given hydraulic boundary conditions and the best fit flow porosity of $\varepsilon_f = 7.3\times10^{-5}$:

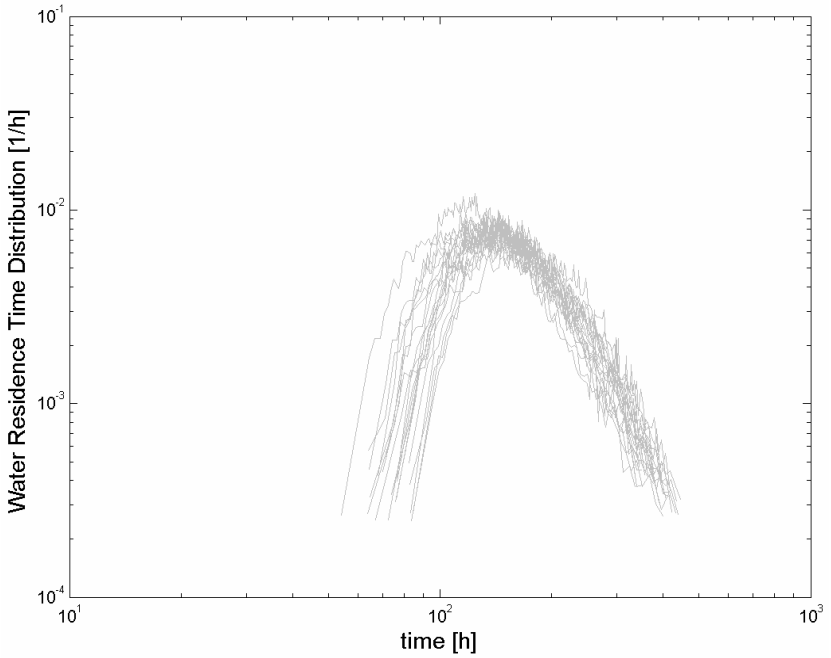

Figure 17. *Water residence time distribution (RTD) for 20 CHAN3D realisations ($\varepsilon_f = 7.3\times10^{-5}$).*

For comparative purposes, three individual realisations have been selected from the original set of 20. These individual runs representing different flow splits between the upper and lower flow paths are shown in Figure 18 below:

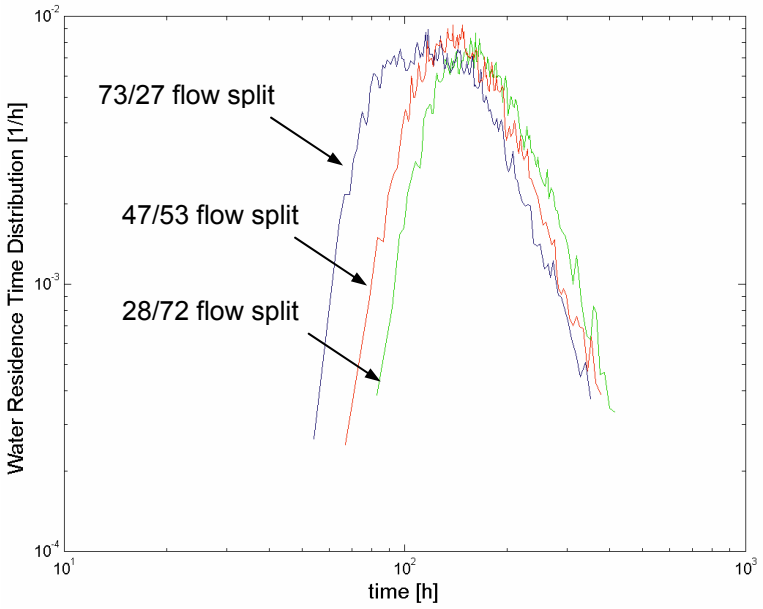

Figure 18. *Water residence time distribution (RTD) for three separate realisations taken from the original set of 20. Each curve represents water RTD data for separate flow splits (i.e., upper/lower flowpath) as indicated in the figure.*

These data sub-sets were chosen as they approximately represent the minimum, median, and maximum tracer transport splits observed in the larger data set. The results indicate that the upper flowpath has a slightly shorter water residence time than the lower flowpath.

4.3.2 Transport

In the CHAN3D-transport simulations the radiotracers ^{129}I (assumed to have the same retention properties as ReO_4^-), ^{47}Ca, ^{137}Cs, ^{226}Ra, ^{99}Tc, and ^{241}Am have been simulated for both a Dirac pulse release scenario as well as for the experimental injection time history data as specified in the task specification. The following sections detail the results of the individual tracer transport simulations.

β-factor

The β-factor for tracer transport is a parameter describing the flow-wetted surface to flow ratio (FWS/Q). It is the dominant parameter governing the transport of sorbing tracers and also the least well characterised for actual fracture systems. The CHAN3D-transport program calculates two related parameters, ϕ and ψ which describe the average transport properties of channels integrated over the paths taken by tracer particles through the system. They are calculated separately for each individual particle thereby giving a distribution of values. These parameters are defined in the following way:

$$\phi = \int_0^z \frac{R_*}{u}\, dz = \sum_i \left(t_{w(i)} + K_{a(i)} \times \frac{FWS_{(i)}}{q_{(i)}} \right) \tag{26}$$

$$\psi = \int_0^z \frac{W\sqrt{D_e K_d \rho_p}}{q}\, dz = \sum_i \frac{FWS_{(i)}}{2\, q_{(i)}} \sqrt{D_{e(i)} K_{d(i)} \rho_{p(i)}} \tag{27}$$

Where z is the ultimate distance travelled along the particular flowpath, u is the local fluid velocity, and i relates to the individual channels encountered along that flowpath.

For a strongly sorbing tracer such as ^{241}Am, the water residence time, t_w is negligible compared to the second term on the right hand side of equation 26. The β-factor (FWS/Q) can therefore be estimated from the flowpath-integrated value of ϕ using:

$$\beta = \frac{\phi}{K_a} = \sum_i \left(\frac{FWS_{(i)}}{q_{(i)}} \right) \tag{28}$$

Using the breakthrough data for ^{241}Am, the following distribution was obtained for the three realisations discussed in section 0:

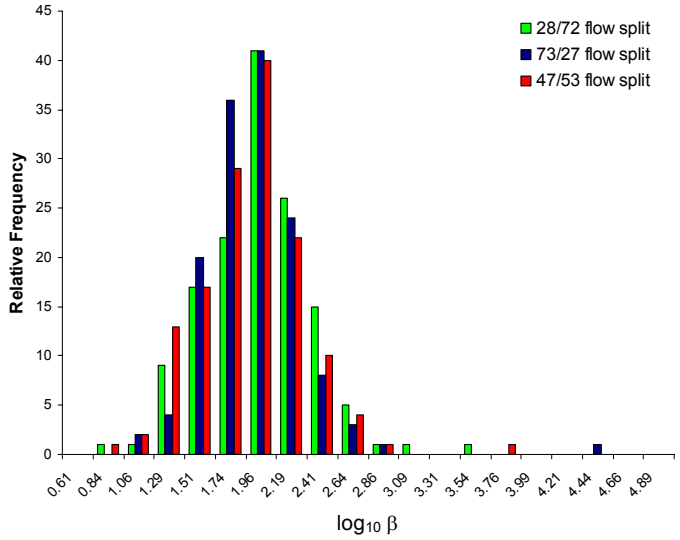

Figure 19. *β-factor frequency histogram for three separate realisations taken from the original set of 20. Each data set represents results for separate flow splits (i.e., upper/lower flowpath) as indicated in the figure.*

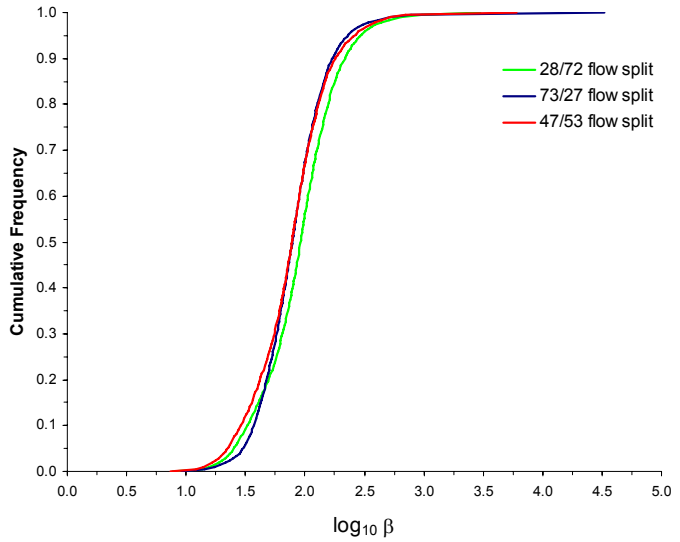

Figure 20. *β-factor cumulative frequency histogram for three separate realisations taken from the original set of 20. Each data set represents results for separate flow splits (i.e., upper/lower flowpath) as indicated in the figure.*

Breakthrough time history for the tracers

Breakthrough curves for measured injection curves

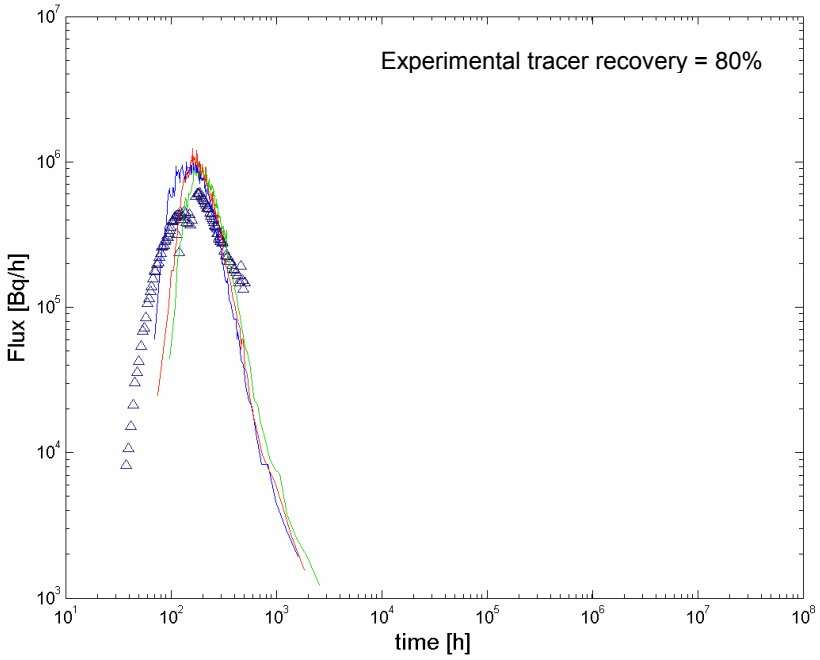

Figure 21. *Radionuclide flux vs. time, breakthrough curve for ^{131}I. Plotted symbols represent breakthrough curve for ReO_4^- obtained in tracer test C2, field experiment. Results are shown for three separate realisations (blue curve is for 73/27 split, red curve is 47/53 split, and green curve is for 28/72 split).*

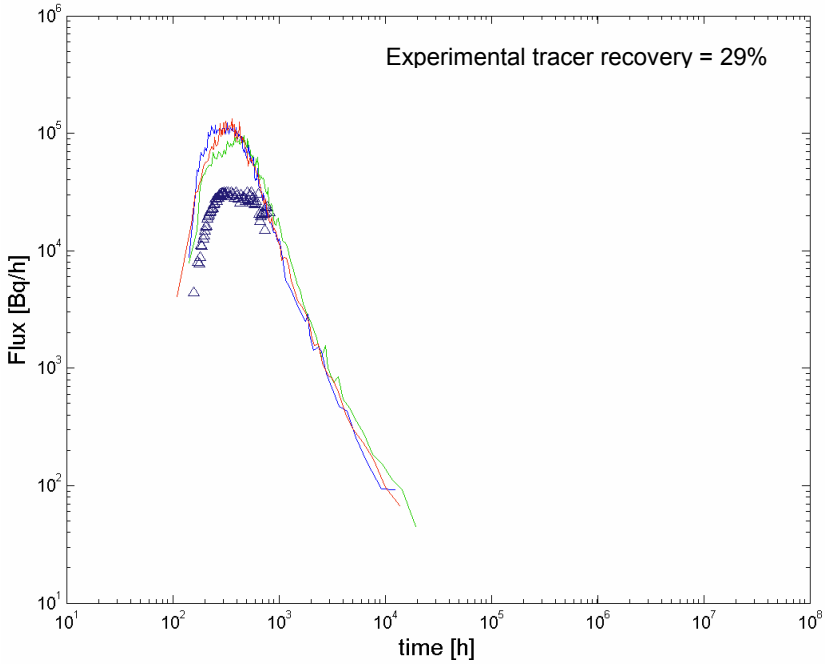

Figure 22. *Radionuclide flux vs. time, breakthrough curve for ^{47}Ca. Plotted symbols represent breakthrough curve obtained in tracer test C2, field experiment. Results are shown for three separate realisations (blue curve is for 73/27 split, red curve is 47/53 split, and green curve is for 28/72 split).*

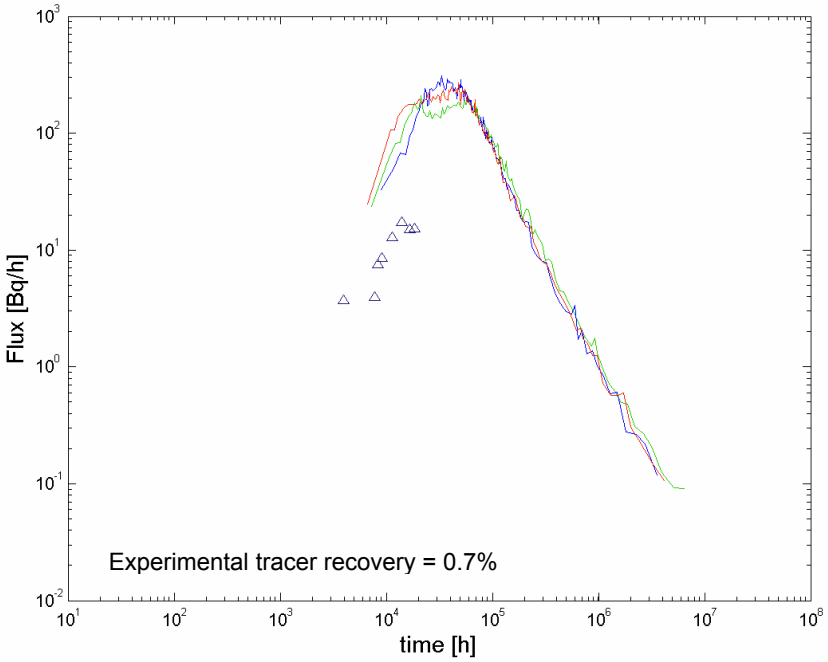

Figure 23. *Radionuclide flux vs. time, breakthrough curve for ^{137}Cs. Plotted symbols represent breakthrough curve obtained in tracer test C2, field experiment. Results are shown for three separate realisations (blue curve is for 73/27 split, red curve is 47/53 split, and green curve is for 28/72 split).*

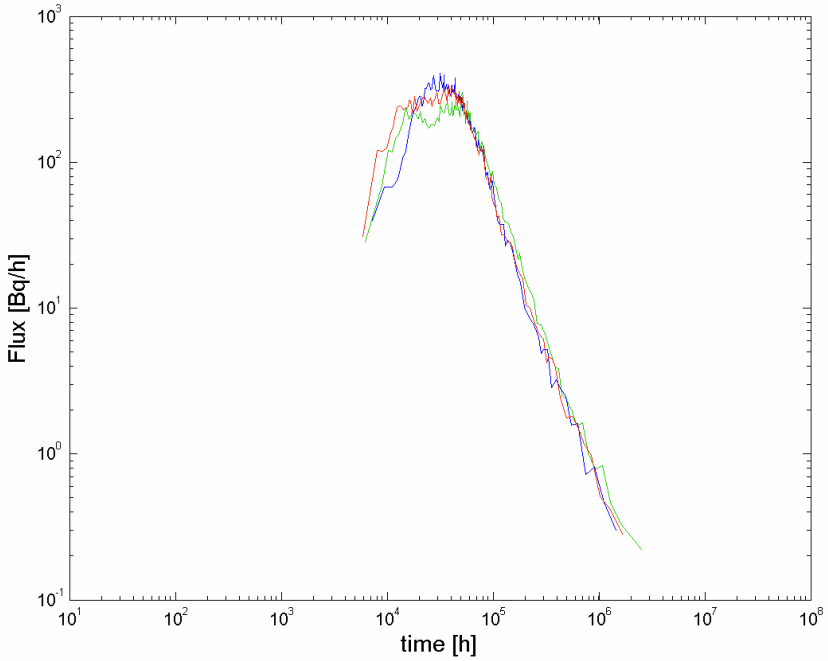

Figure 24. *Radionuclide flux vs. time, breakthrough curve for ^{226}Ra. Results are shown for three separate realisations (blue curve is for 73/27 split, red curve is 47/53 split, and green curve is for 28/72 split).*

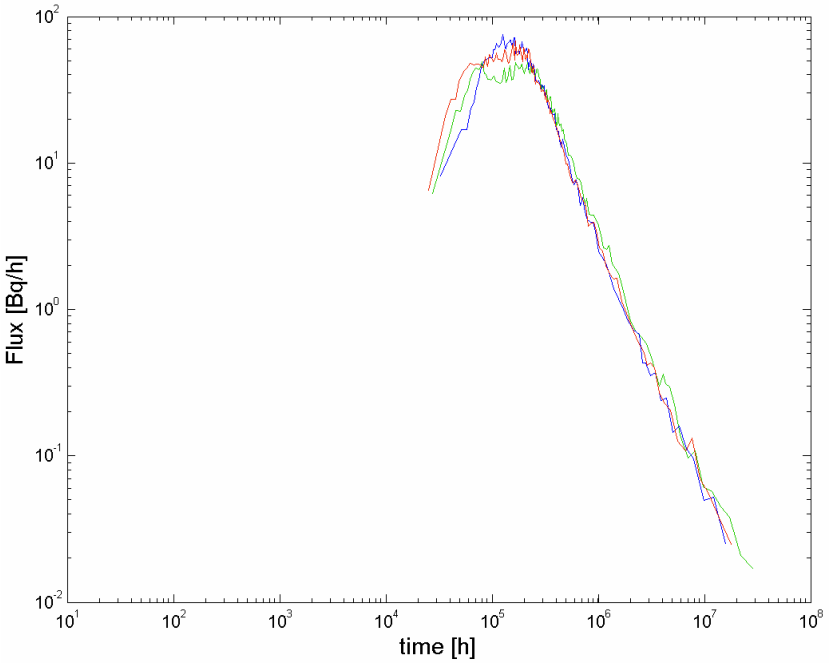

Figure 25. *Radionuclide flux vs. time, breakthrough curve for ^{99}Tc. Results are shown for three separate realisations (blue curve is for 73/27 split, red curve is 47/53 split, and green curve is for 28/72 split).*

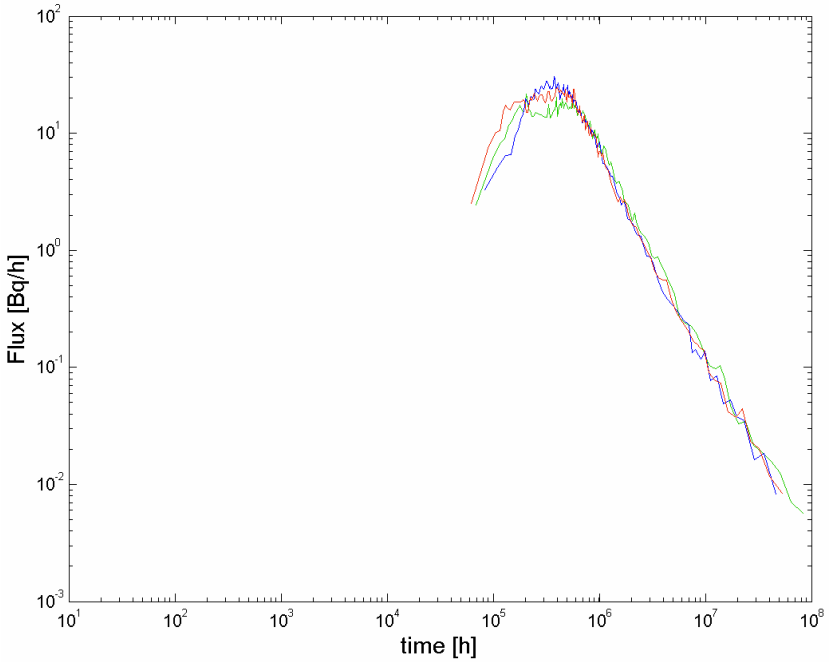

Figure 26. *Radionuclide flux vs. time, breakthrough curve for ^{241}Am. Results are shown for three separate realisations (blue curve is for 73/27 split, red curve is 47/53 split, and green curve is for 28/72 split).*

Breakthrough times for recovery of 5, 50 and 95% of the injected mass

Table 4. Simulated recovery times for 5%, 50%, and 95% of injected ^{131}I tracer activity. Realisations 2, 4, and 13 (bold text) correspond to breakthrough curves depicted previously.

Realisation #	Recovery Times [h]			Tracer Flowpath Split	
	t_{05} (5%)	t_{50} (50%)	t_{95} (95%)	upper path	lower path
1	129	226	1032	0.44	0.56
2	**136**	**239**	**1246**	**0.28**	**0.72**
3	140	231	892	0.46	0.54
4	**98**	**191**	**817**	**0.73**	**0.27**
5	111	200	844	0.51	0.49
6	114	206	1015	0.33	0.67
7	132	243	1027	0.46	0.54
8	128	223	1104	0.40	0.60
9	122	208	897	0.44	0.56
10	123	228	996	0.40	0.60
11	108	206	850	0.20	0.80
12	144	257	1205	0.43	0.57
13	**123**	**211**	**942**	**0.47**	**0.53**
14	130	221	1060	0.38	0.62
15	120	228	1142	0.55	0.45
16	111	214	952	0.62	0.38
17	129	220	943	0.57	0.43
18	113	187	897	0.56	0.44
19	128	235	1063	0.35	0.65
20	135	230	1019	0.56	0.44

Table 5. Simulated recovery times for 5%, 50%, and 95% of injected ^{47}Ca tracer activity. Realisations 2, 4, and 13 (bold text) correspond to breakthrough curves depicted previously.

Realisation #	Recovery Times [h]			Tracer Flowpath Split	
	t_{05} (5%)	t_{50} (50%)	t_{95} (95%)	upper path	lower path
1	261	536	8728	0.44	0.56
2	**227**	**559**	**11579**	**0.28**	**0.72**
3	251	524	6847	0.46	0.54
4	**205**	**451**	**6580**	**0.73**	**0.27**
5	215	462	6156	0.51	0.49
6	186	480	8157	0.33	0.67
7	258	583	8598	0.46	0.54
8	238	524	9179	0.40	0.60
9	217	478	6928	0.44	0.56
10	237	543	7858	0.40	0.60
11	170	470	6292	0.20	0.80
12	279	599	10925	0.43	0.57
13	**212**	**470**	**7589**	**0.47**	**0.53**
14	244	507	8651	0.38	0.62
15	258	538	10284	0.55	0.45
16	251	509	8068	0.62	0.38
17	253	502	7469	0.57	0.43
18	200	444	7932	0.56	0.44
19	249	557	9324	0.35	0.65
20	242	528	8726	0.56	0.44

Table 6. Simulated recovery times for 5%, 50%, and 95% of injected ^{137}Cs tracer activity. Realisations 2, 4, and 13 (bold text) correspond to breakthrough curves depicted previously.

Realisation #	Recovery Times [h]			Tracer Flowpath Split	
	t_{05} (5%)	t_{50} (50%)	t_{95} (95%)	upper path	lower path
1	2.51×10^{4}	8.35×10^{4}	3.14×10^{6}	0.44	0.56
2	$\mathbf{1.92\times10^{4}}$	$\mathbf{8.64\times10^{4}}$	$\mathbf{3.73\times10^{6}}$	**0.28**	**0.72**
3	2.15×10^{4}	7.93×10^{4}	2.28×10^{6}	0.46	0.54
4	$\mathbf{2.17\times10^{4}}$	$\mathbf{6.84\times10^{4}}$	$\mathbf{2.23\times10^{6}}$	**0.73**	**0.27**
5	2.15×10^{4}	6.93×10^{4}	2.16×10^{6}	0.51	0.49
6	1.54×10^{4}	7.31×10^{4}	2.58×10^{6}	0.33	0.67
7	2.56×10^{4}	9.04×10^{4}	2.90×10^{6}	0.46	0.54
8	2.31×10^{4}	8.07×10^{4}	2.99×10^{6}	0.40	0.60
9	1.91×10^{4}	7.17×10^{4}	2.27×10^{6}	0.44	0.56
10	2.07×10^{4}	8.38×10^{4}	2.78×10^{6}	0.40	0.60
11	1.32×10^{4}	6.92×10^{4}	2.19×10^{6}	0.20	0.80
12	2.68×10^{4}	9.51×10^{4}	3.58×10^{6}	0.43	0.57
13	$\mathbf{1.70\times10^{4}}$	$\mathbf{6.93\times10^{4}}$	$\mathbf{2.41\times10^{6}}$	**0.47**	**0.53**
14	2.14×10^{4}	7.82×10^{4}	2.75×10^{6}	0.38	0.62
15	2.74×10^{4}	8.52×10^{4}	3.28×10^{6}	0.55	0.45
16	2.84×10^{4}	7.85×10^{4}	2.74×10^{6}	0.62	0.38
17	2.35×10^{4}	7.47×10^{4}	2.40×10^{6}	0.57	0.43
18	1.68×10^{4}	6.77×10^{4}	2.42×10^{6}	0.56	0.44
19	2.30×10^{4}	8.79×10^{4}	3.34×10^{6}	0.35	0.65
20	2.08×10^{4}	7.94×10^{4}	2.95×10^{6}	0.56	0.44

Table 7. Simulated recovery times for 5%, 50%, and 95% of injected ^{226}Ra tracer activity. Realisations 2, 4, and 13 (bold text) correspond to breakthrough curves depicted previously.

Realisation #	Recovery Times [h]			Tracer Flowpath Split	
	t_{05} (5%)	t_{50} (50%)	t_{95} (95%)	upper path	lower path
1	2.05×10^{4}	6.33×10^{4}	1.28×10^{6}	0.44	0.56
2	$\mathbf{1.56\times10^{4}}$	$\mathbf{6.48\times10^{4}}$	$\mathbf{1.55\times10^{6}}$	**0.28**	**0.72**
3	1.75×10^{4}	6.00×10^{4}	9.32×10^{5}	0.46	0.54
4	$\mathbf{1.82\times10^{4}}$	$\mathbf{5.27\times10^{4}}$	$\mathbf{8.95\times10^{5}}$	**0.73**	**0.27**
5	1.79×10^{4}	5.29×10^{4}	8.85×10^{5}	0.51	0.49
6	1.25×10^{4}	5.53×10^{4}	1.11×10^{6}	0.33	0.67
7	2.07×10^{4}	6.82×10^{4}	1.19×10^{6}	0.46	0.54
8	1.88×10^{4}	6.02×10^{4}	1.25×10^{6}	0.40	0.60
9	1.58×10^{4}	5.45×10^{4}	9.39×10^{5}	0.44	0.56
10	1.72×10^{4}	6.39×10^{4}	1.14×10^{6}	0.40	0.60
11	1.09×10^{4}	5.28×10^{4}	9.13×10^{5}	0.20	0.80
12	2.17×10^{4}	6.99×10^{4}	1.48×10^{6}	0.43	0.57
13	$\mathbf{1.39\times10^{4}}$	$\mathbf{5.31\times10^{4}}$	$\mathbf{1.00\times10^{6}}$	**0.47**	**0.53**
14	1.75×10^{4}	5.92×10^{4}	1.11×10^{6}	0.38	0.62
15	2.27×10^{4}	6.39×10^{4}	1.33×10^{6}	0.55	0.45
16	2.38×10^{4}	5.98×10^{4}	1.10×10^{6}	0.62	0.38
17	1.91×10^{4}	5.68×10^{4}	9.71×10^{5}	0.57	0.43
18	1.37×10^{4}	5.20×10^{4}	9.91×10^{5}	0.56	0.44
19	1.88×10^{4}	6.58×10^{4}	1.35×10^{6}	0.35	0.65
20	1.68×10^{4}	6.02×10^{4}	1.18×10^{6}	0.56	0.44

Table 8. Simulated recovery times for 5%, 50%, and 95% of injected ^{99}Tc tracer activity. Realisations 2, 4, and 13 (bold text) correspond to breakthrough curves depicted previously.

Realisation #	Recovery Times [h]			Tracer Flowpath Split	
	t_{05} (5%)	t_{50} (50%)	t_{95} (95%)	upper path	lower path
1	9.60×10^{4}	3.32×10^{5}	1.43×10^{7}	0.44	0.56
2	**7.28×10^{4}**	**3.42×10^{5}**	**1.66×10^{7}**	**0.28**	**0.72**
3	8.20×10^{4}	3.13×10^{5}	1.01×10^{7}	0.46	0.54
4	**8.29×10^{4}**	**2.72×10^{5}**	**9.64×10^{6}**	**0.73**	**0.27**
5	8.19×10^{4}	2.73×10^{5}	9.90×10^{6}	0.51	0.49
6	5.82×10^{4}	2.87×10^{5}	1.16×10^{7}	0.33	0.67
7	9.79×10^{4}	3.62×10^{5}	1.30×10^{7}	0.46	0.54
8	8.79×10^{4}	3.19×10^{5}	1.32×10^{7}	0.40	0.60
9	7.28×10^{4}	2.84×10^{5}	1.02×10^{7}	0.44	0.56
10	7.83×10^{4}	3.32×10^{5}	1.21×10^{7}	0.40	0.60
11	4.99×10^{4}	2.73×10^{5}	9.60×10^{6}	0.20	0.80
12	1.02×10^{5}	3.78×10^{5}	1.62×10^{7}	0.43	0.57
13	**6.44×10^{4}**	**2.74×10^{5}**	**1.05×10^{7}**	**0.47**	**0.53**
14	8.19×10^{4}	3.10×10^{5}	1.18×10^{7}	0.38	0.62
15	1.05×10^{5}	3.39×10^{5}	1.51×10^{7}	0.55	0.45
16	1.10×10^{5}	3.14×10^{5}	1.24×10^{7}	0.62	0.38
17	8.94×10^{4}	2.98×10^{5}	1.10×10^{7}	0.57	0.43
18	6.37×10^{4}	2.67×10^{5}	1.10×10^{7}	0.56	0.44
19	8.75×10^{4}	3.48×10^{5}	1.45×10^{7}	0.35	0.65
20	7.91×10^{4}	3.15×10^{5}	1.35×10^{7}	0.56	0.44

Table 9. Simulated recovery times for 5%, 50%, and 95% of injected ^{241}Am tracer activity. Realisations 2, 4, and 13 (bold text) correspond to breakthrough curves depicted previously.

Realisation #	Recovery Times [h]			Tracer Flowpath Split	
	t_{05} (5%)	t_{50} (50%)	t_{95} (95%)	upper path	lower path
1	2.45×10^{5}	8.66×10^{5}	4.21×10^{7}	0.44	0.56
2	1.85×10^{5}	8.97×10^{5}	4.91×10^{7}	**0.28**	**0.72**
3	2.08×10^{5}	8.17×10^{5}	2.98×10^{7}	0.46	0.54
4	2.09×10^{5}	7.09×10^{5}	2.82×10^{7}	**0.73**	**0.27**
5	2.08×10^{5}	7.12×10^{5}	2.89×10^{7}	0.51	0.49
6	1.48×10^{5}	7.48×10^{5}	3.37×10^{7}	0.33	0.67
7	2.48×10^{5}	9.50×10^{5}	3.85×10^{7}	0.46	0.54
8	2.24×10^{5}	8.35×10^{5}	3.91×10^{7}	0.40	0.60
9	1.85×10^{5}	7.38×10^{5}	2.96×10^{7}	0.44	0.56
10	1.99×10^{5}	8.65×10^{5}	3.59×10^{7}	0.40	0.60
11	1.26×10^{5}	7.07×10^{5}	2.81×10^{7}	0.20	0.80
12	2.60×10^{5}	9.89×10^{5}	4.78×10^{7}	0.43	0.57
13	1.64×10^{5}	7.12×10^{5}	3.08×10^{7}	**0.47**	**0.53**
14	2.07×10^{5}	8.13×10^{5}	3.50×10^{7}	0.38	0.62
15	2.66×10^{5}	8.87×10^{5}	4.43×10^{7}	0.55	0.45
16	2.77×10^{5}	8.22×10^{5}	3.66×10^{7}	0.62	0.38
17	2.27×10^{5}	7.79×10^{5}	3.23×10^{7}	0.57	0.43
18	1.61×10^{5}	6.93×10^{5}	3.23×10^{7}	0.56	0.44
19	2.22×10^{5}	9.10×10^{5}	4.28×10^{7}	0.35	0.65
20	2.01×10^{5}	8.24×10^{5}	3.98×10^{7}	0.56	0.44

Breakthrough curves for Dirac pulse injection

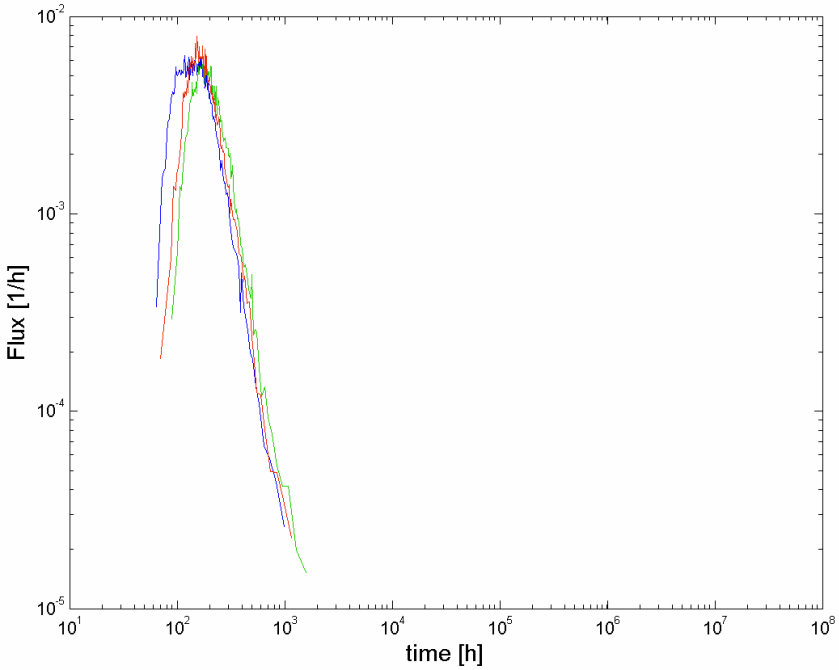

Figure 27. *Radionuclide flux vs. time, breakthrough curve for ^{131}I. Results are shown for three separate realisations of a Dirac pulse injection (blue curve is for 73/27 split, red curve is 47/53 split, and green curve is for 28/72 split).*

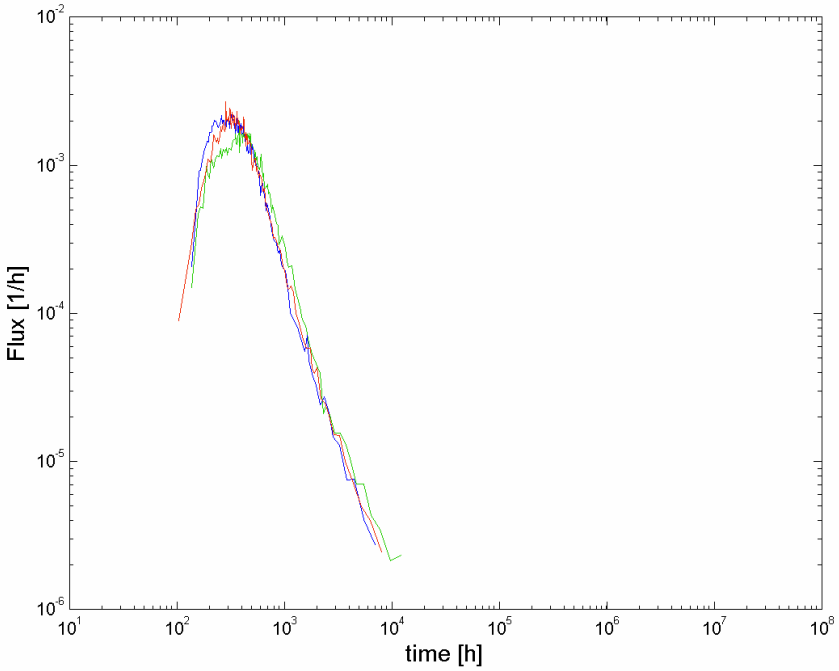

Figure 28. *Radionuclide flux vs. time, breakthrough curve for ^{47}Ca. Results are shown for three separate realisations of a Dirac pulse injection (blue curve is for 73/27 split, red curve is 47/53 split, and green curve is for 28/72 split).*

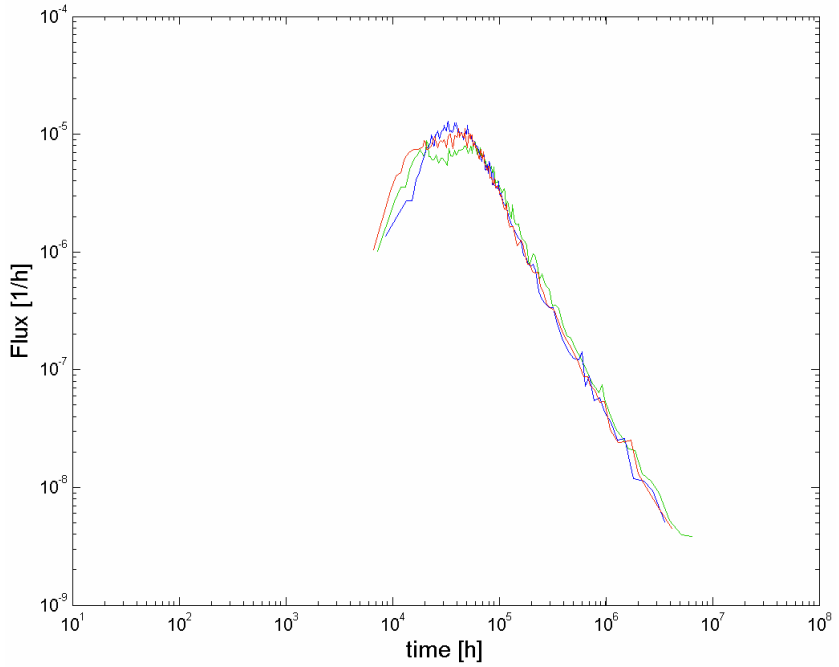

Figure 29. *Radionuclide flux vs. time, breakthrough curve for ^{137}Cs. Results are shown for three separate realisations of a Dirac pulse injection (blue curve is for 73/27 split, red curve is 47/53 split, and green curve is for 28/72 split).*

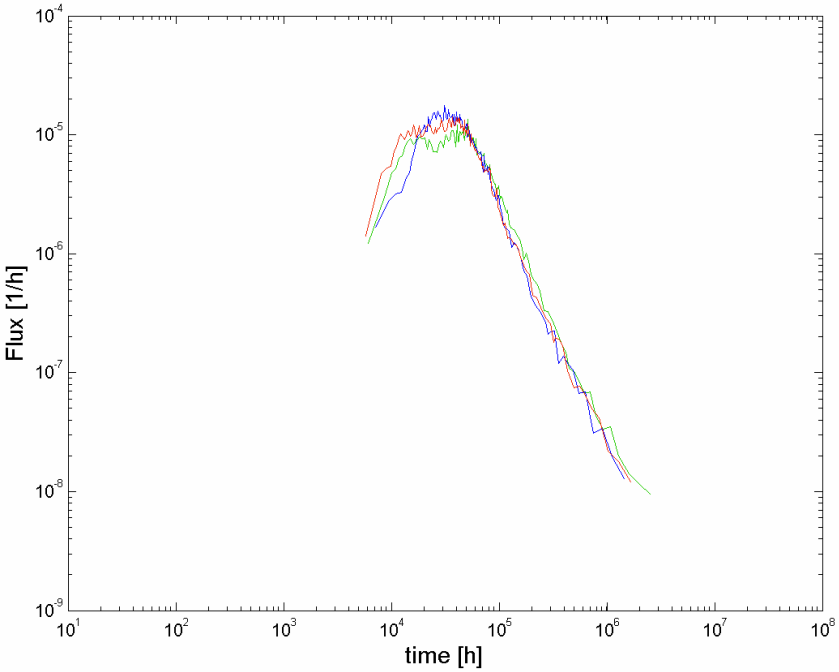

Figure 30. *Radionuclide flux vs. time, breakthrough curve for ^{226}Ra. Results are shown for three separate realisations of a Dirac pulse injection (blue curve is for 73/27 split, red curve is 47/53 split, and green curve is for 28/72 split).*

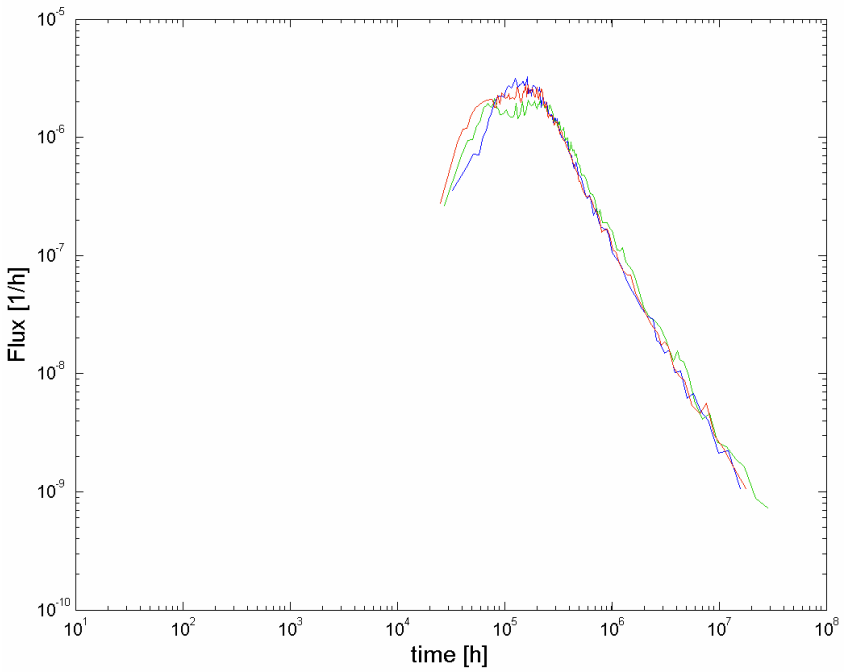

Figure 31. *Radionuclide flux vs. time, breakthrough curve for ^{99}Tc. Results are shown for three separate realisations of a Dirac pulse injection (blue curve is for 73/27 split, red curve is 47/53 split, and green curve is for 28/72 split).*

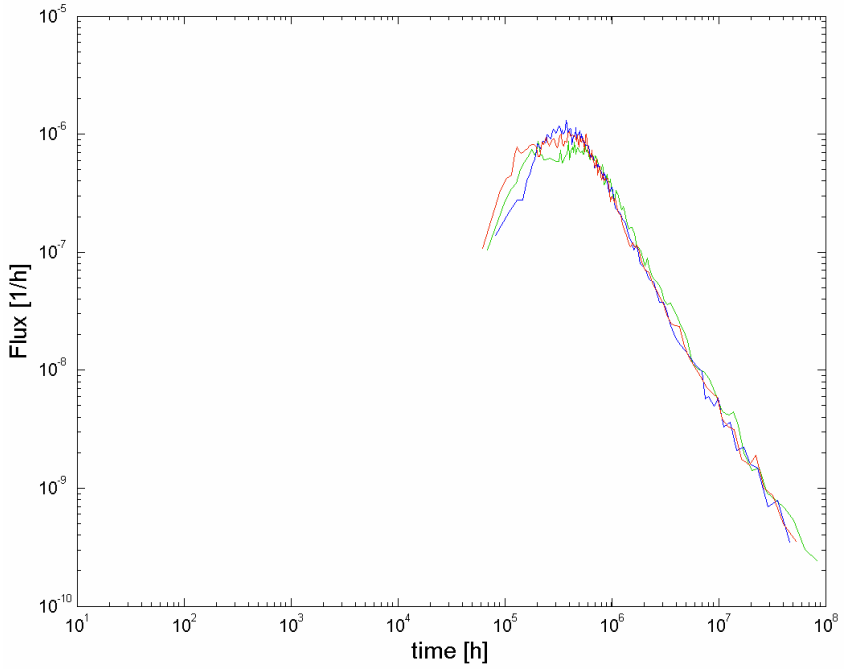

Figure 32. *Radionuclide flux vs. time, breakthrough curve for ^{241}Am. Results are shown for three separate realisations of a Dirac pulse injection (blue curve is for 73/27 split, red curve is 47/53 split, and green curve is for 28/72 split).*

Breakthrough times for recovery of 5, 50 and 95% of the Dirac pulse injection

Table 10. Simulated recovery times for 5%, 50%, and 95% of injected ^{131}I tracer activity (Dirac pulse). Realisations 2, 4, and 13 (bold text) correspond to breakthrough curves depicted previously.

Realisation #	Recovery Times [h]			Tracer Flowpath Split	
	t_{05} (5%)	t_{50} (50%)	t_{95} (95%)	upper path	lower path
1	119	208	802	0.44	0.56
2	**126**	**221**	**947**	**0.28**	**0.72**
3	130	213	690	0.46	0.54
4	**90**	**173**	**631**	**0.73**	**0.27**
5	101	183	642	0.51	0.49
6	104	188	783	0.33	0.67
7	121	227	818	0.46	0.54
8	117	205	817	0.40	0.60
9	112	191	712	0.44	0.56
10	112	211	798	0.40	0.60
11	97	189	683	0.20	0.80
12	133	240	927	0.43	0.57
13	**113**	**193**	**730**	**0.47**	**0.53**
14	120	203	806	0.38	0.62
15	109	210	906	0.55	0.45
16	101	197	744	0.62	0.38
17	119	202	762	0.57	0.43
18	103	171	704	0.56	0.44
19	117	218	786	0.35	0.65
20	125	211	816	0.56	0.44

Table 11. Simulated recovery times for 5%, 50%, and 95% of injected ^{47}Ca tracer activity (Dirac pulse). Realisations 2, 4, and 13 (bold text) correspond to breakthrough curves depicted previously.

Realisation #	Recovery Times [h]			Tracer Flowpath Split	
	t_{05} (5%)	t_{50} (50%)	t_{95} (95%)	upper path	lower path
1	250	515	6284	0.44	0.56
2	**214**	**540**	**7673**	**0.28**	**0.72**
3	239	508	4677	0.46	0.54
4	**193**	**435**	**4432**	**0.73**	**0.27**
5	204	444	4522	0.51	0.49
6	174	461	5557	0.33	0.67
7	247	563	5984	0.46	0.54
8	226	507	6155	0.40	0.60
9	205	461	4805	0.44	0.56
10	224	526	5707	0.40	0.60
11	157	451	4704	0.20	0.80
12	267	581	7400	0.43	0.57
13	**200**	**452**	**5055**	**0.47**	**0.53**
14	233	490	5488	0.38	0.62
15	248	519	6728	0.55	0.45
16	240	489	5444	0.62	0.38
17	240	484	4959	0.57	0.43
18	188	427	4977	0.56	0.44
19	237	541	6574	0.35	0.65
20	230	509	5879	0.56	0.44

Table 12. Simulated recovery times for 5%, 50%, and 95% of injected ^{137}Cs tracer activity (Dirac pulse). Realisations 2, 4, and 13 (bold text) correspond to breakthrough curves depicted previously.

Realisation #	Recovery Times [h]			Tracer Flowpath Split	
	t_{05} (5%)	t_{50} (50%)	t_{95} (95%)	upper path	lower path
1	2.50×10^{4}	8.33×10^{4}	3.14×10^{6}	0.44	0.56
2	$\mathbf{1.90\times10^{4}}$	$\mathbf{8.61\times10^{4}}$	$\mathbf{3.73\times10^{6}}$	**0.28**	**0.72**
3	2.13×10^{4}	7.90×10^{4}	2.28×10^{6}	0.46	0.54
4	$\mathbf{2.15\times10^{4}}$	$\mathbf{6.80\times10^{4}}$	$\mathbf{2.23\times10^{6}}$	**0.73**	**0.27**
5	2.13×10^{4}	6.89×10^{4}	2.16×10^{6}	0.51	0.49
6	1.53×10^{4}	7.27×10^{4}	2.58×10^{6}	0.33	0.67
7	2.55×10^{4}	9.01×10^{4}	2.90×10^{6}	0.46	0.54
8	2.30×10^{4}	8.05×10^{4}	2.99×10^{6}	0.40	0.60
9	1.89×10^{4}	7.16×10^{4}	2.27×10^{6}	0.44	0.56
10	2.04×10^{4}	8.36×10^{4}	2.78×10^{6}	0.40	0.60
11	1.31×10^{4}	6.89×10^{4}	2.19×10^{6}	0.20	0.80
12	2.67×10^{4}	9.49×10^{4}	3.58×10^{6}	0.43	0.57
13	$\mathbf{1.69\times10^{4}}$	$\mathbf{6.92\times10^{4}}$	$\mathbf{2.41\times10^{6}}$	**0.47**	**0.53**
14	2.12×10^{4}	7.80×10^{4}	2.75×10^{6}	0.38	0.62
15	2.72×10^{4}	8.50×10^{4}	3.28×10^{6}	0.55	0.45
16	2.82×10^{4}	7.83×10^{4}	2.74×10^{6}	0.62	0.38
17	2.33×10^{4}	7.46×10^{4}	2.40×10^{6}	0.57	0.43
18	1.66×10^{4}	6.74×10^{4}	2.42×10^{6}	0.56	0.44
19	2.28×10^{4}	8.77×10^{4}	3.34×10^{6}	0.35	0.65
20	2.06×10^{4}	7.92×10^{4}	2.95×10^{6}	0.56	0.44

Table 13. Simulated recovery times for 5%, 50%, and 95% of injected ^{226}Ra tracer activity (Dirac pulse). Realisations 2, 4, and 13 (bold text) correspond to breakthrough curves depicted previously.

Realisation #	Recovery Times [h]			Tracer Flowpath Split	
	t_{05} (5%)	t_{50} (50%)	t_{95} (95%)	upper path	lower path
1	2.03×10^{4}	6.30×10^{4}	1.28×10^{6}	0.44	0.56
2	$\mathbf{1.54\times10^{4}}$	$\mathbf{6.46\times10^{4}}$	$\mathbf{1.55\times10^{6}}$	**0.28**	**0.72**
3	1.73×10^{4}	5.97×10^{4}	9.32×10^{5}	0.46	0.54
4	$\mathbf{1.80\times10^{4}}$	$\mathbf{5.24\times10^{4}}$	$\mathbf{8.95\times10^{5}}$	**0.73**	**0.27**
5	1.77×10^{4}	5.25×10^{4}	8.85×10^{5}	0.51	0.49
6	1.23×10^{4}	5.51×10^{4}	1.11×10^{6}	0.33	0.67
7	2.06×10^{4}	6.80×10^{4}	1.19×10^{6}	0.46	0.54
8	1.87×10^{4}	5.99×10^{4}	1.25×10^{6}	0.40	0.60
9	1.57×10^{4}	5.42×10^{4}	9.35×10^{5}	0.44	0.56
10	1.70×10^{4}	6.36×10^{4}	1.14×10^{6}	0.40	0.60
11	1.08×10^{4}	5.26×10^{4}	9.13×10^{5}	0.20	0.80
12	2.14×10^{4}	6.95×10^{4}	1.48×10^{6}	0.43	0.57
13	$\mathbf{1.38\times10^{4}}$	$\mathbf{5.28\times10^{4}}$	$\mathbf{1.00\times10^{6}}$	**0.47**	**0.53**
14	1.73×10^{4}	5.89×10^{4}	1.11×10^{6}	0.38	0.62
15	2.24×10^{4}	6.36×10^{4}	1.33×10^{6}	0.55	0.45
16	2.37×10^{4}	5.96×10^{4}	1.10×10^{6}	0.62	0.38
17	1.90×10^{4}	5.66×10^{4}	9.71×10^{5}	0.57	0.43
18	1.35×10^{4}	5.19×10^{4}	9.91×10^{5}	0.56	0.44
19	1.86×10^{4}	6.57×10^{4}	1.35×10^{6}	0.35	0.65
20	1.66×10^{4}	5.99×10^{4}	1.18×10^{6}	0.56	0.44

Table 14. Simulated recovery times for 5%, 50%, and 95% of injected ^{99}Tc tracer activity (Dirac pulse). Realisations 2, 4, and 13 (bold text) correspond to breakthrough curves depicted previously.

Realisation #	Recovery Times [h]			Tracer Flowpath Split	
	t_{05} (5%)	t_{50} (50%)	t_{95} (95%)	upper path	lower path
1	9.58×10^{4}	3.31×10^{5}	1.43×10^{7}	0.44	0.56
2	**7.25×10^{4}**	**3.41×10^{5}**	**1.66×10^{7}**	**0.28**	**0.72**
3	8.20×10^{4}	3.13×10^{5}	1.01×10^{7}	0.46	0.54
4	**8.28×10^{4}**	**2.72×10^{5}**	**9.64×10^{6}**	**0.73**	**0.27**
5	8.16×10^{4}	2.72×10^{5}	9.89×10^{6}	0.51	0.49
6	5.80×10^{4}	2.87×10^{5}	1.16×10^{7}	0.33	0.67
7	9.76×10^{4}	3.61×10^{5}	1.30×10^{7}	0.46	0.54
8	8.77×10^{4}	3.19×10^{5}	1.32×10^{7}	0.40	0.60
9	7.26×10^{4}	2.83×10^{5}	1.02×10^{7}	0.44	0.56
10	7.81×10^{4}	3.32×10^{5}	1.21×10^{7}	0.40	0.60
11	4.98×10^{4}	2.72×10^{5}	9.60×10^{6}	0.20	0.80
12	1.02×10^{5}	3.77×10^{5}	1.62×10^{7}	0.43	0.57
13	**6.43×10^{4}**	**2.74×10^{5}**	**1.05×10^{7}**	**0.47**	**0.53**
14	8.11×10^{4}	3.10×10^{5}	1.18×10^{7}	0.38	0.62
15	1.05×10^{5}	3.38×10^{5}	1.51×10^{7}	0.55	0.45
16	1.09×10^{5}	3.14×10^{5}	1.24×10^{7}	0.62	0.38
17	8.93×10^{4}	2.97×10^{5}	1.10×10^{7}	0.57	0.43
18	6.35×10^{4}	2.67×10^{5}	1.10×10^{7}	0.56	0.44
19	8.75×10^{4}	3.47×10^{5}	1.45×10^{7}	0.35	0.65
20	7.86×10^{4}	3.15×10^{5}	1.35×10^{7}	0.56	0.44

Table 15. Simulated recovery times for 5%, 50%, and 95% of injected ^{241}Am tracer activity (Dirac pulse). Realisations 2, 4, and 13 (bold text) correspond to breakthrough curves depicted previously.

Realisation #	Recovery Times [h]			Tracer Flowpath Split	
	t_{05} (5%)	t_{50} (50%)	t_{95} (95%)	upper path	lower path
1	2.45×10^{5}	8.66×10^{5}	4.21×10^{7}	0.44	0.56
2	**1.85×10^{5}**	**8.97×10^{5}**	**4.91×10^{7}**	**0.28**	**0.72**
3	2.08×10^{5}	8.16×10^{5}	2.98×10^{7}	0.46	0.54
4	**2.09×10^{5}**	**7.09×10^{5}**	**2.82×10^{7}**	**0.73**	**0.27**
5	2.08×10^{5}	7.12×10^{5}	2.89×10^{7}	0.51	0.49
6	1.48×10^{5}	7.48×10^{5}	3.37×10^{7}	0.33	0.67
7	2.48×10^{5}	9.50×10^{5}	3.85×10^{7}	0.46	0.54
8	2.24×10^{5}	8.35×10^{5}	3.91×10^{7}	0.40	0.60
9	1.85×10^{5}	7.38×10^{5}	2.96×10^{7}	0.44	0.56
10	1.99×10^{5}	8.65×10^{5}	3.59×10^{7}	0.40	0.60
11	1.26×10^{5}	7.07×10^{5}	2.81×10^{7}	0.20	0.80
12	2.60×10^{5}	9.88×10^{5}	4.78×10^{7}	0.43	0.57
13	**1.64×10^{5}**	**7.12×10^{5}**	**3.08×10^{7}**	**0.47**	**0.53**
14	2.07×10^{5}	8.13×10^{5}	3.50×10^{7}	0.38	0.62
15	2.66×10^{5}	8.86×10^{5}	4.43×10^{7}	0.55	0.45
16	2.77×10^{5}	8.22×10^{5}	3.66×10^{7}	0.62	0.38
17	2.27×10^{5}	7.79×10^{5}	3.23×10^{7}	0.57	0.43
18	1.61×10^{5}	6.93×10^{5}	3.23×10^{7}	0.56	0.44
19	2.22×10^{5}	9.10×10^{5}	4.28×10^{7}	0.35	0.65
20	2.01×10^{5}	8.23×10^{5}	3.98×10^{7}	0.56	0.44

Maximum release rate

Maximum release rate using measured injection curves

Table 16. Maximum release rate [Bq/h] for radiotracers simulated using measured injection curves

Realisation #	^{131}I	^{47}Ca	^{137}Cs	^{226}Ra	^{99}Tc	^{241}Am
1	1.35×10^{6}	1.28×10^{5}	2.91×10^{2}	3.71×10^{2}	6.59×10^{1}	2.49×10^{1}
2	**1.03×10^{6}**	**1.02×10^{5}**	**2.08×10^{2}**	**3.01×10^{2}**	**5.01×10^{1}**	**2.18×10^{1}**
3	1.26×10^{6}	1.21×10^{5}	2.32×10^{2}	3.04×10^{2}	6.20×10^{1}	2.36×10^{1}
4	**1.03×10^{6}**	**1.23×10^{5}**	**3.12×10^{2}**	**4.06×10^{2}**	**7.58×10^{1}**	**3.07×10^{1}**
5	1.14×10^{6}	1.40×10^{5}	3.06×10^{2}	3.97×10^{2}	8.03×10^{1}	2.76×10^{1}
6	1.32×10^{6}	1.19×10^{5}	2.85×10^{2}	3.49×10^{2}	6.65×10^{1}	2.61×10^{1}
7	9.18×10^{5}	1.03×10^{5}	2.22×10^{2}	3.15×10^{2}	5.66×10^{1}	2.33×10^{1}
8	1.07×10^{6}	1.30×10^{5}	2.80×10^{2}	3.52×10^{2}	7.27×10^{1}	2.51×10^{1}
9	1.09×10^{6}	1.34×10^{5}	2.60×10^{2}	3.48×10^{2}	6.77×10^{1}	2.40×10^{1}
10	1.00×10^{6}	1.05×10^{5}	2.16×10^{2}	2.93×10^{2}	5.27×10^{1}	2.11×10^{1}
11	1.10×10^{6}	1.18×10^{5}	2.40×10^{2}	3.54×10^{2}	6.89×10^{1}	2.50×10^{1}
12	8.69×10^{5}	1.11×10^{5}	2.39×10^{2}	2.90×10^{2}	5.36×10^{1}	2.09×10^{1}
13	**1.24×10^{6}**	**1.33×10^{5}**	**2.68×10^{2}**	**3.39×10^{2}**	**6.80×10^{1}**	**2.44×10^{1}**
14	1.09×10^{6}	1.27×10^{5}	2.69×10^{2}	3.49×10^{2}	7.51×10^{1}	2.90×10^{1}
15	9.32×10^{5}	1.17×10^{5}	2.65×10^{2}	3.50×10^{2}	6.83×10^{1}	2.31×10^{1}
16	1.02×10^{6}	1.29×10^{5}	3.01×10^{2}	4.00×10^{2}	7.89×10^{1}	2.82×10^{1}
17	1.13×10^{6}	1.35×10^{5}	3.44×10^{2}	3.82×10^{2}	8.20×10^{1}	3.02×10^{1}
18	1.31×10^{6}	1.33×10^{5}	2.89×10^{2}	3.61×10^{2}	6.82×10^{1}	2.79×10^{1}
19	9.45×10^{5}	1.22×10^{5}	2.24×10^{2}	3.16×10^{2}	5.59×10^{1}	2.17×10^{1}
20	1.05×10^{6}	1.25×10^{5}	3.18×10^{2}	3.84×10^{2}	6.88×10^{1}	2.94×10^{1}

Maximum release rate using Dirac pulse injection

Table 17. Maximum release rate [1/h] for radiotracers simulated using a Dirac pulse boundary condition.

Realisation #	^{131}I	^{47}Ca	^{137}Cs	^{226}Ra	^{99}Tc	^{241}Am
1	8.12×10^{-3}	2.23×10^{-3}	1.23×10^{-5}	1.50×10^{-5}	2.87×10^{-6}	1.05×10^{-6}
2	**6.22×10^{-3}**	**2.00×10^{-3}**	**8.88×10^{-6}**	**1.35×10^{-5}**	**2.13×10^{-6}**	**8.68×10^{-7}**
3	6.83×10^{-3}	2.23×10^{-3}	9.95×10^{-6}	1.31×10^{-5}	2.63×10^{-6}	9.85×10^{-7}
4	**6.32×10^{-3}**	**2.21×10^{-3}**	**1.30×10^{-5}**	**1.77×10^{-5}**	**3.24×10^{-6}**	**1.30×10^{-6}**
5	6.89×10^{-3}	2.56×10^{-3}	1.25×10^{-5}	1.80×10^{-5}	3.47×10^{-6}	1.17×10^{-6}
6	6.59×10^{-3}	2.10×10^{-3}	1.15×10^{-5}	1.62×10^{-5}	2.88×10^{-6}	1.10×10^{-6}
7	6.00×10^{-3}	1.86×10^{-3}	9.17×10^{-6}	1.27×10^{-5}	2.48×10^{-6}	9.59×10^{-7}
8	6.89×10^{-3}	2.12×10^{-3}	1.14×10^{-5}	1.51×10^{-5}	3.05×10^{-6}	1.06×10^{-6}
9	7.93×10^{-3}	2.55×10^{-3}	1.09×10^{-5}	1.53×10^{-5}	2.96×10^{-6}	1.04×10^{-6}
10	5.91×10^{-3}	2.07×10^{-3}	9.72×10^{-6}	1.16×10^{-5}	2.26×10^{-6}	8.97×10^{-7}
11	6.86×10^{-3}	1.88×10^{-3}	1.07×10^{-5}	1.46×10^{-5}	2.88×10^{-6}	1.05×10^{-6}
12	5.34×10^{-3}	1.97×10^{-3}	9.66×10^{-6}	1.26×10^{-5}	2.29×10^{-6}	8.98×10^{-7}
13	**7.92×10^{-3}**	**2.68×10^{-3}**	**1.13×10^{-5}**	**1.42×10^{-5}**	**2.78×10^{-6}**	**1.05×10^{-6}**
14	7.33×10^{-3}	2.43×10^{-3}	1.12×10^{-5}	1.56×10^{-5}	3.16×10^{-6}	1.23×10^{-6}
15	5.74×10^{-3}	2.15×10^{-3}	1.11×10^{-5}	1.66×10^{-5}	2.90×10^{-6}	9.86×10^{-7}
16	5.73×10^{-3}	2.23×10^{-3}	1.35×10^{-5}	1.74×10^{-5}	3.40×10^{-6}	1.26×10^{-6}
17	7.69×10^{-3}	2.37×10^{-3}	1.43×10^{-5}	1.70×10^{-5}	3.64×10^{-6}	1.25×10^{-6}
18	8.38×10^{-3}	2.52×10^{-3}	1.26×10^{-5}	1.66×10^{-5}	2.92×10^{-6}	1.20×10^{-6}
19	5.76×10^{-3}	1.98×10^{-3}	9.96×10^{-6}	1.30×10^{-5}	2.39×10^{-6}	9.31×10^{-7}
20	6.55×10^{-3}	2.24×10^{-3}	1.25×10^{-5}	1.51×10^{-5}	2.90×10^{-6}	1.25×10^{-6}

4.3.3 Sensitivity Studies

The role of background channels

In the Task 6D simulations it was found that the partitioning of tracer particles between an upper and lower flowpath was entirely contingent upon the existence of the stochastically generated background fracture, 1925B as can be seen from Figure 33 below:

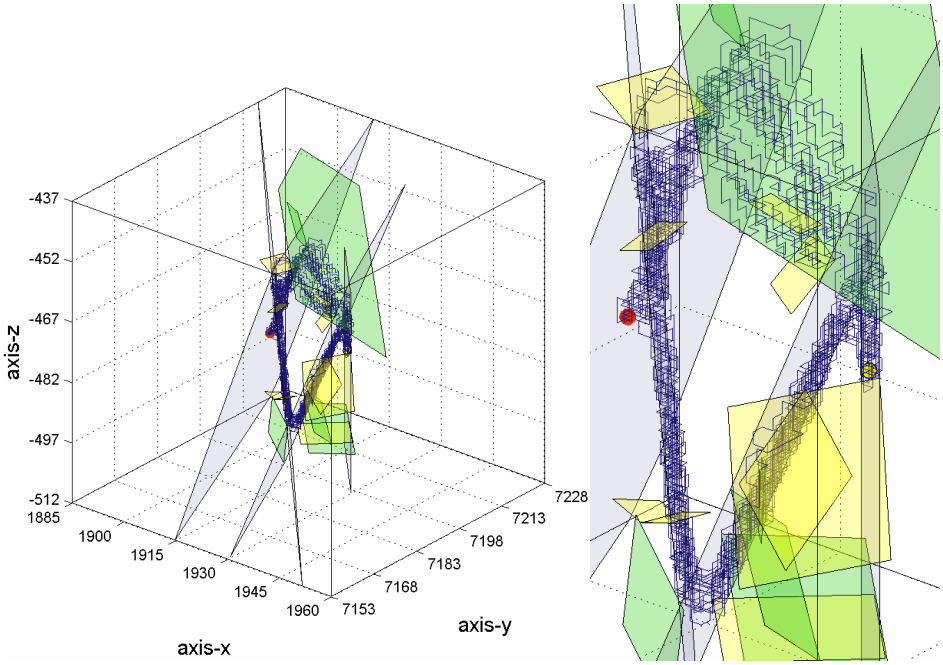

Figure 33. *Visualisation of tracer particle trajectory from a typical realisation of Task 6D where all background fractures in the Task 6C DFN have been used. Fracture 1925B is the large green polygon visible in the top right hand side of the particle trace. Tracer injection location is indicated with a yellow marker, while tracer recovery location is shown with a red marker.*

As this fracture is a "synthetic" feature (in the terminology of the Task 6C report), and given that the 5648 synthetic background fractures in the data distribution essentially represent one single realisation of a stochastically generated discrete fracture network, the authors of this report question whether it is prudent to use detailed simulations of this single DFN realisation to explain the outcome of tracer test C2.

The peak arrival time for a non-sorbing tracer can be adjusted by altering the flow porosity of the system to match the mean arrival time (i.e., t_{50} or some equivalent measure) of the experimentally recovered tracer. Thus, there are conceivably, many different possible realisations of the background fracture network that could approximately match the non-sorbing tracer breakthrough data equally well. Some of these realisations may have multiple and distinct flowpaths as indicated in Figure 33, although many may also not exhibit this characteristic.

An alternative approach would be to only include the major "deterministic" features and allow flow and transport to occur in the background channel network without the need for explicitly defined background fractures. By setting the background channel conductivities to arbitrarily low values (i.e., -12 in $\log_{10}$ units as in the base case scenario presented previously) and using only the 11 deterministic (D-features) and 19 synthetic features (S-features) specified in the data distribution, tracer transport can only occur via the lower flowpath as shown in Figure 34 below:

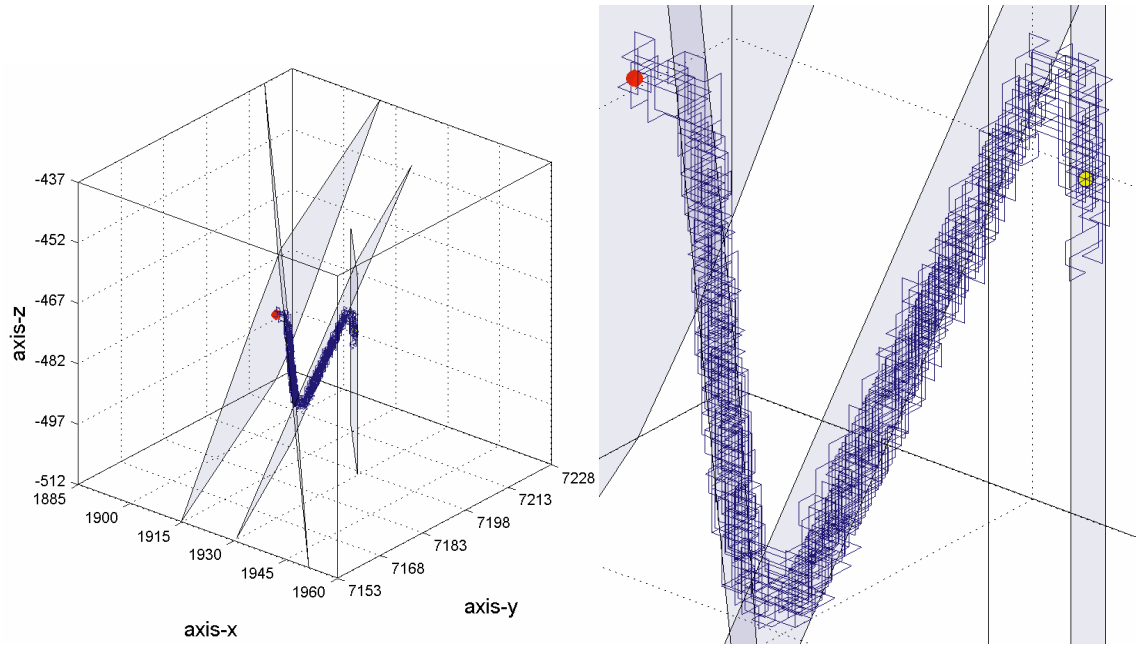

Figure 34. *Visualisation of tracer particle trajectory from a typical realisation of Task 6D where no background fractures in the Task 6C DFN have been used. In this case tracer transport occurs solely in the channels resident in the "deterministic" fractures 20D, 21D, 22D, and 23D.*

If the conductivity of the background channel network is raised, tracer transport can then occur via alternative flowpaths. For a background channel conductance of $\mu_c = -4$ with standard deviation of $\sigma_c = 2$ (both in $\log_{10}$ units), tracer transport also occurs through a sparse set of background channels as can be seen in Figure 35 below:

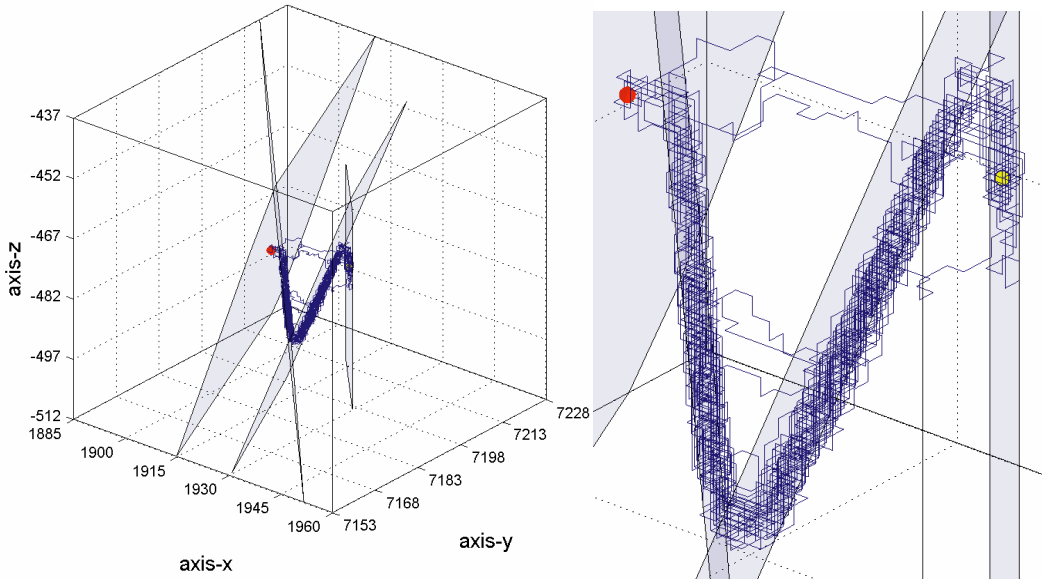

Figure 35. *Visualisation of tracer particle trajectory from a typical realisation of Task 6D where no background fractures in the Task 6C DFN have been used. Tracer transport occurs both in "deterministic" fractures (20D-23D) as well as in stochastically generated background flowpaths (μ_c = -4, σ_c = 2).*

For the same mean background conductance although with increased variance ($\sigma_c = 3$), the proportion of tracer transported through the sparse background network can be increased as shown below in Figure 36:

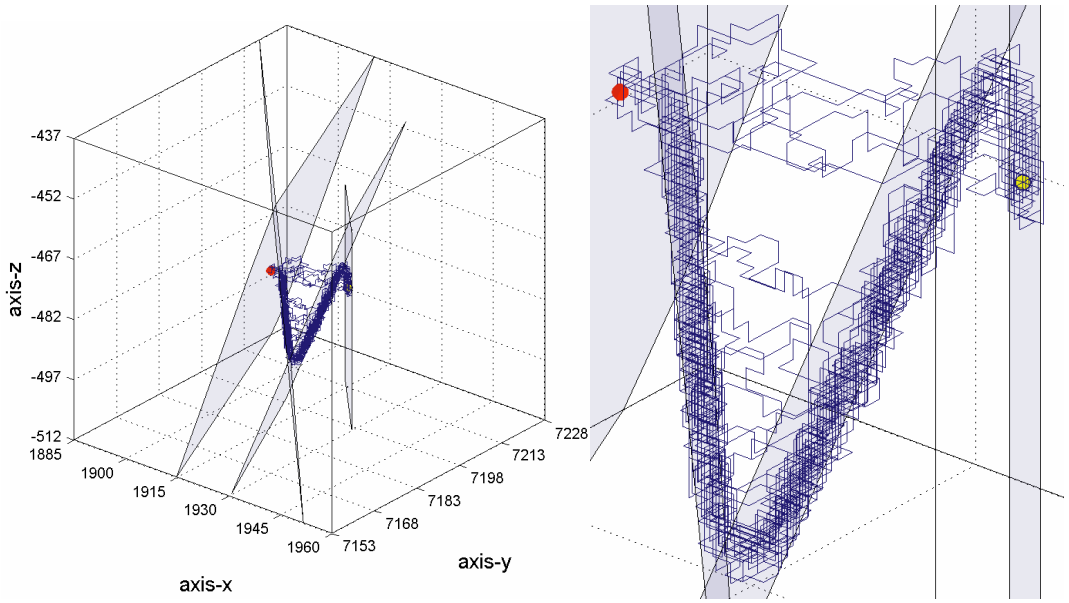

Figure 36. *Visualisation of tracer particle trajectory from a typical realisation of Task 6D where no background fractures in the Task 6C DFN have been used. In this case tracer transport occurs both in channels resident in the "deterministic" fractures (20D-23D) as well as in a set of stochastically generated background flowpaths.*

As the channel network is stochastically redefined in each realisation, the transport flowpaths through the background network vary from run to run. Some flowpaths are short, with transport occurring along a direct trajectory between tracer injection and recovery locations. Other flowpaths are longer, with a much more circuitous trajectory that can be up to five times farther than the direct trajectory. Although not explored in the context of the present Task 6D simulations, it is possible that this "short-circuiting" of transport flowpaths can give rise to extensive peak broadening of the breakthrough data depending upon the flow distribution (related to the variance of the background channel conductances) and the proportion of tracer travelling through the background channel network.

Using the full DFN model as presented in Figure 33 does not allow the same flowpath short-circuiting, although it may be possible to obtain the same peak broadening by increasing the variance of channels resident in the various deterministic and synthetic features. This would have the effect of increasing the amount of flowpath channelling within these features.

Differences between predictions made with a channel network model and a streamtube model

Although we have been unable to fully capture the broad peak of the experimental breakthrough data using the CHAN3D analogue of the Task 6C DFN model, one of the strengths of channel network models over streamtube modelling approaches is the ability to simulate multiple flowpaths and channelling effects. In CHAN3D, dispersion is neglected in individual channels as it is overwhelmingly dominated by differences in travel times between different flowpath channels. Flowpaths with fast flow and little flow-wetted surface result in rapid, early breakthrough of tracers. Tracers travelling along slower flowpaths with proportionally larger amounts of flow-wetted surface, on the other hand, experience greater retardation and are thus delayed.

In streamtube models, however, the total flow-wetted surface is proportioned evenly over the entire flow, with a dispersion operator accounting for mixing effects along the flowpath. As there is no explicit treatment of channelling effects, this approach gives non-conservative results for solute transport, particularly in the case of sorbing species.

In this section we have attempted to compare the simulations made by CHAN3D with a well-known streamtube model (Tang et al., 1981) using the same input data in order to illustrate some of the differences between the two different approaches. The Tang model considered here conceptualises flow and solute transport to occur along a single flowpath with dispersion and unlimited matrix diffusion.

The longitudinal dispersion coefficient may be obtained from the transport Peclet number, which is customarily calculated from the first moment and variance of the water residence time distribution (Levenspiel, 1972):

$$\mathrm{Pe} = \frac{2\bar{t}_w^{\,2}}{\sigma_w^2} = \frac{D_L}{u\,z} \tag{29}$$

Where, u is the average fluid velocity, D_L is the longitudinal dispersion coefficient, and z is the length of the flowpath.

For distributions with strong tailing, however, the estimated Peclet number is highly sensitive to small variations in late arrival times in the RTD. Neretnieks et al. (1981) demonstrate that the Peclet number (or longitudinal dispersion coefficient) can be estimated by making use of the inverse relation that exists between the Peclet number and a parameter (D_{159}), which is defined as:

$$\mathrm{D}_{159} = \frac{t_{95} - t_{05}}{t_{50}} \tag{30}$$

Figure 37 below shows the theoretical relation between transport Peclet number (Pe) and D_{159}, calculated using the advection-dispersion equation for a step input boundary condition (Lapidus and Amundsen, 1952):

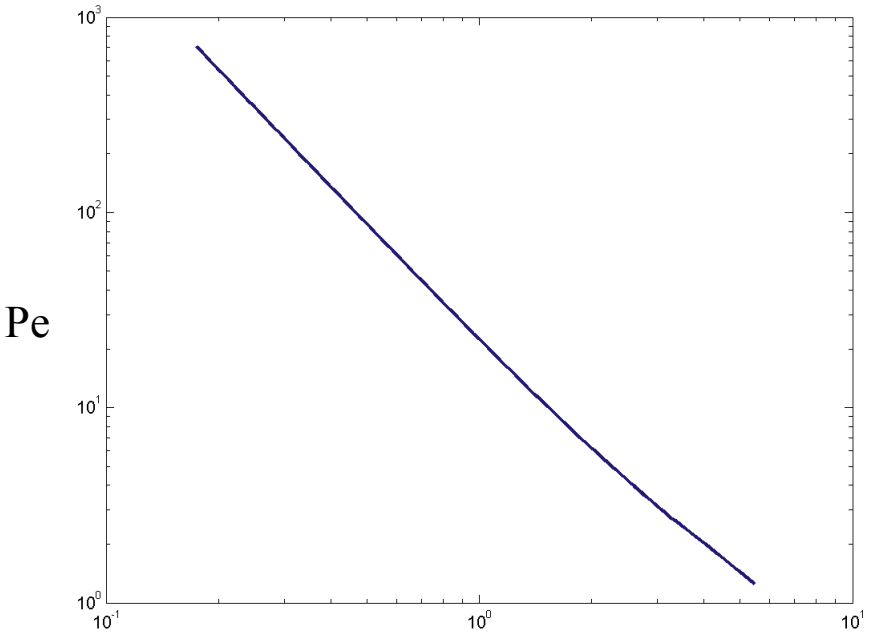

Figure 37. *Theoretical relation between transport Peclet number (Pe) and D_{159} parameter. This curve can be used to estimate the Peclet number from water residence time distribution data.*

The flow-wetted surface to flow ratio (FWS/Q, or β-factor) in the stream tube model was assumed to be equal to the mean value obtained in the CHAN3D simulations, and the water residence time was taken to be the median water residence time (t_{w50}) value taken from the CHAN3D-calculated water residence time distribution. The parameters used in the stream-tube simulation model are summarised in Table 18 below:

Table 18. Parameters used for comparison of CHAN3D and streamtube models.

Parameter:	Value:	Comments
t_w [h]	168	median t_{w50} in CHAN3D simulations
δ [m]	3.3×10^{-4}	mean fracture aperture from CHAN3D simulations
FWS/Q [m^2y/m^3]	117.3	mean value from CHAN3D simulations
MPG [$m/y^{½}$]	5.6×10^{-4}	^{131}I (assumed value for Cataclasite)
	1.1×10^{-1}	^{241}Am (assumed value for Cataclasite)
K_a [m]	2.5×10^{-5}	^{131}I (assumed value for fracture coating)
	6.5×10^{-1}	^{241}Am (assumed value for fracture coating)
D_{159}	1.54	mean D_{159} from CHAN3D simulations
Pe	9.98	estimated from Figure 37

The breakthrough characteristic for a Dirac pulse boundary condition calculated using the streamtube model is shown in Figure 38 below for the non-sorbing tracer ^{131}I:

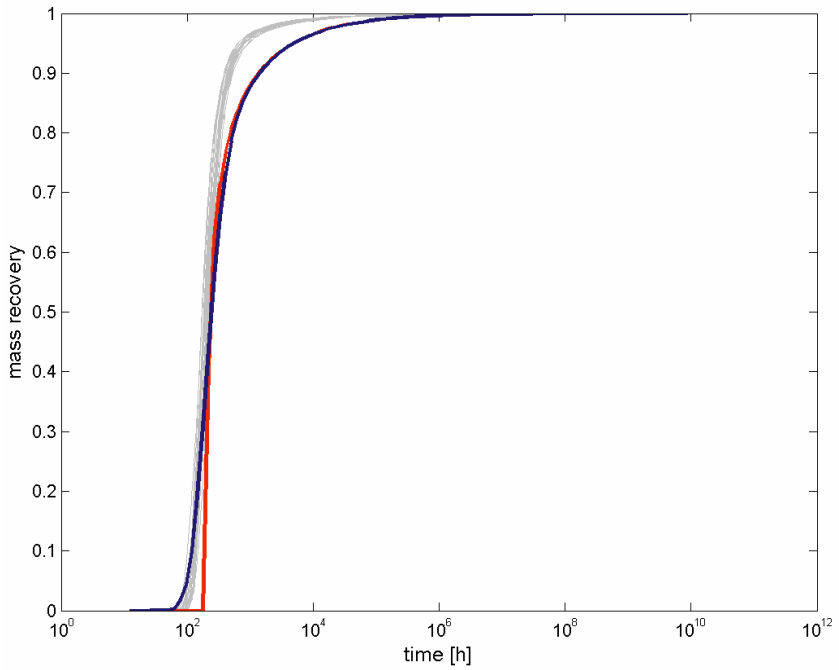

Figure 38. *Breakthrough data for the non-sorbing tracer ^{131}I. Grey curves represent 20 realisations of the base case CHAN3D model. Blue curve represents results obtained using the Tang model. Red curve is data for a single channel with purely advective flow and unlimited matrix diffusion (equation 17).*

The Tang model and CHAN3D both predict similar recovery times for the leading edge of the breakthrough curve. As the late arriving tracer encounters less flow wetted surface in the CHAN3D model, however, the tracer is less well retarded than the Tang model predicts. For the short times characteristic of the tracer test C2, matrix interaction plays only a very minor role in the retardation of ^{131}I. In the case of ^{241}Am, however, the differences are quite dramatic as can be seen in Figure 39:

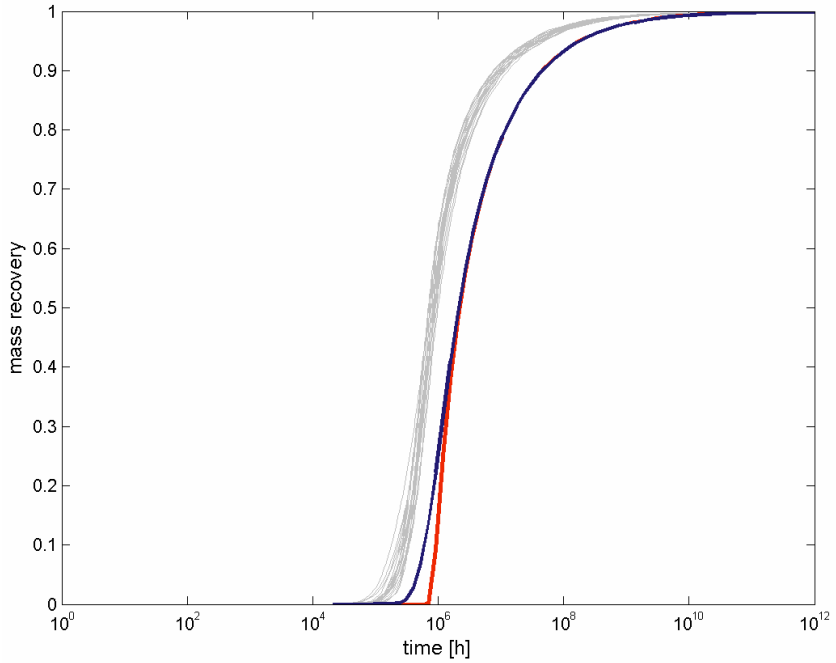

Figure 39. *Breakthrough data for the strongly-sorbing tracer ^{241}Am. Grey curves represent 20 realisations of the base case CHAN3D model. Blue curve represents results obtained using the Tang model. Red curve is data for a single channel with purely advective flow and unlimited matrix diffusion (equation 17).*

The simulated arrival times for 5%, 50%, and 95% of the injected tracer are given in Table 19 below:

Table 19. Simulated arrival times for 5%, 50%, and 95% of the injected tracer.

Tracer:	CHAN3D	Tang Model	Single Channel (no dispersion)
^{131}I			
t_{05} [h]	1.14×10^{2}	9.95×10^{1}	2.83×10^{2}
t_{50} [h]	2.03×10^{2}	2.49×10^{2}	4.53×10^{2}
t_{95} [h]	7.75×10^{2}	5.11×10^{3}	2.98×10^{3}
^{241}Am			
t_{05} [h]	2.09×10^{5}	4.75×10^{5}	8.19×10^{5}
t_{50} [h]	8.13×10^{5}	2.14×10^{6}	1.11×10^{6}
t_{95} [h]	3.62×10^{7}	1.85×10^{8}	5.37×10^{6}

In the case of ^{241}Am, the lower FWS/Q ratio encountered by tracer particles in the CHAN3D simulation has a strong impact on both the early and late arrival times of tracer. This example illustrates clearly how the assumptions surrounding the distribution of the flow-wetted surface to flow ratio can have an impact on simulation results even with identical input parameters. Although the differences are probably not too significant in an SC framework, it is likely that the stream tube model presented here would give somewhat non-conservative results in a PA calculation owing to the much stronger influence of the FWS/Q parameter when using PA-relevant boundary conditions.

5 Task 6E

5.1 Modelling strategy

The DFN definitions given in the data distribution were used to generate an equivalent channel network representation in CHAN3D. Initially, the entire 200 m Block Scale volume was simulated for the purpose of obtaining new boundary conditions. The 200 m Block Scale volume was discretised into a cube with dimensions of 101×101×101 nodes. The individual channel members making up the channel network were 2 m in length for these initial simulations.

In Task 6E, there were no flow injection or pumping boundary conditions (unlike Task 6D) and flow occurs due to a hydraulic head gradient of 0.5% from East to West across the simulation volume. Tracer injection was performed passively at three adjacent locations (i.e., a so-called "line source") resident in deterministic feature 23D, located near the centre of the TRUE Block Scale volume. Tracer recovery was performed passively at three different locations, 10 m, 50 m, and 70 m downstream of the injection point in separate simulations.

The injection and recovery nodes (resident in conductive fractures) were selected on the basis of closest proximity to the given injection and recovery coordinates specified in the Task 6E specification. The coordinates of the tracer injection locations were:

Table 20. Coordinates of tracer injection locations as defined in Task 6E specification.

	Endpoint 1	Centre	Endpoint 2
Easting	1930.758	1929.741	1928.724
Northing	7193.742	7194.840	7195.938
Elevation	-476.100	-476.100	-476.100

Owing to that the extent of the line source is roughly 3 m and the channel network is defined using 2 m channel lengths, the line source is truncated necessarily to two adjacent nodes in the Task 6E simulations detailed in this report.

For tracer recovery, nodes resident in the vertical planes defined by Easting = 1920, Easting = 1880, and the Western boundary (Easting = 1800) of the 200 m simulation volume were used for tracer recovery.

For channels identified as belonging to multiple fractures, the fault-type geological class was given precedence over non-fault geological class when assigning material properties. As was done previously for Task 6D, channels resident in fault-type fractures were assigned properties for Cataclasite; Non-fault type channels were assigned material properties for unaltered rock. Surface sorption, K_a parameters were identically assumed to be for fracture coating material in both fault and non-fault fracture types. Similarly, the highest complexity factor was assumed to take precedence where there were conflicting fracture complexity definitions for channels shared between multiple fractures.

The flow-wetted surface of channels was normalised to give a total flow wetted surface corresponding to twice the DFN polygon surface area resident within the simulation volume (i.e., the polygon vertices were truncated to the simulation volume extents). The flow-wetted surface of individual channels was then multiplied by a scaling factor dependent upon the assigned complexity as defined in the data distribution (see Table 21).

Table 21. FWS-multiplier used to scale flow wetted surface of individual channels based upon complexity factor assigned in the Task 6D data distribution.

Complexity Factor	FWS-multiplier
1	1
2	2
3	3
4	5
5	10

5.2 Model calibration

The hydraulic boundary condition was a head gradient of 0.5% from East to West across the simulation volume. The hydraulic head at the Eastern plane was therefore set to 1 m and the corresponding Western plane to 0 m. All other boundaries were defined as no-flow boundary planes.

For the simulations described in this report, a flow-porosity of $\varepsilon_f = 7.3\times10^{-5}$ has been assumed as a basis for the transport calculations. This was the same porosity as was used earlier in the Task 6D simulations.

5.3 Results

5.3.1 Flow

Using CHAN3D, 20 flow and transport realisations were performed. Owing to the large contrast in conductance between the active channels comprising the fracture system and the background network channels (see Section 3.2.2), there was some difficulty in obtaining a completely convergent solution to the groundwater problem problem. For a conductance standard deviation of $\sigma_c = 1$, however, the numerical non-convergence was largely restricted to non-active background channels in the network and therefore not significant for the flow mass balance along the main flowpaths. If there is significant non-convergence of the groundwater mass balance along major transport pathways, there is a strong tendency for non-physical "looping" effects to occur during the transport simulation particle tracking. There was no evidence of such looping effects occurring during any of the transport simulations carried out.

Description of flow paths

Over the short distance to the first recovery plane 10 m downstream from the tracer release location (Easting = 1920), the tracer particles appear to take two routes although with a somewhat larger proportion traversing the upper flowpath involving background feature 1925B as shown in Figure 40 and Figure 41.

For the second recovery plane 50 m distant from the injection location, tracer particles largely follow a single flowpath through the channel network with only small numbers of particles taking alternate routes to the recovery plane. In these simulations, tracer transport is associated primarily with features 20D-23D and the background fracture 1925B (see Figure 42 and Figure 43).

Overall, tracer transport was found to occur along a single principal flowpath in the channel network, although with small numbers of particles taking alternate routes. The tracer particles were observed to travel predominantly in features 20D-23D and 17S. Background features 1925B and 2292B were also found to be crucial for tracer transport as these fractures link the aforementioned D and S features into a continuous pathway from the injection location to the Western boundary plane. In total, 11 D- and S-type features as well as 152 B- and C-type background fractures were found to be associated with tracer transport for recovery at the Western boundary plane of the simulation volume (see Figure 44 and Figure 45).

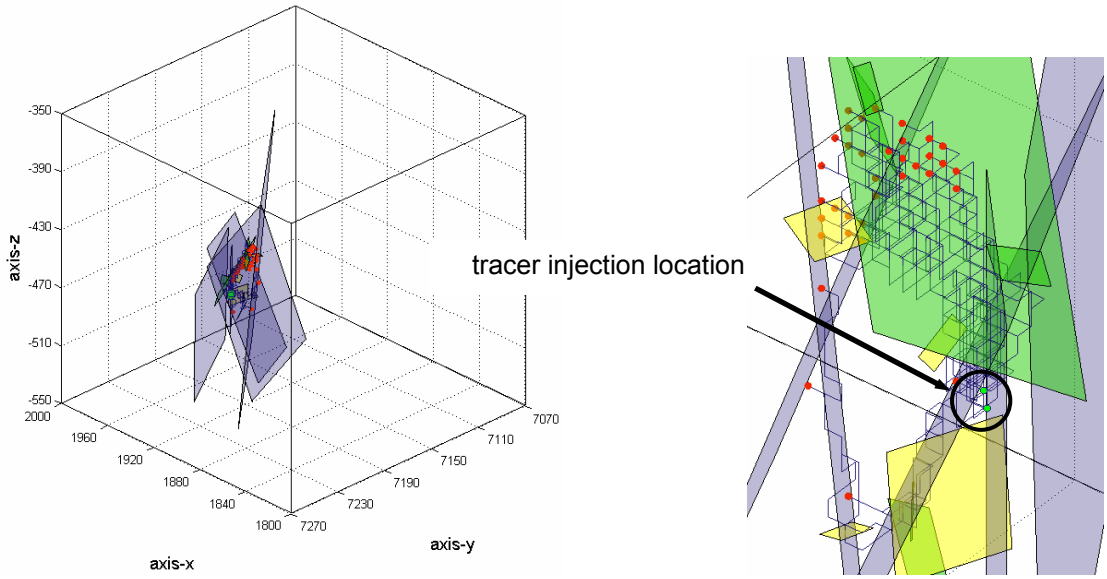

Figure 40. *Visualisation of tracer flowpaths for a typical CHAN3D-transport realisation simulating tracer transport from the release location to the first recovery plane at Easting = 1920 (roughly 10 m downstream). Particle tracks are shown in the context of DFN fracture planes within which tracer transport occurs. Tracer injection location is indicated with green marker symbols (encircled area in right-hand image) while tracer recovery locations are shown with red markers.*

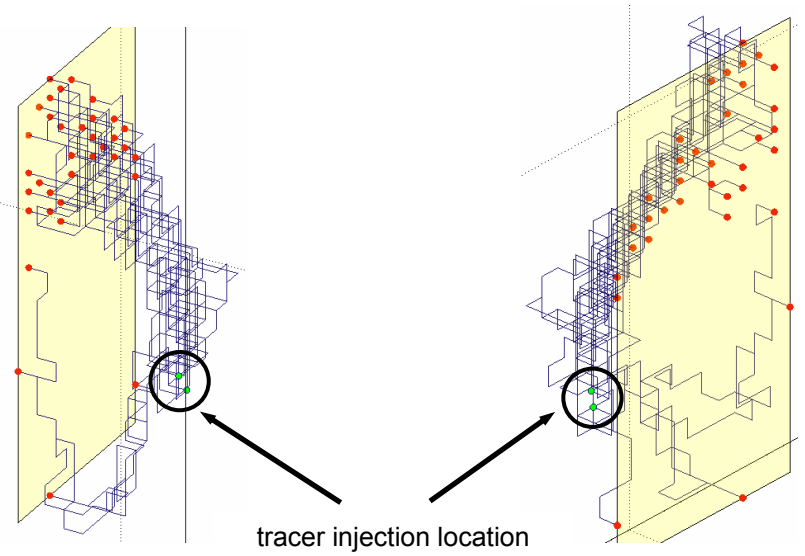

Figure 41. *Visualisation of tracer flowpaths for a typical CHAN3D-transport realisation simulating tracer transport from the release location to the first recovery plane at Easting = 1920 (roughly 10 m downstream). Tracer injection location is indicated with green marker symbols (encircled areas) while tracer recovery locations are shown with red markers. Yellow polygon corresponds to recovery plane location.*

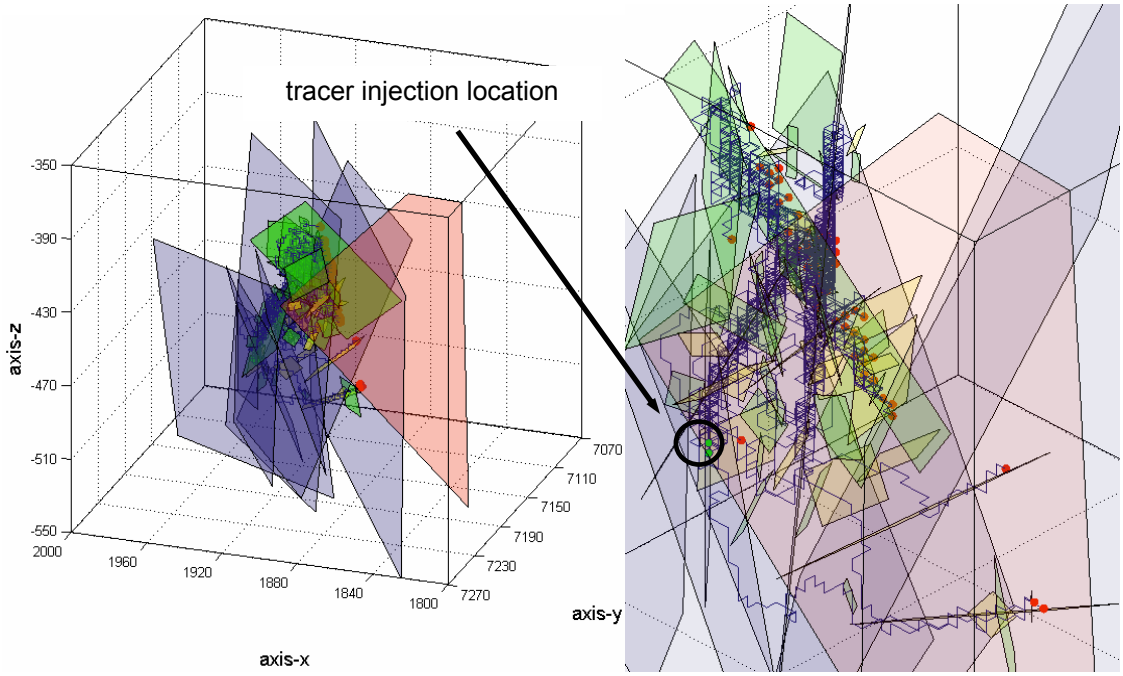

Figure 42. *Visualisation of tracer flowpaths for a typical CHAN3D-transport realisation simulating tracer transport from the release location to the second recovery plane at Easting = 1880 (roughly 50 m downstream). Particle tracks are shown in the context of DFN fracture planes within which tracer transport occurs. Tracer injection location is indicated with green marker symbols (encircled area in right-hand image) while tracer recovery locations are shown with red markers.*

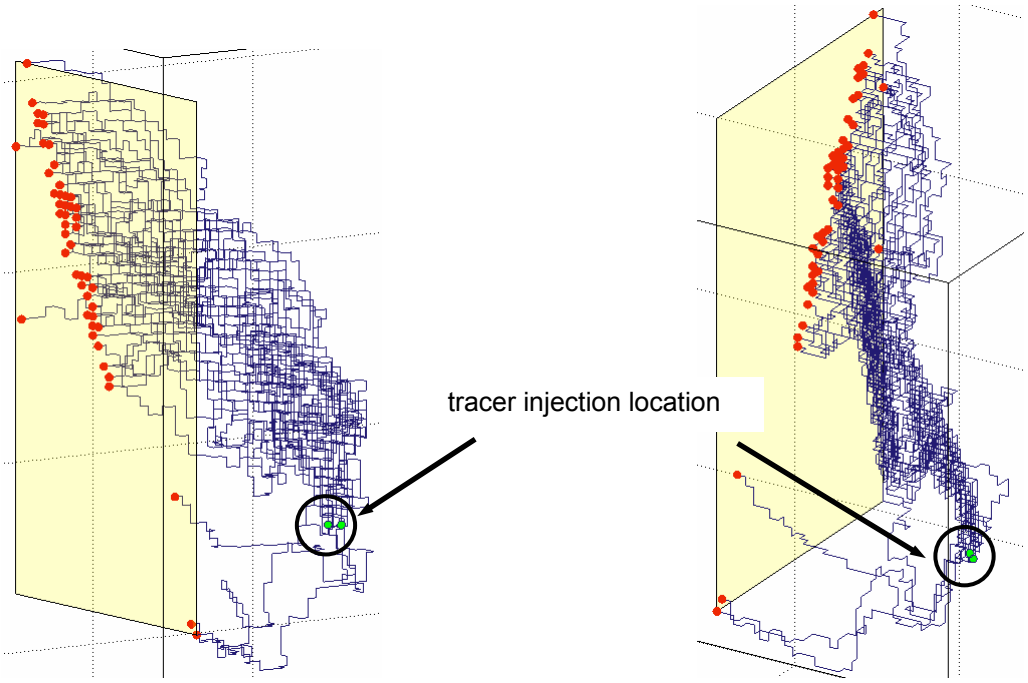

Figure 43. *Visualisation of tracer flowpaths for a typical CHAN3D-transport realisation simulating tracer transport from the release location to the second recovery plane at Easting = 1880 (roughly 50 m downstream). Tracer injection location is indicated with green marker symbols (encircled areas) while tracer recovery locations are shown with red markers. Yellow polygon corresponds to recovery plane location.*

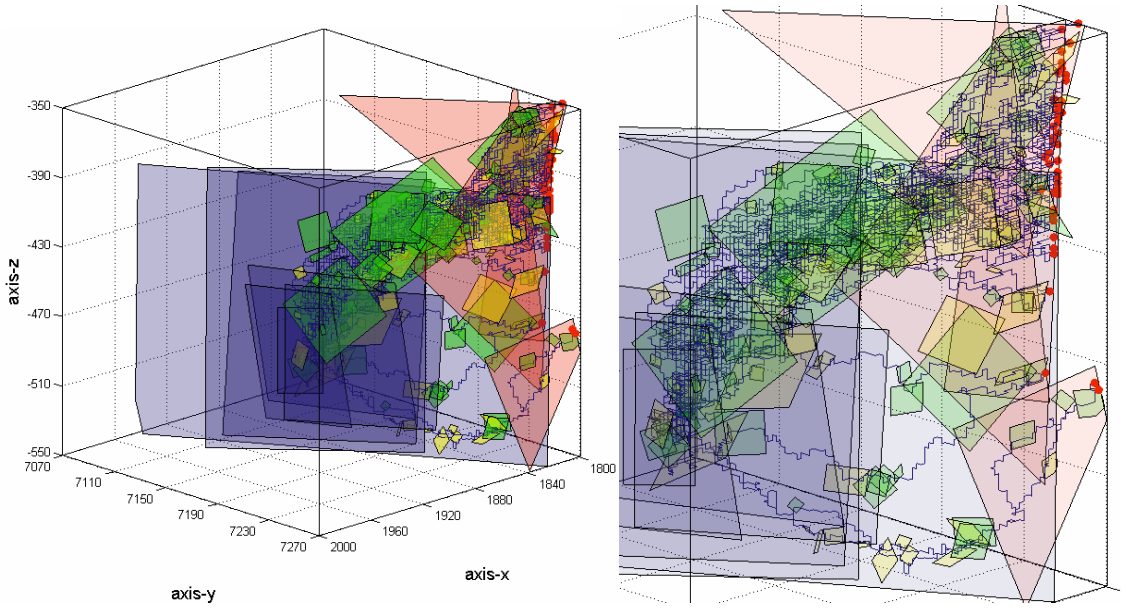

Figure 44. *Visualisation of tracer flowpaths for a typical CHAN3D-transport realisation simulating tracer transport from the release location to the recovery plane at the Western simulation boundary (roughly 70 m downstream). Particle tracks are shown in the context of DFN fracture planes within which tracer transport occurs. Tracer recovery locations are shown with red markers (tracer injection location is not visible in the images).*

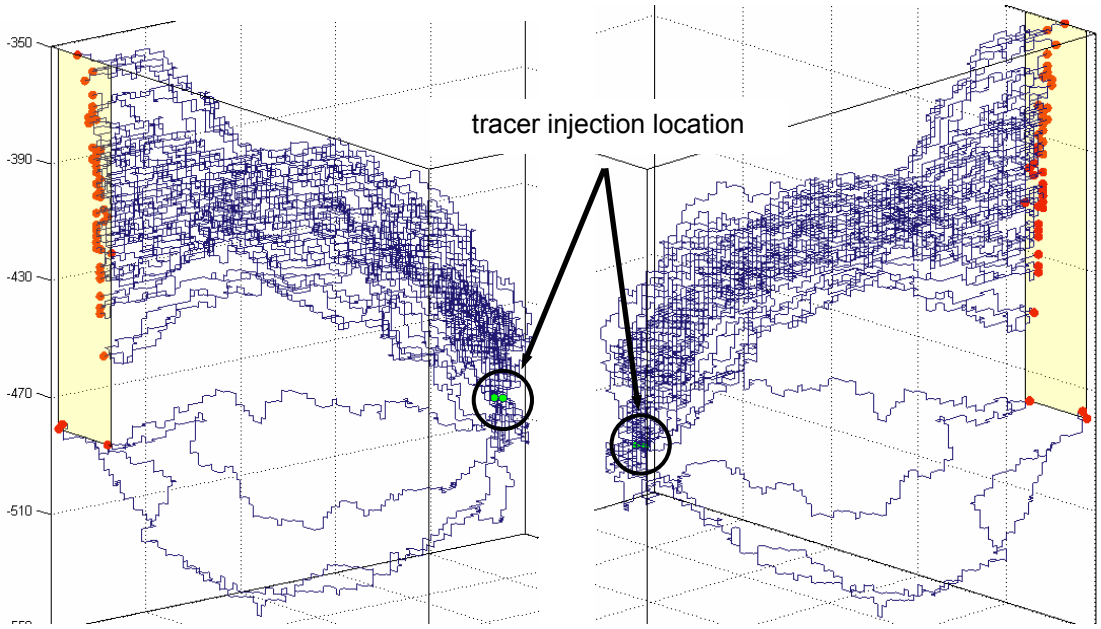

Figure 45. *Visualisation of tracer flowpaths for a typical CHAN3D-transport realisation simulating tracer transport from the release location to the recovery plane at the Western simulation boundary (roughly 70 m downstream). Tracer injection location is indicated with green marker symbols (encircled areas) while tracer recovery locations are shown with red markers. Yellow polygon corresponds to recovery plane location.*

Water residence time distribution

Owing to the short transport distance for tracer recovery at Easting = 1920, the water residence time distribution (RTD) is difficult to interpret owing to the heterogeneity of the pathways taken by individual tracer particles, which gives rise to very "jittery" breakthrough data. To avoid this, a set of 3 representative realisations has been selected from the original ensemble of 20, for visualisation purposes. These data correspond to the realisations with the lowest-, largest-, and approximately average FWS/Q ratio encountered. In the interest of consistency and to facilitate intercomparison, the same realisations have been used for visualisation of the water RTD at the other two recovery planes (i.e., Easting = 1880 and 1800)

Figure 46, Figure 47, and Figure 48 below show the water residence time distribution obtained for recovery at the different tracer recovery planes with the given hydraulic boundary conditions and the assumed flow porosity of $\varepsilon_f = 7.3\times10^{-5}$.

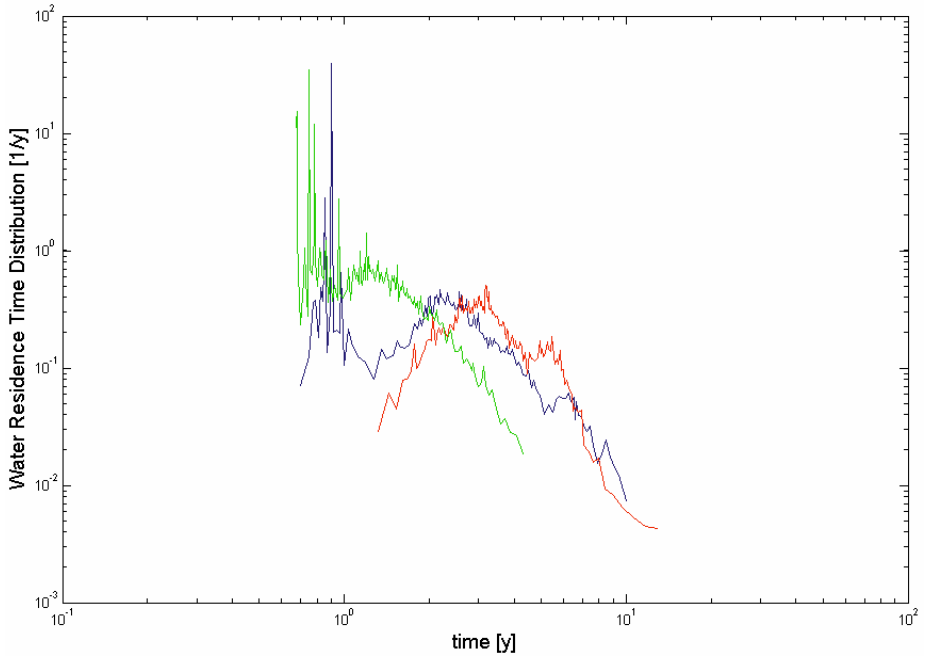

Figure 46. *Water residence time distribution (RTD) for transport from injection location to first recovery plane (Easting = 1920) with a flow porosity of $\varepsilon_f = 7.3\times10^{-5}$. Green, blue, and red curves correspond to realisations with minimum, mean, and maximum FWS/Q ratio, respectively.*

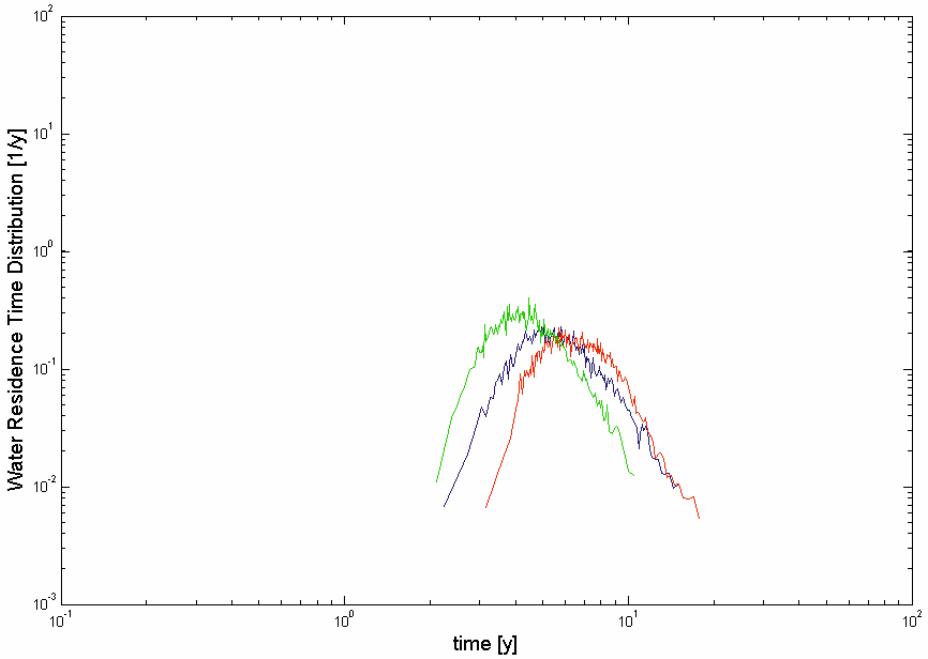

Figure 47. *Water residence time distribution (RTD) for transport from injection location to second recovery plane (Easting = 1880) with a flow porosity of $\varepsilon_f = 7.3\times10^{-5}$. Green, blue, and red curves correspond to realisations with minimum, mean, and maximum FWS/Q ratio, respectively.*

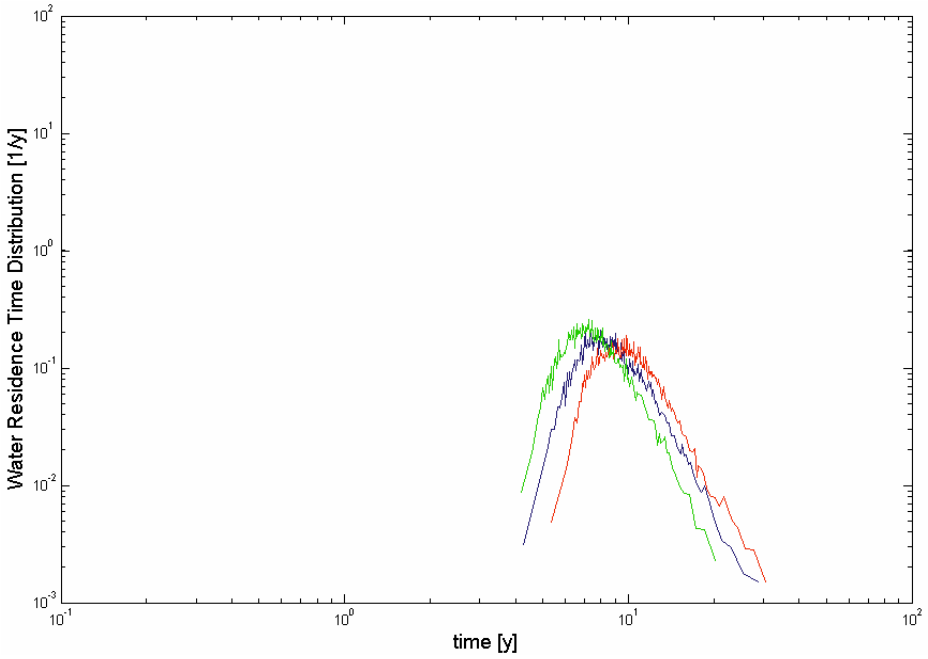

Figure 48. *Water residence time distribution (RTD) for transport from injection location to Western boundary plane (Easting = 1800) with a flow porosity of $\varepsilon_f = 7.3\times10^{-5}$. Green, blue, and red curves correspond to realisations with minimum, mean, and maximum FWS/Q ratio, respectively.*

5.3.2 Transport

In the CHAN3D-transport simulations the radiotracers ^{129}I, ^{47}Ca, ^{137}Cs, ^{226}Ra, ^{99}Tc, and ^{241}Am have been simulated for both a Dirac pulse release scenario as well as for an extended pulse of 1 MBq/y for 1000 y as specified in the task specification. The following sections detail the results of the individual tracer transport simulations.

β-factor

The β-factor for tracer transport is a parameter describing the flow-wetted surface to flow ratio (FWS/Q). It is the dominant parameter governing the transport of sorbing tracers and also the least well characterised for actual fracture systems. The CHAN3D-transport program calculates two related parameters, ϕ and ψ which describe the average transport properties of channels integrated over the paths taken by tracer particles through the system. They are calculated separately for each individual particle thereby giving a distribution of values. These parameters are defined in the following way:

$$\phi = \int_0^z \frac{R_*}{u}\, dz = \sum_i \left(t_{w(i)} + K_{a(i)} \times \frac{FWS_{(i)}}{q_{(i)}} \right) \tag{31}$$

$$\psi = \int_0^z \frac{W\sqrt{D_e K_d \rho_p}}{q}\, dz = \sum_i \frac{FWS_{(i)}}{2\, q_{(i)}} \sqrt{D_{e(i)} K_{d(i)} \rho_{p(i)}} \tag{32}$$

Where z is the ultimate distance travelled along the particular flowpath, u is the local fluid velocity, and i relates to the individual channels encountered along that flowpath.

For a strongly sorbing tracer such as ^{241}Am, the water residence time, t_w is negligible compared to the second term on the right hand side of equation 26. The β-factor (FWS/Q) can therefore be estimated from the flowpath-integrated value of ϕ using:

$$\beta = \frac{\phi}{K_a} = \sum_i \left(\frac{FWS_{(i)}}{q_{(i)}} \right) \tag{33}$$

Using the breakthrough data for ^{241}Am, the following Beta distributions (Figure 49 below) were obtained for tracer recovery at Easting = 1920:

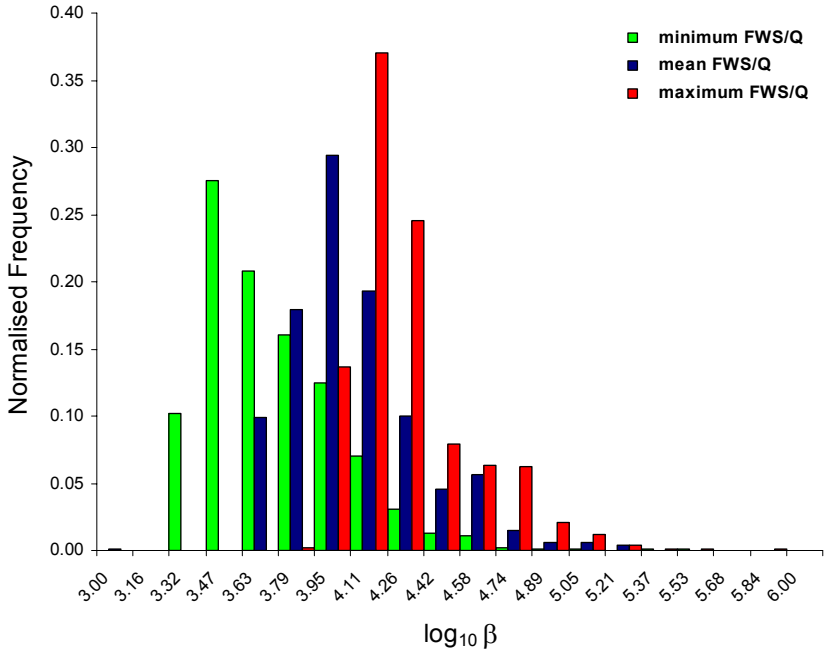

Figure 49. *β-factor (FWS/Q) frequency histogram for three separate realisations taken from the original set of 20 for tracer recovery at Easting = 1920. Green, blue, and red curves correspond to realisations with minimum, mean, and maximum FWS/Q ratio, respectively.*

Figure 50 below shows the Beta distributions obtained for tracer recovery at Easting = 1880:

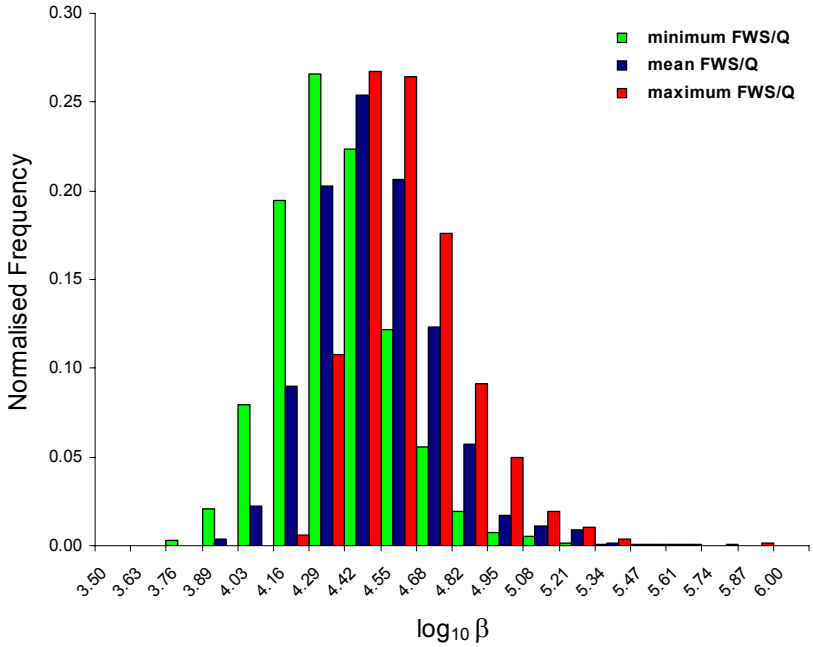

Figure 50. *β-factor (FWS/Q) frequency histogram for three separate realisations taken from the original set of 20 for tracer recovery at Easting = 1920. Green, blue, and red data sets correspond to realisations with minimum, mean, and maximum FWS/Q ratio, respectively.*

Figure 51 below shows the Beta distributions obtained for tracer recovery at the Western boundary plane (Easting = 1800):

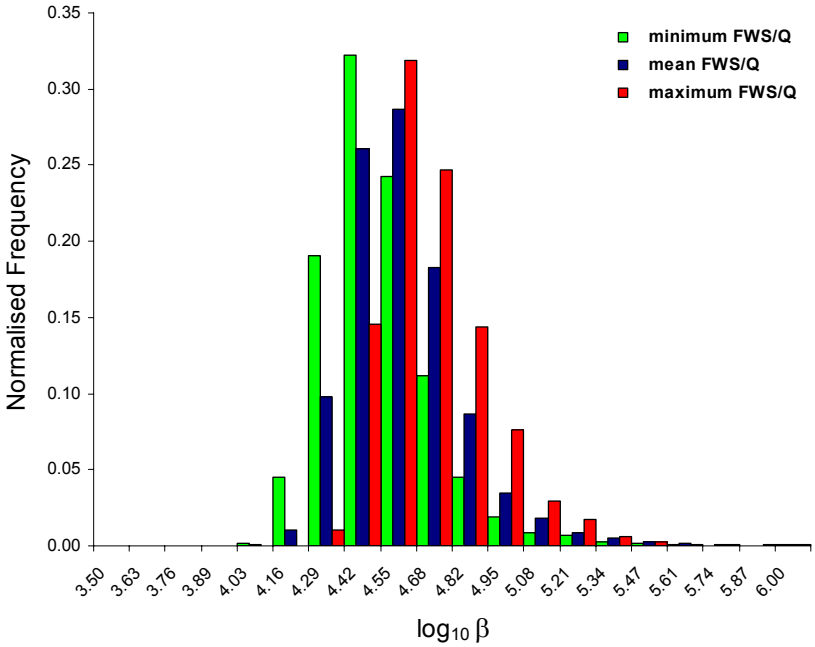

Figure 51. *β-factor (FWS/Q) frequency histogram for three separate realisations taken from the original set of 20 for tracer recovery at Easting = 1920. Green, blue, and red data sets correspond to realisations with minimum, mean, and maximum FWS/Q ratio, respectively.*

Breakthrough time history for the tracers at recovery plane 1 (Easting = 1920)

Breakthrough curves for extended pulse injection boundary condition

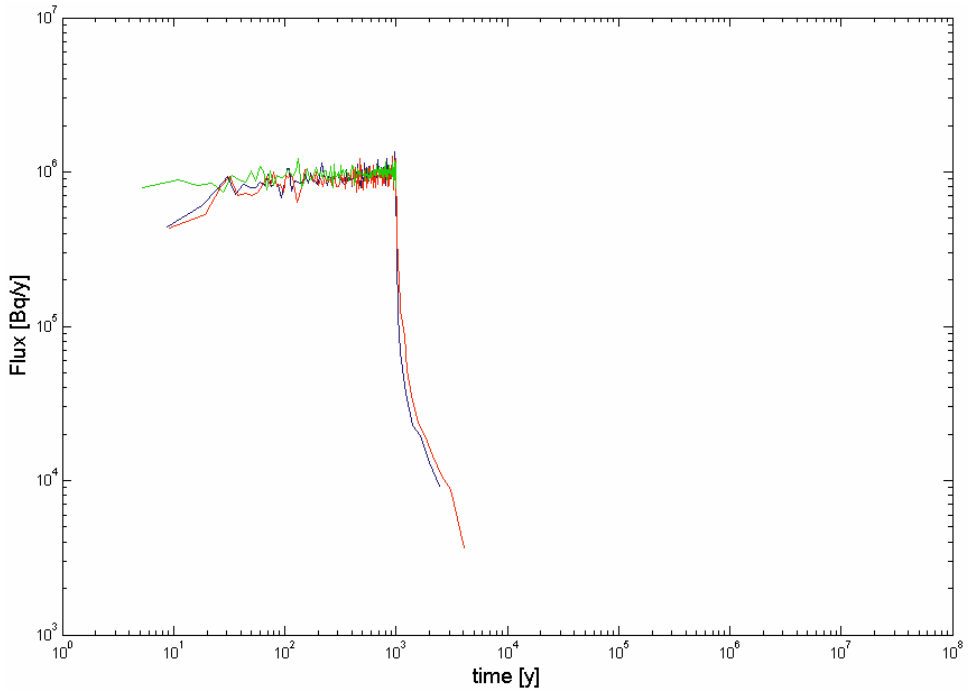

Figure 52. *Radionuclide flux vs. time, breakthrough curve for ^{129}I.*

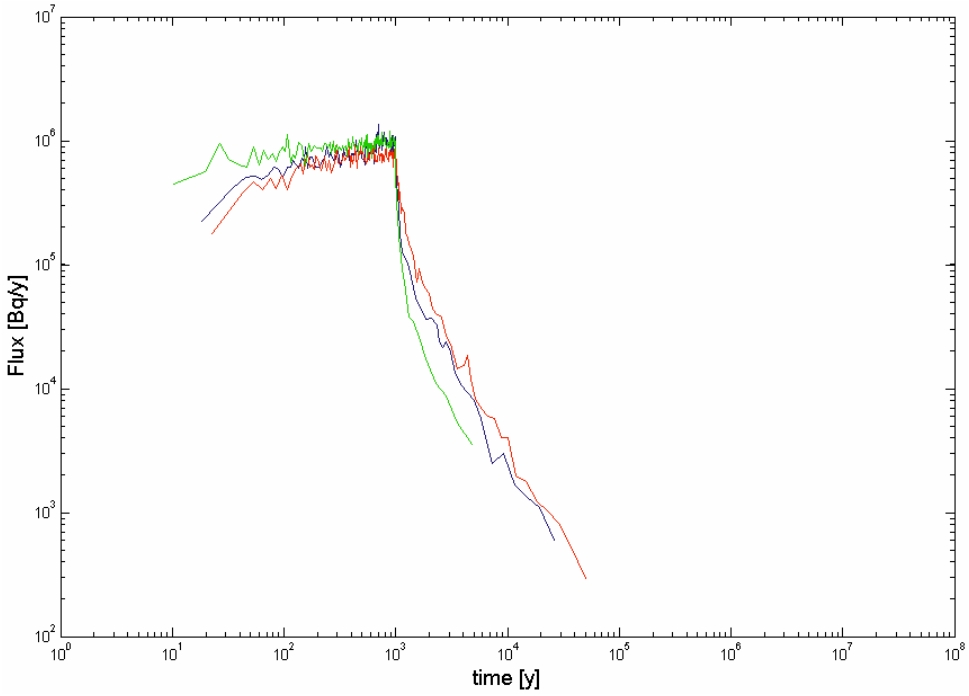

Figure 53. *Radionuclide flux vs. time, breakthrough curve for ^{47}Ca.*

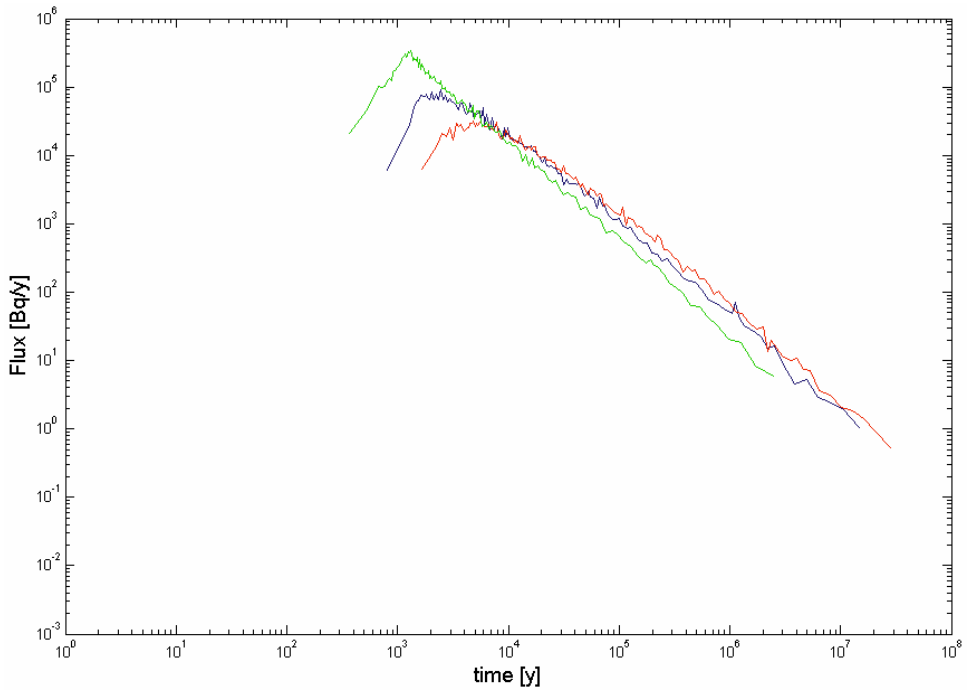

Figure 54. *Radionuclide flux vs. time, breakthrough curve for ^{137}Cs.*

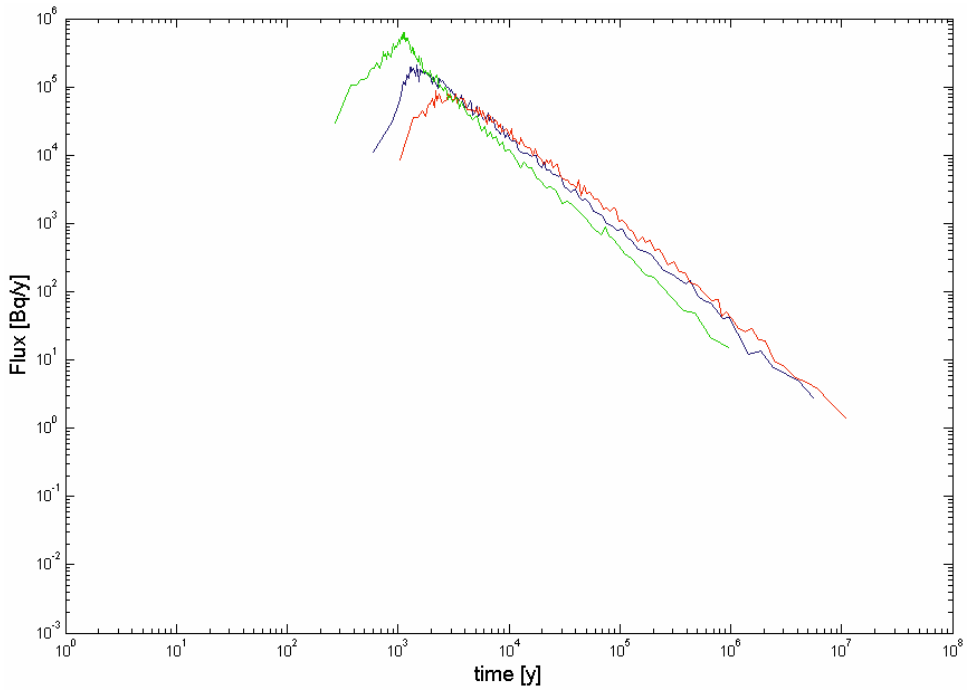

Figure 55. *Radionuclide flux vs. time, breakthrough curve for ^{226}Ra.*

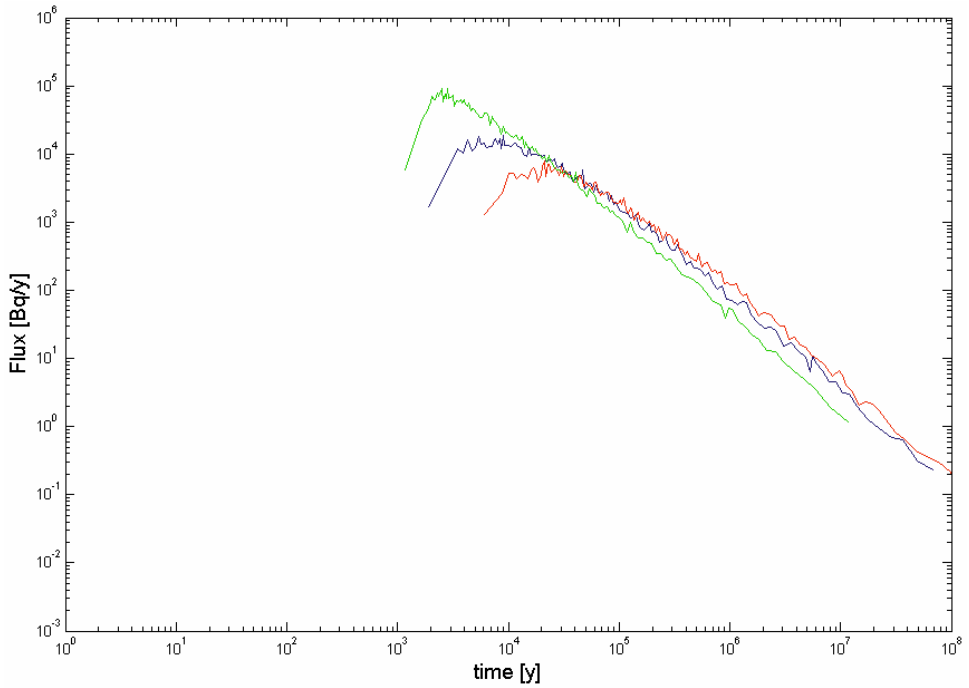

Figure 56. *Radionuclide flux vs. time, breakthrough curve for ^{99}Tc.*

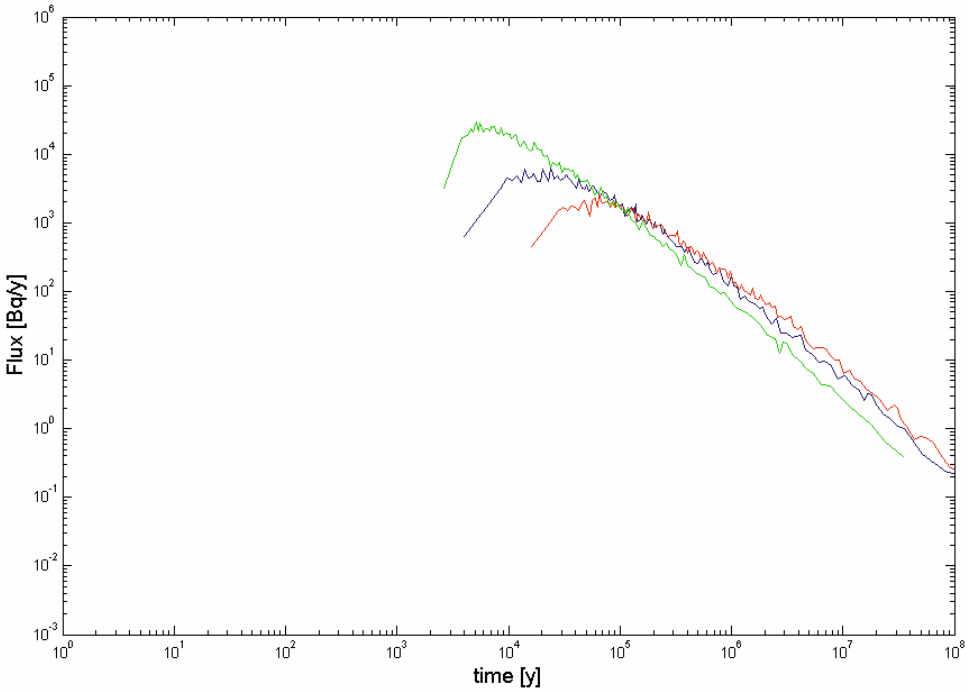

Figure 57. *Radionuclide flux vs. time, breakthrough curve for ^{241}Am.*

Breakthrough times for recovery of 5, 50 and 95% of the injected mass

Table 22. Simulated recovery times for 5%, 50%, and 95% of injected ^{129}I tracer activity. Realisations in figures correspond to runs 16 (blue), 18 (red), and 20 (green).

Realisation #	Recovery Times [y]		
	t_{05} (5%)	t_{50} (50%)	t_{95} (95%)
1	6.71×10^{1}	5.49×10^{2}	1.27×10^{3}
2	6.12×10^{1}	5.30×10^{2}	1.04×10^{3}
3	6.36×10^{1}	5.40×10^{2}	1.02×10^{3}
4	6.99×10^{1}	5.62×10^{2}	1.06×10^{3}
5	6.95×10^{1}	5.58×10^{2}	1.19×10^{3}
6	6.96×10^{1}	5.57×10^{2}	1.35×10^{3}
7	7.12×10^{1}	5.59×10^{2}	1.26×10^{3}
8	7.22×10^{1}	5.57×10^{2}	1.10×10^{3}
9	6.31×10^{1}	5.42×10^{2}	1.02×10^{3}
10	5.88×10^{1}	5.24×10^{2}	9.95×10^{2}
11	6.17×10^{1}	5.34×10^{2}	1.00×10^{3}
12	6.25×10^{1}	5.39×10^{2}	9.88×10^{2}
13	6.58×10^{1}	5.46×10^{2}	1.17×10^{3}
14	6.14×10^{1}	5.32×10^{2}	1.00×10^{3}
15	6.97×10^{1}	5.54×10^{2}	1.15×10^{3}
16	$\mathbf{7.11\times10^{1}}$	$\mathbf{5.65\times10^{2}}$	$\mathbf{1.20\times10^{3}}$
17	6.77×10^{1}	5.63×10^{2}	1.30×10^{3}
18	$\mathbf{7.47\times10^{1}}$	$\mathbf{5.78\times10^{2}}$	$\mathbf{1.79\times10^{3}}$
19	6.26×10^{1}	5.34×10^{2}	1.01×10^{3}
20	$\mathbf{5.94\times10^{1}}$	$\mathbf{5.26\times10^{2}}$	$\mathbf{9.80\times10^{2}}$

Table 23. Simulated recovery times for 5%, 50%, and 95% of injected ^{47}Ca tracer activity. Realisations in figures correspond to runs 16 (blue), 18 (red), and 20 (green).

Realisation #	Recovery Times [y]		
	t_{05} (5%)	t_{50} (50%)	t_{95} (95%)
1	1.09×10^{2}	6.74×10^{2}	9.26×10^{3}
2	8.95×10^{1}	6.13×10^{2}	4.95×10^{3}
3	9.26×10^{1}	6.28×10^{2}	4.93×10^{3}
4	1.16×10^{2}	7.04×10^{2}	7.42×10^{3}
5	1.08×10^{2}	6.90×10^{2}	8.67×10^{3}
6	1.15×10^{2}	7.00×10^{2}	1.15×10^{4}
7	1.21×10^{2}	7.13×10^{2}	1.00×10^{4}
8	1.14×10^{2}	6.92×10^{2}	7.92×10^{3}
9	9.64×10^{1}	6.49×10^{2}	5.56×10^{3}
10	7.99×10^{1}	5.91×10^{2}	2.82×10^{3}
11	9.04×10^{1}	6.25×10^{2}	4.48×10^{3}
12	9.00×10^{1}	6.24×10^{2}	3.15×10^{3}
13	1.02×10^{2}	6.60×10^{2}	8.82×10^{3}
14	8.59×10^{1}	6.23×10^{2}	3.71×10^{3}
15	1.15×10^{2}	6.89×10^{2}	8.20×10^{3}
16	$\mathbf{1.15\times10^{2}}$	$\mathbf{6.96\times10^{2}}$	$\mathbf{9.02\times10^{3}}$
17	1.22×10^{2}	7.10×10^{2}	1.13×10^{4}
18	$\mathbf{1.34\times10^{2}}$	$\mathbf{7.56\times10^{2}}$	$\mathbf{1.78\times10^{4}}$
19	8.59×10^{1}	6.25×10^{2}	4.48×10^{3}
20	$\mathbf{7.93\times10^{1}}$	$\mathbf{5.89\times10^{2}}$	$\mathbf{1.82\times10^{3}}$

Table 24. Simulated recovery times for 5%, 50%, and 95% of injected ^{137}Cs tracer activity. Realisations in figures correspond to runs 16 (blue), 18 (red), and 20 (green).

Realisation #	Recovery Times [y]		
	t_{05} (5%)	t_{50} (50%)	t_{95} (95%)
1	2.64×10^{3}	2.95×10^{4}	4.99×10^{6}
2	1.34×10^{3}	1.34×10^{4}	2.55×10^{6}
3	1.39×10^{3}	1.35×10^{4}	2.42×10^{6}
4	1.82×10^{3}	2.30×10^{4}	4.04×10^{6}
5	1.98×10^{3}	2.23×10^{4}	4.68×10^{6}
6	3.22×10^{3}	3.46×10^{4}	6.25×10^{6}
7	3.63×10^{3}	3.68×10^{4}	5.38×10^{6}
8	1.95×10^{3}	2.21×10^{4}	4.14×10^{6}
9	1.86×10^{3}	1.63×10^{4}	2.91×10^{6}
10	1.11×10^{3}	8.45×10^{3}	1.27×10^{6}
11	1.47×10^{3}	1.23×10^{4}	2.20×10^{6}
12	1.16×10^{3}	7.67×10^{3}	1.53×10^{6}
13	2.38×10^{3}	2.23×10^{4}	4.69×10^{6}
14	1.56×10^{3}	1.27×10^{4}	1.84×10^{6}
15	2.70×10^{3}	2.61×10^{4}	4.39×10^{6}
16	$\mathbf{1.95\times10^{3}}$	$\mathbf{2.01\times10^{4}}$	$\mathbf{4.86\times10^{6}}$
17	2.39×10^{3}	3.12×10^{4}	6.26×10^{6}
18	$\mathbf{4.15\times10^{3}}$	$\mathbf{4.93\times10^{4}}$	$\mathbf{9.92\times10^{6}}$
19	1.27×10^{3}	1.28×10^{4}	2.21×10^{6}
20	$\mathbf{9.42\times10^{2}}$	$\mathbf{4.77\times10^{3}}$	$\mathbf{7.65\times10^{5}}$

Table 25. Simulated recovery times for 5%, 50%, and 95% of injected ^{226}Ra tracer activity. Realisations in figures correspond to runs 16 (blue), 18 (red), and 20 (green).

Realisation #	Recovery Times [y]		
	t_{05} (5%)	t_{50} (50%)	t_{95} (95%)
1	1.54×10^{3}	1.21×10^{4}	1.90×10^{6}
2	8.84×10^{2}	5.78×10^{3}	9.73×10^{5}
3	9.05×10^{2}	5.85×10^{3}	9.22×10^{5}
4	1.33×10^{3}	9.53×10^{3}	1.54×10^{6}
5	1.30×10^{3}	9.25×10^{3}	1.79×10^{6}
6	1.86×10^{3}	1.41×10^{4}	2.39×10^{6}
7	2.01×10^{3}	1.49×10^{4}	2.06×10^{6}
8	1.28×10^{3}	9.21×10^{3}	1.58×10^{6}
9	1.20×10^{3}	6.91×10^{3}	1.11×10^{6}
10	7.42×10^{2}	3.86×10^{3}	4.85×10^{5}
11	1.00×10^{3}	5.35×10^{3}	8.41×10^{5}
12	8.99×10^{2}	3.49×10^{3}	5.85×10^{5}
13	1.46×10^{3}	9.31×10^{3}	1.79×10^{6}
14	1.01×10^{3}	5.53×10^{3}	7.07×10^{5}
15	1.61×10^{3}	1.08×10^{4}	1.67×10^{6}
16	$\mathbf{1.33\times10^{3}}$	$\mathbf{8.45\times10^{3}}$	$\mathbf{1.85\times10^{6}}$
17	1.52×10^{3}	1.27×10^{4}	2.39×10^{6}
18	$\mathbf{2.25\times10^{3}}$	$\mathbf{1.98\times10^{4}}$	$\mathbf{3.79\times10^{6}}$
19	8.43×10^{2}	5.54×10^{3}	8.47×10^{5}
20	$\mathbf{6.58\times10^{2}}$	$\mathbf{2.32\times10^{3}}$	$\mathbf{2.92\times10^{5}}$

Table 26. Simulated recovery times for 5%, 50%, and 95% of injected ^{99}Tc tracer activity. Realisations in figures correspond to runs 16 (blue), 18 (red), and 20 (green).

Realisation #	Recovery Times [y]		
	t_{05} (5%)	t_{50} (50%)	t_{95} (95%)
1	1.07×10^{4}	1.41×10^{5}	2.43×10^{7}
2	4.92×10^{3}	6.29×10^{4}	1.25×10^{7}
3	4.94×10^{3}	6.25×10^{4}	1.15×10^{7}
4	5.69×10^{3}	1.10×10^{5}	1.99×10^{7}
5	6.97×10^{3}	1.05×10^{5}	2.24×10^{7}
6	1.31×10^{4}	1.67×10^{5}	3.04×10^{7}
7	1.54×10^{4}	1.77×10^{5}	2.65×10^{7}
8	6.90×10^{3}	1.04×10^{5}	2.02×10^{7}
9	6.69×10^{3}	7.77×10^{4}	1.43×10^{7}
10	3.72×10^{3}	3.89×10^{4}	6.26×10^{6}
11	4.89×10^{3}	5.82×10^{4}	1.07×10^{7}
12	2.83×10^{3}	3.48×10^{4}	7.20×10^{6}
13	9.20×10^{3}	1.07×10^{5}	2.28×10^{7}
14	5.59×10^{3}	6.00×10^{4}	9.09×10^{6}
15	1.05×10^{4}	1.24×10^{5}	2.12×10^{7}
16	**6.75×10^{3}**	**9.37×10^{4}**	**2.26×10^{7}**
17	8.75×10^{3}	1.49×10^{5}	2.97×10^{7}
18	**1.76×10^{4}**	**2.37×10^{5}**	**4.77×10^{7}**
19	4.23×10^{3}	6.02×10^{4}	1.09×10^{7}
20	**2.39×10^{3}**	**2.12×10^{4}**	**3.73×10^{6}**

Table 27. Simulated recovery times for 5%, 50%, and 95% of injected ^{241}Am tracer activity. Realisations in figures correspond to runs 16 (blue), 18 (red), and 20 (green).

Realisation #	Recovery Times [y]		
	t_{05} (5%)	t_{50} (50%)	t_{95} (95%)
1	3.00×10^{4}	4.16×10^{5}	7.21×10^{7}
2	1.33×10^{4}	1.84×10^{5}	3.72×10^{7}
3	1.33×10^{4}	1.84×10^{5}	3.43×10^{7}
4	1.48×10^{4}	3.24×10^{5}	5.93×10^{7}
5	1.88×10^{4}	3.09×10^{5}	6.62×10^{7}
6	3.70×10^{4}	4.94×10^{5}	9.03×10^{7}
7	4.34×10^{4}	5.24×10^{5}	7.89×10^{7}
8	1.87×10^{4}	3.06×10^{5}	6.02×10^{7}
9	1.81×10^{4}	2.29×10^{5}	4.26×10^{7}
10	9.70×10^{3}	1.13×10^{5}	1.86×10^{7}
11	1.28×10^{4}	1.71×10^{5}	3.17×10^{7}
12	6.58×10^{3}	1.02×10^{5}	2.14×10^{7}
13	2.53×10^{4}	3.17×10^{5}	6.78×10^{7}
14	1.49×10^{4}	1.76×10^{5}	2.70×10^{7}
15	2.92×10^{4}	3.65×10^{5}	6.31×10^{7}
16	**1.80×10^{4}**	**2.76×10^{5}**	**6.72×10^{7}**
17	2.39×10^{4}	4.40×10^{5}	8.82×10^{7}
18	**4.98×10^{4}**	**7.01×10^{5}**	**1.39×10^{8}**
19	1.11×10^{4}	1.77×10^{5}	3.24×10^{7}
20	**5.56×10^{3}**	**6.13×10^{4}**	**1.11×10^{7}**

Breakthrough curves for Dirac pulse injection

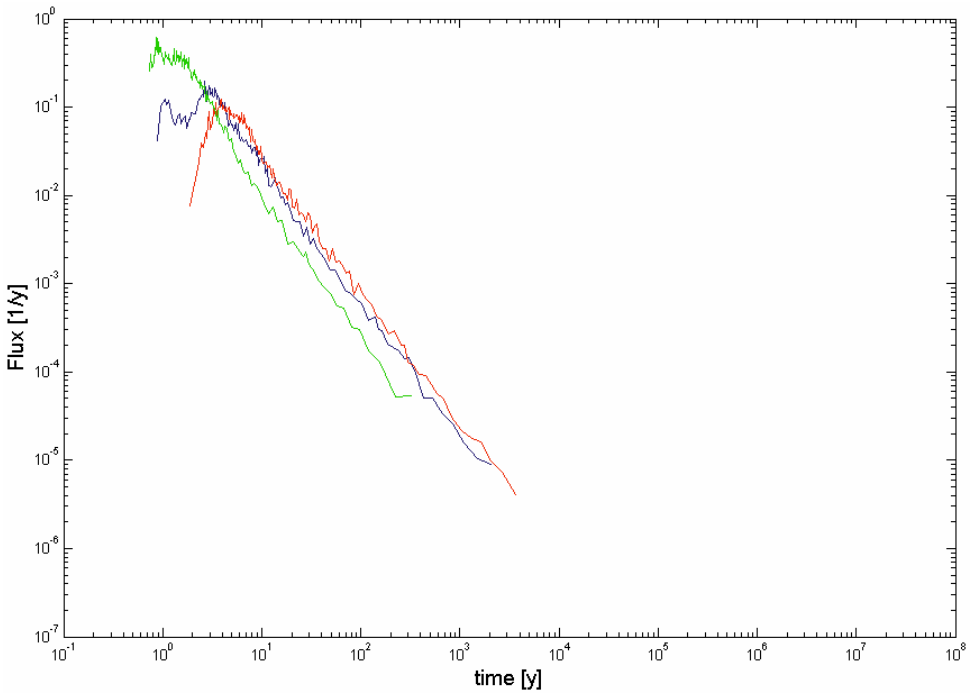

Figure 58. *Radionuclide flux vs. time, breakthrough curve for ^{129}I.*

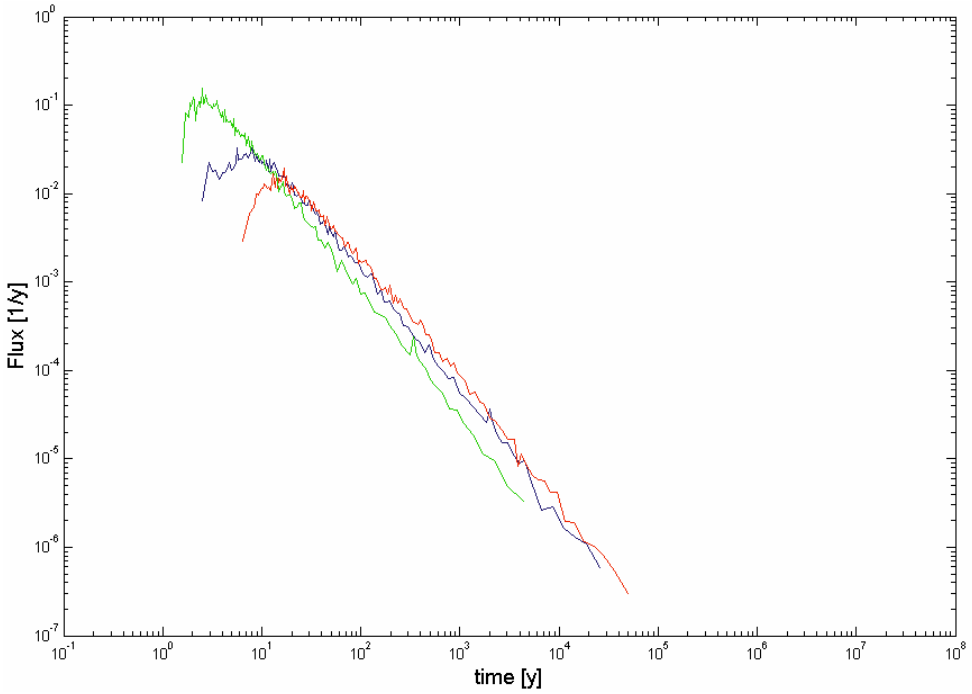

Figure 59. *Radionuclide flux vs. time, breakthrough curve for ^{47}Ca.*

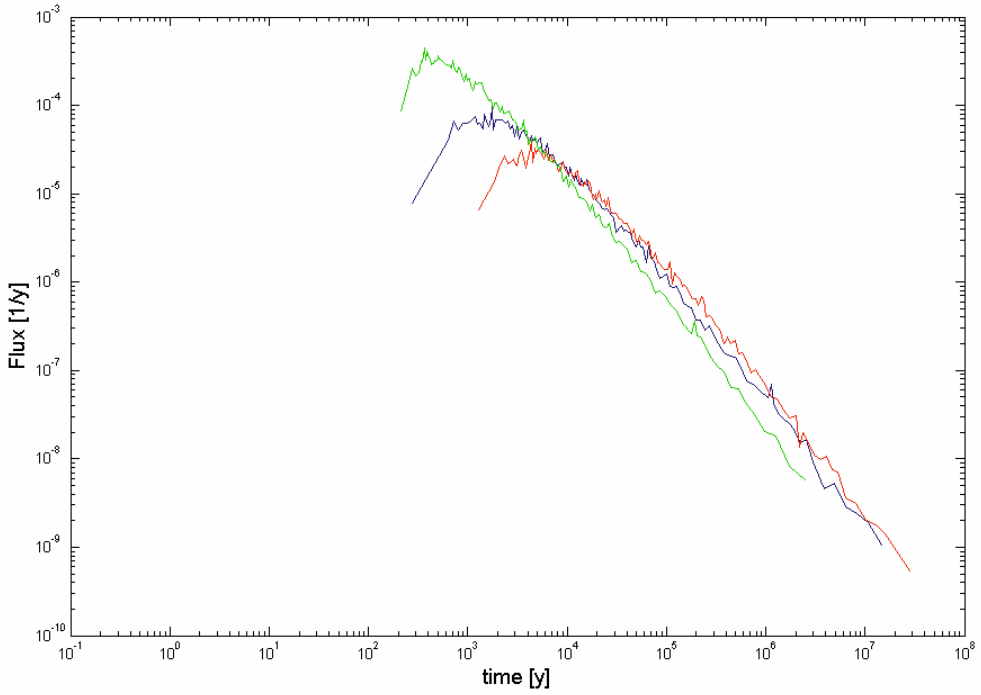

Figure 60. *Radionuclide flux vs. time, breakthrough curve for ^{137}Cs.*

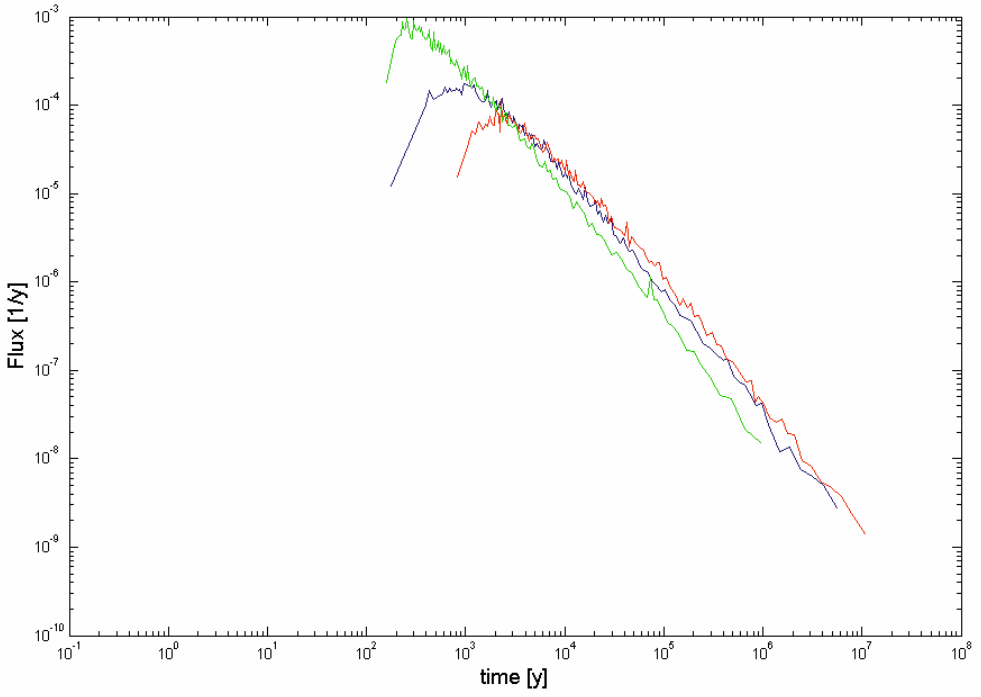

Figure 61. *Radionuclide flux vs. time, breakthrough curve for ^{226}Ra.*

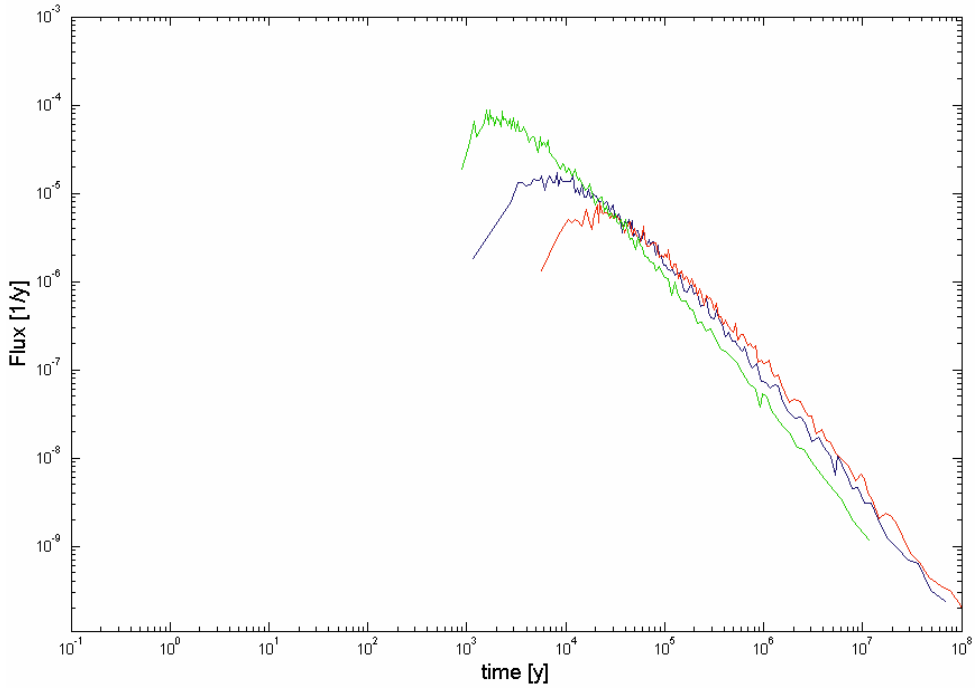

Figure 62. *Radionuclide flux vs. time, breakthrough curve for ^{99}Tc.*

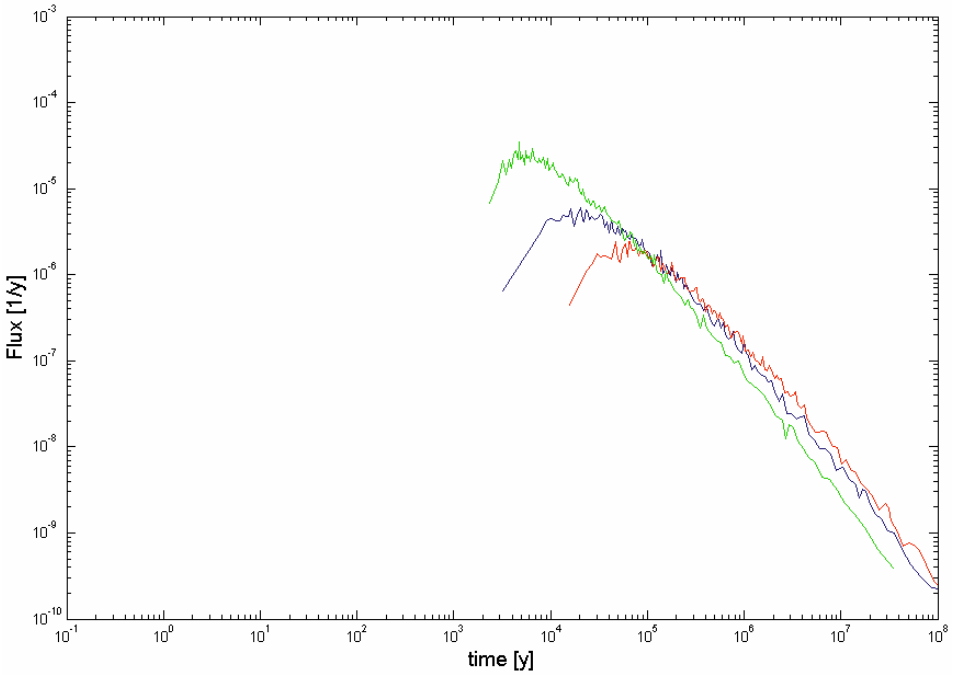

Figure 63. *Radionuclide flux vs. time, breakthrough curve for ^{241}Am.*

Breakthrough times for recovery of 5, 50 and 95% of the Dirac pulse injection

Table 28. Simulated recovery times for 5%, 50%, and 95% of injected ^{129}I tracer activity (Dirac pulse). Realisations in figures correspond to runs 16 (blue), 18 (red), and 20 (green).

Realisation #	Recovery Times [y]		
	t_{05} (5%)	t_{50} (50%)	t_{95} (95%)
1	2.45	7.42	6.16×10^{2}
2	1.70	4.25	3.02×10^{2}
3	1.60	4.21	3.32×10^{2}
4	1.00	5.79	4.79×10^{2}
5	1.60	6.07	6.05×10^{2}
6	2.38	7.87	7.53×10^{2}
7	2.83	8.09	6.39×10^{2}
8	1.74	5.9	5.30×10^{2}
9	1.80	4.55	3.50×10^{2}
10	1.20	3.05	1.52×10^{2}
11	1.50	3.65	2.63×10^{2}
12	9.23×10^{-1}	3.18	2.02×10^{2}
13	2.05	5.97	5.62×10^{2}
14	1.45	4.00	2.23×10^{2}
15	2.49	6.73	5.21×10^{2}
16	**1.43**	**6.28**	**6.34×10^{2}**
17	2.18	7.15	7.48×10^{2}
18	**3.18**	**1.03×10^{1}**	**1.26×10^{3}**
19	1.53	4.15	2.75×10^{2}
20	**8.68×10^{-1}**	**2.27**	**9.53×10^{1}**

Table 29. Simulated recovery times for 5%, 50%, and 95% of injected ^{47}Ca tracer activity (Dirac pulse). Realisations in figures correspond to runs 16 (blue), 18 (red), and 20 (green).

Realisation #	Recovery Times [y]		
	t_{05} (5%)	t_{50} (50%)	t_{95} (95%)
1	8.24	5.73×10^{1}	8.77×10^{3}
2	4.43	2.70×10^{1}	4.46×10^{3}
3	4.37	2.72×10^{1}	4.30×10^{3}
4	3.72	4.51×10^{1}	7.07×10^{3}
5	5.37	4.40×10^{1}	8.21×10^{3}
6	9.16	6.66×10^{1}	1.09×10^{4}
7	1.03×10^{1}	7.04×10^{1}	9.42×10^{3}
8	5.49	4.39×10^{1}	7.23×10^{3}
9	5.43	3.22×10^{1}	5.09×10^{3}
10	3.33	1.75×10^{1}	2.22×10^{3}
11	4.13	2.48×10^{1}	3.90×10^{3}
12	2.39	1.64×10^{1}	2.68×10^{3}
13	6.96	4.42×10^{1}	8.22×10^{3}
14	4.54	2.55×10^{1}	3.25×10^{3}
15	7.89	5.09×10^{1}	7.69×10^{3}
16	**5.24**	**4.08×10^{1}**	**8.51×10^{3}**
17	6.47	6.05×10^{1}	1.09×10^{4}
18	**1.18×10^{1}**	**9.33×10^{1}**	**1.74×10^{4}**
19	3.88	2.60×10^{1}	3.89×10^{3}
20	**2.16**	**1.03×10^{1}**	**1.34×10^{3}**

Table 30. Simulated recovery times for 5%, 50%, and 95% of injected ^{137}Cs tracer activity (Dirac pulse). Realisations in figures correspond to runs 16 (blue), 18 (red), and 20 (green).

Realisation #	Recovery Times [y]		
	t_{05} (5%)	t_{50} (50%)	t_{95} (95%)
1	2.23×10^{3}	2.90×10^{4}	4.98×10^{6}
2	1.01×10^{3}	1.28×10^{4}	2.55×10^{6}
3	1.00×10^{3}	1.30×10^{4}	2.42×10^{6}
4	1.07×10^{3}	2.25×10^{4}	4.04×10^{6}
5	1.40×10^{3}	2.19×10^{4}	4.68×10^{6}
6	2.73×10^{3}	3.41×10^{4}	6.25×10^{6}
7	3.19×10^{3}	3.63×10^{4}	5.38×10^{6}
8	1.39×10^{3}	2.16×10^{4}	4.14×10^{6}
9	1.36×10^{3}	1.58×10^{4}	2.91×10^{6}
10	7.33×10^{2}	7.90×10^{3}	1.27×10^{6}
11	9.67×10^{2}	1.19×10^{4}	2.20×10^{6}
12	4.74×10^{2}	7.21×10^{3}	1.53×10^{6}
13	1.88×10^{3}	2.19×10^{4}	4.69×10^{6}
14	1.12×10^{3}	1.22×10^{4}	1.84×10^{6}
15	2.16×10^{3}	2.57×10^{4}	4.39×10^{6}
16	$\mathbf{1.33\times10^{3}}$	$\mathbf{1.96\times10^{4}}$	$\mathbf{4.86\times10^{6}}$
17	1.76×10^{3}	3.08×10^{4}	6.26×10^{6}
18	$\mathbf{3.66\times10^{3}}$	$\mathbf{4.88\times10^{4}}$	$\mathbf{9.92\times10^{6}}$
19	8.40×10^{2}	1.23×10^{4}	2.21×10^{6}
20	$\mathbf{4.01\times10^{2}}$	$\mathbf{4.31\times10^{3}}$	$\mathbf{7.65\times10^{5}}$

Table 31. Simulated recovery times for 5%, 50%, and 95% of injected ^{226}Ra tracer activity (Dirac pulse). Realisations in figures correspond to runs 16 (blue), 18 (red), and 20 (green).

Realisation #	Recovery Times [y]		
	t_{05} (5%)	t_{50} (50%)	t_{95} (95%)
1	1.15×10^{3}	1.15×10^{4}	1.90×10^{6}
2	5.48×10^{2}	5.24×10^{3}	9.73×10^{5}
3	5.56×10^{2}	5.26×10^{3}	9.22×10^{5}
4	5.59×10^{2}	9.01×10^{3}	1.54×10^{6}
5	7.51×10^{2}	8.78×10^{3}	1.78×10^{6}
6	1.38×10^{3}	1.36×10^{4}	2.38×10^{6}
7	1.57×10^{3}	1.44×10^{4}	2.05×10^{6}
8	7.33×10^{2}	8.75×10^{3}	1.58×10^{6}
9	7.36×10^{2}	6.40×10^{3}	1.11×10^{6}
10	4.21×10^{2}	3.29×10^{3}	4.85×10^{5}
11	5.38×10^{2}	4.84×10^{3}	8.41×10^{5}
12	2.78×10^{2}	3.02×10^{3}	5.85×10^{5}
13	9.95×10^{2}	8.86×10^{3}	1.79×10^{6}
14	6.30×10^{2}	4.99×10^{3}	7.06×10^{5}
15	1.11×10^{3}	1.03×10^{4}	1.67×10^{6}
16	$\mathbf{7.15\times10^{2}}$	$\mathbf{7.95\times10^{3}}$	$\mathbf{1.85\times10^{6}}$
17	8.89×10^{2}	1.23×10^{4}	2.39×10^{6}
18	$\mathbf{1.80\times10^{3}}$	$\mathbf{1.93\times10^{4}}$	$\mathbf{3.78\times10^{6}}$
19	4.78×10^{2}	4.99×10^{3}	8.47×10^{5}
20	$\mathbf{2.50\times10^{2}}$	$\mathbf{1.84\times10^{3}}$	$\mathbf{2.92\times10^{5}}$

Table 32. Simulated recovery times for 5%, 50%, and 95% of injected ^{99}Tc tracer activity (Dirac pulse). Realisations in figures correspond to runs 16 (blue), 18 (red), and 20 (green).

Realisation #	Recovery Times [y]		
	t_{05} (5%)	t_{50} (50%)	t_{95} (95%)
1	1.03×10^{4}	1.41×10^{5}	2.43×10^{7}
2	4.57×10^{3}	6.24×10^{4}	1.25×10^{7}
3	4.53×10^{3}	6.21×10^{4}	1.15×10^{7}
4	4.95×10^{3}	1.09×10^{5}	1.99×10^{7}
5	6.39×10^{3}	1.04×10^{5}	2.24×10^{7}
6	1.27×10^{4}	1.66×10^{5}	3.04×10^{7}
7	1.49×10^{4}	1.77×10^{5}	2.65×10^{7}
8	6.34×10^{3}	1.03×10^{5}	2.02×10^{7}
9	6.22×10^{3}	7.72×10^{4}	1.43×10^{7}
10	3.29×10^{3}	3.83×10^{4}	6.26×10^{6}
11	4.38×10^{3}	5.78×10^{4}	1.07×10^{7}
12	2.11×10^{3}	3.45×10^{4}	7.20×10^{6}
13	8.70×10^{3}	1.07×10^{5}	2.28×10^{7}
14	5.10×10^{3}	5.94×10^{4}	9.09×10^{6}
15	9.99×10^{3}	1.23×10^{5}	2.12×10^{7}
16	**6.09×10^{3}**	**9.32×10^{4}**	**2.26×10^{7}**
17	8.10×10^{3}	1.49×10^{5}	2.97×10^{7}
18	**1.71×10^{4}**	**2.37×10^{5}**	**4.77×10^{7}**
19	3.79×10^{3}	5.97×10^{4}	1.09×10^{7}
20	**1.77×10^{3}**	**2.07×10^{4}**	**3.73×10^{6}**

Table 33. Simulated recovery times for 5%, 50%, and 95% of injected ^{241}Am tracer activity (Dirac pulse). Realisations in figures correspond to runs 16 (blue), 18 (red), and 20 (green).

Realisation #	Recovery Times [y]		
	t_{05} (5%)	t_{50} (50%)	t_{95} (95%)
1	2.96×10^{4}	4.15×10^{5}	7.21×10^{7}
2	1.30×10^{4}	1.84×10^{5}	3.72×10^{7}
3	1.28×10^{4}	1.83×10^{5}	3.43×10^{7}
4	1.41×10^{4}	3.24×10^{5}	5.93×10^{7}
5	1.82×10^{4}	3.08×10^{5}	6.62×10^{7}
6	3.66×10^{4}	4.93×10^{5}	9.03×10^{7}
7	4.29×10^{4}	5.23×10^{5}	7.89×10^{7}
8	1.82×10^{4}	3.05×10^{5}	6.02×10^{7}
9	1.76×10^{4}	2.28×10^{5}	4.26×10^{7}
10	9.26×10^{3}	1.13×10^{5}	1.86×10^{7}
11	1.24×10^{4}	1.71×10^{5}	3.17×10^{7}
12	5.88×10^{3}	1.01×10^{5}	2.14×10^{7}
13	2.49×10^{4}	3.17×10^{5}	6.78×10^{7}
14	1.44×10^{4}	1.76×10^{5}	2.70×10^{7}
15	2.86×10^{4}	3.64×10^{5}	6.31×10^{7}
16	**1.75×10^{4}**	**2.75×10^{5}**	**6.72×10^{7}**
17	2.34×10^{4}	4.39×10^{5}	8.82×10^{7}
18	**4.93×10^{4}**	**7.00×10^{5}**	**1.39×10^{8}**
19	1.07×10^{4}	1.76×10^{5}	3.24×10^{7}
20	**4.93×10^{3}**	**6.08×10^{4}**	**1.11×10^{7}**

Breakthrough time history for the tracers at recovery plane 2 (Easting = 1880)

Breakthrough curves for extended pulse injection boundary condition

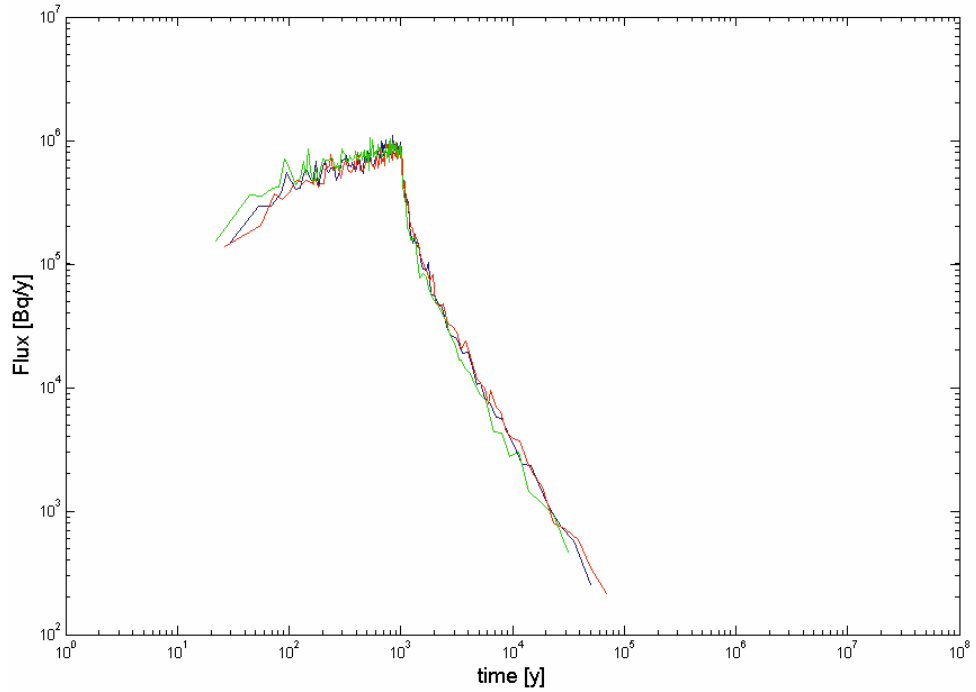

Figure 64. *Radionuclide flux vs. time, breakthrough curve for ^{129}I.*

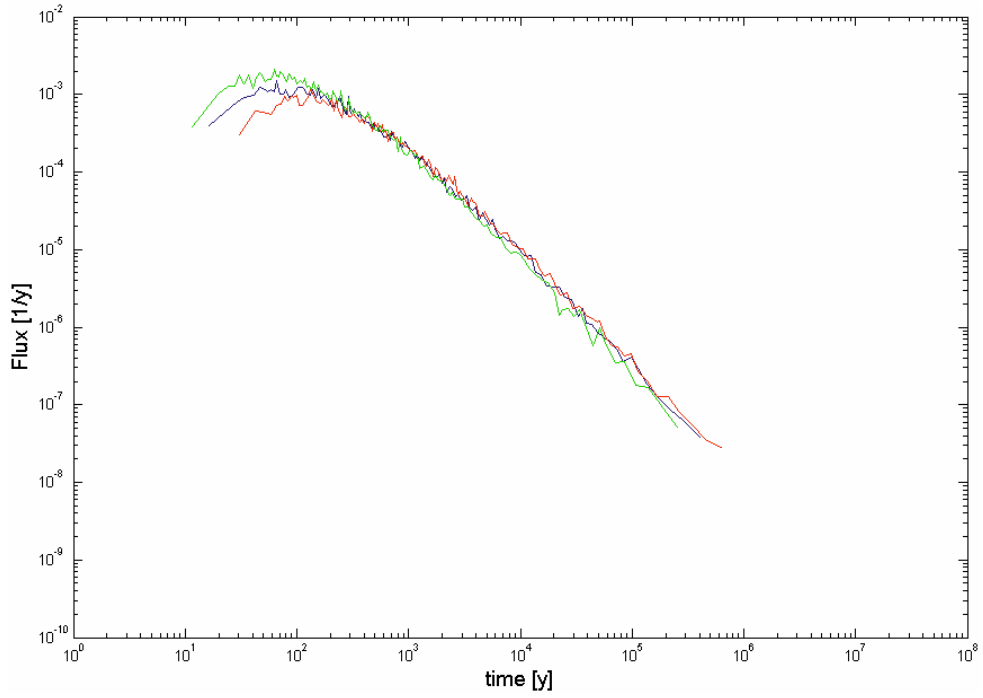

Figure 65. *Radionuclide flux vs. time, breakthrough curve for ^{47}Ca.*

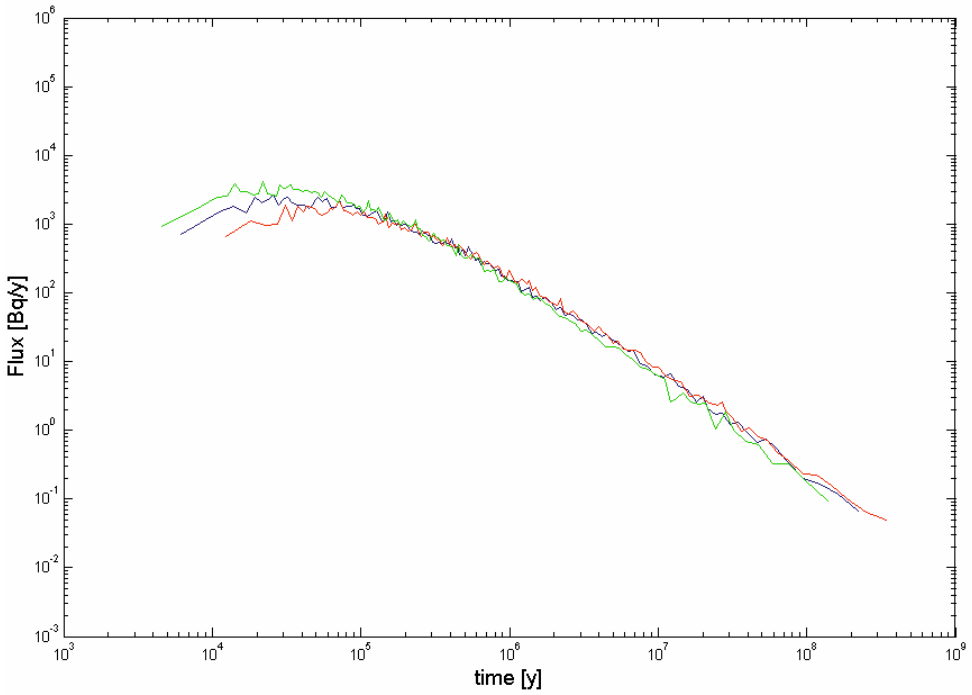

Figure 66. *Radionuclide flux vs. time, breakthrough curve for ^{137}Cs.*

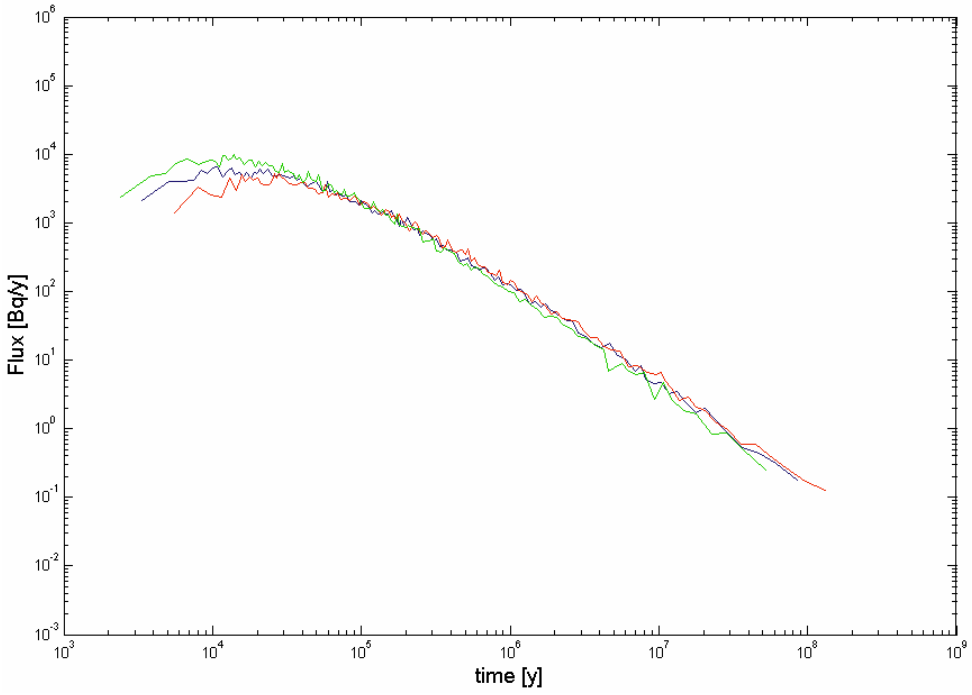

Figure 67. *Radionuclide flux vs. time, breakthrough curve for ^{226}Ra.*

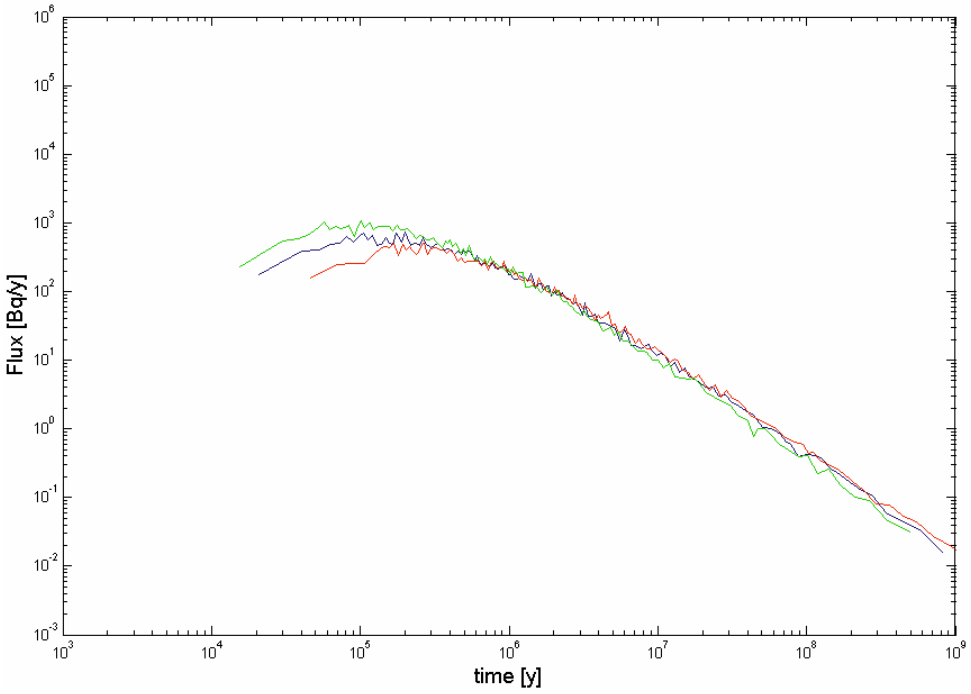

Figure 68. *Radionuclide flux vs. time, breakthrough curve for* ^{99}Tc.

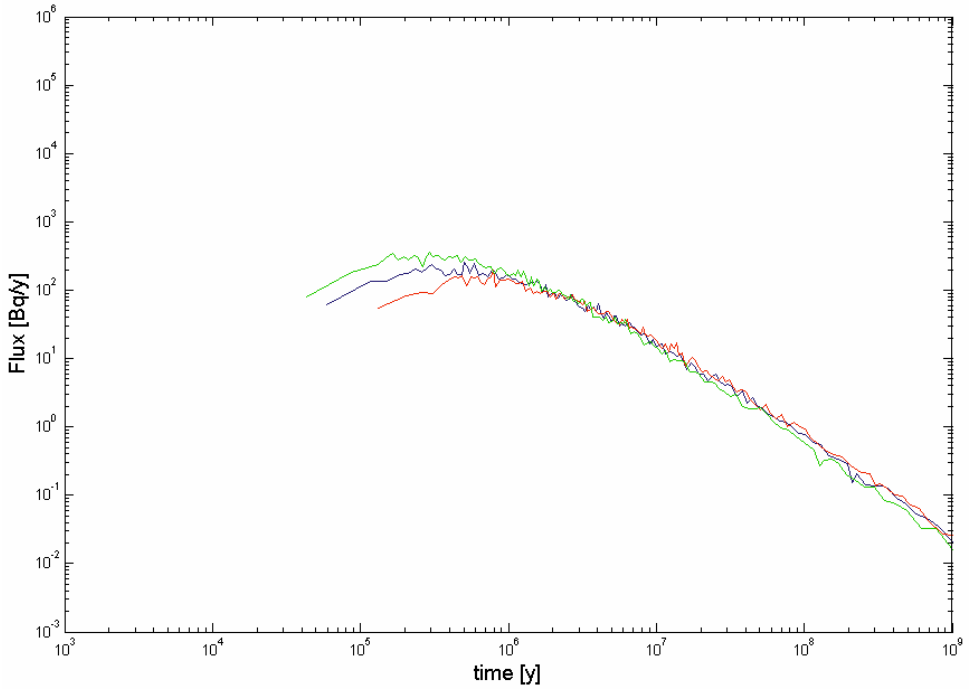

Figure 69. *Radionuclide flux vs. time, breakthrough curve for* ^{241}Am.

Breakthrough times for recovery of 5, 50 and 95% of the injected mass

Table 34. Simulated recovery times for 5%, 50%, and 95% of injected ^{129}I tracer activity. Realisations in figures correspond to runs 16 (blue), 18 (red), and 20 (green).

Realisation #	Recovery Times [y]		
	t_{05} (5%)	t_{50} (50%)	t_{95} (95%)
1	1.56×10^{2}	8.22×10^{2}	2.34×10^{4}
2	1.39×10^{2}	7.79×10^{2}	1.64×10^{4}
3	1.50×10^{2}	7.96×10^{2}	1.72×10^{4}
4	1.55×10^{2}	7.92×10^{2}	1.87×10^{4}
5	1.52×10^{2}	7.94×10^{2}	1.77×10^{4}
6	1.50×10^{2}	7.92×10^{2}	1.65×10^{4}
7	1.47×10^{2}	8.02×10^{2}	1.63×10^{4}
8	1.53×10^{2}	8.09×10^{2}	2.25×10^{4}
9	1.43×10^{2}	7.78×10^{2}	1.48×10^{4}
10	1.26×10^{2}	7.38×10^{2}	1.27×10^{4}
11	1.29×10^{2}	7.53×10^{2}	1.22×10^{4}
12	1.43×10^{2}	7.71×10^{2}	1.26×10^{4}
13	1.44×10^{2}	7.82×10^{2}	1.53×10^{4}
14	1.20×10^{2}	7.27×10^{2}	1.11×10^{4}
15	1.55×10^{2}	7.86×10^{2}	1.71×10^{4}
16	$\mathbf{1.54\times10^{2}}$	$\mathbf{8.08\times10^{2}}$	$\mathbf{1.66\times10^{4}}$
17	1.56×10^{2}	8.23×10^{2}	2.61×10^{4}
18	$\mathbf{1.62\times10^{2}}$	$\mathbf{8.37\times10^{2}}$	$\mathbf{2.24\times10^{4}}$
19	1.41×10^{2}	7.85×10^{2}	1.60×10^{4}
20	$\mathbf{1.34\times10^{2}}$	$\mathbf{7.44\times10^{2}}$	$\mathbf{1.13\times10^{4}}$

Table 35. Simulated recovery times for 5%, 50%, and 95% of injected ^{47}Ca tracer activity. Realisations in figures correspond to runs 16 (blue), 18 (red), and 20 (green).

Realisation #	Recovery Times [y]		
	t_{05} (5%)	t_{50} (50%)	t_{95} (95%)
1	3.75×10^{2}	1.87×10^{3}	1.99×10^{5}
2	3.21×10^{2}	1.53×10^{3}	1.31×10^{5}
3	3.47×10^{2}	1.58×10^{3}	1.37×10^{5}
4	3.85×10^{2}	1.56×10^{3}	1.60×10^{5}
5	3.51×10^{2}	1.52×10^{3}	1.39×10^{5}
6	3.59×10^{2}	1.61×10^{3}	1.48×10^{5}
7	3.55×10^{2}	1.68×10^{3}	1.50×10^{5}
8	3.69×10^{2}	1.67×10^{3}	1.87×10^{5}
9	3.40×10^{2}	1.50×10^{3}	1.15×10^{5}
10	2.77×10^{2}	1.25×10^{3}	9.92×10^{4}
11	3.02×10^{2}	1.35×10^{3}	1.00×10^{5}
12	3.19×10^{2}	1.35×10^{3}	1.11×10^{5}
13	3.39×10^{2}	1.55×10^{3}	1.39×10^{5}
14	2.71×10^{2}	1.21×10^{3}	8.78×10^{4}
15	3.76×10^{2}	1.56×10^{3}	1.49×10^{5}
16	$\mathbf{3.68\times10^{2}}$	$\mathbf{1.58\times10^{3}}$	$\mathbf{1.34\times10^{5}}$
17	3.84×10^{2}	1.82×10^{3}	2.13×10^{5}
18	$\mathbf{4.03\times10^{2}}$	$\mathbf{1.92\times10^{3}}$	$\mathbf{2.04\times10^{5}}$
19	3.30×10^{2}	1.55×10^{3}	1.34×10^{5}
20	$\mathbf{2.94\times10^{2}}$	$\mathbf{1.25\times10^{3}}$	$\mathbf{8.53\times10^{4}}$

Table 36. Simulated recovery times for 5%, 50%, and 95% of injected ^{137}Cs tracer activity. Realisations in figures correspond to runs 16 (blue), 18 (red), and 20 (green).

Realisation #	Recovery Times [y]		
	t_{05} (5%)	t_{50} (50%)	t_{95} (95%)
1	4.65×10^{4}	7.18×10^{5}	1.10×10^{8}
2	3.43×10^{4}	5.31×10^{5}	7.18×10^{7}
3	3.45×10^{4}	5.50×10^{5}	7.40×10^{7}
4	3.50×10^{4}	5.75×10^{5}	8.74×10^{7}
5	3.29×10^{4}	5.28×10^{5}	7.73×10^{7}
6	3.79×10^{4}	5.81×10^{5}	8.16×10^{7}
7	4.21×10^{4}	6.24×10^{5}	8.19×10^{7}
8	3.92×10^{4}	5.96×10^{5}	1.02×10^{8}
9	3.12×10^{4}	5.15×10^{5}	6.30×10^{7}
10	2.26×10^{4}	3.62×10^{5}	5.41×10^{7}
11	2.83×10^{4}	4.20×10^{5}	5.60×10^{7}
12	2.52×10^{4}	4.44×10^{5}	6.11×10^{7}
13	3.78×10^{4}	5.53×10^{5}	7.63×10^{7}
14	2.06×10^{4}	3.35×10^{5}	4.83×10^{7}
15	3.69×10^{4}	5.58×10^{5}	8.18×10^{7}
16	$\mathbf{3.22\times10^{4}}$	$\mathbf{5.65\times10^{5}}$	$\mathbf{7.38\times10^{7}}$
17	4.50×10^{4}	7.11×10^{5}	1.16×10^{8}
18	$\mathbf{4.90\times10^{4}}$	$\mathbf{7.59\times10^{5}}$	$\mathbf{1.11\times10^{8}}$
19	3.42×10^{4}	5.38×10^{5}	7.31×10^{7}
20	$\mathbf{2.37\times10^{4}}$	$\mathbf{3.63\times10^{5}}$	$\mathbf{4.64\times10^{7}}$

Table 37. Simulated recovery times for 5%, 50%, and 95% of injected ^{226}Ra tracer activity. Realisations in figures correspond to runs 16 (blue), 18 (red), and 20 (green).

Realisation #	Recovery Times [y]		
	t_{05} (5%)	t_{50} (50%)	t_{95} (95%)
1	1.89×10^{4}	2.76×10^{5}	4.20×10^{7}
2	1.41×10^{4}	2.04×10^{5}	2.74×10^{7}
3	1.42×10^{4}	2.11×10^{5}	2.82×10^{7}
4	1.46×10^{4}	2.21×10^{5}	3.33×10^{7}
5	1.36×10^{4}	2.03×10^{5}	2.95×10^{7}
6	1.56×10^{4}	2.23×10^{5}	3.11×10^{7}
7	1.73×10^{4}	2.40×10^{5}	3.12×10^{7}
8	1.60×10^{4}	2.29×10^{5}	3.89×10^{7}
9	1.29×10^{4}	1.97×10^{5}	2.40×10^{7}
10	9.52×10^{3}	1.39×10^{5}	2.06×10^{7}
11	1.17×10^{4}	1.62×10^{5}	2.14×10^{7}
12	1.05×10^{4}	1.70×10^{5}	2.33×10^{7}
13	1.54×10^{4}	2.12×10^{5}	2.91×10^{7}
14	8.71×10^{3}	1.29×10^{5}	1.84×10^{7}
15	1.52×10^{4}	2.14×10^{5}	3.12×10^{7}
16	$\mathbf{1.32\times10^{4}}$	$\mathbf{2.17\times10^{5}}$	$\mathbf{2.81\times10^{7}}$
17	1.83×10^{4}	2.73×10^{5}	4.42×10^{7}
18	$\mathbf{1.99\times10^{4}}$	$\mathbf{2.91\times10^{5}}$	$\mathbf{4.23\times10^{7}}$
19	1.40×10^{4}	2.06×10^{5}	2.79×10^{7}
20	$\mathbf{9.87\times10^{3}}$	$\mathbf{1.40\times10^{5}}$	$\mathbf{1.77\times10^{7}}$

Table 38. Simulated recovery times for 5%, 50%, and 95% of injected ^{99}Tc tracer activity. Realisations in figures correspond to runs 16 (blue), 18 (red), and 20 (green).

Realisation #	Recovery Times [y]		
	t_{05} (5%)	t_{50} (50%)	t_{95} (95%)
1	1.79×10^{5}	2.69×10^{6}	4.22×10^{8}
2	1.29×10^{5}	1.97×10^{6}	2.72×10^{8}
3	1.27×10^{5}	2.00×10^{6}	2.67×10^{8}
4	1.37×10^{5}	2.18×10^{6}	3.32×10^{8}
5	1.25×10^{5}	1.98×10^{6}	2.92×10^{8}
6	1.48×10^{5}	2.27×10^{6}	3.10×10^{8}
7	1.68×10^{5}	2.39×10^{6}	3.22×10^{8}
8	1.47×10^{5}	2.26×10^{6}	3.70×10^{8}
9	1.18×10^{5}	1.92×10^{6}	2.36×10^{8}
10	8.47×10^{4}	1.33×10^{6}	2.02×10^{8}
11	1.05×10^{5}	1.57×10^{6}	2.06×10^{8}
12	9.20×10^{4}	1.62×10^{6}	2.23×10^{8}
13	1.42×10^{5}	2.06×10^{6}	2.91×10^{8}
14	7.73×10^{4}	1.26×10^{6}	1.83×10^{8}
15	1.41×10^{5}	2.11×10^{6}	3.15×10^{8}
16	$\mathbf{1.20\times10^{5}}$	$\mathbf{2.11\times10^{6}}$	$\mathbf{2.68\times10^{8}}$
17	1.73×10^{5}	2.65×10^{6}	4.21×10^{8}
18	$\mathbf{1.92\times10^{5}}$	$\mathbf{2.88\times10^{6}}$	$\mathbf{4.40\times10^{8}}$
19	1.28×10^{5}	1.97×10^{6}	2.60×10^{8}
20	$\mathbf{8.48\times10^{4}}$	$\mathbf{1.29\times10^{6}}$	$\mathbf{1.64\times10^{8}}$

Table 39. Simulated recovery times for 5%, 50%, and 95% of injected ^{241}Am tracer activity. Realisations in figures correspond to runs 16 (blue), 18 (red), and 20 (green).

Realisation #	Recovery Times [y]		
	t_{05} (5%)	t_{50} (50%)	t_{95} (95%)
1	5.23×10^{5}	7.84×10^{6}	1.23×10^{9}
2	3.75×10^{5}	5.74×10^{6}	7.97×10^{8}
3	3.70×10^{5}	5.82×10^{6}	7.77×10^{8}
4	3.96×10^{5}	6.39×10^{6}	9.65×10^{8}
5	3.63×10^{5}	5.76×10^{6}	8.60×10^{8}
6	4.32×10^{5}	6.63×10^{6}	9.05×10^{8}
7	4.85×10^{5}	7.01×10^{6}	9.52×10^{8}
8	4.25×10^{5}	6.60×10^{6}	1.08×10^{9}
9	3.42×10^{5}	5.57×10^{6}	6.86×10^{8}
10	2.45×10^{5}	3.88×10^{6}	5.85×10^{8}
11	3.04×10^{5}	4.57×10^{6}	6.02×10^{8}
12	2.66×10^{5}	4.74×10^{6}	6.46×10^{8}
13	4.11×10^{5}	6.02×10^{6}	8.44×10^{8}
14	2.24×10^{5}	3.69×10^{6}	5.33×10^{8}
15	4.11×10^{5}	6.17×10^{6}	9.24×10^{8}
16	$\mathbf{3.50\times10^{5}}$	$\mathbf{6.15\times10^{6}}$	$\mathbf{7.95\times10^{8}}$
17	5.03×10^{5}	7.75×10^{6}	1.22×10^{9}
18	$\mathbf{5.58\times10^{5}}$	$\mathbf{8.42\times10^{6}}$	$\mathbf{1.28\times10^{9}}$
19	3.73×10^{5}	5.75×10^{6}	7.61×10^{8}
20	$\mathbf{2.46\times10^{5}}$	$\mathbf{3.75\times10^{6}}$	$\mathbf{4.75\times10^{8}}$

Breakthrough curves for Dirac pulse injection

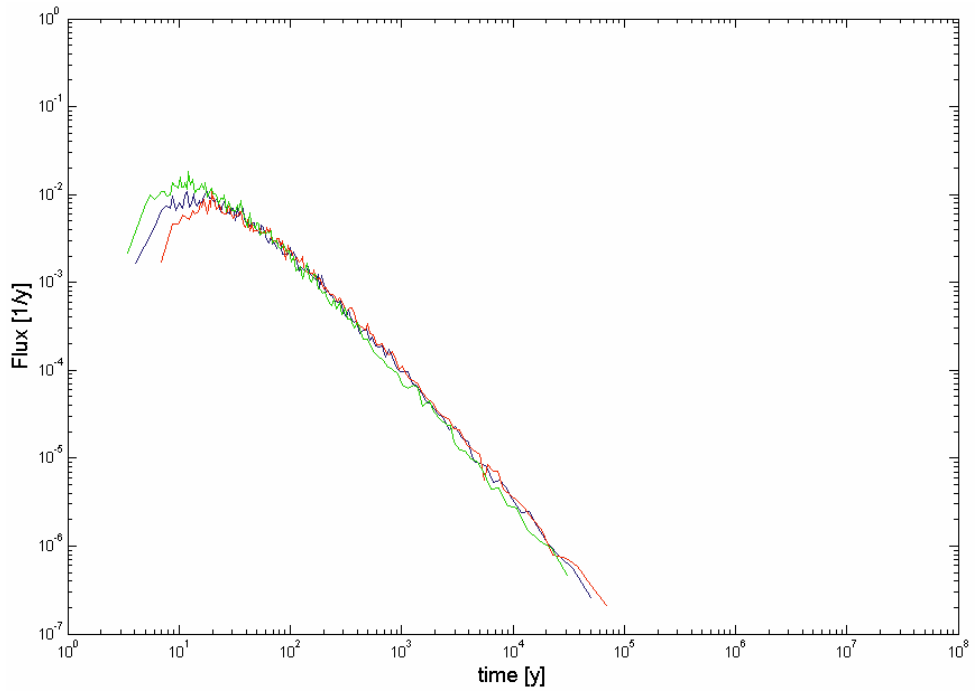

Figure 70. *Radionuclide flux vs. time, breakthrough curve for ^{129}I.*

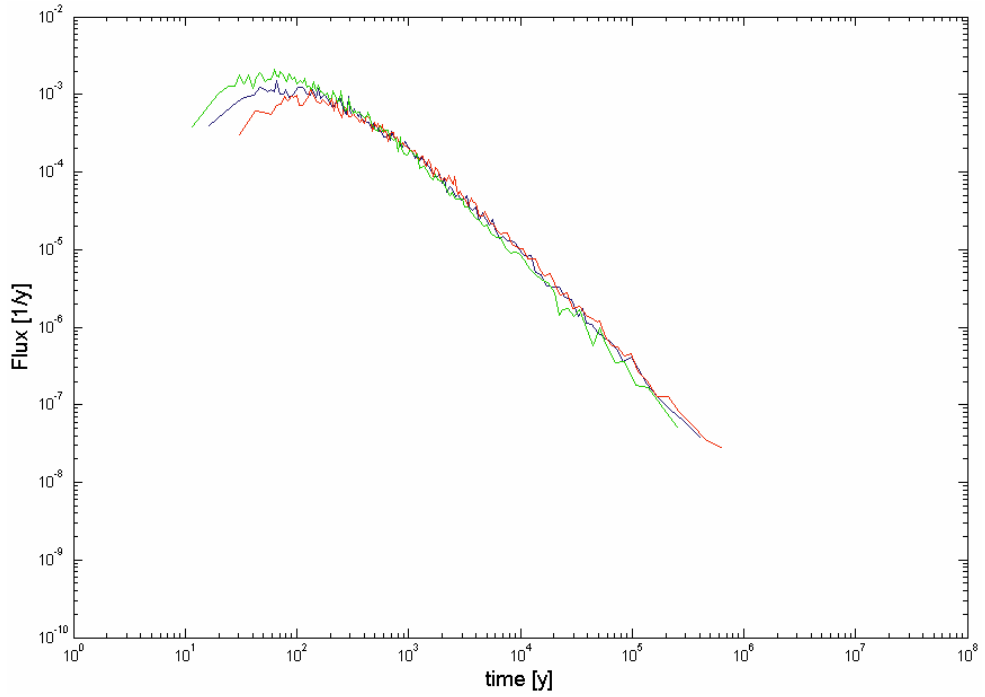

Figure 71. *Radionuclide flux vs. time, breakthrough curve for ^{47}Ca.*

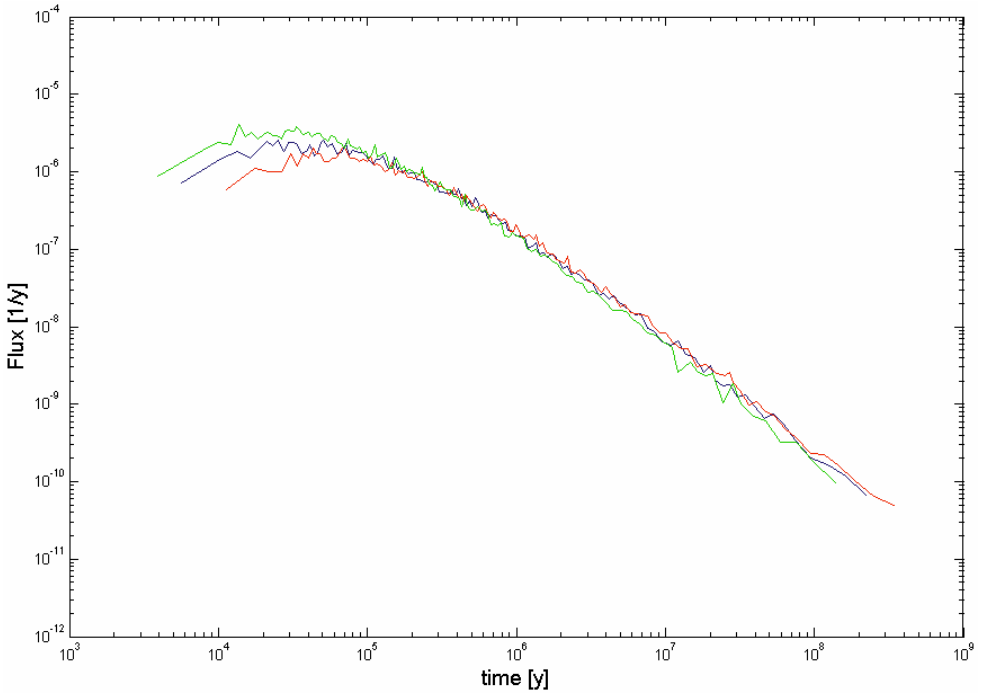

Figure 72. *Radionuclide flux vs. time, breakthrough curve for ^{137}Cs.*

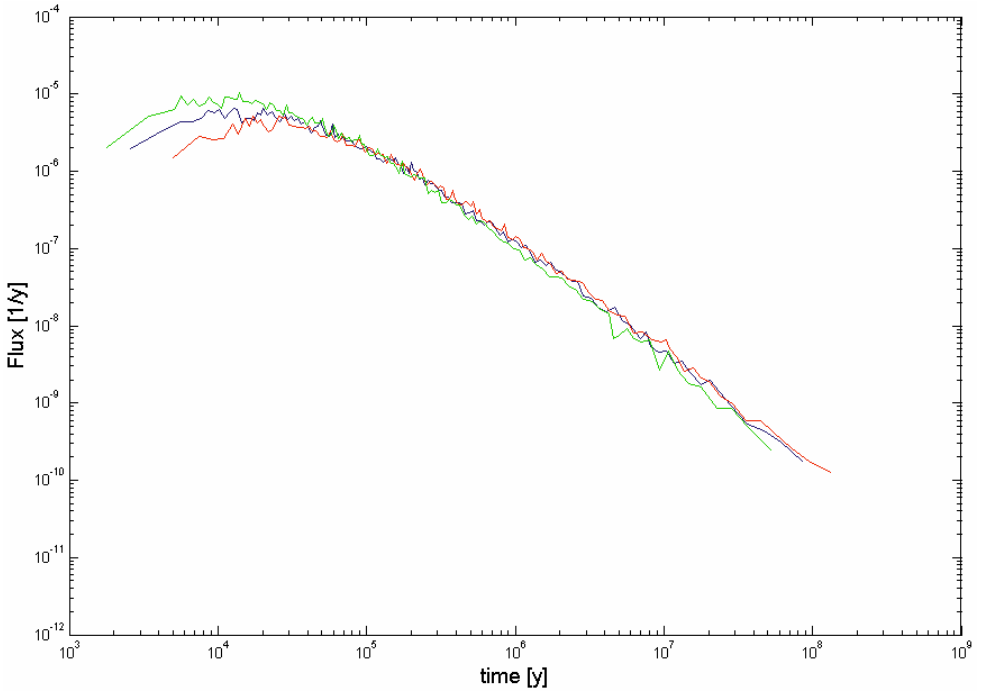

Figure 73. *Radionuclide flux vs. time, breakthrough curve for ^{226}Ra.*

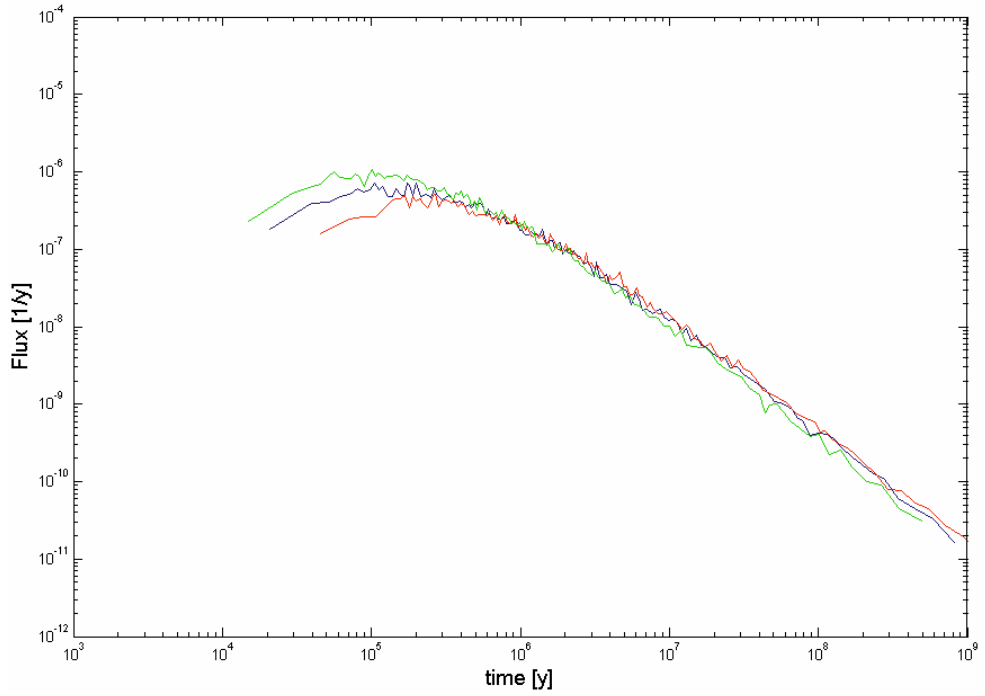

Figure 74. *Radionuclide flux vs. time, breakthrough curve for ^{99}Tc.*

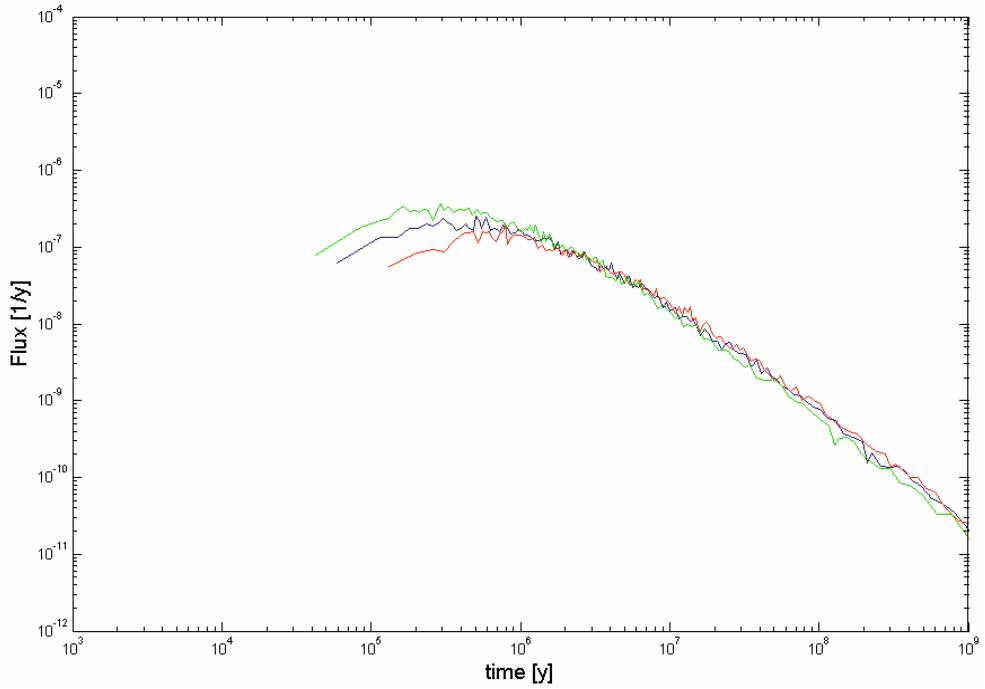

Figure 75. *Radionuclide flux vs. time, breakthrough curve for ^{241}Am.*

Breakthrough times for recovery of 5, 50 and 95% of the Dirac pulse injection

Table 40. Simulated recovery times for 5%, 50%, and 95% of injected ^{129}I tracer activity (Dirac pulse). Realisations in figures correspond to runs 16 (blue), 18 (red), and 20 (green).

Realisation #	Recovery Times [y]		
	t_{05} (5%)	t_{50} (50%)	t_{95} (95%)
1	1.53×10^{1}	1.59×10^{2}	2.29×10^{4}
2	1.19×10^{1}	1.19×10^{2}	1.57×10^{4}
3	1.21×10^{1}	1.29×10^{2}	1.66×10^{4}
4	1.20×10^{1}	1.23×10^{2}	1.84×10^{4}
5	1.18×10^{1}	1.21×10^{2}	1.71×10^{4}
6	1.31×10^{1}	1.24×10^{2}	1.62×10^{4}
7	1.41×10^{1}	1.32×10^{2}	1.58×10^{4}
8	1.32×10^{1}	1.35×10^{2}	2.18×10^{4}
9	1.11×10^{1}	1.17×10^{2}	1.42×10^{4}
10	8.86	8.53×10^{1}	1.19×10^{4}
11	1.05×10^{1}	9.40×10^{1}	1.17×10^{4}
12	9.24	1.04×10^{2}	1.20×10^{4}
13	1.30×10^{1}	1.20×10^{2}	1.50×10^{4}
14	8.16	7.71×10^{1}	1.07×10^{4}
15	1.29×10^{1}	1.23×10^{2}	1.66×10^{4}
16	**1.18×10^{1}**	**1.32×10^{2}**	**1.63×10^{4}**
17	1.46×10^{1}	1.56×10^{2}	2.57×10^{4}
18	**1.61×10^{1}**	**1.63×10^{2}**	**2.20×10^{4}**
19	1.20×10^{1}	1.25×10^{2}	1.55×10^{4}
20	**9.12**	**8.74×10^{1}**	**1.08×10^{4}**

Table 41. Simulated recovery times for 5%, 50%, and 95% of injected ^{47}Ca tracer activity (Dirac pulse). Realisations in figures correspond to runs 16 (blue), 18 (red), and 20 (green).

Realisation #	Recovery Times [y]		
	t_{05} (5%)	t_{50} (50%)	t_{95} (95%)
1	9.39×10^{1}	1.32×10^{3}	1.98×10^{5}
2	7.03×10^{1}	9.79×10^{2}	1.31×10^{5}
3	7.04×10^{1}	1.01×10^{3}	1.36×10^{5}
4	7.24×10^{1}	1.05×10^{3}	1.59×10^{5}
5	6.78×10^{1}	9.71×10^{2}	1.39×10^{5}
6	7.80×10^{1}	1.07×10^{3}	1.47×10^{5}
7	8.63×10^{1}	1.15×10^{3}	1.50×10^{5}
8	7.89×10^{1}	1.10×10^{3}	1.86×10^{5}
9	6.45×10^{1}	9.48×10^{2}	1.15×10^{5}
10	4.77×10^{1}	6.70×10^{2}	9.83×10^{4}
11	5.84×10^{1}	7.73×10^{2}	9.99×10^{4}
12	5.16×10^{1}	8.20×10^{2}	1.10×10^{5}
13	7.73×10^{1}	1.01×10^{3}	1.38×10^{5}
14	4.39×10^{1}	6.15×10^{2}	8.76×10^{4}
15	7.56×10^{1}	1.02×10^{3}	1.49×10^{5}
16	**6.67×10^{1}**	**1.04×10^{3}**	**1.34×10^{5}**
17	9.11×10^{1}	1.31×10^{3}	2.13×10^{5}
18	**1.00×10^{2}**	**1.39×10^{3}**	**2.04×10^{5}**
19	6.94×10^{1}	9.92×10^{2}	1.33×10^{5}
20	**4.94×10^{1}**	**6.72×10^{2}**	**8.53×10^{4}**

Table 42. Simulated recovery times for 5%, 50%, and 95% of injected ^{137}Cs tracer activity (Dirac pulse). Realisations in figures correspond to runs 16 (blue), 18 (red), and 20 (green).

Realisation #	Recovery Times [y]		
	t_{05} (5%)	t_{50} (50%)	t_{95} (95%)
1	4.61×10^{4}	7.17×10^{5}	1.10×10^{8}
2	3.40×10^{4}	5.30×10^{5}	7.18×10^{7}
3	3.39×10^{4}	5.50×10^{5}	7.40×10^{7}
4	3.45×10^{4}	5.75×10^{5}	8.74×10^{7}
5	3.24×10^{4}	5.27×10^{5}	7.73×10^{7}
6	3.75×10^{4}	5.81×10^{5}	8.16×10^{7}
7	4.17×10^{4}	6.24×10^{5}	8.19×10^{7}
8	3.87×10^{4}	5.96×10^{5}	1.02×10^{8}
9	3.07×10^{4}	5.14×10^{5}	6.30×10^{7}
10	2.21×10^{4}	3.61×10^{5}	5.41×10^{7}
11	2.77×10^{4}	4.19×10^{5}	5.60×10^{7}
12	2.45×10^{4}	4.43×10^{5}	6.11×10^{7}
13	3.73×10^{4}	5.52×10^{5}	7.63×10^{7}
14	1.99×10^{4}	3.34×10^{5}	4.83×10^{7}
15	3.64×10^{4}	5.57×10^{5}	8.18×10^{7}
16	$\mathbf{3.16\times10^{4}}$	$\mathbf{5.64\times10^{5}}$	$\mathbf{7.38\times10^{7}}$
17	4.46×10^{4}	7.10×10^{5}	1.16×10^{8}
18	$\mathbf{4.85\times10^{4}}$	$\mathbf{7.59\times10^{5}}$	$\mathbf{1.11\times10^{8}}$
19	3.35×10^{4}	5.37×10^{5}	7.31×10^{7}
20	$\mathbf{2.32\times10^{4}}$	$\mathbf{3.63\times10^{5}}$	$\mathbf{4.64\times10^{7}}$

Table 43. Simulated recovery times for 5%, 50%, and 95% of injected ^{226}Ra tracer activity (Dirac pulse). Realisations in figures correspond to runs 16 (blue), 18 (red), and 20 (green).

Realisation #	Recovery Times [y]		
	t_{05} (5%)	t_{50} (50%)	t_{95} (95%)
1	1.83×10^{4}	2.75×10^{5}	4.20×10^{7}
2	1.37×10^{4}	2.03×10^{5}	2.74×10^{7}
3	1.37×10^{4}	2.11×10^{5}	2.82×10^{7}
4	1.40×10^{4}	2.21×10^{5}	3.33×10^{7}
5	1.30×10^{4}	2.02×10^{5}	2.95×10^{7}
6	1.51×10^{4}	2.23×10^{5}	3.11×10^{7}
7	1.68×10^{4}	2.40×10^{5}	3.12×10^{7}
8	1.55×10^{4}	2.28×10^{5}	3.89×10^{7}
9	1.24×10^{4}	1.97×10^{5}	2.40×10^{7}
10	9.01×10^{3}	1.39×10^{5}	2.06×10^{7}
11	1.12×10^{4}	1.61×10^{5}	2.14×10^{7}
12	9.87×10^{3}	1.70×10^{5}	2.33×10^{7}
13	1.49×10^{4}	2.11×10^{5}	2.91×10^{7}
14	8.16×10^{3}	1.29×10^{5}	1.84×10^{7}
15	1.47×10^{4}	2.14×10^{5}	3.12×10^{7}
16	$\mathbf{1.27\times10^{4}}$	$\mathbf{2.16\times10^{5}}$	$\mathbf{2.81\times10^{7}}$
17	1.78×10^{4}	2.72×10^{5}	4.42×10^{7}
18	$\mathbf{1.93\times10^{4}}$	$\mathbf{2.91\times10^{5}}$	$\mathbf{4.23\times10^{7}}$
19	1.34×10^{4}	2.06×10^{5}	2.79×10^{7}
20	$\mathbf{9.36\times10^{3}}$	$\mathbf{1.39\times10^{5}}$	$\mathbf{1.77\times10^{7}}$

Table 44. Simulated recovery times for 5%, 50%, and 95% of injected ^{99}Tc tracer activity (Dirac pulse). Realisations in figures correspond to runs 16 (blue), 18 (red), and 20 (green).

Realisation #	Recovery Times [y]		
	t_{05} (5%)	t_{50} (50%)	t_{95} (95%)
1	1.79×10^{5}	2.69×10^{6}	4.22×10^{8}
2	1.29×10^{5}	1.97×10^{6}	2.72×10^{8}
3	1.27×10^{5}	2.00×10^{6}	2.67×10^{8}
4	1.36×10^{5}	2.18×10^{6}	3.32×10^{8}
5	1.24×10^{5}	1.98×10^{6}	2.92×10^{8}
6	1.48×10^{5}	2.26×10^{6}	3.10×10^{8}
7	1.67×10^{5}	2.39×10^{6}	3.22×10^{8}
8	1.46×10^{5}	2.26×10^{6}	3.70×10^{8}
9	1.17×10^{5}	1.92×10^{6}	2.36×10^{8}
10	8.41×10^{4}	1.33×10^{6}	2.02×10^{8}
11	1.04×10^{5}	1.57×10^{6}	2.06×10^{8}
12	9.16×10^{4}	1.62×10^{6}	2.23×10^{8}
13	1.41×10^{5}	2.06×10^{6}	2.91×10^{8}
14	7.69×10^{4}	1.26×10^{6}	1.83×10^{8}
15	1.41×10^{5}	2.11×10^{6}	3.15×10^{8}
16	$\mathbf{1.20\times10^{5}}$	$\mathbf{2.11\times10^{6}}$	$\mathbf{2.68\times10^{8}}$
17	1.73×10^{5}	2.65×10^{6}	4.21×10^{8}
18	$\mathbf{1.91\times10^{5}}$	$\mathbf{2.88\times10^{6}}$	$\mathbf{4.40\times10^{8}}$
19	1.28×10^{5}	1.97×10^{6}	2.60×10^{8}
20	$\mathbf{8.44\times10^{4}}$	$\mathbf{1.29\times10^{6}}$	$\mathbf{1.64\times10^{8}}$

Table 45. Simulated recovery times for 5%, 50%, and 95% of injected ^{241}Am tracer activity (Dirac pulse). Realisations in figures correspond to runs 16 (blue), 18 (red), and 20 (green).

Realisation #	Recovery Times [y]		
	t_{05} (5%)	t_{50} (50%)	t_{95} (95%)
1	5.22×10^{5}	7.84×10^{6}	1.23×10^{9}
2	3.75×10^{5}	5.74×10^{6}	7.97×10^{8}
3	3.69×10^{5}	5.82×10^{6}	7.77×10^{8}
4	3.95×10^{5}	6.39×10^{6}	9.65×10^{8}
5	3.62×10^{5}	5.76×10^{6}	8.60×10^{8}
6	4.31×10^{5}	6.63×10^{6}	9.05×10^{8}
7	4.84×10^{5}	7.01×10^{6}	9.52×10^{8}
8	4.25×10^{5}	6.60×10^{6}	1.08×10^{9}
9	3.41×10^{5}	5.57×10^{6}	6.86×10^{8}
10	2.44×10^{5}	3.88×10^{6}	5.85×10^{8}
11	3.03×10^{5}	4.57×10^{6}	6.02×10^{8}
12	2.66×10^{5}	4.74×10^{6}	6.46×10^{8}
13	4.11×10^{5}	6.02×10^{6}	8.44×10^{8}
14	2.24×10^{5}	3.69×10^{6}	5.33×10^{8}
15	4.10×10^{5}	6.17×10^{6}	9.24×10^{8}
16	$\mathbf{3.50\times10^{5}}$	$\mathbf{6.15\times10^{6}}$	$\mathbf{7.95\times10^{8}}$
17	5.03×10^{5}	7.75×10^{6}	1.22×10^{9}
18	$\mathbf{5.58\times10^{5}}$	$\mathbf{8.42\times10^{6}}$	$\mathbf{1.28\times10^{9}}$
19	3.72×10^{5}	5.75×10^{6}	7.61×10^{8}
20	$\mathbf{2.46\times10^{5}}$	$\mathbf{3.75\times10^{6}}$	$\mathbf{4.75\times10^{8}}$

Breakthrough time history for the tracers at Western boundary plane (Easting = 1800)

Breakthrough curves for extended pulse injection boundary condition

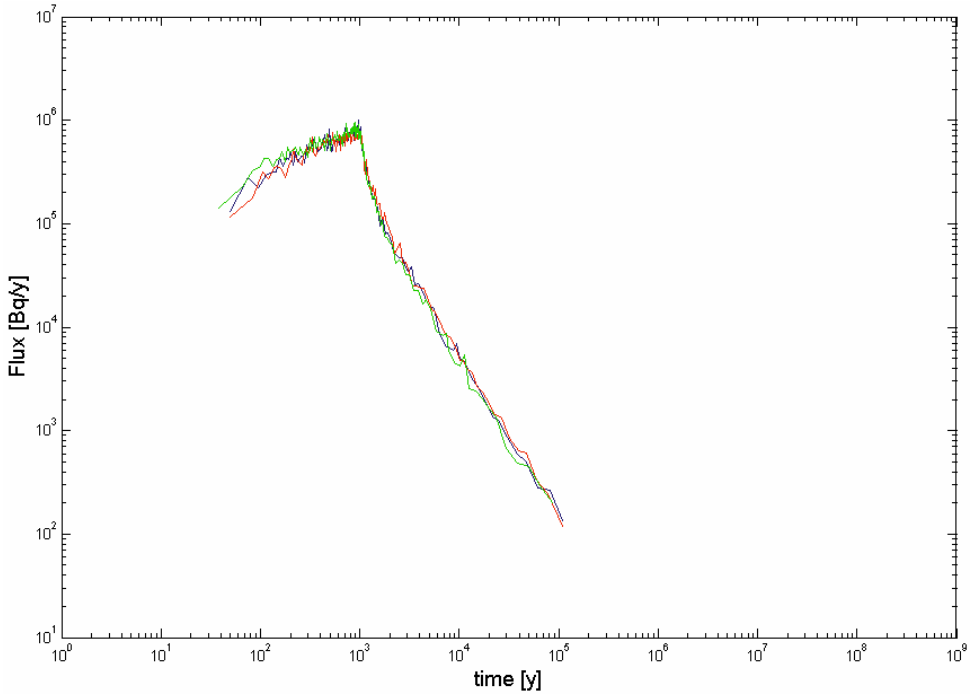

Figure 76. *Radionuclide flux vs. time, breakthrough curve for ^{129}I.*

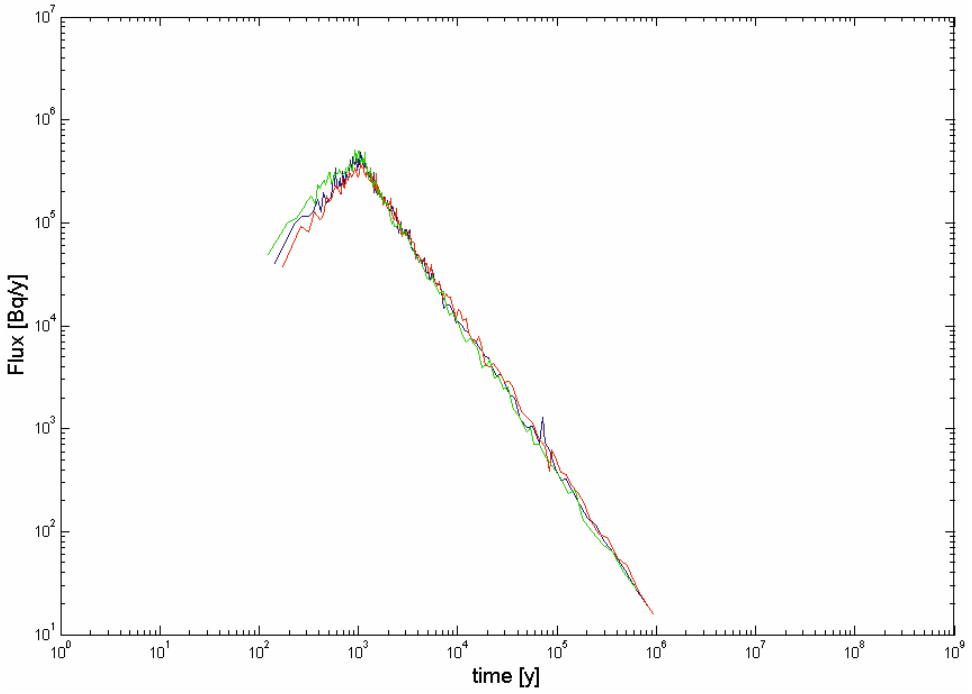

Figure 77. *Radionuclide flux vs. time, breakthrough curve for ^{47}Ca.*

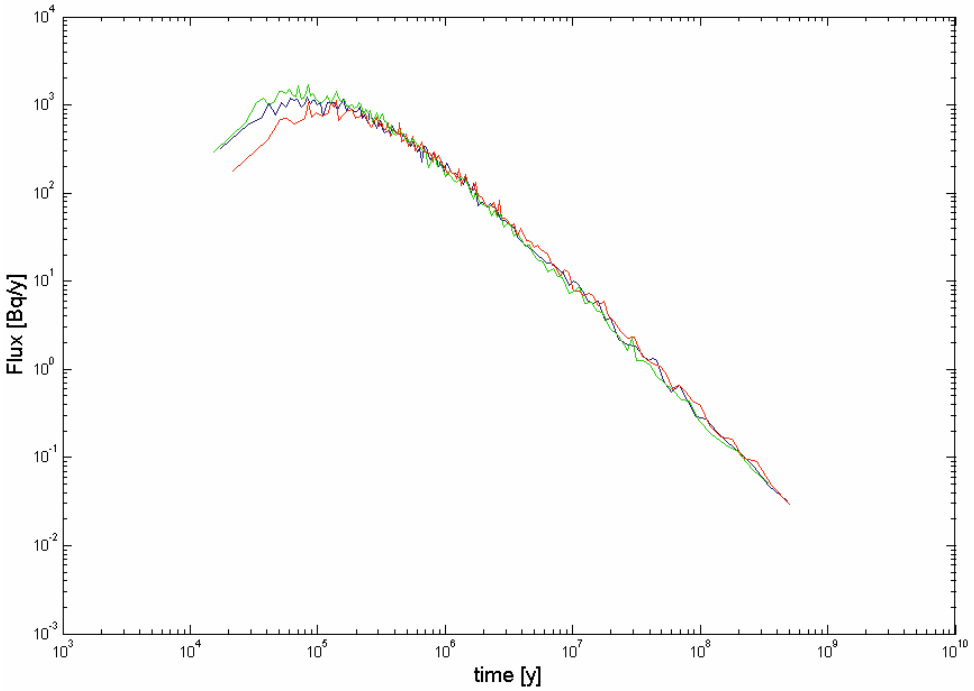

Figure 78. *Radionuclide flux vs. time, breakthrough curve for ^{137}Cs.*

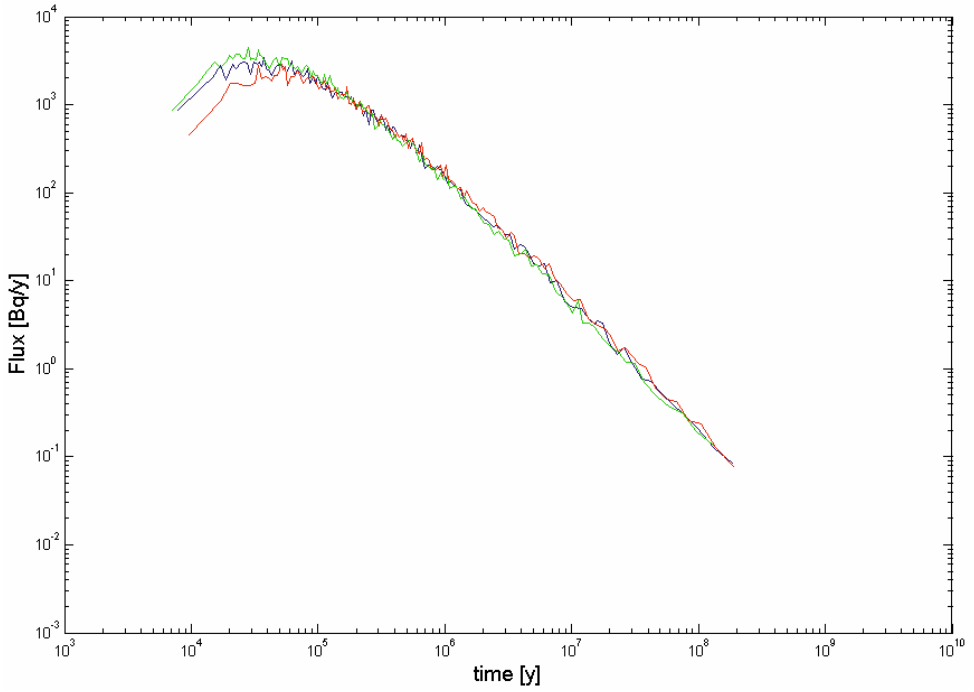

Figure 79. *Radionuclide flux vs. time, breakthrough curve for ^{226}Ra.*

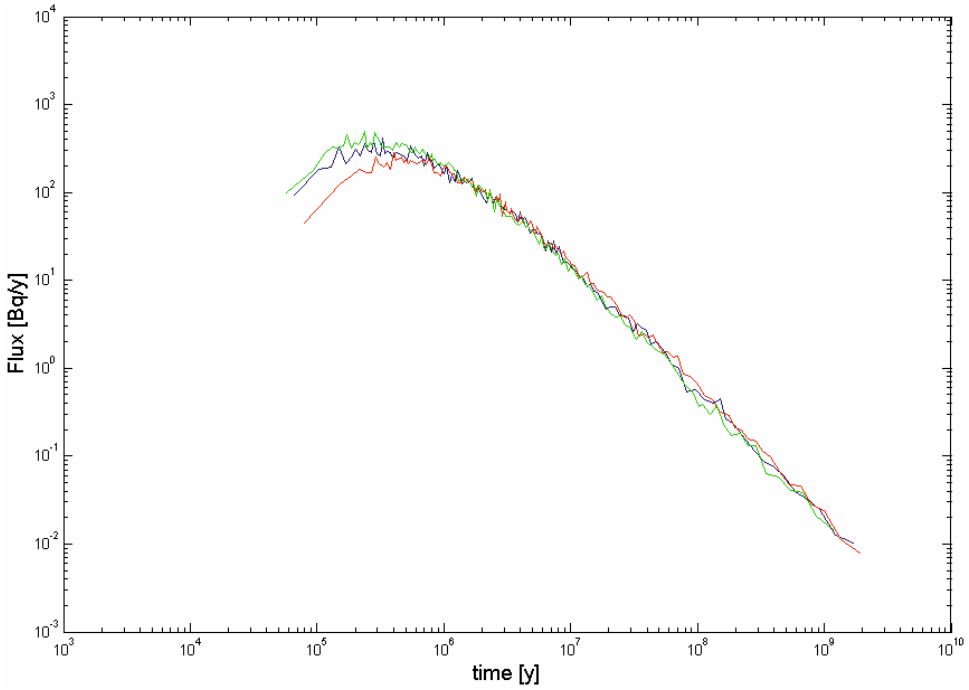

Figure 80. *Radionuclide flux vs. time, breakthrough curve for ^{99}Tc.*

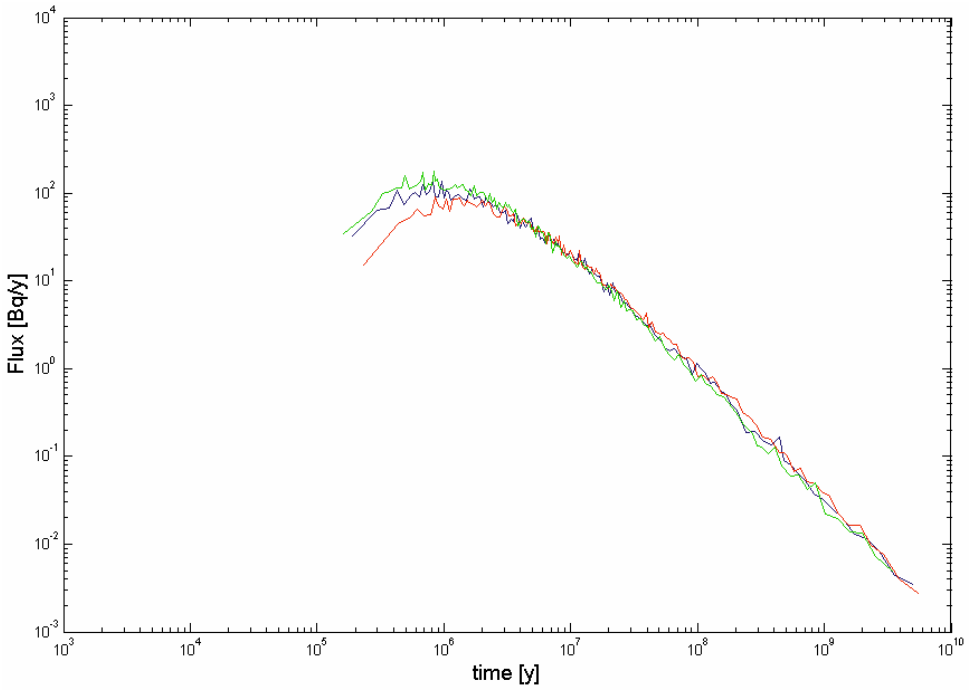

Figure 81. *Radionuclide flux vs. time, breakthrough curve for ^{241}Am.*

Breakthrough times for recovery of 5, 50 and 95% of the injected mass

Table 46. Simulated recovery times for 5%, 50%, and 95% of injected ^{129}I tracer activity. Realisations in figures correspond to runs 16 (blue), 18 (red), and 20 (green).

Realisation #	Recovery Times [y]		
	t_{05} (5%)	t_{50} (50%)	t_{95} (95%)
1	2.00×10^{2}	9.69×10^{2}	4.31×10^{4}
2	1.85×10^{2}	9.16×10^{2}	3.56×10^{4}
3	1.89×10^{2}	9.15×10^{2}	3.71×10^{4}
4	1.97×10^{2}	9.30×10^{2}	3.73×10^{4}
5	2.06×10^{2}	9.16×10^{2}	3.86×10^{4}
6	1.95×10^{2}	9.14×10^{2}	4.00×10^{4}
7	1.88×10^{2}	9.12×10^{2}	2.91×10^{4}
8	1.99×10^{2}	9.20×10^{2}	3.82×10^{4}
9	2.03×10^{2}	9.24×10^{2}	3.79×10^{4}
10	1.81×10^{2}	8.82×10^{2}	3.36×10^{4}
11	1.81×10^{2}	8.88×10^{2}	3.48×10^{4}
12	1.85×10^{2}	8.83×10^{2}	3.24×10^{4}
13	1.91×10^{2}	9.17×10^{2}	3.52×10^{4}
14	1.73×10^{2}	8.49×10^{2}	2.35×10^{4}
15	1.98×10^{2}	9.19×10^{2}	3.46×10^{4}
16	$\mathbf{2.03\times10^{2}}$	$\mathbf{9.19\times10^{2}}$	$\mathbf{3.72\times10^{4}}$
17	2.05×10^{2}	9.44×10^{2}	4.53×10^{4}
18	$\mathbf{2.15\times10^{2}}$	$\mathbf{9.55\times10^{2}}$	$\mathbf{3.83\times10^{4}}$
19	1.91×10^{2}	9.09×10^{2}	3.86×10^{4}
20	$\mathbf{1.76\times10^{2}}$	$\mathbf{8.77\times10^{2}}$	$\mathbf{2.98\times10^{4}}$

Table 47. Simulated recovery times for 5%, 50%, and 95% of injected ^{47}Ca tracer activity. Realisations in figures correspond to runs 16 (blue), 18 (red), and 20 (green).

Realisation #	Recovery Times [y]		
	t_{05} (5%)	t_{50} (50%)	t_{95} (95%)
1	5.42×10^{2}	3.06×10^{3}	3.43×10^{5}
2	4.67×10^{2}	2.52×10^{3}	2.78×10^{5}
3	4.88×10^{2}	2.41×10^{3}	2.95×10^{5}
4	5.39×10^{2}	2.65×10^{3}	3.21×10^{5}
5	5.12×10^{2}	2.45×10^{3}	3.03×10^{5}
6	5.22×10^{2}	2.61×10^{3}	3.43×10^{5}
7	5.02×10^{2}	2.58×10^{3}	2.36×10^{5}
8	5.21×10^{2}	2.52×10^{3}	2.97×10^{5}
9	5.13×10^{2}	2.56×10^{3}	2.97×10^{5}
10	4.31×10^{2}	2.13×10^{3}	2.62×10^{5}
11	4.57×10^{2}	2.25×10^{3}	2.79×10^{5}
12	4.57×10^{2}	2.15×10^{3}	2.56×10^{5}
13	4.97×10^{2}	2.59×10^{3}	2.90×10^{5}
14	4.34×10^{2}	1.99×10^{3}	1.81×10^{5}
15	5.36×10^{2}	2.58×10^{3}	2.80×10^{5}
16	$\mathbf{5.34\times10^{2}}$	$\mathbf{2.51\times10^{3}}$	$\mathbf{2.92\times10^{5}}$
17	5.66×10^{2}	2.86×10^{3}	3.75×10^{5}
18	$\mathbf{5.85\times10^{2}}$	$\mathbf{2.98\times10^{3}}$	$\mathbf{3.20\times10^{5}}$
19	4.91×10^{2}	2.51×10^{3}	3.14×10^{5}
20	$\mathbf{4.50\times10^{2}}$	$\mathbf{2.09\times10^{3}}$	$\mathbf{2.19\times10^{5}}$

Table 48. Simulated recovery times for 5%, 50%, and 95% of injected ^{137}Cs tracer activity. Realisations in figures correspond to runs 16 (blue), 18 (red), and 20 (green).

Realisation #	Recovery Times [y]		
	t_{05} (5%)	t_{50} (50%)	t_{95} (95%)
1	1.03×10^{5}	1.38×10^{6}	1.88×10^{8}
2	7.61×10^{4}	1.08×10^{6}	1.51×10^{8}
3	7.89×10^{4}	1.03×10^{6}	1.60×10^{8}
4	8.70×10^{4}	1.16×10^{6}	1.78×10^{8}
5	7.80×10^{4}	1.06×10^{6}	1.65×10^{8}
6	8.59×10^{4}	1.14×10^{6}	1.88×10^{8}
7	9.13×10^{4}	1.11×10^{6}	1.30×10^{8}
8	8.25×10^{4}	1.09×10^{6}	1.63×10^{8}
9	8.01×10^{4}	1.11×10^{6}	1.61×10^{8}
10	6.48×10^{4}	8.78×10^{5}	1.43×10^{8}
11	7.23×10^{4}	9.37×10^{5}	1.52×10^{8}
12	6.13×10^{4}	8.92×10^{5}	1.42×10^{8}
13	8.72×10^{4}	1.12×10^{6}	1.60×10^{8}
14	6.25×10^{4}	7.91×10^{5}	9.78×10^{7}
15	8.52×10^{4}	1.11×10^{6}	1.52×10^{8}
16	$\mathbf{7.40\times10^{4}}$	$\mathbf{1.09\times10^{6}}$	$\mathbf{1.59\times10^{8}}$
17	9.62×10^{4}	1.27×10^{6}	2.05×10^{8}
18	$\mathbf{1.03\times10^{5}}$	$\mathbf{1.34\times10^{6}}$	$\mathbf{1.75\times10^{8}}$
19	7.59×10^{4}	1.06×10^{6}	1.70×10^{8}
20	$\mathbf{6.35\times10^{4}}$	$\mathbf{8.40\times10^{5}}$	$\mathbf{1.20\times10^{8}}$

Table 49. Simulated recovery times for 5%, 50%, and 95% of injected ^{226}Ra tracer activity. Realisations in figures correspond to runs 16 (blue), 18 (red), and 20 (green).

Realisation #	Recovery Times [y]		
	t_{05} (5%)	t_{50} (50%)	t_{95} (95%)
1	4.05×10^{4}	5.28×10^{5}	7.15×10^{7}
2	3.00×10^{4}	4.16×10^{5}	5.75×10^{7}
3	3.13×10^{4}	3.96×10^{5}	6.11×10^{7}
4	3.44×10^{4}	4.45×10^{5}	6.79×10^{7}
5	3.11×10^{4}	4.05×10^{5}	6.29×10^{7}
6	3.41×10^{4}	4.35×10^{5}	7.16×10^{7}
7	3.63×10^{4}	4.24×10^{5}	4.94×10^{7}
8	3.27×10^{4}	4.18×10^{5}	6.23×10^{7}
9	3.19×10^{4}	4.23×10^{5}	6.13×10^{7}
10	2.59×10^{4}	3.36×10^{5}	5.47×10^{7}
11	2.88×10^{4}	3.59×10^{5}	5.79×10^{7}
12	2.44×10^{4}	3.42×10^{5}	5.41×10^{7}
13	3.46×10^{4}	4.27×10^{5}	6.11×10^{7}
14	2.50×10^{4}	3.03×10^{5}	3.73×10^{7}
15	3.38×10^{4}	4.26×10^{5}	5.79×10^{7}
16	$\mathbf{2.94\times10^{4}}$	$\mathbf{4.18\times10^{5}}$	$\mathbf{6.06\times10^{7}}$
17	3.82×10^{4}	4.86×10^{5}	7.81×10^{7}
18	$\mathbf{4.07\times10^{4}}$	$\mathbf{5.14\times10^{5}}$	$\mathbf{6.68\times10^{7}}$
19	3.03×10^{4}	4.06×10^{5}	6.50×10^{7}
20	$\mathbf{2.53\times10^{4}}$	$\mathbf{3.22\times10^{5}}$	$\mathbf{4.58\times10^{7}}$

Table 50. Simulated recovery times for 5%, 50%, and 95% of injected ^{99}Tc tracer activity. Realisations in figures correspond to runs 16 (blue), 18 (red), and 20 (green).

Realisation #	Recovery Times [y]		
	t_{05} (5%)	t_{50} (50%)	t_{95} (95%)
1	3.78×10^{5}	4.99×10^{6}	6.86×10^{8}
2	2.76×10^{5}	3.88×10^{6}	5.59×10^{8}
3	2.89×10^{5}	3.65×10^{6}	5.71×10^{8}
4	3.18×10^{5}	4.27×10^{6}	6.46×10^{8}
5	2.86×10^{5}	3.83×10^{6}	5.84×10^{8}
6	3.20×10^{5}	4.18×10^{6}	7.13×10^{8}
7	3.40×10^{5}	4.12×10^{6}	4.70×10^{8}
8	3.01×10^{5}	3.92×10^{6}	6.02×10^{8}
9	2.88×10^{5}	4.02×10^{6}	5.48×10^{8}
10	2.31×10^{5}	3.13×10^{6}	5.13×10^{8}
11	2.61×10^{5}	3.38×10^{6}	5.49×10^{8}
12	2.20×10^{5}	3.14×10^{6}	4.96×10^{8}
13	3.17×10^{5}	4.02×10^{6}	5.63×10^{8}
14	2.28×10^{5}	2.88×10^{6}	3.47×10^{8}
15	3.15×10^{5}	4.03×10^{6}	5.48×10^{8}
16	$\mathbf{2.69\times10^{5}}$	$\mathbf{3.97\times10^{6}}$	$\mathbf{5.67\times10^{8}}$
17	3.57×10^{5}	4.66×10^{6}	7.47×10^{8}
18	$\mathbf{3.83\times10^{5}}$	$\mathbf{4.94\times10^{6}}$	$\mathbf{6.30\times10^{8}}$
19	2.74×10^{5}	3.81×10^{6}	6.26×10^{8}
20	$\mathbf{2.25\times10^{5}}$	$\mathbf{2.95\times10^{6}}$	$\mathbf{4.20\times10^{8}}$

Table 51. Simulated recovery times for 5%, 50%, and 95% of injected ^{241}Am tracer activity. Realisations in figures correspond to runs 16 (blue), 18 (red), and 20 (green).

Realisation #	Recovery Times [y]		
	t_{05} (5%)	t_{50} (50%)	t_{95} (95%)
1	1.09×10^{6}	1.46×10^{7}	2.01×10^{9}
2	8.01×10^{5}	1.13×10^{7}	1.63×10^{9}
3	8.38×10^{5}	1.06×10^{7}	1.66×10^{9}
4	9.23×10^{5}	1.25×10^{7}	1.88×10^{9}
5	8.30×10^{5}	1.11×10^{7}	1.71×10^{9}
6	9.34×10^{5}	1.22×10^{7}	2.09×10^{9}
7	9.86×10^{5}	1.20×10^{7}	1.37×10^{9}
8	8.74×10^{5}	1.15×10^{7}	1.75×10^{9}
9	8.35×10^{5}	1.17×10^{7}	1.59×10^{9}
10	6.67×10^{5}	9.10×10^{6}	1.49×10^{9}
11	7.55×10^{5}	9.82×10^{6}	1.62×10^{9}
12	6.38×10^{5}	9.14×10^{6}	1.45×10^{9}
13	9.20×10^{5}	1.17×10^{7}	1.64×10^{9}
14	6.61×10^{5}	8.37×10^{6}	1.01×10^{9}
15	9.15×10^{5}	1.17×10^{7}	1.61×10^{9}
16	$\mathbf{7.77\times10^{5}}$	$\mathbf{1.16\times10^{7}}$	$\mathbf{1.64\times10^{9}}$
17	1.04×10^{6}	1.37×10^{7}	2.17×10^{9}
18	$\mathbf{1.12\times10^{6}}$	$\mathbf{1.45\times10^{7}}$	$\mathbf{1.84\times10^{9}}$
19	7.97×10^{5}	1.11×10^{7}	1.82×10^{9}
20	$\mathbf{6.51\times10^{5}}$	$\mathbf{8.58\times10^{6}}$	$\mathbf{1.23\times10^{9}}$

Breakthrough curves for Dirac pulse injection

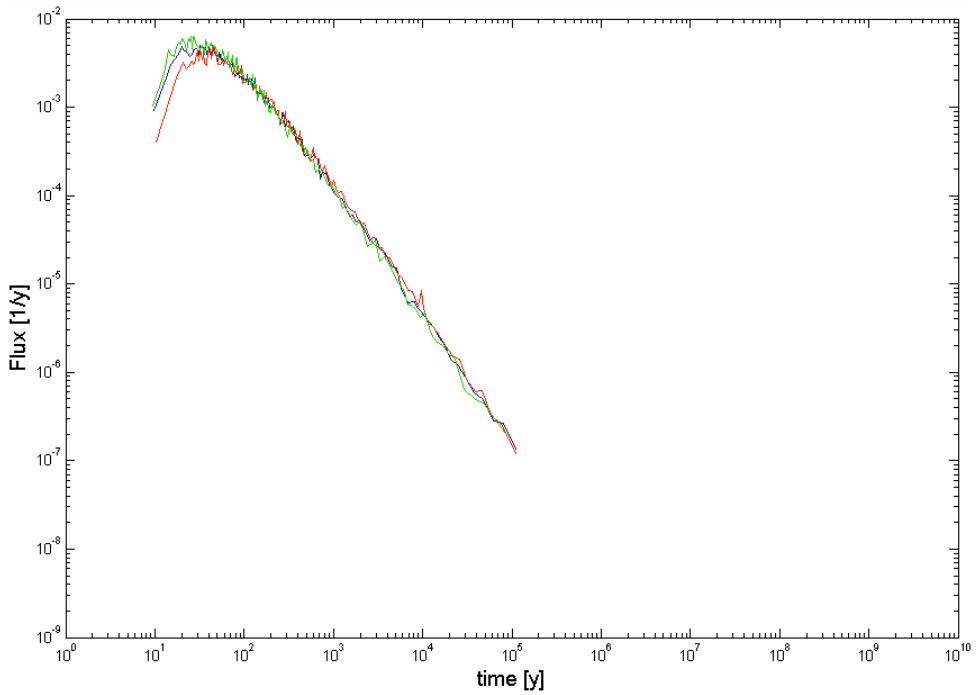

Figure 82. *Radionuclide flux vs. time, breakthrough curve for ^{129}I.*

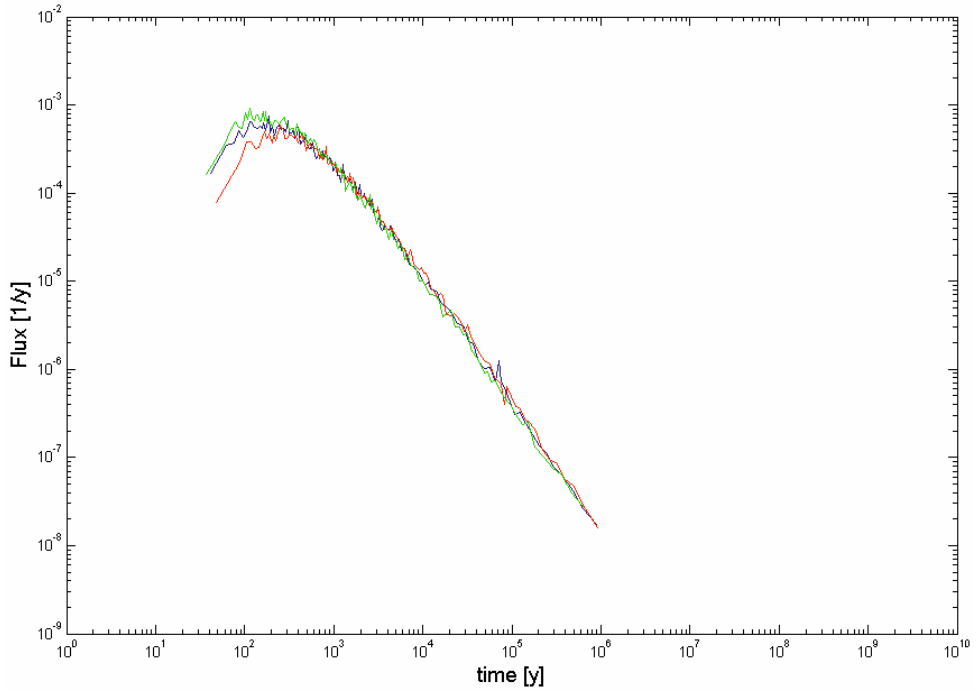

Figure 83. *Radionuclide flux vs. time, breakthrough curve for ^{47}Ca.*

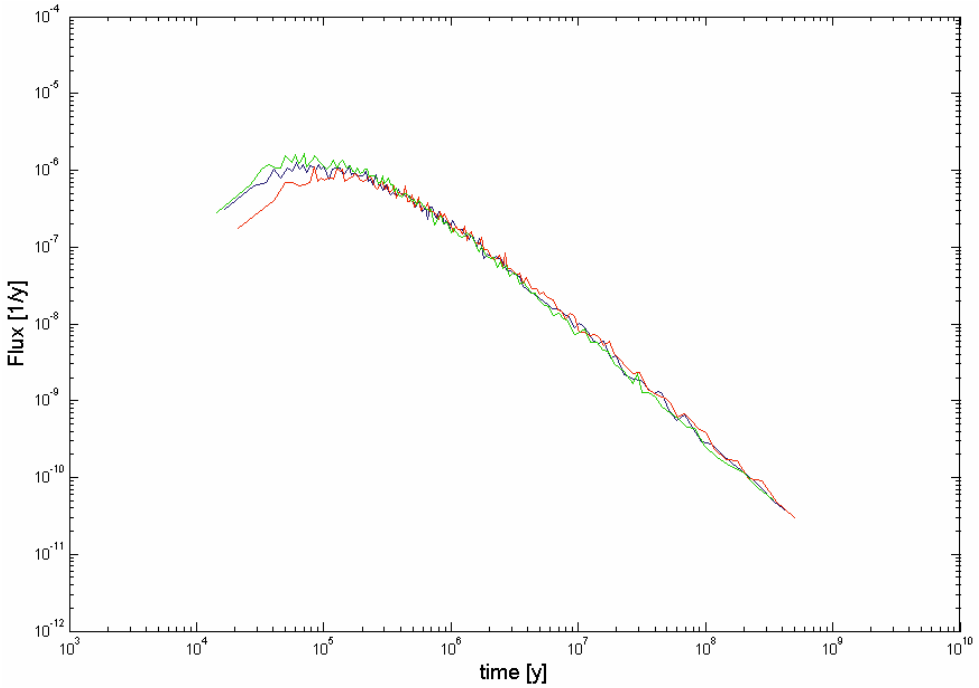

Figure 84. *Radionuclide flux vs. time, breakthrough curve for ^{137}Cs.*

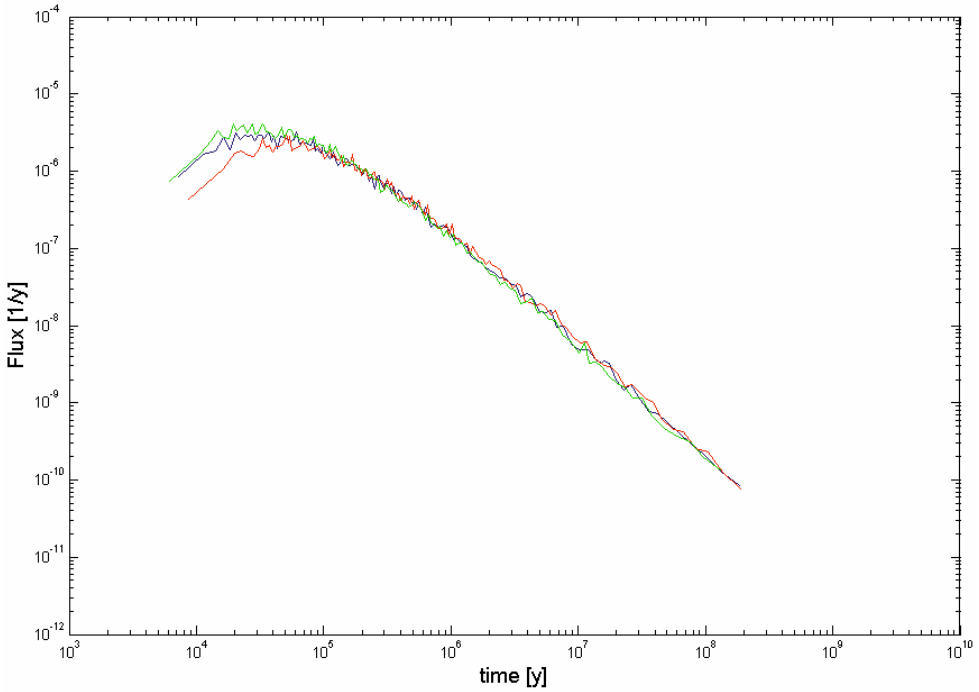

Figure 85. *Radionuclide flux vs. time, breakthrough curve for ^{226}Ra.*

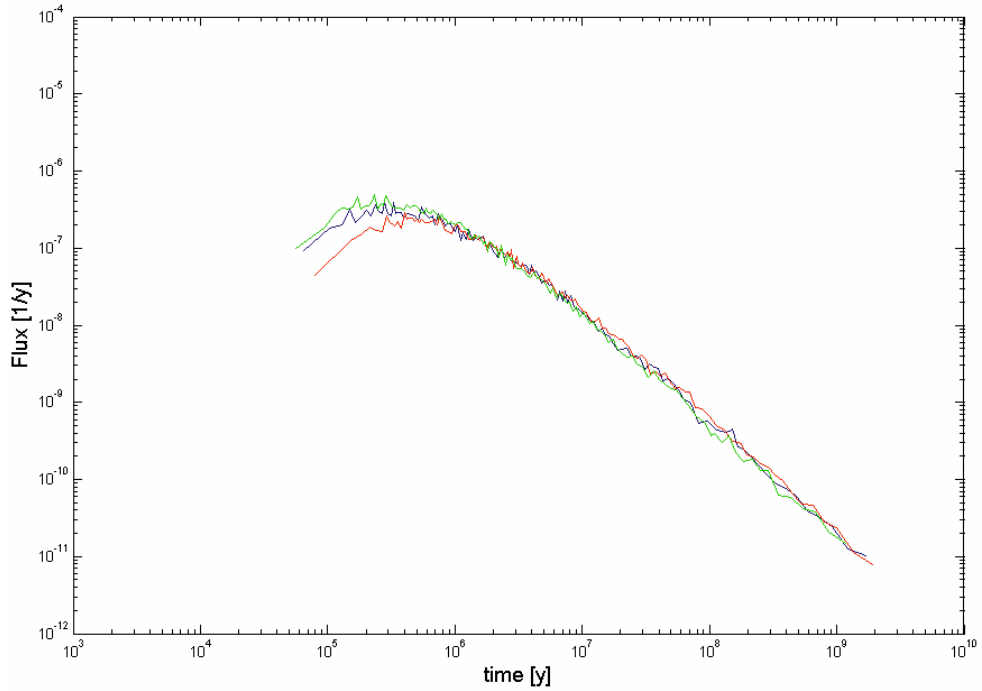

Figure 86. *Radionuclide flux vs. time, breakthrough curve for ^{99}Tc.*

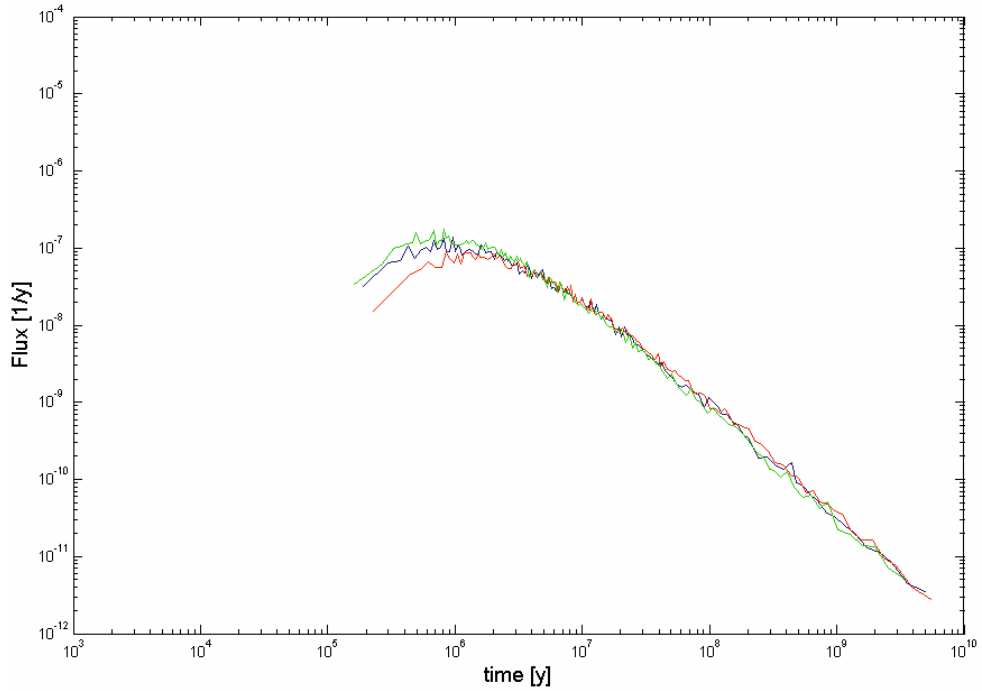

Figure 87. *Radionuclide flux vs. time, breakthrough curve for ^{241}Am.*

Breakthrough times for recovery of 5, 50 and 95% of the Dirac pulse injection

Table 52. Simulated recovery times for 5%, 50%, and 95% of injected ^{129}I tracer activity (Dirac pulse). Realisations in figures correspond to runs 16 (blue), 18 (red), and 20 (green).

Realisation #	Recovery Times [y]		
	t_{05} (5%)	t_{50} (50%)	t_{95} (95%)
1	3.15×10^{1}	3.16×10^{2}	4.25×10^{4}
2	2.49×10^{1}	2.54×10^{2}	3.53×10^{4}
3	2.57×10^{1}	2.46×10^{2}	3.61×10^{4}
4	2.69×10^{1}	2.64×10^{2}	3.67×10^{4}
5	2.54×10^{1}	2.46×10^{2}	3.83×10^{4}
6	2.72×10^{1}	2.58×10^{2}	3.93×10^{4}
7	2.83×10^{1}	2.46×10^{2}	2.83×10^{4}
8	2.64×10^{1}	2.52×10^{2}	3.75×10^{4}
9	2.57×10^{1}	2.57×10^{2}	3.73×10^{4}
10	2.21×10^{1}	2.12×10^{2}	3.30×10^{4}
11	2.39×10^{1}	2.19×10^{2}	3.41×10^{4}
12	2.11×10^{1}	2.16×10^{2}	3.19×10^{4}
13	2.75×10^{1}	2.57×10^{2}	3.45×10^{4}
14	2.12×10^{1}	1.88×10^{2}	2.27×10^{4}
15	2.72×10^{1}	2.57×10^{2}	3.40×10^{4}
16	$\mathbf{2.47\times10^{1}}$	$\mathbf{2.57\times10^{2}}$	$\mathbf{3.67\times10^{4}}$
17	2.90×10^{1}	2.90×10^{2}	4.46×10^{4}
18	$\mathbf{3.12\times10^{1}}$	$\mathbf{2.99\times10^{2}}$	$\mathbf{3.78\times10^{4}}$
19	2.52×10^{1}	2.50×10^{2}	3.80×10^{4}
20	$\mathbf{2.20\times10^{1}}$	$\mathbf{2.07\times10^{2}}$	$\mathbf{2.94\times10^{4}}$

Table 53. Simulated recovery times for 5%, 50%, and 95% of injected ^{47}Ca tracer activity (Dirac pulse). Realisations in figures correspond to runs 16 (blue), 18 (red), and 20 (green).

Realisation #	Recovery Times [y]		
	t_{05} (5%)	t_{50} (50%)	t_{95} (95%)
1	2.01×10^{2}	2.53×10^{3}	3.43×10^{5}
2	1.51×10^{2}	1.99×10^{3}	2.78×10^{5}
3	1.57×10^{2}	1.91×10^{3}	2.95×10^{5}
4	1.71×10^{2}	2.13×10^{3}	3.20×10^{5}
5	1.55×10^{2}	1.95×10^{3}	3.03×10^{5}
6	1.70×10^{2}	2.08×10^{3}	3.43×10^{5}
7	1.80×10^{2}	2.02×10^{3}	2.35×10^{5}
8	1.63×10^{2}	2.01×10^{3}	2.96×10^{5}
9	1.59×10^{2}	2.04×10^{3}	2.96×10^{5}
10	1.30×10^{2}	1.62×10^{3}	2.62×10^{5}
11	1.43×10^{2}	1.72×10^{3}	2.79×10^{5}
12	1.23×10^{2}	1.65×10^{3}	2.56×10^{5}
13	1.73×10^{2}	2.06×10^{3}	2.89×10^{5}
14	1.25×10^{2}	1.47×10^{3}	1.80×10^{5}
15	1.69×10^{2}	2.05×10^{3}	2.80×10^{5}
16	$\mathbf{1.46\times10^{2}}$	$\mathbf{2.01\times10^{3}}$	$\mathbf{2.92\times10^{5}}$
17	1.90×10^{2}	2.34×10^{3}	3.74×10^{5}
18	$\mathbf{2.02\times10^{2}}$	$\mathbf{2.46\times10^{3}}$	$\mathbf{3.19\times10^{5}}$
19	1.51×10^{2}	1.95×10^{3}	3.13×10^{5}
20	$\mathbf{1.27\times10^{2}}$	$\mathbf{1.55\times10^{3}}$	$\mathbf{2.18\times10^{5}}$

Table 54. Simulated recovery times for 5%, 50%, and 95% of injected ^{137}Cs tracer activity (Dirac pulse). Realisations in figures correspond to runs 16 (blue), 18 (red), and 20 (green).

Realisation #	Recovery Times [y]		
	t_{05} (5%)	t_{50} (50%)	t_{95} (95%)
1	1.02×10^{5}	1.38×10^{6}	1.88×10^{8}
2	7.58×10^{4}	1.08×10^{6}	1.51×10^{8}
3	7.85×10^{4}	1.03×10^{6}	1.60×10^{8}
4	8.64×10^{4}	1.16×10^{6}	1.78×10^{8}
5	7.74×10^{4}	1.06×10^{6}	1.65×10^{8}
6	8.52×10^{4}	1.13×10^{6}	1.88×10^{8}
7	9.11×10^{4}	1.11×10^{6}	1.30×10^{8}
8	8.19×10^{4}	1.09×10^{6}	1.63×10^{8}
9	7.95×10^{4}	1.11×10^{6}	1.61×10^{8}
10	6.43×10^{4}	8.77×10^{5}	1.43×10^{8}
11	7.18×10^{4}	9.36×10^{5}	1.52×10^{8}
12	6.08×10^{4}	8.92×10^{5}	1.42×10^{8}
13	8.67×10^{4}	1.12×10^{6}	1.60×10^{8}
14	6.21×10^{4}	7.90×10^{5}	9.78×10^{7}
15	8.46×10^{4}	1.11×10^{6}	1.52×10^{8}
16	$\mathbf{7.35\times10^{4}}$	$\mathbf{1.09\times10^{6}}$	$\mathbf{1.59\times10^{8}}$
17	9.57×10^{4}	1.27×10^{6}	2.05×10^{8}
18	$\mathbf{1.02\times10^{5}}$	$\mathbf{1.34\times10^{6}}$	$\mathbf{1.75\times10^{8}}$
19	7.54×10^{4}	1.06×10^{6}	1.70×10^{8}
20	$\mathbf{6.30\times10^{4}}$	$\mathbf{8.40\times10^{5}}$	$\mathbf{1.20\times10^{8}}$

Table 55. Simulated recovery times for 5%, 50%, and 95% of injected ^{226}Ra tracer activity (Dirac pulse). Realisations in figures correspond to runs 16 (blue), 18 (red), and 20 (green).

Realisation #	Recovery Times [y]		
	t_{05} (5%)	t_{50} (50%)	t_{95} (95%)
1	4.02×10^{4}	5.27×10^{5}	7.15×10^{7}
2	2.97×10^{4}	4.16×10^{5}	5.75×10^{7}
3	3.09×10^{4}	3.95×10^{5}	6.11×10^{7}
4	3.39×10^{4}	4.44×10^{5}	6.79×10^{7}
5	3.05×10^{4}	4.05×10^{5}	6.29×10^{7}
6	3.36×10^{4}	4.35×10^{5}	7.16×10^{7}
7	3.59×10^{4}	4.23×10^{5}	4.94×10^{7}
8	3.22×10^{4}	4.18×10^{5}	6.23×10^{7}
9	3.14×10^{4}	4.23×10^{5}	6.13×10^{7}
10	2.53×10^{4}	3.36×10^{5}	5.47×10^{7}
11	2.84×10^{4}	3.58×10^{5}	5.79×10^{7}
12	2.39×10^{4}	3.41×10^{5}	5.41×10^{7}
13	3.42×10^{4}	4.27×10^{5}	6.11×10^{7}
14	2.45×10^{4}	3.03×10^{5}	3.73×10^{7}
15	3.33×10^{4}	4.26×10^{5}	5.79×10^{7}
16	$\mathbf{2.88\times10^{4}}$	$\mathbf{4.18\times10^{5}}$	$\mathbf{6.06\times10^{7}}$
17	3.77×10^{4}	4.86×10^{5}	7.81×10^{7}
18	$\mathbf{4.00\times10^{4}}$	$\mathbf{5.14\times10^{5}}$	$\mathbf{6.68\times10^{7}}$
19	2.97×10^{4}	4.05×10^{5}	6.50×10^{7}
20	$\mathbf{2.48\times10^{4}}$	$\mathbf{3.22\times10^{5}}$	$\mathbf{4.58\times10^{7}}$

Table 56. Simulated recovery times for 5%, 50%, and 95% of injected ^{99}Tc tracer activity (Dirac pulse). Realisations in figures correspond to runs 16 (blue), 18 (red), and 20 (green).

Realisation #	Recovery Times [y]		
	t_{05} (5%)	t_{50} (50%)	t_{95} (95%)
1	3.77×10^{5}	4.99×10^{6}	6.86×10^{8}
2	2.75×10^{5}	3.88×10^{6}	5.59×10^{8}
3	2.88×10^{5}	3.65×10^{6}	5.71×10^{8}
4	3.17×10^{5}	4.27×10^{6}	6.46×10^{8}
5	2.86×10^{5}	3.83×10^{6}	5.84×10^{8}
6	3.19×10^{5}	4.18×10^{6}	7.13×10^{8}
7	3.39×10^{5}	4.12×10^{6}	4.70×10^{8}
8	3.01×10^{5}	3.92×10^{6}	6.02×10^{8}
9	2.88×10^{5}	4.02×10^{6}	5.48×10^{8}
10	2.30×10^{5}	3.13×10^{6}	5.13×10^{8}
11	2.60×10^{5}	3.38×10^{6}	5.49×10^{8}
12	2.20×10^{5}	3.14×10^{6}	4.96×10^{8}
13	3.17×10^{5}	4.02×10^{6}	5.63×10^{8}
14	2.27×10^{5}	2.88×10^{6}	3.47×10^{8}
15	3.15×10^{5}	4.03×10^{6}	5.48×10^{8}
16	$\mathbf{2.68\times10^{5}}$	$\mathbf{3.97\times10^{6}}$	$\mathbf{5.67\times10^{8}}$
17	3.57×10^{5}	4.66×10^{6}	7.47×10^{8}
18	$\mathbf{3.82\times10^{5}}$	$\mathbf{4.94\times10^{6}}$	$\mathbf{6.30\times10^{8}}$
19	2.74×10^{5}	3.81×10^{6}	6.26×10^{8}
20	$\mathbf{2.24\times10^{5}}$	$\mathbf{2.95\times10^{6}}$	$\mathbf{4.20\times10^{8}}$

Table 57. Simulated recovery times for 5%, 50%, and 95% of injected ^{241}Am tracer activity (Dirac pulse). Realisations in figures correspond to runs 16 (blue), 18 (red), and 20 (green).

Realisation #	Recovery Times [y]		
	t_{05} (5%)	t_{50} (50%)	t_{95} (95%)
1	1.09×10^{6}	1.46×10^{7}	2.01×10^{9}
2	8.00×10^{5}	1.13×10^{7}	1.63×10^{9}
3	8.38×10^{5}	1.06×10^{7}	1.66×10^{9}
4	9.23×10^{5}	1.25×10^{7}	1.88×10^{9}
5	8.29×10^{5}	1.11×10^{7}	1.71×10^{9}
6	9.33×10^{5}	1.22×10^{7}	2.09×10^{9}
7	9.85×10^{5}	1.20×10^{7}	1.37×10^{9}
8	8.74×10^{5}	1.15×10^{7}	1.75×10^{9}
9	8.34×10^{5}	1.17×10^{7}	1.59×10^{9}
10	6.67×10^{5}	9.10×10^{6}	1.49×10^{9}
11	7.55×10^{5}	9.82×10^{6}	1.62×10^{9}
12	6.38×10^{5}	9.14×10^{6}	1.45×10^{9}
13	9.20×10^{5}	1.17×10^{7}	1.64×10^{9}
14	6.61×10^{5}	8.36×10^{6}	1.01×10^{9}
15	9.14×10^{5}	1.17×10^{7}	1.61×10^{9}
16	$\mathbf{7.77\times10^{5}}$	$\mathbf{1.16\times10^{7}}$	$\mathbf{1.64\times10^{9}}$
17	1.04×10^{6}	1.37×10^{7}	2.17×10^{9}
18	$\mathbf{1.12\times10^{6}}$	$\mathbf{1.45\times10^{7}}$	$\mathbf{1.84\times10^{9}}$
19	7.97×10^{5}	1.11×10^{7}	1.82×10^{9}
20	$\mathbf{6.50\times10^{5}}$	$\mathbf{8.58\times10^{6}}$	$\mathbf{1.23\times10^{9}}$

Maximum release rate for the tracers at recovery plane 1 (Easting = 1920)

Maximum release rate using extended pulse injection boundary condition

Table 58. Maximum release rate [Bq/y] for radiotracers simulated using measured injection curves. Realisations in figures correspond to runs 16 (blue), 18 (red), and 20 (green).

Realisation #	^{129}I	^{47}Ca	^{137}Cs	^{226}Ra	^{99}Tc	^{241}Am
1	1.50×10^{6}	1.19×10^{6}	6.93×10^{4}	1.26×10^{5}	1.22×10^{4}	4.25×10^{3}
2	1.25×10^{6}	1.08×10^{6}	1.07×10^{5}	2.19×10^{5}	2.39×10^{4}	7.93×10^{3}
3	1.17×10^{6}	1.23×10^{6}	1.21×10^{5}	2.33×10^{5}	2.96×10^{4}	9.97×10^{3}
4	1.43×10^{6}	1.45×10^{6}	9.28×10^{4}	2.18×10^{5}	1.91×10^{4}	5.89×10^{3}
5	1.22×10^{6}	1.15×10^{6}	7.76×10^{4}	1.69×10^{5}	1.67×10^{4}	5.63×10^{3}
6	1.13×10^{6}	1.12×10^{6}	4.73×10^{4}	1.14×10^{5}	9.11×10^{3}	3.25×10^{3}
7	1.19×10^{6}	1.01×10^{6}	3.70×10^{4}	8.54×10^{4}	8.30×10^{3}	2.50×10^{3}
8	1.18×10^{6}	1.16×10^{6}	7.77×10^{4}	2.06×10^{5}	2.22×10^{4}	5.65×10^{3}
9	1.16×10^{6}	1.10×10^{6}	1.10×10^{5}	1.97×10^{5}	1.82×10^{4}	6.36×10^{3}
10	1.35×10^{6}	1.08×10^{6}	1.57×10^{5}	2.95×10^{5}	3.91×10^{4}	1.38×10^{4}
11	1.34×10^{6}	1.20×10^{6}	1.35×10^{5}	2.48×10^{5}	2.86×10^{4}	9.67×10^{3}
12	1.23×10^{6}	1.32×10^{6}	3.05×10^{5}	5.33×10^{5}	4.86×10^{4}	1.70×10^{4}
13	1.23×10^{6}	1.11×10^{6}	6.35×10^{4}	1.50×10^{5}	1.52×10^{4}	5.31×10^{3}
14	1.19×10^{6}	1.12×10^{6}	1.39×10^{5}	2.09×10^{5}	2.75×10^{4}	8.78×10^{3}
15	1.23×10^{6}	1.10×10^{6}	6.32×10^{4}	1.48×10^{5}	1.34×10^{4}	4.24×10^{3}
16	$\mathbf{1.36\times10^{6}}$	$\mathbf{1.36\times10^{6}}$	$\mathbf{9.24\times10^{4}}$	$\mathbf{2.09\times10^{5}}$	$\mathbf{1.86\times10^{4}}$	$\mathbf{6.25\times10^{3}}$
17	1.27×10^{6}	1.13×10^{6}	5.24×10^{4}	1.44×10^{5}	1.03×10^{4}	3.29×10^{3}
18	$\mathbf{1.27\times10^{6}}$	$\mathbf{9.70\times10^{5}}$	$\mathbf{3.22\times10^{4}}$	$\mathbf{8.82\times10^{4}}$	$\mathbf{8.03\times10^{3}}$	$\mathbf{2.51\times10^{3}}$
19	1.21×10^{6}	1.14×10^{6}	1.38×10^{5}	2.77×10^{5}	2.86×10^{4}	1.03×10^{4}
20	$\mathbf{1.23\times10^{6}}$	$\mathbf{1.19\times10^{6}}$	$\mathbf{3.41\times10^{5}}$	$\mathbf{6.33\times10^{5}}$	$\mathbf{9.07\times10^{4}}$	$\mathbf{2.91\times10^{4}}$

Maximum release rate using Dirac pulse injection

Table 59. Maximum release rate [1/y] for radiotracers simulated using a Dirac pulse boundary condition. Realisations in figures correspond to runs 16 (blue), 18 (red), and 20 (green).

Realisation #	^{129}I	^{47}Ca	^{137}Cs	^{226}Ra	^{99}Tc	^{241}Am
1	1.85×10^{-1}	3.20×10^{-2}	6.40×10^{-5}	1.57×10^{-4}	1.23×10^{-5}	4.13×10^{-6}
2	2.89×10^{-1}	4.37×10^{-2}	1.10×10^{-4}	2.25×10^{-4}	2.25×10^{-5}	7.59×10^{-6}
3	2.93×10^{-1}	5.36×10^{-2}	1.42×10^{-4}	2.68×10^{-4}	2.72×10^{-5}	9.43×10^{-6}
4	2.68×10^{-1}	3.94×10^{-2}	1.01×10^{-4}	1.86×10^{-4}	1.67×10^{-5}	5.50×10^{-6}
5	2.00×10^{-1}	3.56×10^{-2}	8.22×10^{-5}	1.85×10^{-4}	1.65×10^{-5}	6.59×10^{-6}
6	1.45×10^{-1}	2.17×10^{-2}	4.27×10^{-5}	9.84×10^{-5}	9.78×10^{-6}	3.48×10^{-6}
7	1.69×10^{-1}	2.05×10^{-2}	3.96×10^{-5}	1.03×10^{-4}	7.61×10^{-6}	2.66×10^{-6}
8	1.84×10^{-1}	3.52×10^{-2}	8.96×10^{-5}	2.12×10^{-4}	1.69×10^{-5}	5.76×10^{-6}
9	2.85×10^{-1}	5.21×10^{-2}	9.33×10^{-5}	2.18×10^{-4}	1.90×10^{-5}	6.52×10^{-6}
10	3.54×10^{-1}	7.36×10^{-2}	2.22×10^{-4}	4.30×10^{-4}	4.98×10^{-5}	1.64×10^{-5}
11	3.34×10^{-1}	5.81×10^{-2}	1.26×10^{-4}	3.01×10^{-4}	3.25×10^{-5}	8.96×10^{-6}
12	3.65×10^{-1}	7.40×10^{-2}	2.07×10^{-4}	4.51×10^{-4}	5.58×10^{-5}	1.80×10^{-5}
13	1.99×10^{-1}	3.10×10^{-2}	6.94×10^{-5}	1.72×10^{-4}	1.59×10^{-5}	5.31×10^{-6}
14	3.45×10^{-1}	5.89×10^{-2}	1.38×10^{-4}	2.98×10^{-4}	2.92×10^{-5}	9.88×10^{-6}
15	1.80×10^{-1}	3.12×10^{-2}	5.85×10^{-5}	1.47×10^{-4}	1.22×10^{-5}	4.37×10^{-6}
16	$\mathbf{1.99\times10^{-1}}$	$\mathbf{3.29\times10^{-2}}$	$\mathbf{9.46\times10^{-5}}$	$\mathbf{1.76\times10^{-4}}$	$\mathbf{1.69\times10^{-5}}$	$\mathbf{5.95\times10^{-6}}$
17	1.54×10^{-1}	2.43×10^{-2}	4.60×10^{-5}	1.05×10^{-4}	1.11×10^{-5}	3.79×10^{-6}
18	$\mathbf{1.25\times10^{-1}}$	$\mathbf{1.92\times10^{-2}}$	$\mathbf{4.07\times10^{-5}}$	$\mathbf{1.15\times10^{-4}}$	$\mathbf{7.87\times10^{-6}}$	$\mathbf{2.46\times10^{-6}}$
19	3.36×10^{-1}	5.54×10^{-2}	1.46×10^{-4}	3.43×10^{-4}	2.79×10^{-5}	1.04×10^{-5}
20	$\mathbf{6.25\times10^{-1}}$	$\mathbf{1.54\times10^{-1}}$	$\mathbf{4.42\times10^{-4}}$	$\mathbf{1.05\times10^{-3}}$	$\mathbf{8.87\times10^{-5}}$	$\mathbf{3.46\times10^{-5}}$

Maximum release rate for the tracers at recovery plane 2 (Easting = 1880)

Maximum release rate using extended pulse injection boundary condition

Table 60. Maximum release rate [Bq/y] for radiotracers simulated using measured injection curves. Realisations in figures correspond to runs 16 (blue), 18 (red), and 20 (green).

Realisation #	^{129}I	^{47}Ca	^{137}Cs	^{226}Ra	^{99}Tc	^{241}Am
1	9.33×10^{5}	5.10×10^{5}	2.07×10^{3}	5.25×10^{3}	5.70×10^{2}	2.02×10^{2}
2	9.94×10^{5}	5.93×10^{5}	2.81×10^{3}	7.20×10^{3}	8.45×10^{2}	2.92×10^{2}
3	9.95×10^{5}	5.91×10^{5}	2.96×10^{3}	7.36×10^{3}	8.32×10^{2}	2.83×10^{2}
4	1.00×10^{6}	6.78×10^{5}	2.75×10^{3}	7.18×10^{3}	6.87×10^{2}	2.37×10^{2}
5	1.06×10^{6}	6.18×10^{5}	3.06×10^{3}	7.39×10^{3}	7.07×10^{2}	2.60×10^{2}
6	1.10×10^{6}	5.63×10^{5}	2.55×10^{3}	6.69×10^{3}	6.57×10^{2}	2.24×10^{2}
7	1.15×10^{6}	5.45×10^{5}	2.31×10^{3}	6.24×10^{3}	5.64×10^{2}	1.93×10^{2}
8	1.35×10^{6}	5.57×10^{5}	2.35×10^{3}	6.04×10^{3}	6.57×10^{2}	2.34×10^{2}
9	1.14×10^{6}	6.37×10^{5}	3.05×10^{3}	6.99×10^{3}	7.97×10^{2}	2.69×10^{2}
10	1.01×10^{6}	6.75×10^{5}	3.90×10^{3}	1.02×10^{4}	1.29×10^{3}	4.19×10^{2}
11	9.95×10^{5}	6.67×10^{5}	3.47×10^{3}	9.51×10^{3}	9.55×10^{2}	3.56×10^{2}
12	1.06×10^{6}	6.37×10^{5}	3.90×10^{3}	1.09×10^{4}	1.05×10^{3}	3.59×10^{2}
13	9.91×10^{5}	6.08×10^{5}	2.73×10^{3}	6.94×10^{3}	7.03×10^{2}	2.36×10^{2}
14	1.08×10^{6}	6.98×10^{5}	4.22×10^{3}	1.15×10^{4}	1.21×10^{3}	3.92×10^{2}
15	1.04×10^{6}	6.55×10^{5}	2.37×10^{3}	6.14×10^{3}	6.89×10^{2}	2.21×10^{2}
16	$\mathbf{1.10\times10^{6}}$	$\mathbf{7.33\times10^{5}}$	$\mathbf{2.63\times10^{3}}$	$\mathbf{6.47\times10^{3}}$	$\mathbf{7.24\times10^{2}}$	$\mathbf{2.53\times10^{2}}$
17	1.00×10^{6}	5.44×10^{5}	2.23×10^{3}	5.65×10^{3}	6.08×10^{2}	2.16×10^{2}
18	$\mathbf{9.81\times10^{5}}$	$\mathbf{5.13\times10^{5}}$	$\mathbf{2.09\times10^{3}}$	$\mathbf{5.49\times10^{3}}$	$\mathbf{5.09\times10^{2}}$	$\mathbf{1.98\times10^{2}}$
19	9.97×10^{5}	6.10×10^{5}	2.45×10^{3}	6.90×10^{3}	8.30×10^{2}	2.76×10^{2}
20	$\mathbf{1.05\times10^{6}}$	$\mathbf{6.88\times10^{5}}$	$\mathbf{4.19\times10^{3}}$	$\mathbf{9.86\times10^{3}}$	$\mathbf{1.08\times10^{3}}$	$\mathbf{3.59\times10^{2}}$

Maximum release rate using Dirac pulse injection

Table 61. Maximum release rate [1/y] for radiotracers simulated using a Dirac pulse boundary condition. Realisations in figures correspond to runs 16 (blue), 18 (red), and 20 (green).

Realisation #	^{129}I	^{47}Ca	^{137}Cs	^{226}Ra	^{99}Tc	^{241}Am
1	8.94×10^{-3}	1.06×10^{-3}	1.89×10^{-6}	5.63×10^{-6}	5.56×10^{-7}	2.00×10^{-7}
2	1.13×10^{-2}	1.50×10^{-3}	2.64×10^{-6}	7.02×10^{-6}	8.84×10^{-7}	2.98×10^{-7}
3	1.14×10^{-2}	1.37×10^{-3}	2.79×10^{-6}	7.52×10^{-6}	8.61×10^{-7}	2.84×10^{-7}
4	1.25×10^{-2}	1.40×10^{-3}	2.93×10^{-6}	7.42×10^{-6}	6.99×10^{-7}	2.35×10^{-7}
5	1.26×10^{-2}	1.78×10^{-3}	3.10×10^{-6}	8.19×10^{-6}	7.17×10^{-7}	2.69×10^{-7}
6	1.21×10^{-2}	1.58×10^{-3}	2.49×10^{-6}	6.63×10^{-6}	6.44×10^{-7}	2.24×10^{-7}
7	1.01×10^{-2}	1.34×10^{-3}	2.35×10^{-6}	6.24×10^{-6}	5.57×10^{-7}	1.94×10^{-7}
8	1.10×10^{-2}	1.28×10^{-3}	2.60×10^{-6}	6.53×10^{-6}	6.56×10^{-7}	2.30×10^{-7}
9	1.23×10^{-2}	1.63×10^{-3}	2.84×10^{-6}	7.11×10^{-6}	7.61×10^{-7}	2.70×10^{-7}
10	1.71×10^{-2}	2.23×10^{-3}	4.19×10^{-6}	1.14×10^{-5}	1.34×10^{-6}	4.14×10^{-7}
11	1.60×10^{-2}	1.87×10^{-3}	3.71×10^{-6}	9.16×10^{-6}	9.93×10^{-7}	3.52×10^{-7}
12	1.36×10^{-2}	2.09×10^{-3}	3.95×10^{-6}	1.04×10^{-5}	1.10×10^{-6}	3.58×10^{-7}
13	1.31×10^{-2}	1.43×10^{-3}	2.49×10^{-6}	6.65×10^{-6}	7.10×10^{-7}	2.32×10^{-7}
14	1.94×10^{-2}	2.30×10^{-3}	4.13×10^{-6}	1.17×10^{-5}	1.20×10^{-6}	3.88×10^{-7}
15	1.15×10^{-2}	1.38×10^{-3}	2.37×10^{-6}	6.72×10^{-6}	7.08×10^{-7}	2.17×10^{-7}
16	$\mathbf{1.09\times10^{-2}}$	$\mathbf{1.49\times10^{-3}}$	$\mathbf{2.53\times10^{-6}}$	$\mathbf{6.62\times10^{-6}}$	$\mathbf{7.20\times10^{-7}}$	$\mathbf{2.57\times10^{-7}}$
17	1.12×10^{-2}	1.11×10^{-3}	2.23×10^{-6}	5.24×10^{-6}	6.07×10^{-7}	2.17×10^{-7}
18	$\mathbf{1.08\times10^{-2}}$	$\mathbf{1.18\times10^{-3}}$	$\mathbf{2.09\times10^{-6}}$	$\mathbf{5.18\times10^{-6}}$	$\mathbf{5.07\times10^{-7}}$	$\mathbf{1.99\times10^{-7}}$
19	1.20×10^{-2}	1.37×10^{-3}	2.63×10^{-6}	6.57×10^{-6}	8.01×10^{-7}	2.78×10^{-7}
20	$\mathbf{1.85\times10^{-2}}$	$\mathbf{2.08\times10^{-3}}$	$\mathbf{4.09\times10^{-6}}$	$\mathbf{1.04\times10^{-5}}$	$\mathbf{1.08\times10^{-6}}$	$\mathbf{3.67\times10^{-7}}$

Maximum release rate for the tracers at Western boundary plane (Easting = 1800)

Maximum release rate using extended pulse injection boundary condition

Table 62. Maximum release rate [Bq/y] for radiotracers simulated using measured injection curves. Realisations in figures correspond to runs 16 (blue), 18 (red), and 20 (green).

Realisation #	^{129}I	^{47}Ca	^{137}Cs	^{226}Ra	^{99}Tc	^{241}Am
1	8.50×10^{5}	3.41×10^{5}	1.00×10^{3}	2.63×10^{3}	2.73×10^{2}	9.45×10^{1}
2	8.51×10^{5}	4.13×10^{5}	1.32×10^{3}	3.77×10^{3}	3.90×10^{2}	1.28×10^{2}
3	8.89×10^{5}	4.75×10^{5}	1.43×10^{3}	3.63×10^{3}	4.07×10^{2}	1.32×10^{2}
4	8.71×10^{5}	4.46×10^{5}	1.25×10^{3}	3.37×10^{3}	3.39×10^{2}	1.17×10^{2}
5	9.76×10^{5}	4.47×10^{5}	1.31×10^{3}	4.09×10^{3}	4.20×10^{2}	1.54×10^{2}
6	8.94×10^{5}	4.32×10^{5}	1.52×10^{3}	3.61×10^{3}	3.82×10^{2}	1.23×10^{2}
7	9.35×10^{5}	3.87×10^{5}	1.32×10^{3}	3.74×10^{3}	3.54×10^{2}	1.14×10^{2}
8	8.67×10^{5}	4.18×10^{5}	1.60×10^{3}	3.93×10^{3}	4.37×10^{2}	1.37×10^{2}
9	9.02×10^{5}	4.19×10^{5}	1.23×10^{3}	3.41×10^{3}	3.34×10^{2}	1.10×10^{2}
10	8.68×10^{5}	4.60×10^{5}	1.72×10^{3}	4.74×10^{3}	5.30×10^{2}	1.80×10^{2}
11	9.35×10^{5}	4.55×10^{5}	1.52×10^{3}	4.27×10^{3}	4.96×10^{2}	1.52×10^{2}
12	1.19×10^{6}	5.56×10^{5}	2.43×10^{3}	5.22×10^{3}	5.09×10^{2}	1.58×10^{2}
13	8.93×10^{5}	3.90×10^{5}	1.22×10^{3}	3.18×10^{3}	3.38×10^{2}	1.30×10^{2}
14	9.24×10^{5}	5.85×10^{5}	1.69×10^{3}	4.63×10^{3}	4.84×10^{2}	1.63×10^{2}
15	8.97×10^{5}	4.56×10^{5}	1.23×10^{3}	3.07×10^{3}	3.47×10^{2}	1.21×10^{2}
16	$\mathbf{1.01\times10^{6}}$	$\mathbf{4.83\times10^{5}}$	$\mathbf{1.22\times10^{3}}$	$\mathbf{3.46\times10^{3}}$	$\mathbf{4.11\times10^{2}}$	$\mathbf{1.38\times10^{2}}$
17	8.26×10^{5}	3.82×10^{5}	1.04×10^{3}	2.71×10^{3}	3.02×10^{2}	9.74×10^{1}
18	$\mathbf{7.94\times10^{5}}$	$\mathbf{3.75\times10^{5}}$	$\mathbf{1.12\times10^{3}}$	$\mathbf{3.01\times10^{3}}$	$\mathbf{2.88\times10^{2}}$	$\mathbf{8.97\times10^{1}}$
19	8.32×10^{5}	4.96×10^{5}	1.42×10^{3}	3.51×10^{3}	3.89×10^{2}	1.34×10^{2}
20	$\mathbf{9.49\times10^{5}}$	$\mathbf{5.14\times10^{5}}$	$\mathbf{1.70\times10^{3}}$	$\mathbf{4.43\times10^{3}}$	$\mathbf{4.94\times10^{2}}$	$\mathbf{1.76\times10^{2}}$

Maximum release rate using Dirac pulse injection

Table 63. Maximum release rate [1/y] for radiotracers simulated using a Dirac pulse boundary condition. Realisations in figures correspond to runs 16 (blue), 18 (red), and 20 (green).

Realisation #	^{129}I	^{47}Ca	^{137}Cs	^{226}Ra	^{99}Tc	^{241}Am
1	4.04×10^{-3}	5.36×10^{-4}	9.69×10^{-7}	2.60×10^{-6}	2.72×10^{-7}	9.49×10^{-8}
2	6.12×10^{-3}	8.34×10^{-4}	1.36×10^{-6}	3.39×10^{-6}	3.80×10^{-7}	1.29×10^{-7}
3	5.11×10^{-3}	7.50×10^{-4}	1.48×10^{-6}	3.81×10^{-6}	3.97×10^{-7}	1.32×10^{-7}
4	5.98×10^{-3}	6.94×10^{-4}	1.25×10^{-6}	3.61×10^{-6}	3.36×10^{-7}	1.18×10^{-7}
5	5.14×10^{-3}	7.55×10^{-4}	1.32×10^{-6}	3.39×10^{-6}	4.04×10^{-7}	1.54×10^{-7}
6	5.73×10^{-3}	7.45×10^{-4}	1.46×10^{-6}	3.64×10^{-6}	3.85×10^{-7}	1.24×10^{-7}
7	5.86×10^{-3}	7.19×10^{-4}	1.34×10^{-6}	3.49×10^{-6}	3.38×10^{-7}	1.13×10^{-7}
8	6.09×10^{-3}	9.07×10^{-4}	1.64×10^{-6}	3.90×10^{-6}	4.32×10^{-7}	1.38×10^{-7}
9	5.07×10^{-3}	6.71×10^{-4}	1.22×10^{-6}	3.31×10^{-6}	3.36×10^{-7}	1.11×10^{-7}
10	7.52×10^{-3}	8.98×10^{-4}	1.59×10^{-6}	4.07×10^{-6}	5.24×10^{-7}	1.83×10^{-7}
11	6.46×10^{-3}	9.28×10^{-4}	1.59×10^{-6}	4.11×10^{-6}	4.97×10^{-7}	1.53×10^{-7}
12	7.12×10^{-3}	9.21×10^{-4}	1.94×10^{-6}	4.65×10^{-6}	5.08×10^{-7}	1.60×10^{-7}
13	5.24×10^{-3}	6.78×10^{-4}	1.20×10^{-6}	3.13×10^{-6}	3.48×10^{-7}	1.32×10^{-7}
14	7.77×10^{-3}	9.32×10^{-4}	1.84×10^{-6}	4.81×10^{-6}	4.70×10^{-7}	1.62×10^{-7}
15	5.08×10^{-3}	6.65×10^{-4}	1.32×10^{-6}	3.39×10^{-6}	3.45×10^{-7}	1.19×10^{-7}
16	$\mathbf{5.05\times10^{-3}}$	$\mathbf{7.39\times10^{-4}}$	$\mathbf{1.25\times10^{-6}}$	$\mathbf{3.19\times10^{-6}}$	$\mathbf{3.98\times10^{-7}}$	$\mathbf{1.39\times10^{-7}}$
17	5.42×10^{-3}	5.42×10^{-4}	1.08×10^{-6}	2.82×10^{-6}	2.95×10^{-7}	9.72×10^{-8}
18	$\mathbf{4.99\times10^{-3}}$	$\mathbf{5.96\times10^{-4}}$	$\mathbf{1.09\times10^{-6}}$	$\mathbf{3.10\times10^{-6}}$	$\mathbf{2.91\times10^{-7}}$	$\mathbf{8.99\times10^{-8}}$
19	6.01×10^{-3}	7.12×10^{-4}	1.46×10^{-6}	3.65×10^{-6}	3.98×10^{-7}	1.33×10^{-7}
20	$\mathbf{6.42\times10^{-3}}$	$\mathbf{9.26\times10^{-4}}$	$\mathbf{1.63\times10^{-6}}$	$\mathbf{4.13\times10^{-6}}$	$\mathbf{4.99\times10^{-7}}$	$\mathbf{1.77\times10^{-7}}$

6 Task 6F

6.1 Modelling strategy

Task 6 seeks to provide a bridge between Site Characterisation (SC) and performance assessment (PA) approaches to solute transport in fractured rock. In Task 6, both PA-type and SC-type models are applied to tracer experiments considering both the experimental boundary conditions and boundary conditions for a PA scale.

In the first tasks (Task 6A, 6B and 6B2), solute transport on a 5-10 meter scale in a single feature was modelled. These tasks were based upon the TRUE-1 tracer test STT-1b performed between packed off borehole sections containing a water-conducting geological feature with an interpreted "simple" planar structure (Feature A). The tracer test STT-1b in Task 6A (previously modelled in Task 4E) was revisited with the purpose to provide a common basis for future comparison of the modelling carried out within Task 6. Similarly, in Task 6B the injection and withdrawal of tracer were assumed to occur in the same borehole sections as in the STT-1b test, but with a flow rate that was only 1/1000 of that in Task 6A in order to mimic PA time scales. In Task 6B2, the boundary conditions were modified to produce flow and transport over a larger area of Feature A. The input boundary was in this case a line source and the tracers were assumed to be collected in a hypothetical fracture, intersecting Feature A.

In Tasks 6D and 6E solute transport over longer distances including several geological features are modelled. The basis for the modelling is the block scale semi-synthetic hydrostructural model developed within Task 6C (Dershowitz et al., 2003) at two different scales, 200 m and 2000 m. In this task a semi-synthetic hydrostructural model was developed based on the conditions at the TRUE Block scale site in the southwest of the Äspö Hard Rock Laboratory. The model was built through a combination of deterministic and stochastic analyses of hydraulically significant structural features at scales from millimetres to kilometres. At each scale the geometric, hydraulic and transport properties of the structures are described.

This subtask Task 6F was proposed due to the high level of complexity in Task 6E, with large networks of fractures of different type being conceptually and mathematically modelled in different ways by the various Modelling Groups, thus making comparison and analysis of reasons for differences tremendously difficult. Thus, a series of "benchmark" runs on a simplified system were proposed.

The task consists of simulating flow and transport in a single Type 1 and a Type 2 feature, respectively. The features will follow the geometrical description from Task 6C. However, the implementation of the Task 6C hydrogeostructural model in a flow and transport model may be done in several ways. An important step in this subtask is to describe how the Task 6C model is implemented and what assumptions are made in the process.

Hydrological properties of the features (Transmissivity, aperture, storativity) are taken from distinct features of the Task 6C model. Tracers Iodide (I-129), Caesium (Cs-137, and Americium (Am-241) selected from Task 6E were used. The transport and sorption data for these tracers were as prescribed for Task 6E.

The source term was a Dirac pulse from a spatially extended source as in Task 6E. Breakthrough over a "collection line" at a distance of 20 meters was used for the performance measures. A prescribed hydraulic head was used, giving water transit times of roughly 0.1, 1 and 10 years.

6.1.1 Geological structure types and Complexity factors

In the hydrostructural model the geological structures are divided into two basic Geologic Structure Types, Type 1 "Fault" and Type 2 "Non-fault" (Dershowitz et al, 2003). Details about these two types of features and their characteristic components, including intact unaltered wall rock, altered zone, cataclasite, fault gouge and fracture coating may be found in Task 6C report (Dershowitz et al., 2003)

Investigations at Äspö have shown that many structures are made up of several conductive features and the number of sub-parallel features may vary over the extent of the structure. Thus, a structure may at one location consist of a single fracture of Geological Structure Type 1, while at another location it may consist of two fractures of Geological Structure Type 1 and 2, respectively. Larger scale structures may consist of tens, or more of sub-parallel and hydraulically conductive fracture splays and similar features. As the possible combination of fracture-features within a structure is immense, a simplified classification scheme is introduced. A Complexity Factor ranging from 1 to 5 is defined. The Complexity Factor 1 represents structures consisting of a single feature while Complexity Factor 5 represents structures consisting of more than 10 features (Dershowitz et al., 2003).

6.1.2 Selected features

Two features of Geological Type 1 and Type 2, respectively, have been chosen from the discrete features specified in the Task 6C. In the selection of the features, it is required that they should be of Complexity Factor 1, i.e., only contain a single conductive fracture and with the primary geological structure type covering 90 – 100% of the area. Moreover, the length of the feature should be at least 20 meters and the features should have "average" values for transmissivity, storativity and aperture.

All of the deterministic or synthetic features have a Complexity Factor 2 or greater. Thus, two features with Complexity factor 2 have been chosen, but for the purpose of this exercise they should be considered to consist of a single fracture; i.e., Complexity factor 1. The selected features are:

- Geological Type 1: Synthetic feature 1S
- Geological Type 2: Synthetic feature 4S

These fractures actually lie on the boundaries of the 200-m box. However, for the purpose of this exercise they should not be truncated at the box boundaries.

6.1.3 Structure properties

For the synthetic structures the properties were assigned depending on their size, see Chapter 3 of Task 6C report. A stepwise procedure was used to derive the properties from stochastic correlation relationships as described in Chapter 4 of the Task 6C report, see Figure 4-2 in the Task 6C report. The properties of the selected features as given in the Task 6C database are presented in Table 64.

Table 64. Properties of selected features.

Structure Name	Width & Length	Geological Type	Complexity Factor	Transmissivity (m2/s)	Storativity	Aperture (m)
1S	112.44	1	2*	3.14E-07	2.80E-04	2.58E-04
4S	80.55	2	2*	1.90E-07	2.18E-04	2.01E-04

* For the purpose of this exercise considered to consist of a single fracture.

6.1.4 Geometry

For the simulations the transport along a 20 meter long part of the fractures were considered as described in Figure 88. Each of the two fractures was calculated as a separate case. Note, for the purpose of this exercise the fractures are not truncated at the boundaries of the 200-meter box.

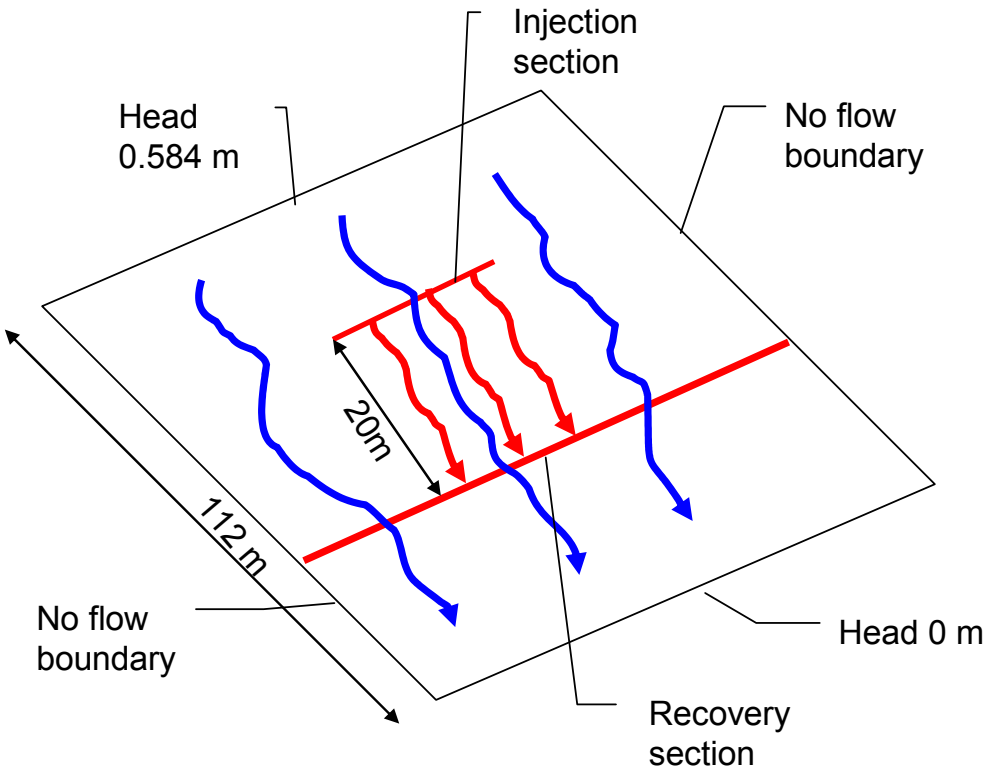

Figure 88. *Description of the geometry and boundary conditions (Example for Case A1).*

6.1.5 Boundary conditions

The boundary conditions are simplified with fixed head boundary conditions at two opposing boundaries of the selected features, while the other sides are treated as no-flow boundaries, se Figure 2.1. The heads were set as to have an estimated groundwater travel time through the 20 meter section of the features of 0.1, 1 and 10 years, respectively. The head differences required for this are presented in Table 65.

Table 65. Head boundary conditions for the different cases.

Case	Travel time (yr)	Head difference (m)	
		1S	4S
A	0.1	0.584	0.539
B	1	0.0584	0.0539
C	10	0.00584	0.00539

The tracer source section was assumed to be an intersecting fracture with a linear extension of 3 meters. The source may be modelled as several point sources on a line.

The recovery section was assumed to be an intersecting factor of a length of 3 meters at a distance of 20 meters from the tracer source section extending over the entire width of the fracture.

In Task 6F, the breakthrough of the tracers I-129, Cs-137 and Am-241 were to be simulated. The purpose was to relate to the behaviour of radionuclides relevant for PA and in the case of Americium also to study how the retardation of more sorbing radionuclides can be extrapolated in time. Simulations are requested for a Dirac pulse input (unit input).

6.1.6 Material properties

The available database for transport and sorption properties of the two main types of structures may be found in Task 6C report (Dershowitz et al., 2003).

The properties of the 100-m Scale Geological Structure Type 1 and 2 in terms of extent, porosity and formation factors are shown in Table 66 and Table 67.

Table 66. Properties of 100-m Scale Geological Structure Type 1 (Fault).

Rock type	Extent (cm)	Porosity, %	Formation Factor
Intact wall rock	-	0.3	7.E-5
Altered zone	20	0.6	2.E-4
Cataclasite	2	1	5.E-4
Fault gouge	0.5	20	5.E-2
Fracture coating	0.05	5	6.E-3

Table 67. Properties of 100-m Scale Geological Structure Type 2 (Non-Fault).

Rock type	Extent (cm)	Porosity, %	Formation Factor
Intact wall rock	-	0.3	7.E-5
Altered zone	10	0.6	2.E-4
Fracture coating	0.05	5	6.E-3

Effective diffusivities for the different types of geological material are presented in Table 68. The volumetric sorption coefficients (Kd-values) for TRUE Block Scale groundwater are presented in Table 69.

Table 68. Effective diffusivities for the different radionuclides in different types of geological material.

Geological material	Iodide (m2/s)	Caesium (m2/s)	Americium (m2/s)
Intact rock	1.50E-13	1.50E-13	4.40E-14
Altered zone	4.40E-13	4.50E-13	1.30E-13
Cataclasite	9.80E-13	1.00E-12	2.90E-13
Fault gouge	1.10E-10	1.20E-10	3.30E-11
Fracture coating	1.20E-11	1.30E-11	3.70E-12

Table 69. Volumetric sorption coefficients (Kd-values) for TRUE Block Scale groundwater.

Geological material	Iodide (m3/kg)	Caesium (m3/kg)	Americium (m3/kg)
Intact rock	0.0	0.010	0.500
Altered zone	0.0	0.020	0.500
Cataclasite	0.0	0.015	0.500
Fault gouge	0.0	0.160	0.500
Fracture coating	0.0	0.052	0.500

Regarding the surface sorption coefficient Ka, this should be calculated using the Kd-values for the respective material (coating, gouge).The values specified for the fracture coatings were used. It should further be assumed (within the time perspective used in these calculations) that all of the sorption sites of this 0.5 mm thick fracture coating material are in immediate contact with the groundwater. Ka can thus be calculated from the Kd according to:

$$K_a = (K_d \rho + \varepsilon) \cdot d \qquad (34)$$

where d is the thickness of the fracture coating (0.05 mm), ε is the porosity (0.05) and ρ is the density of the fracture coating (~2600 kg/m3).

For shorter time scales (e.g., time scales for in situ experiments) it could be questionable if the tracers will fully penetrate the 0.5 mm thick fracture coating. Therefore the validity of the concept of transforming Kd for the fracture coatings to Ka were checked and verified.

It was stipulated that radioactive decay should not be considered in the modelling. Simulations should be performed up until a full recovery is obtained for all tracers, or to a maximum time of 10^8 years.

6.1.7 Implementation of the model

The following sections detail how the Task 6F modelling exercise was carried out within the framework of the CHAN3D program. The modelled fracture is represented in the CHAN3D program by a two-dimensional grid formed by 225 nodes in the x- and y-directions. No channels are located in the z-direction. This means that the grid is formed by about 100 000 channels with a length of 0.5 m.

It is assumed that the conductance of the channels is lognormally distributed with a standard deviation of 1.2 in logarithmic scale. A standard deviation of 0.8 was also tested. The mean conductance of the channels was chosen to match the transmissivity of the fractures.

The aperture of the channels (fractures) was assumed to be proportional to the channel conductance cubed. The porosity (mean channel volume) was chosen to match the channel water residence time; 0.1, 1.0 and 10.0 years for the cases A, B, and C respectively.

The particles (radionuclides) were injected in the channel intersections located at the injection zone, a total of seven injection points were used. Two types of injection were tested. In the first case, the particles were uniformly distributed between the seven injection points, independent of the flow rate in the particular location. This means different concentrations in the injection points. In the second case, the number of particles injected in each intersection was proportional to the flow in that location. The same concentration is found in each injection point. No important differences in the results are observed between these cases.

Description of the fracture space

The different geological materials in the fracture plane have different response times regarding diffusion and sorption. We can expect that even for relatively short times the coating material will be almost in equilibrium with the concentration of the radionuclides dissolved in the water in the fracture. This is due to the large effective diffusivity (about 10^{-11} m^2/s) and the small thickness of the coating material (0.5 mm). The same situation may be assumed for the gouge material since its effective diffusivity is much larger (about 10^{-10} m^2/s).

The validity of these assumptions may be verified by calculating the penetration length for a particular time. Two penetration lengths are usually defined. One is the distance where the concentration reaches a given concentration, e.g., 1% of the concentration at the surface ($\eta_{0.01}$). The other is the average penetration length $\overline{\eta}$, which represents the thickness of a hypothetical zone with a concentration equal to the concentration at the surface that contents an amount of solute equal to the amount of solute that has diffused into the material. These penetration lengths may be calculated as

$$\eta_{0.01} \approx 4\sqrt{\frac{D_e \cdot t}{\varepsilon + K_d \rho_p}} \tag{35}$$

$$\overline{\eta} = \frac{2}{\sqrt{\pi}}\sqrt{\frac{D_e \cdot t}{\varepsilon + K_d \rho_p}} \approx \sqrt{\frac{D_e \cdot t}{\varepsilon + K_d \rho_p}} \tag{36}$$

From these penetration lengths, it is possible to estimate the time to equilibrate the coating and gouge material. It is expected that these times are very short for non-sorbing radionuclides, on the order of hours for the coating material and days for the gouge material. These times are negligible compared with the residence time in the fracture, which varies from one tenth of a year to some decades.

The same situation is observed for the sorbing radionuclides (slightly and strongly sorbing radionuclides). The time to equilibrate the coating and gouge material is only a small fraction of the residence time. The explanation for this is that the time to reach the equilibrium is proportional to the sorption constant (See Equation 36) and the residence time in the channel is proportional to the sorption constant. This means that the ratio to reach the equilibrium with the coating or gouge material and the residence time is the same, independent of the sorption constant and depends only on the effective diffusivity (Moreno et al., 2004).

6.2 Model description

The simulations were made using the CHAN3D computer program (Gylling, 1997), which is based on the Channel Network model (Moreno and Neretnieks, 1993). The model takes into account the uneven flow distribution observed in fractured rock and the stochastic nature of hydraulic features as well as solute transport retarding processes such as diffusion and sorption within the rock matrix.

The code CHAN3D is actually two separate programs; the CHAN3D-flow program that computes the flow field in the rock fracture system, and the CHAN3D-transport program that computes the transport of solutes once the flow field is established using CHAN3D-flow.

6.2.1 Flow model

The Channel Network model, upon which the CHAN3D program is based, assumes that fluid flow takes place within a network of interconnected flow channels in the rock. Channels are conceptualised in the model as being purely hydrological entities representing paths of preferential flow within individual fractures. Flows in individual channels may diverge along separate flowpaths or converge and mix. Channels contained within a given fracture may also interconnect with channels belonging to intersecting fractures thereby giving rise to three-dimensional connectivity in the channel network. For sake of visualisation, the Channel Network model considers a regular, grid of orthogonal channels.

Each member of the channel network is assigned a hydraulic conductance. This is the only entity required to calculate the flow, if the head field is known. The conductance is defined by analogy with electrical networks where it is the reciprocal of resistance. Here, the flow may be expressed as the channel conductance multiplied by the hydraulic head difference between its ends. In the current model, we assume that the conductances of the channel members are log-normally distributed (with a characteristic mean, μ_c, and standard deviation, σ_c) and not correlated in space.

The corresponding flow, q_{ij} is then given by:

$$q_{ij} = C_{ij}\left(H_i - H_j\right) \tag{37}$$

where C_{ij} is the channel conductance connecting the nodes *i* and *j* and H_i and H_j are the hydraulic heads at the nodes *i* and *j*. Furthermore, at each node i, we have the hydraulic analogy of Kirchoff's current law:

$$\sum_j q_{ij} = 0 \tag{38}$$

This is simply a mass balance stating that the net flow of water into a node should also equal the flow out of the node under steady state conditions.

The solution of this system of equations gives the hydraulic head at each node. For a network of nodes interconnected in this way, we must solve a sparse system of linear equations. Once the hydraulic head at each node is known, the flow between adjacent channels may be calculated using Equation 38.

The properties of individual channels may differ considerably and this leads to a sparse flow system where there will be a few channels with relatively large flowrates and some with almost no flow at all. This is similar to what is observed in fractured rock when hydraulic tests are carried out.

6.2.2 Transport model

First the solute transport in a single channel is presented. The model includes advection in the channel, sorption on the fracture surface, diffusion into the rock matrix and sorption onto the micro-surfaces within the rock matrix. Here, it is assumed that the matrix thickness where the radionuclides may diffuse is infinite. The case, where the matrix connectivity is limited or where the matrix is formed by several layers (skins) in addition to the matrix proper is presented later.

Solute transport in a channel - Mathematical description

Within an individual channel, the tracer is transported by advective flow. At the same time, the tracer may diffuse from the channel into the rock matrix. For an instantaneous step change in inlet concentration, the penetration of tracer substance into the rock matrix may appear as shown schematically in Figure 89. Advective flow occurs in the channel along the x-axis, while matrix diffusion is outwards into the rock volume perpendicular to the fracture plane.

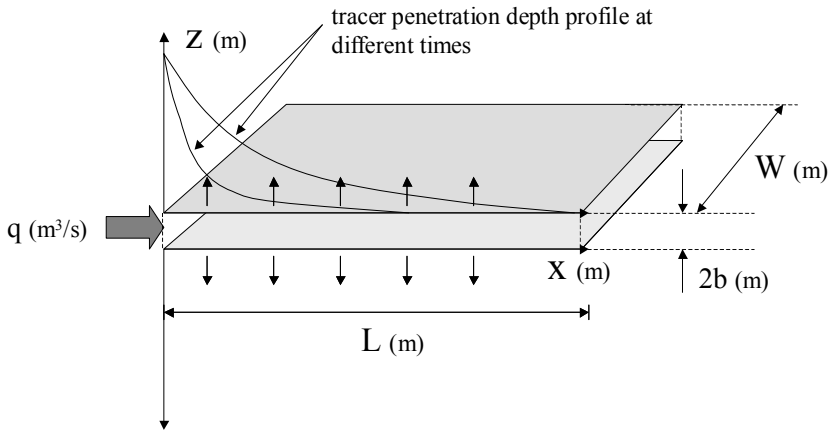

Figure 89. *Conceptual illustration of tracer transport within a channel.*

A transient, differential mass balance is used to describe the advective transport of the tracer, linear sorption on the fracture surface, and diffusion from an individual channel into the rock matrix (assumed to be infinite in extent). In the absence of radioactive decay, this mass balance is:

$$\left(1+\frac{K_a}{b}\right)\frac{\partial C_f}{\partial t} = -\frac{q}{2Wb}\frac{\partial C_f}{\partial x} + \frac{D_e}{b}\frac{\partial C_p}{\partial z}\bigg|_{z=0} \tag{39}$$

Here, C_f is the aqueous concentration in the fracture, C_p is the pore-water concentration, K_a is the surface sorption coefficient, b is the fracture half-aperture, W is the channel width, D_e is the effective diffusivity, and q is the advective flowrate in the channel. The term on the left-hand side of the equation is the accumulation term describing the rate of change of concentration in the fracture water, where sorption of tracer on the fracture surface is accounted for. On the right-hand side of the equation the advective flux term and the matrix diffusive flux term are represented. The flow-wetted surface (FWS) of the channel is defined as 2WL.

The multiplier on the left-hand side of the mass balance is frequently referred to as the retardation factor, R_*:

$$R_* = 1+\frac{K_a}{b} \tag{40}$$

The mean residence time of the trace in the channel, t_T, may then be written as

$$t_T = t_W\left(1+\frac{K_a}{b}\right) = \frac{2\cdot LWb}{Q}\left(1+\frac{K_a}{b}\right) = t_W + K_a\frac{FWS}{Q} \tag{41}$$

where FWS is the flow wetted surface of the channel (2LW). For sorbing species and even for non-sorbing species at PA conditions, the residence time of the tracer in the channel is independent of the channel aperture. This shows that the use of the term "retardation factor" may be inconvenient and in some cases misleading (Moreno et al., 1997).

A similar mass balance is used to describe the diffusive transport and linear sorption of a tracer within the rock matrix:

$$K_d \rho_b \frac{\partial C_p}{\partial t} = D_e \frac{\partial^2 C_p}{\partial z^2} \tag{42}$$

where,

$$K_d \rho_b = \varepsilon_p + \left(1 - \varepsilon_p\right) \cdot K_d' \rho_s \tag{43}$$

K_d and K_d' are the matrix sorption coefficients based upon the bulk (ρ_b) and solid densities (ρ_s), respectively; ε_p is the matrix porosity. In the rock matrix differential mass balance, the accumulation term on the left-hand side of the equation gives the rate of change of the pore water concentration within the rock matrix, where the sorbed concentration of tracer is simultaneously accounted for. The term on the right-hand side of the equation is the diffusive flux term for the tracer.

For an instantaneous "step" change in concentration at the mouth of the channel, the coupled mass balances can be solved to give an analytical solution for the tracer concentration at the channel outlet. This is the breakthrough curve (BTC) for the channel. In terms of the flow-wetted surface to flow ratio, this is:

$$\frac{C(t)}{C_0} = \begin{cases} 0 & \text{for } t \le t_T \\ \operatorname{erfc}\left[\dfrac{1}{2}\dfrac{MPG}{(t - t_T)^{0.5}} \cdot \left(\dfrac{FWS}{Q}\right)\right] & \text{for } t > t_T \end{cases} \tag{44}$$

The strength of matrix interaction for a tracer is determined by the material property group (MPG), which is defined as:

$$MPG = \sqrt{D_e K_d \rho_b} \tag{45}$$

6.2.3 Implementation of solute transport in a Channel Network model

The problem of assessing the Residence Time Distribution (RTD) of a solute in a channel network can be divided into two distinct steps. First, the water flow rate distribution must be determined. This makes it possible to follow a particle or a small water parcel along the flow path. We follow a tiny water stream with constant flow rate q along the entire path. The stream q is smaller than any of the flow rates in the network. Its magnitude need not be defined. At an intersection the whole stream q will follow one of the exit channels only and is not split into parts. The path of the water stream through a channel network is shown in Figure 90. The channel has a flowrate Q_i and a flow wetted surface A_{Qi}. For the water stream the flow wetted surface and the water flow rate are A_{qi} and q respectively.

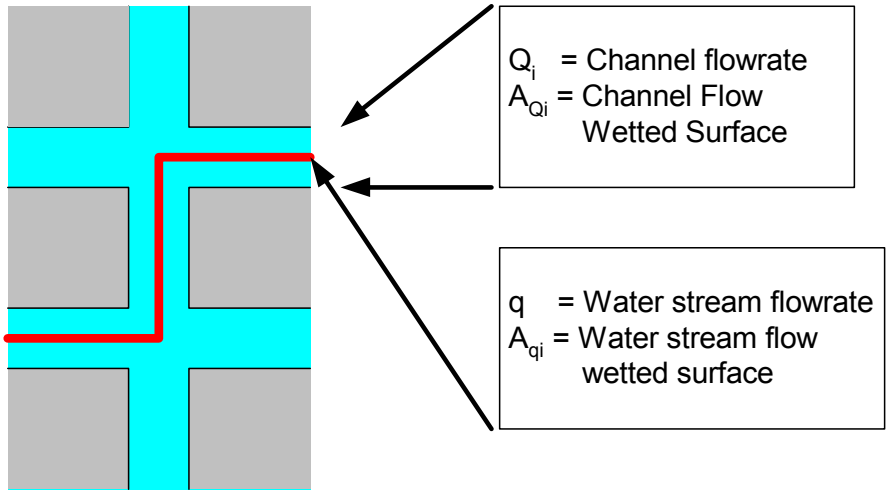

Figure 90. *Schematic picture of a water stream through a channel network.*

It is assumed that the flow rate Q_i is evenly distributed over the surface of the channel. The flow wetted surface A_q, encountered by the water stream q, is a fraction of the total flow wetted surface in the channel/fracture A_{Qi}. The proportionality is assumed to be equal to the ratio between the water stream flow rate, q, and the total flow rate in the channel, Q_i,

$$\frac{A_{qi}}{q} = \frac{A_{Qi}}{Q_i} = \frac{(\text{Total fracture surface})}{(\text{Total flowrate})} \tag{46}$$

The total flow wetted surface for the water stream with flowrate q along the entire trajectory is the sum of the flow-wetted surface in each channel:

$$\frac{FWS}{q} = \frac{1}{q}\sum_{1}^{n} A_{qi} = \sum_{1}^{n} \frac{A_{Qi}}{Q_i} \tag{47}$$

The water residence time for the stream is the sum of the residence times in each of the individual channels traversed.

Solute transport is then simulated using a particle following technique in the CHAN3D-transport program (Robinson, 1984; Moreno et al., 1988). Many particles are introduced, one at a time, into the known flow field at the tracer injection location. Particles arriving at an intersection are distributed in the outlet channel members with a probability proportional to their flow rates. This is equivalent to assuming total mixing at the intersections. Each individual particle is followed through the network until it arrives at either the recovery borehole or a system boundary. Therefore, for each channel that the particle has traversed, the water residence time and the ratio $(MPG)_i \cdot A_{Qi} / Qi$ are recorded. If the properties of the matrix vary along the paths, they would also be recorded. For each specific path, the breakthrough curve may then be calculated. Finally, the addition of the breakthrough curves for a large number of particles yields the breakthrough curve for the solute in the network.

This procedure may be applied to solute transport when diffusion takes place into a matrix with an infinite connectivity and homogeneous properties in entire network. In the next section, solutions for other cases are discussed.

The residence time for water (or a non-interacting solute) in a given channel is determined by the flow through the channel member and by its volume. The channel volume is estimated by assuming that the conductance of a channel is proportional to the cube of the channel aperture. The proportionality constant is determined, based upon the estimated flow porosity of the system. The flow porosity can be determined from the experimental residence time distribution (RTD) of a non-sorbing (conservative) tracer.

Hydrodynamic dispersion in individual channels is considered to be negligible. Dispersion arises instead as a result of the varying transit times for particles taking alternative routes through the channel network.

Implementation of particle tracking for the case of unlimited pore connectivity

Once that the water flowrate distribution in the Channel Network is known, a large number of particles (or water parcels) are followed from the release point to the exit points. The path that an individual particle travels from the inlet to the outlet may be formed by tens to hundreds of channels with different properties (MPG:s, ω:s, and σ:s). To calculate the breakthrough curve for this path where the channels are coupled in series, the output concentration from a channel is used as the input concentration into the adjacent channel downstream. The final output concentration is then calculated by applying the convolution integral in the time domain. This may be done in a very straightforward way using Laplace transforms.

For the "infinite matrix case," the solution for solute transport in a channel (fracture) including diffusion and sorption within the matrix and for no dispersion in the fracture is used as a starting point (Tang et al., 1981). For illustrative purposes, a path formed for n channels is considered. For a Dirac pulse the Laplace transform of the effluent concentration for the channel i is,

$$\tilde{c}_i = \mathrm{Exp}\left(-2\cdot A_i\sqrt{s} - t_{Ti}s\right) \qquad \text{for } i = 1,2,.....n \tag{48}$$

Where A is defined as

$$A = \frac{(\mathrm{MPG})_i \cdot (\mathrm{LW})_i}{Q} \tag{49}$$

The convolution integral in the time domain is equivalent to a multiplication of transfer functions in Laplace space:

$$\tilde{c}_{path} = F\cdot\tilde{c}(\mathrm{Ch\_1})\cdot\tilde{c}(\mathrm{Ch\_2})\cdot\ldots\cdot\tilde{c}(\mathrm{Ch\_n}) \tag{50}$$

where F is the Laplace transform for the input function. Inserting the Laplace transform for each channel, the output concentration for this path may be obtained

$$\tilde{c}_{path} = F\cdot\mathrm{Exp}\left[-2\sqrt{s}\left(A_1 + A_2 + \ldots + A_n\right) - s\cdot\left(t_{T1} + t_{T2} + \ldots + t_{Tn}\right)\right] \tag{51}$$

Comparing Equations (48) and (51), it may be concluded that that the solution (in the time domain) for a channel may be used for calculating the breakthrough curves for the path if the parameters t_T and $\frac{(MPG)_i \cdot A_{Qi}}{Q_i}$ are replaced by the respective summed terms along the path.

$$\frac{C(t)}{C_0} = \begin{cases} 0 & \text{for } t \le \sum_{i=1}^{n} t_{Ti} \\ \operatorname{erfc}\left[\frac{1}{2} \frac{1}{\left(t - \sum_{i=1}^{n} t_{Ti} \right)^{0.5}} \sum_{i=1}^{n} \frac{(MPG)_i \cdot A_{Qi}}{Q_i} \right] & \text{for } t > \sum_{i=1}^{n} t_{Ti} \end{cases} \quad (52)$$

Therefore, for each channel that the particle has traversed, the residence time and the ratio $(MPG)_i \cdot A_{Qi} / Qi$ should be recorded. When the particle reaches the exit, the sum of these two parameters is determined. For each specific path, the breakthrough curve may then be calculated by using Equation 52. Finally, the addition of the breakthrough curves for a large number of particles yields the breakthrough curve for the solute in the network.

6.3 Calculated cases

Calculations were done for the two features (1S and 4S) and for the three hydraulic head differences (Case A, B, and C). Two sub-cases were calculated for the Case C. In the first one, equilibrium was assumed between the solute in the channel and the solute sorbed on the coating, gouge, and cataclasite. In the second one, the altered zone is also set in equilibrium with the solute in the channel. The calculated cases and their properties are shown in Table 70 for Feature 1S and Table 71 for Feature 4S.

The calculations were performed with the CHAN3D code. The version considering diffusion into an infinite matrix was used in this occasion. The limitations found in this version were the motivation to develop a version that could handle diffusion into a matrix formed by several layers (materials)

Table 70. Calculated cases for the Feature 1S.

Case	Hydraulic head difference, m	Solute in the channel in equilibrium with:	Matrix with properties as
Case-A1	0.584	Coating and gouge	Cataclasite
Case-B1	0.0584	Coating, gouge, and cataclasite	Altered zone
Case-C1a	0.00584	Coating, gouge, and cataclasite	Altered zone
Case-C1b	0.00584	Coating, gouge, cataclasite, and altered zone	Intact wall rock

Table 71. Calculated cases for the Feature 4S.

Case	Hydraulic head difference, m	Solute in the channel in equilibrium with:	Matrix with properties as
Case-A2	0.539	Coating	Altered zone
Case-B2	0.0539	Coating	Altered zone
Case-C2a	0.00539	Coating	Altered zone
Case-C2b	0.00539	Coating and altered zone	Intact wall rock

As discussed above, even for the highest water flowrate, it is expected that the coating material and the gouge material reach the equilibrium with the radionuclide in the fracture water. This time is significantly shorter than the residence time in the fracture. However, due to limitations in the present version of CHAN3D (rock matrix is composed only of one geological material) it is assumed that some materials in the fracture wall (e.g., cataclasite) may also reach the equilibrium with the radionuclides dissolved in the fracture water. The consequences of these assumptions on the residence time will be discussed and checked later.

For the Case-A1 (shortest residence time or highest water flowrate), it is assumed that the coating material and the gouge material have sufficient time to reach equilibrium. For the Case-B1, it is assumed that even cataclasite reaches equilibrium with the solute in the channel. The Case-C1a is similar to the Case-B1. But, due to the long residence time, it is expected that an important part of the diffusion takes place in the intact rock in addition to the altered zone. For this reason a new case is defined, the Case-C1b, in which the solute is also equilibrated with the altered zone and the diffusion takes place into an infinite matrix with properties of intact rock. A similar approach is followed when the cases for the Feature 4S are defined.

6.4 Results

6.4.1 β-factor

The values for the ratio FWS/Q are shown in Table 72.

Table 72. Ratio FWS/Q, y/m.

	Feature 1S	Feature 4S
Case A	704	1 260
Case B	7 040	12 600
Case Cxa	70 400	126 000
Case Dxb	70 400	126 000

6.4.2 Breakthrough time history for the tracers

Breakthrough curves for feature 1S

Breakthrough curves for the Feature 1S are determined for five realisations. Figure 91, Figure 92, and Figure 93 show the breakthrough curves for iodide, caesium, and americium. In general, no large differences are observed between different realisations. It is interesting to observe the differences between the cases C1a and C1b. In the Case-

C1a, the water in the fracture/channel is equilibrated with coating, gouge and cataclasite and in the Case-C1b, the water is equilibrated even with altered rock. The second case, in general, shows a higher peak in the release curve. However, the first case shows an earlier arrival in the breakthrough. This may be due to the larger retention in the channel when the altered zone is included in the equilibrium. The peak of the curve and the arrival of the 50% occur earlier for the Cases-C1b due to the lower effective diffusion in the intact rock.

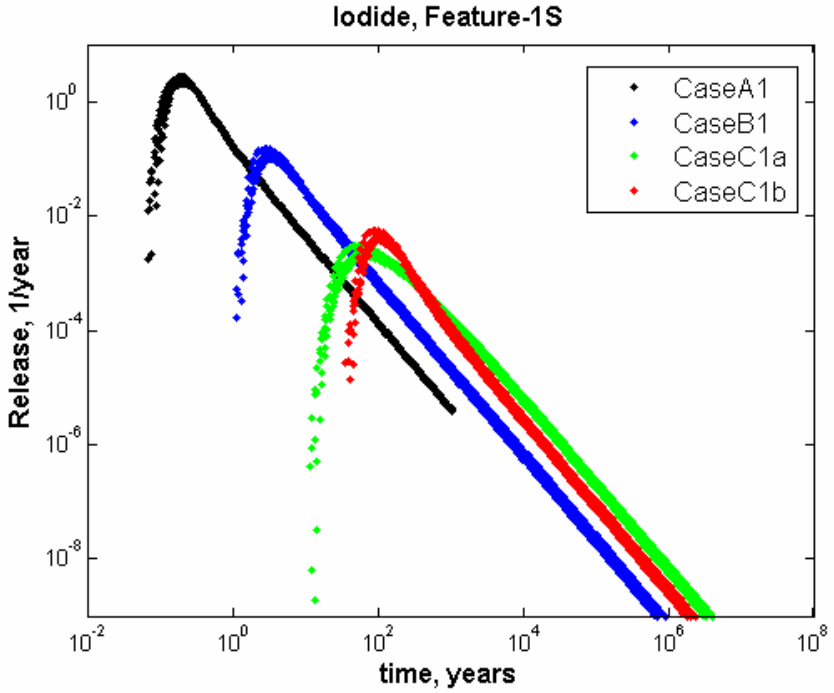

Figure 91. *Breakthrough curve for iodide in Feature 1S.*

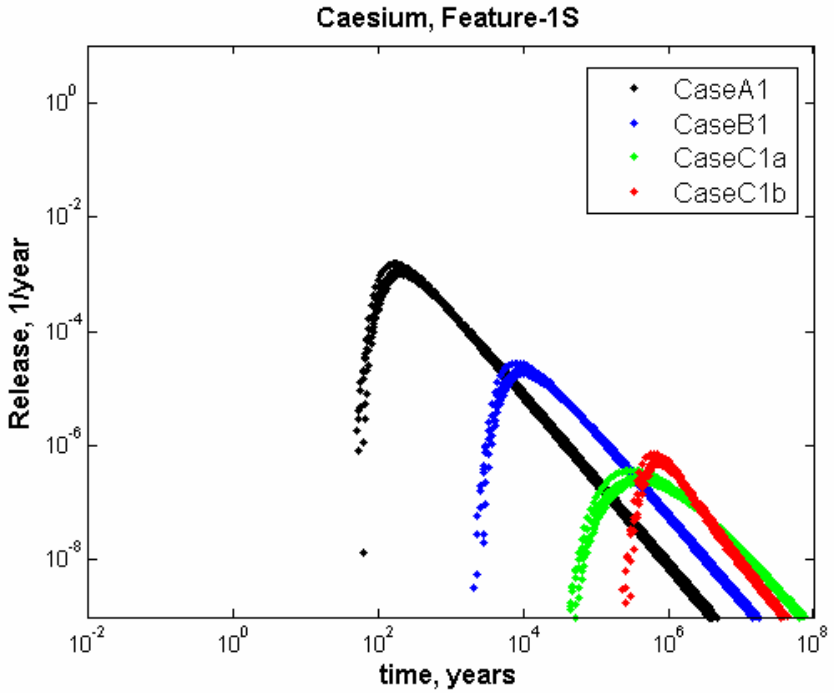

Figure 92. *Breakthrough curve for caesium in Feature 1S.*

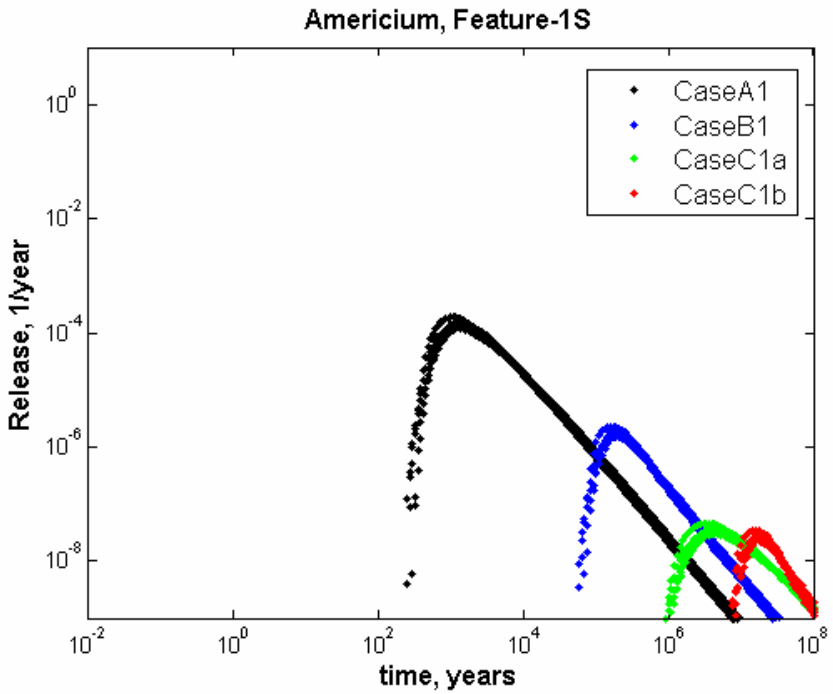

Figure 93. *Breakthrough curve for americium in Feature 1S.*

Breakthrough curves for feature 4S

Breakthrough curves for the Feature 4S are determined for five realisations. Figure 94, Figure 95, and Figure 96 show the breakthrough curves for iodide, caesium, and americium respectively. In general, no large differences are observed between different realisations. It is interesting to observe the differences between the cases C2a and C2b, with the same water flow rate. The Case-C2b, in general, shows a higher peak in the release curve.

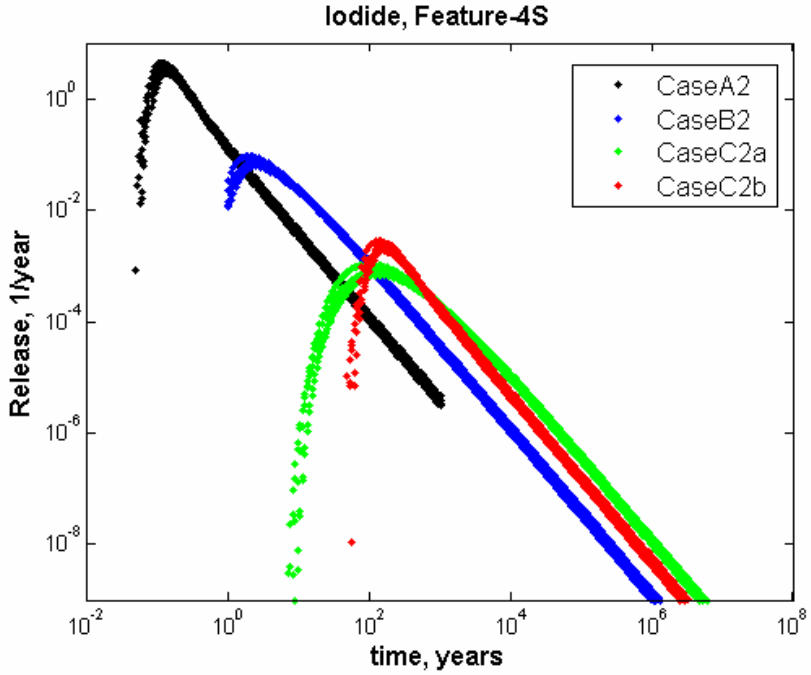

Figure 94. *Breakthrough curve for iodide in Feature 4S.*

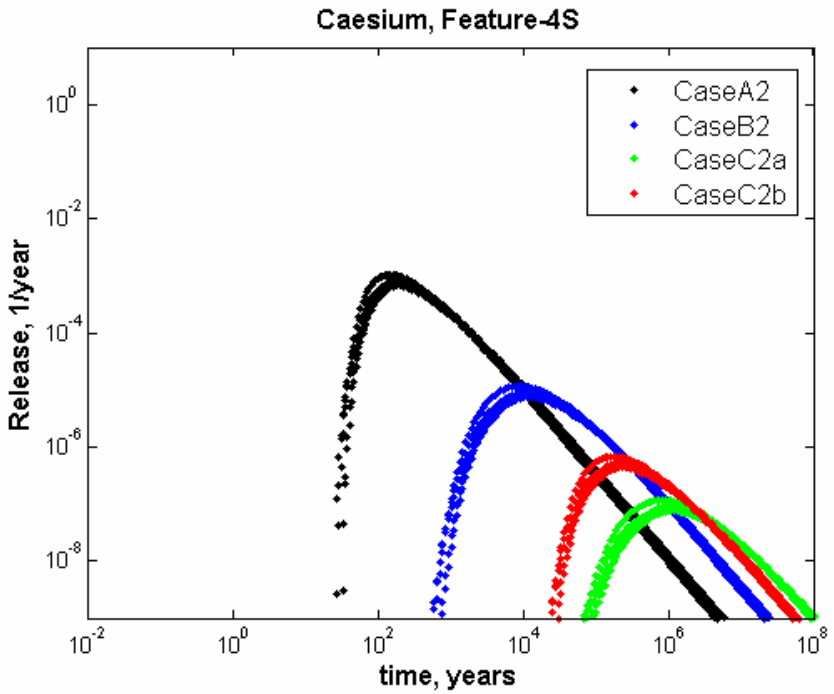

Figure 95. *Breakthrough curve for caesium in Feature 4S.*

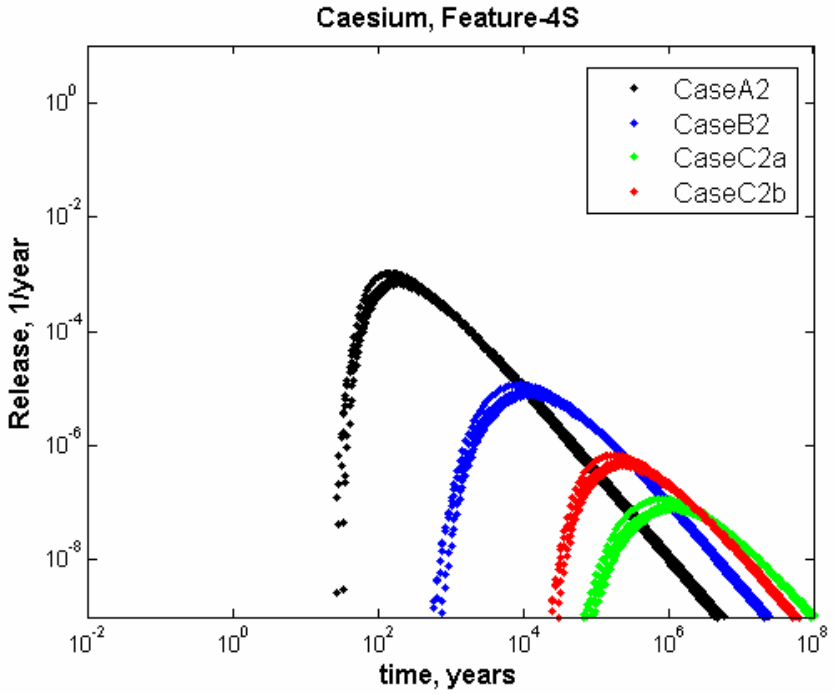

Figure 96. *Breakthrough curve for americium in Feature 4S.*

6.4.3 Maximum release rate

The values for the maximum release for Feature 1S are shown for the different cases and different radionuclides in Table 73.

Table 73. Maximum release for the radionuclides in Feature 1S.

	CaseA1, 1/year	Case-B1, 1/year	Case-C1a, 1/year	Case-C1b, 1/year
Iodide	2.70E+00	1.22E-01	2.34E-03	4.58E-03
Caesium	1.19E-03	2.15E-05	2.79E-07	5.82E-07
Americium	1.45E-04	1.85E-06	3.54E-08	2.83E-08

The values for the maximum release for Feature 4S are shown for the different cases and different radionuclides in Table 74.

Table 74. Maximum release for the radionuclides in Feature 4S.

	Case-A2, 1/year	Case-B2, 1/year	Case-C2a, 1/year	Case-C2b, 1/year
Iodide	3.60E+00	7.21E-02	8.14E-04	2.25E-03
Caesium	8.00E-04	8.87E-06	8.97E-08	5.16E-07
Americium	1.07E-04	1.22E-06	1.24E-08	3.64E-08

6.4.4 Arrival times

Arrival times for Feature 1S

The arrival times for the 5%, 50%, and 95% of the injected radionuclides are shown in Table 75, Table 76, and Table 77.

Table 75. Arrival time for the 5 % of the injected radionuclides, $t_{05.}$

	Case-A1, years	Case-B1, years	Case-C1a, years	Case-C1b, years
Iodide	0.14E00	0.28E01	0.65E02	0.85E02
Caesium	0.18E03	0.88E04	0.42E06	0.61E06
Americium	0.12E04	0.16E06	0.41E07	0.14E08

Table 76. Arrival time for the 50 % of the injected radionuclides, $t_{50.}$

	Case-A1, years	Case-B1, years	Case-C1a, years	Case-C1b, years
Iodide	0.38E00	0.92E01	0.58E03	0.23E03
Caesium	0.10E04	0.58E05	0.50E07	0.18E07
Americium	0.89E04	0.59E06	0.38E08	0.37E08

Table 77. Arrival time for the 95 % of the injected radionuclides, $t_{95.}$

	Case A1, years	Case B1, years	Case C1, years	Case D1, years
Iodide	0.24E02	0.80E03	0.80E05	0.14E05
Caesium	0.12E06	0.77E07	0.73E09	0.12E09
Americium	0.12E07	0.53E08	0.10E11	0.30E10

Arrival times for Feature 4S

The arrival times for the 5%, 50%, and 95% of the injected radionuclides are shown in Table 78, Table 79, and Table 80.

Table 78. Arrival time for the 5 % of the injected radionuclides, t_{05}.

	Case-A2, years	Case-B2, years	Case-C2a, years	Case-C2b, years
Iodide	0.11E00	0.23E01	0.13E03	0.14E03
Caesium	0.18E03	0.12E05	0.12E07	0.23E06
Americium	0.14E04	0.90E05	0.84E07	0.29E07

Table 79. Arrival time for the 50 % of the injected radionuclides, t_{50}.

	Case-A2, years	Case-B2, years	Case-C2a, years	Case-C2b, years
Iodide	0.32E00	0.19E02	0.17E04	0.49E03
Caesium	0.17E04	0.16E06	0.16E08	0.27E07
Americium	0.12E05	0.11E07	0.12E09	0.39E08

Table 80. Arrival time for the 95 % of the injected radionuclides, t_{95}.

	Case-A2, years	Case-B2, years	Case-C2a, years	Case-C2b, years
Iodide	0.26E02	0.26E04	0.26E06	0.44E05
Caesium	0.23E06	0.23E08	0.10E10	0.39E09
Americium	0.17E07	0.17E09	0.10E11	0.30E10

6.4.5 Additional measures

As discussed above, these calculations were performed using the original version of CHAN3D, which calculated solute transport for channels surrounded by a infinite matrix. Therefore, in each case, assumptions were made to describe the materials in equilibrium with the water in the fracture and the matrix properties. Therefore, it is important to determine the validity of these assumptions; to calculate some parameters to determine, for example, the extent of the penetration in the matrix and if equilibrium is reached with the materials in the fracture. These results are the average value for 50 realisations. They include:

- The residence time of the radionuclide in the fracture/channel. It is composed of two parts. One is the water residence time which is determined by the volume of the channel and the water flow. The other one is the residence time caused by sorption equilibrium with the geological material in the fracture or close to the fracture.
- Tracer mean-residence time. It is the actual tracer residence time and takes into account the residence time in the channel and the retardation caused by the diffusion into the matrix.
- The time required to reach equilibrium between the solute in the fracture and the geological material in the fracture or close to it. It is presented as a fraction of the mean residence time. If this value is small (e.g., less than 0.05), it may be assumed that these geological materials reach equilibrium with the solute in the fracture.

- Penetration in the matrix. In the calculations, it is assumed that the infinite matrix has the properties of one of the materials forming the matrix (e.g., cataclasite or altered zone). This is a good approximation if the mean penetration length is much less than the thickness of the respective material (e.g., less than half of the thickness). If the mean penetration length is larger than the thickness of the respective layer then an important part of the diffusion takes place in the material located deeper in the matrix.

Additional measures for Feature 1S

The results for the Case-A1, with a water residence time in the fracture of 0.1 year, are shown in Table 72. The mean residence time varies from 0.42 year for Iodide to 8 900 years for Americium. The time to equilibrate the solute in the fracture with that sorbed onto the materials in the fracture (coating and gouge) is only a small fraction of the residence time of the respective radionuclide. Therefore, equilibrium is actually achieved.

The material properties of the infinite matrix are assumed to be those of cataclasite. As may be observed in Table 72, the mean penetration length is too large. This means that a part of the diffusion takes place into the altered zone, which has a smaller diffusivity. Therefore, the mean residence times obtained are somewhat longer that the actual values particularly for the iodide tracer. This will be checked, in more detail, in the next section, when several layers are used to describe the matrix.

Table 81. Results for the Case-A1.

Case-A1	Iodide	Caesium	Americium
Channel residence time in the channels, years	0.19	169	832
Mean residence time, years	0.42	1 020	8 910
Relative equilibrium time in the fracture	0.003	0.002	0.003
Relative mean penetration in the cataclasite layer, m	1.80	1.40	0.40

The results for the Case B1, with a water residence time in the fracture of one year, are shown in Table 82. The residence times in the fracture vary from 9.2 years for iodide to more than half a million years for americium. In this case the solute in the fracture is equilibrated with the cataclasite layer in addition to coating and gouge materials. For iodide and caesium, the time to reach the equilibrium with the cataclasite layer is a small fraction of the residence time in the fracture. This means that even cataclasite has sufficient time to equilibrate with the solute in the fracture. For americium, equilibrium is possibly not reached.

The material properties of the infinite matrix are assumed to be those of the altered zone. As may be observed in Table 82, for iodide and caesium, a part of the diffusion takes place into the intact rock, which has a smaller diffusivity. The thickness of the altered zone is 0.20 m. For americium most of the diffusion takes place within the altered zone.

Table 82. Results for the case B1.

Case-B1	Iodide	Caesium	Americium
Channel residence time in the channels, years	3.3	7.31E+03	1.97E+05
Residence time	9.2	5.8E+04	5.9E+05
Relative equilibrium time in the fracture	0.014	0.009	0.099
Relative mean penetration in the altered zone, m	0.75	0.60	0.20

The results for the Case-C1a are shown in Table 83. The residence times in the fracture vary from 580 years for iodide to 38 million years for americium. The times for the solute in the fracture to reach equilibrium with the cataclasite layer is a very small fraction of the mean residence time. This means that the material in the fracture (coating, gouge, and cataclasite) have sufficient time to equilibrate with the solute in the fracture.

The material properties of the infinite matrix are assumed to be those of the altered zone. As may be observed in Table 83, the mean penetration length is too large compared with the thickness of the altered zone and an important part of the diffusion takes place into the intact rock, which has a smaller diffusivity than the altered zone.

Table 83. Results for the Case-C1a.

Case-C1a	Iodide	Caesium	Americium
Channel residence time in the channels, years	33	7.3E+04	2.0E+06
Residence time	578	5.0E+06	3.8E+07
Relative equilibrium time in the fracture	<0.001	<0.001	0.002
Relative mean penetration in the altered zone, m	5.80	5.80	1.70

The results for the Case-C1b are shown in Table 84. The residence times in the fracture vary from 230 years for Iodide to 37 million years for Americium. These times are slightly shorter than those for the Case-C1a with the same water flow rate. This is due to that in the Case-C1b the diffusion into the rock matrix was calculated as taking place in the intact rock instead in the altered zone (Case-C1a), which has a higher effective diffusion coefficient.

The time required for the solute in the fracture water to reach the equilibrium with the altered zone is a significant fraction of the mean residence time. This means that the material in the fracture (coating, gouge, cataclasite, and altered zone) does not have sufficient time to equilibrate with the solute in the fracture water. The penetration length into the intact rock is also calculated.

Table 84. Results for the Case-C1b.

Case-C1b	Iodide	Caesium	Americium
Channel residence time in the channels, years	118	8.3E+05	2.1E+07
Residence time	232	1.8E+06	3.7E+07
Relative equilibrium time in the fracture	0.075	0.083	0.354
Relative mean penetration in the altered zone, m	0.30	0.35	0.17

Additional measures for Feature 4S

The results for the Case-A2 are shown in Table 85. The residence times in the fracture vary from 0.32 year for iodide to 12 000 years for americium. Equilibrium is reached between the solute in the fracture and the coating material, since the equilibration times are a small fraction of the mean residence time.

The material properties of the infinite matrix are assumed to be those of the altered zone (with a thickness of 0.1 m). As may be observed in Table 85, the mean penetration length is about half the thickness of the altered zone. This means that diffusion takes place mainly in the altered zone, but a fraction takes place in the intact rock. This will be checked in the next section, when several layers are used to define the matrix.

Table 85. Results for the Case-A2.

Case-A2	Iodide	Caesium	Americium
Channel residence time in the channel, years	0.13	84	808
Mean residence time, years	0.32	1.7E+03	1.2E+04
Relative equilibrium time in the fracture	< 0.001	< 0.001	< 0.001
Mean penetration in the altered zone, m	0.049	0.072	0.034

The results for the Case B2 are shown in Table 86. The residence times in the fracture vary from 18.8 years for iodide to more than a million years for americium. The time to reach the equilibrium with the coating material is a small fraction of the residence time in the fracture. This means that equilibrium is reached.

The material properties of the infinite matrix are assumed to be those of the altered zone (with a thickness of 0.1 m). As may be observed in Table 86, the mean penetration is too large, particularly for iodide and caesium; this means that diffusion takes place also into the intact rock, which has a smaller diffusivity.

Table 86. Results for the Case-B2.

Case-B2	Iodide	Caesium	Americium
Channel residence time in the channels, years	1.3	849	8.1E+03
Mean residence time	18.8	1.6E+05	1.2E+06
Relative equilibrium time in the fracture	< 0.001	< 0.001	< 0.001
Mean penetration in the altered zone, m	0.21	0.21	0.059

The results for the Case-C2a are shown in Table 87. The residence times in the fracture vary from 1 750 years for iodide to 115 million years for americium. Equilibrium with the coating material is reached.

The material properties of the infinite matrix are assumed to be those of the altered zone. As may be observed in Table 87, the mean penetration is too large compared with the thickness of the altered zone (0.10 m). This means that an important part of the diffusion takes place into the intact rock.

Table 87. Results for the Case-C2a.

Case-C2a	Iodide	Caesium	Americium
Channel residence time in the channels, years	13	8.4E+03	8.1E+04
Mean residence time	1.75E+03	1.6E+07	1.2E+08
Relative equilibrium time in the fracture	< 0.001	< 0.001	< 0.001
Mean penetration in the altered zone, m	2.01	2.05	0.59

The results for the Case-C2b are shown in Table 88. The residence times in the fracture vary from 232 years for Iodide to 21 millions of years for Americium. These times are shorter than those for the Case-C2a, due to that in this case the diffusion was assumed to take place in the intact rock, and while for the Case-C2a the matrix was defined as having the properties of the altered zone.

The time for the solute in the fracture water to reach the equilibrium with the altered zone is not sufficiently small compared with the residence time. This means equilibrium is not reached with the altered zone.

Table 88. Results for the Case-C2b.

Case-C2b	Iodide	Caesium	Americium
Channel residence time in the channels, years	165	4.9E+04	1.2E+05
Mean residence time	491	2.7E+06	3.9E+07
Relative equilibrium time in the fracture	0.035	0.056	0.335

6.5 Sensitivity studies

Sensitivity studies are discussed in Task 6F2.

7 Task 6F2

7.1 Modelling strategy

Two aspects are studied and discussed in this task, namely:

- Comparison of the results obtained with CHAN3D and those obtained with a model handling a matrix composed of several layers
- Factors determining the residence time

7.1.1 Comparison between CHAN3D and a model handling a matrix composed of several layers

Since the present version of CHAN3D can only handle diffusion into matrices formed by one type of material, a new version of the Channel Network model is being developed. The model is presented in detail in Appendix A2. Figure 97 shows a schematic picture of the modelled system.

Figure 97. *Illustration of a matrix formed by two-skin and a semi-infinite matrix.*

As indicated above, the present version of CHAN3D can not handle a matrix composed by two or more geological materials. Therefore, in the calculations presented in Chapter 5, two important assumptions were needed. The first assumption is the choice of the geological materials in equilibrium with the solute. The second one is the choice of the material through which diffusion is taking place. To avoid this type of uncertainty, the Channel Network model was extended to handle rock matrices composed of several skin/layers of different types of geological materials.

Comparison between both models was done. But, since the results obtained with CHAN3D correspond to the addition of breakthrough curves for a large number of paths, a simplified case is defined. The breakthrough curves are calculated for a path with properties representative of the ensemble of many paths. The mean value of the ratio FWS/Q, calculated for a large number of realisations, is used for this path in addition to the MPG (Matrix Property Group). The residence times are then calculated for:

- An infinite matrix with properties as defined in Table 70 and Table 71.
- A matrix formed for 1 or 2 skin-layers and a infinite matrix. For the Feature 1S two skin layers are used, while for the Feature 4S only a skin layer is used. The coating and gouge material is assumed to be in equilibrium with the solute in the fracture as discussed in Chapter 5. For the Feature 4S, equilibrium only with coating material is considered (gouge material is missing).

The ratio between the two residence times is also calculated.

7.1.2 Factors determining the residence time

Regarding the residence time of the radionuclides in a channel (or channel network), three components may be distinguished:

- The water residence time in the channel, which is determined by the volume of the channel and the water flow rate
- The residence time caused by instantaneous sorption on the fracture surface and other materials in the fracture (e.g, coating and gouge material). Equilibrium is assumed between the radionuclides dissolved in the water in the fracture and the radionuclides sorbed on these materials
- The residence time caused by the diffusion into and sorption onto the micro-surfaces within the matrix. This residence time is determined by the extent of the diffusion into the rock matrix and is determined by its RTD (residence time distribution). The arrival time for the 50 % of the injected radionuclide is used in our discussion.

This may be conceptually expressed as

$$\begin{pmatrix}\text{Total}\\ \text{Residence}\\ \text{Time}\end{pmatrix} = \begin{pmatrix}\text{Water}\\ \text{residence}\\ \text{time in the}\\ \text{Channel}\end{pmatrix} + \begin{pmatrix}\text{Residence time due}\\ \text{to instantaneous}\\ \text{sorption in the}\\ \text{channel}\end{pmatrix} + \begin{pmatrix}\text{Residence time}\\ \text{due to diffusion}\\ \text{and sorption}\\ \text{in the matrix}\end{pmatrix} \quad (53)$$

Considering that Erfc(0.48) = 0.5, the mathematical expression for the mean residence time is

$$t_{Radionuclide} = \left[\frac{LW\delta}{Q}\right] + \left[K_a\left(\frac{2LW}{Q}\right)\right] + \left[\frac{\left(D_e K_d \rho_p\right)}{0.48^2}\left(\frac{LW}{Q}\right)^2\right] \quad (54)$$

In writing in function of the FWS (2LW)

$$t_{Radionuclide} = \left[\frac{\delta}{2}\cdot\left(\frac{FWS}{Q}\right)\right] + \left[K_a\left(\frac{FWS}{Q}\right)\right] + \left[\frac{\left(D_e K_d \rho_p\right)}{4\cdot 0.48^2}\left(\frac{FWS}{Q}\right)^2\right] \quad (55)$$

It is an important remark that the only term that is function of the fracture aperture (δ) is the first one, the water residence time in the channel. The other two terms are determined by the ratio (FWS/Q) and the material properties. The residence time due to instantaneous sorption in the channel is proportional to (FWS/Q). While the residence time due to diffusion/sorption in the rock matrix is proportional to $(FWS/Q)^2$.

7.2 Model description

The model used in Task 6F2, is based on CHAN3D, which has been extended for handle diffusion into a matrix formed by several layers with different properties. For sake of completeness, a short description of the model is included in these sections.

7.2.1 Flow model

The Channel Network model, upon which the CHAN3D program is based, assumes that fluid flow takes place within a network of interconnected flow channels in the rock. Channels are conceptualised in the model as being purely hydrological entities representing paths of preferential flow within individual fractures. Flows in individual channels may diverge along separate flowpaths or converge and mix. Channels contained within a given fracture may also interconnect with channels belonging to intersecting fractures thereby giving rise to three-dimensional connectivity in the channel network. For sake of visualisation, the Channel Network model considers a regular, grid of orthogonal channels.

Each member of the channel network is assigned a hydraulic conductance. In the model, it is assumed that the conductances of the channel members are log-normally distributed (with a characteristic mean, μ_c, and standard deviation, σ_c) and not correlated in space.

The corresponding flow, q_{ij} is then given by:

$$q_{ij} = C_{ij}\left(H_i - H_j\right) \tag{56}$$

where C_{ij} is the channel conductance connecting the nodes i and j and H_i and H_j are the hydraulic heads at the nodes i and j. Furthermore, at each node i, we have the hydraulic analogy of Kirchoff's current law:

$$\sum_j q_{ij} = 0 \tag{57}$$

This is simply a mass balance stating that the net flow of water into a node should also equal the flow out of the node under steady state conditions.

The solution of this system of equations gives the hydraulic head at each node. For a network of nodes interconnected in this way, we must solve a sparse system of linear equations. Once the hydraulic head at each node is known, the flow between adjacent channels may be calculated using Equation 23.

The properties of individual channels may differ considerably and this leads to a sparse flow system where there will be a few channels with relatively large flowrates and some with almost no flow at all. This is similar to what is observed in fractured rock when hydraulic tests are carried out.

7.2.2 Transport model

As before, the solute transport in a single channel is firstly presented. The model includes advection in the channel, sorption on the fracture surface, diffusion into the rock matrix and sorption onto the micro-surfaces within the rock matrix. Here, it is assumed that the matrix is formed by several layers of finite thickness in addition to an infinite matrix.

Solute transport in a channel with a matrix formed by three skins and an infinite matrix. - Mathematical description

Within an individual channel, the tracer is transported by advective flow. At the same time, the tracer may diffuse from the channel into the rock matrix. Advective flow occurs in the channel along the x-axis, while matrix diffusion is outwards into the rock volume perpendicular to the fracture plane. The layers have properties different of the matrix proper.

First, the governing equations are written and then the Laplace transform is applied to this system of PDE. The system of ODE resulting is solved in the Laplace space. Finally, the solution in time is obtained by numerical inversion of this solution (Laplace space).

A transient, differential mass balance is used to describe the advective transport of the tracer, linear sorption on the fracture surface, and diffusion from an individual channel into the rock matrix (assumed to be infinite in extent). In the absence of radioactive decay, this mass balance is:

$$\left(1+\frac{K_a}{b}\right)\frac{\partial C_f}{\partial t}+\frac{q}{2Wb}\frac{\partial C_f}{\partial x}=\frac{D_{es1}}{b}\left.\frac{\partial C_{ps1}}{\partial z}\right|_{z=0} \qquad \text{for } (x>0,\ t>0) \qquad (58)$$

Here, C_f is the aqueous concentration in the fracture, C_p is the pore-water concentration, K_a is the surface sorption coefficient, b is the fracture half-aperture, W is the channel width, D_e is the effective diffusivity, and q is the advective flowrate in the channel. The term on the left-hand side of the equation is the accumulation term describing the rate of change of concentration in the fracture water, where sorption of tracer on the fracture surface is accounted for. On the right-hand side of the equation the advective flux term and the matrix diffusive flux term are represented. The flow-wetted surface (FWS) of the channel is defined as 2WL.

The multiplier on the left-hand side of the mass balance is frequently referred to as the retardation factor, R_*:

$$R_* = 1+\frac{K_a}{b} \qquad (59)$$

A similar mass balance is used to describe the diffusive transport and linear sorption of a tracer within the rock matrix formed by three skins and an infinite matrix. Unsteady diffusion of solute in the rock matrix proper is given by:

$$\left(\varepsilon_{pm}+(1-\varepsilon_{pm})K'_{dm}\rho_{sm}\right)\frac{\partial C_{pm}}{\partial t}=D_{em}\frac{\partial^2 C_{pm}}{\partial z^2} \qquad \text{for } (x>0,\ z>\delta_{s1}+\delta_{s2}+\delta_{s3},\ t>0) \qquad (60)$$

The term on the left-hand side considers accumulation in both the pore water as well as the tracer sorbed in the rock matrix. We define a bulk distribution coefficient (K_{dm}) to implicitly include both the sorbed and the pore water concentrations:

$$\left(\varepsilon_{pm}+(1-\varepsilon_{pm})K'_{dm}\rho_{sm}\right)=K_{dm}\rho_{bm} \qquad (61)$$

Then, Equation 60 may be written as

$$K_{dm}\rho_{bm}\frac{\partial C_{pm}}{\partial t} = D_{em}\frac{\partial^2 C_{pm}}{\partial z^2} \qquad \text{for } \left(x > 0,\ z > \delta_{s1} + \delta_{s2} + \delta_{s3},\ t > 0\right) \quad (62)$$

For the matrix material nearest the fracture surface that have differing diffusive and sorptive properties than the proper matrix two "surface skins" are defined. The thicknesses are δ_{s1} and for the first and second layer respectively. The corresponding unsteady diffusion equations for the surface skins are:

For the skin-1

$$K_{ds1}\rho_{bs1}\frac{\partial C_{ps1}}{\partial t} = D_{es1}\frac{\partial^2 C_{ps1}}{\partial z^2} \qquad \text{for } \left(x > 0,\ 0 < z < \delta_{s1},\ t > 0\right) \quad (63)$$

For the skin-2

$$K_{ds2}\rho_{bs2}\frac{\partial C_{ps2}}{\partial t} = D_{es2}\frac{\partial^2 C_{ps2}}{\partial z^2} \qquad \text{for } \left(x > 0,\ \delta_{s1} < z < \delta_{s1} + \delta_{s2},\ t > 0\right) \quad (64)$$

For the skin-3

$$K_{ds3}\rho_{bs3}\frac{\partial C_{ps3}}{\partial t} = D_{es3}\frac{\partial^2 C_{ps3}}{\partial z^2} \qquad \text{for } \left(x > 0,\ \delta_{s1} + \delta_{s2} < z < \delta_{s1} + \delta_{s2} + \delta_{s3},\ t > 0\right) \quad (65)$$

The coupled mass balance is solved for an instantaneous "step" change in concentration at the mouth of the channel, by using Laplace transforms. The inversion of Laplace transforms is done by using numerical tools. More details are presented in Appendix A2

Implementation of solute transport in a channel network model.

The problem of assessing the Residence Time Distribution (RTD) of a solute in a channel network can be divided into two distinct steps. First, the water flow rate distribution must be determined. This makes it possible to follow a particle or a small water parcel along the flow path. We follow a tiny water stream with constant flow rate q along the entire path. The stream q is smaller than any of the flow rates in the network. Its magnitude need not be defined. At an intersection the whole stream q will follow one of the exit channels only and is not split into parts. The channel has a flowrate Q_i and a flow wetted surface A_{Qi}. For the water stream the flow wetted surface and the water flow rate are A_{qi} and q respectively.

It is assumed that the flow rate Q_i is evenly distributed over the surface of the channel. The flow wetted surface A_q, encountered by the water stream q, is a fraction of the total flow wetted surface in the channel/fracture A_{Qi}. The proportionality is assumed to be equal to the ratio between the water stream flow rate, q, and the total flow rate in the channel, Q_i,

$$\frac{A_{qi}}{q} = \frac{A_{Qi}}{Q_i} = \frac{\text{(Total fracture surface)}}{\text{(Total flowrate)}} \quad (66)$$

The total flow wetted surface for the water stream with flowrate q along the entire trajectory is the sum of the flow-wetted surface in each channel:

$$\frac{FWS}{q} = \frac{1}{q}\sum_{1}^{n} A_{qi} = \sum_{1}^{n} \frac{A_{Qi}}{Q_i} \tag{67}$$

The water residence time for the stream is the sum of the residence times in each of the individual channels traversed.

Solute transport is then simulated using a particle following technique in the CHAN3D-transport program (Robinson, 1984; Moreno et al., 1988). Many particles are introduced, one at a time, into the known flow field at the tracer injection location. Particles arriving at an intersection are distributed in the outlet channel members with a probability proportional to their flow rates. This is equivalent to assuming total mixing at the intersections. Each individual particle is followed through the network until it arrives at either the recovery borehole or a system boundary. Therefore, for each channel that the particle has traversed, the water residence time and the geometry and properties of the matrix are recorded. If the properties of the matrix varying along the paths, they would also be recorded. For each specific path, the breakthrough curve may then be calculated by numerical inversion. Finally, the addition of the breakthrough curves for a large number of particles yields the breakthrough curve for the solute in the network.

Hydrodynamic dispersion in individual channels is considered to be negligible. Dispersion arises instead as a result of the varying transit times for particles taking alternative routes through the channel network.

For the case of a limited matrix, an analytical solution exists. Therefore, we present first the implementation for a limited matrix using the solution given by Sudicky and Frind (1982). Later, the solution by using the numerical inversion of Laplace transforms is show.

Implementation of particle tracking for the case of limited diffusion depth

The solution given by Sudicky and Frind (1982) for solute transport in parallel fractures in the absence of dispersion is used. The output concentration for a channel network for the case of a limited pore connectivity is a function of two parameters, ω and σ, in addition to the residence time in the channel, t_T.

$$\omega = \frac{MPG \cdot FWS}{Q} \tag{68}$$

$$\sigma = \left(\frac{K_d \cdot \rho_p}{D_e}\right)^{0.5} \cdot B \tag{69}$$

For a Dirac pulse the Laplace transform of the effluent concentration for the channel i is (Sudicky and Frind, 1982)

$$\tilde{c}_i = Exp\left[-\left(t_T\right)_i \cdot s - \omega_i \cdot s^{1/2} \cdot Tanh\left(\sigma_i \cdot s^{1/2}\right)\right] \tag{70}$$

Applying the convolution integral theorem for a path formed by n channels in series, with different ω:s, σ:s, and channel residence times, the solution in the Laplace space for the entire path $\tilde{c}_i$ is,

$$\tilde{c}_{path} = \text{Exp}... \left[-\sum_{i=1}^{n} (R_a t_w)_i \cdot s - s^{1/2} \cdot \left\{ \omega_1 \text{Tanh}\left(\sigma_1 \cdot s^{1/2}\right) + \omega_2 \text{Tanh}\left(\sigma_2 \cdot s^{1/2}\right) + ... + \omega_n \text{Tanh}\left(\sigma_n \cdot s^{1/2}\right) \right\} \right] \quad (71)$$

From Equation 71, two cases may be distinguished depending, whether the parameter σ is constant along the paths or not. For the case where the values of σ are equal, ($\sigma_1 = \sigma_2 = ...\sigma_n = \sigma_0$ the Equation 71 has the same structure than Equation 70 replacing t_T and ω-parameters by its respective sums along each path. Then, the solution in the Laplace space may be written as

$$\tilde{c}_{path} = \text{Exp}\left[-\sum_{i=1}^{n} (t_T)_i \cdot s - s^{1/2} \cdot \text{Tanh}\left(\sigma_0 \cdot s^{1/2}\right) \cdot \sum_{i=1}^{n} \omega_i \right] \quad (72)$$

Therefore, the technique applied for unlimited pore connectivity is also applicable for limited pore connectivity if the parameter σ is the same in all the channels. This in practice means equal rock properties (diffusion and sorption) and equal maximum depth accessible by diffusion. A large number of particles are followed through the channel network. For each channel that the particle passes, the tracer residence time in the channel t_T and the ratio $(\text{MPG})_i \cdot A_{Qi} / Q_i$ are recorded. When the particle reaches the exit, these two parameters are summed. For each specific path, the breakthrough curve is then calculated using the solution by Sudicky and Frind (1982) with the parameters T^o and ω for the path defined as:

$$T^o_{path} = t - \sum_i (t_T)_i \quad (73)$$

$$\omega_{path} = \sum_i \left(\frac{(\text{MPG})_i \cdot A_{Qi}}{Q_i} \right) \quad (74)$$

Finally, the addition of the breakthrough curves for a large number of particles yields the breakthrough curve for the solute in the network.

If the case where the σ-parameter is not constant along the paths, there is no analytical solution available. An alternative is the numerical inversion of the solution from the Laplace-domain to the time-domain.

Implementation of particle tracking for the case of a matrix with more complex properties

In reality, the matrix may have a more complex structure. Several types of materials may be distinguished in the matrix close to the fracture (e.g., fracture coating, fault gouge, cataclasite, altered zone, intact rock)

For these cases, with complex matrices, analytical solutions are not available. Therefore, an alternative is the numerical inversion of the solution in the Laplace-domain to the time-domain. The solution for a matrix formed by three layers (skins) in addition to the matrix proper is shown in Appendix A2. The cases for two or one skins are directly obtained from the solution for three skins as special cases.

For a matrix with a complex structure (several layers), the procedure shown above can be applied. The solution in the Laplace-space for a channel with a matrix formed by several layers and the matrix proper may be written as

$$\overline{C}_f = \frac{C_0}{s}\,\mathrm{Exp}\left(-t_T s\right)\mathrm{Exp}\left(-\left(\mathrm{MPG}\right)_{s1}\left(\frac{\mathrm{FWS}}{Q}\right)\sqrt{s}\left(1-2R\right)\right) \tag{75}$$

R is a complex function of the matrix geometry and material properties. The solution for a path may then be obtained using the convolution integral. If the complexity of the matrix is the same in the entire path, the value of R is constant, and Equation 75 may written as

$$\overline{C}_{Path} = \frac{C_0}{s}\,\mathrm{Exp}\left(-s\cdot\sum t_T\right)\mathrm{Exp}\left(-\sqrt{s}\left(1-2R\right)\cdot\sum\left(\left(\mathrm{MPG}\right)_{s1}\frac{\mathrm{FWS}}{Q}\right)\right) \tag{76}$$

Therefore for each particle, we have to add the water residence time and the term $\left(\mathrm{MPG}\right)_{s1}\frac{\mathrm{FWS}}{Q}$ for each channel that the particle has passed.

If the properties of the network are spatially variable, the concentration (Laplace-space) is given by

$$\overline{C}_{Path} = \frac{C_0}{s}\,\mathrm{Exp}\left(-s\cdot\sum t_T\right)\mathrm{Exp}\left(-\sum\sqrt{s}\left(1-2R\right)\cdot\left(\mathrm{MPG}\right)_{s1}\left(\frac{\mathrm{FWS}}{Q}\right)\right) \tag{77}$$

Parameters needed in the calculations

Regarding the input data, in addition to the hydraulic parameters (water flowrate and flow porosity), we need the sorption constant for sorption on the fracture surface, the specific flow wetted surface, and the geometry of the matrix (skin thickness) with their respective MPG:s. The input transport parameters that are used in each situation are summarised in Table 89. The parameters to be used in the calculations are shown in Table 90.

Table 89. Input transport parameters.

Case	Fracture	Skin parameters	Matrix parameters
Infinite matrix	K_a, FWS		$(MPG)_m$
Finite matrix	K_a, FWS	σ_s	$(MPG)_s$
One-skin matrix and an infinite matrix	K_a, FWS	σ_s	$(MPG)_m$, $(MPG)_s$
Two-skin-matrix and an infinite matrix	K_a, FWS	σ_{s1} σ_{s2}	$(MPG)_m$, $(MPG)_{s2}$, $(MPG)_{s1}$
Three-skin matrix and an infinite matrix	K_a, FWS	σ_{s1} σ_{s2} σ_{s3}	$(MPG)_m$, $(MPG)_{s3}$, $(MPG)_{s2}$ $(MPG)_{s1}$

Table 90. Transport parameters used in the calculations.

Case	Fracture	Skin parameters	Matrix ratio
Infinite matrix	t_W, K_a		ω
Finite matrix	t_W, K_a	σ_s	ω
One-skin matrix and an infinite matrix	t_W, K_a	σ_s	ω, RMS
Two-skin-matrix and an infinite matrix	t_W, K_a	σ_{s1} σ_{s2}	ω, RMS2, RS2S1
Three-skin matrix and an infinite matrix	t_W, K_a	σ_{s1} σ_{s2} σ_{s3}	ω, RMS3, RS3S2, RS2S1

Where

$$\omega_s = \frac{(MPG)_s \cdot FWS}{Q} \tag{78}$$

$$\sigma = \left(\frac{K_d \cdot \rho_p}{D_e} \right)^{0.5} \cdot B \tag{79}$$

RXXYY is the ratio between the MPG:s for the material "xx" and that for the material "yy". M is for the matrix and S for the skins.

If the geometry of the skins and the MPG for the skins and matrix proper are invariable in the network, we have only to record the sum of t_T and ω. Actually, we need only the water residence time and the sum of 1/Q.

7.3 Calculated cases

Calculations were made for the two features (1S and 4S) and for the three hydraulic head differences (Case A, B, and C). Two sub-cases were calculated for the Case C. In the first one, equilibrium was assumed between the solute in the channel and the solute sorbed on the coating, gouge, and cataclasite. In the second one, the altered zone in also set in equilibrium with the solute in the channel. The calculated cases and their properties are shown in Table 70 for Feature 1S and Table 71 for Feature 4S.

The calculations were performed with the CHAN3D code. The version considering diffusion into an infinite matrix was used on this occasion. The limitations found in this version were the motivation to develop a version that could handle diffusion into a matrix formed by several layers (materials)

Table 91. Calculated cases for the Feature 1S.

Case	Hydraulic head difference, m	Solute in the channel in equilibrium with:	Matrix with properties as
Case-A1	0.584	Coating and gouge	Cataclasite
Case-B1	0.0584	Coating, gouge, and cataclasite	Altered zone
Case-C1a	0.00584	Coating, gouge, and cataclasite	Altered zone
Case-C1b	0.00584	Coating, gouge, cataclasite, and altered zone	Intact wall rock

Table 92. Calculated cases for the Feature 4S.

Case	Hydraulic head difference, m	Solute in the channel in equilibrium with:	Matrix with properties as
Case-A2	0.539	Coating	Altered zone
Case-B2	0.0539	Coating	Altered zone
Case-C2a	0.00539	Coating	Altered zone
Case-C2b	0.00539	Coating and altered zone	Intact wall rock

As discussed above, even for the highest water flowrate, it is expected that the coating material and the gouge material reach equilibrium with the radionuclide in the fracture water. This time is significantly shorter than the residence time in the fracture. However, due to limitations in the present version of CHAN3D (rock matrix is composed only of one geological material) it is assumed that some materials in the fracture wall (e.g., cataclasite) may also reach the equilibrium with the radionuclides dissolved in the fracture water. The consequences of these assumptions on the residence time will be discussed and checked later.

For the Case-A1 (shortest residence time or highest water flowrate), it is assumed that the coating material and the gouge material have sufficient time to reach the equilibrium. For the Case-B1, it is assumed that even cataclasite reaches equilibrium with the solute in the channel. The Case-C1a is similar to the Case-B1, although, due to the long residence time, it is expected that an important part of the diffusion takes place in the intact rock in addition to the altered zone. For this reason a new case is defined, the Case-C1b, in which the solute is also equilibrated with the altered zone and diffusion takes place into an infinite matrix with properties of intact rock. A similar approach is followed when the cases for the Feature 4S are defined.

7.4 Results

7.4.1 Comparison with a model handling a matrix composed of several layers

Comparisons for the Feature 1S

The results for the Case-A1 are shown in Table 93 and Figure 98. For an infinite matrix with properties similar to those of cataclasite, the residence time is slightly longer than when all layers forming the matrix are considered. This is due to that part of the diffusion takes place in the altered zone, which has an effective diffusivity less than that for cataclasite as discussed above (See Table 72). Small differences are observed in the cumulative release curves in both cases.

Table 93. Residence times for the Case-A1.

Case-A1	Iodide	Caesium	Americium
Residence time, infinite matrix, years (Time-1)	0.357	857	7 480
Residence time, two skin layers and infinite matrix, years, (Time-2)	0.327	795	7 500
Ratio Time-1/Time-2	1.09	1.08	1.00

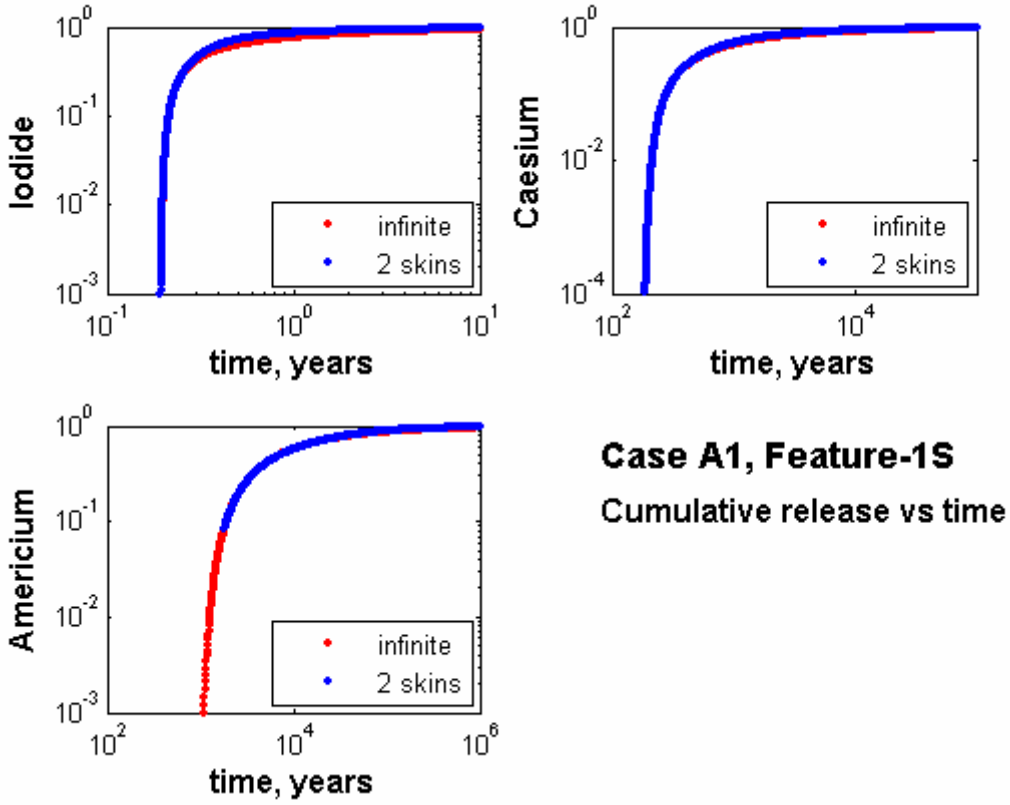

Figure 98. *Breakthrough curves for Case-A1 for an infinite matrix and for a matrix formed for two skin layers and a semi-infinite matrix.*

The results for the Case-B1 are shown in Table 94 and Figure 99. For diffusion into an infinite matrix with properties similar to those of the altered zone, the residence time is somewhat longer than when all the layers forming the matrix are considered. This is due to that part of the diffusion takes place in the intact rock, which has an effective diffusivity smaller than that of the altered zone. The cumulative release curves obtained using two skin layers and a semi-infinite matrix, show an earlier arrival of the solute. This is due to that no equilibrium is reached between the solute in the fracture water and that sorbed on the cataclasite, as assumed in the Case-B1.

Table 94. Residence times for the Case B1.

Case B1	Iodide	Caesium	Americium
Residence time, infinite matrix, years (Time-1)	7.75	4.84E+04	4.92E+05
Residence time, two skin layers and infinite matrix, years, (Time-2)	7.47	4.52E+04	4.23E+05
Ratio Time-1/Time-2	1.04	1.07	1.16

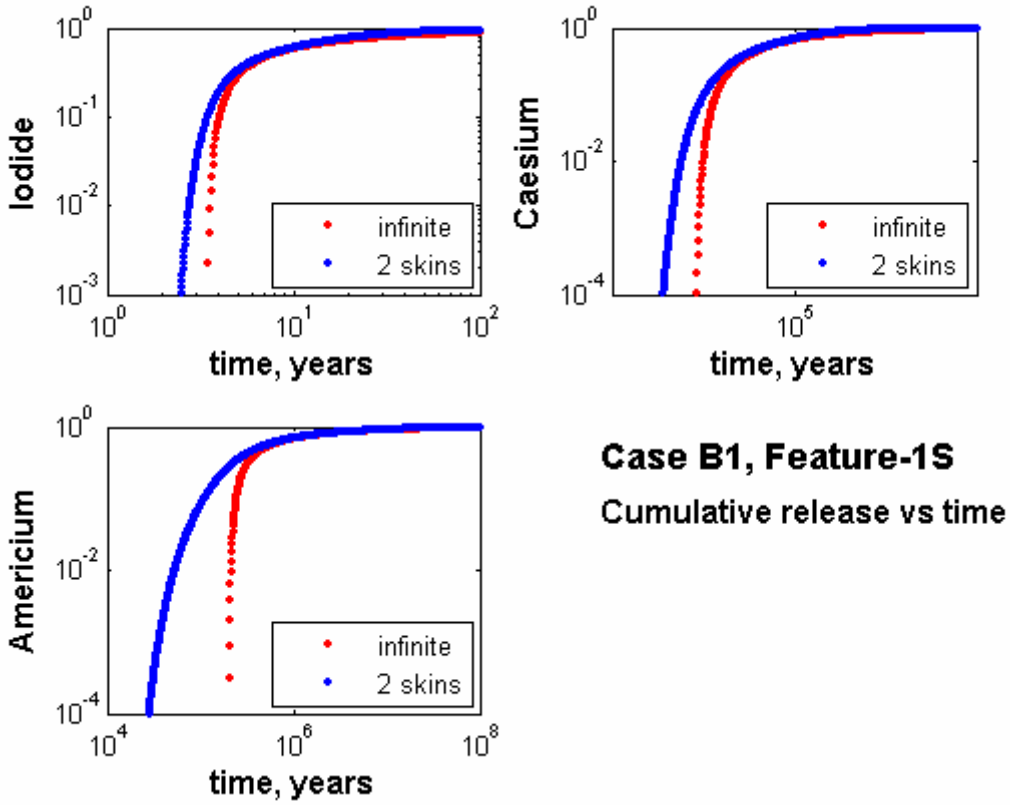

Figure 99. *Breakthrough curves for Case-B1 for an infinite matrix and for a matrix formed for two skin layers and a semi-infinite matrix.*

The results for the Case-C1a are shown in Table 95 and Figure 100. For diffusion into a semi-infinite matrix with properties similar to those of the altered zone, the residence times are longer than when all the layers forming the matrix are considered. This is due to that part of the diffusion takes place in the intact rock, which has an effective diffusivity lower than that of the altered zone. Large differences are observed in the recovery curves, particularly for iodide and caesium. The recovery times are longer when diffusion into a semi-infinite matrix is considered.

Table 95. Residence times for the Case-C1a.

Case-C1a	Iodide	Caesium	Americium
Residence time, infinite matrix, years (Time-1)	486	4.23E+06	3.20E+07
Residence time, two skin layers and infinite matrix, years, (Time-2)	200	1.51E+06	2.63E+07
Ratio Time-1/Time-2	2.43	2.80	1.22

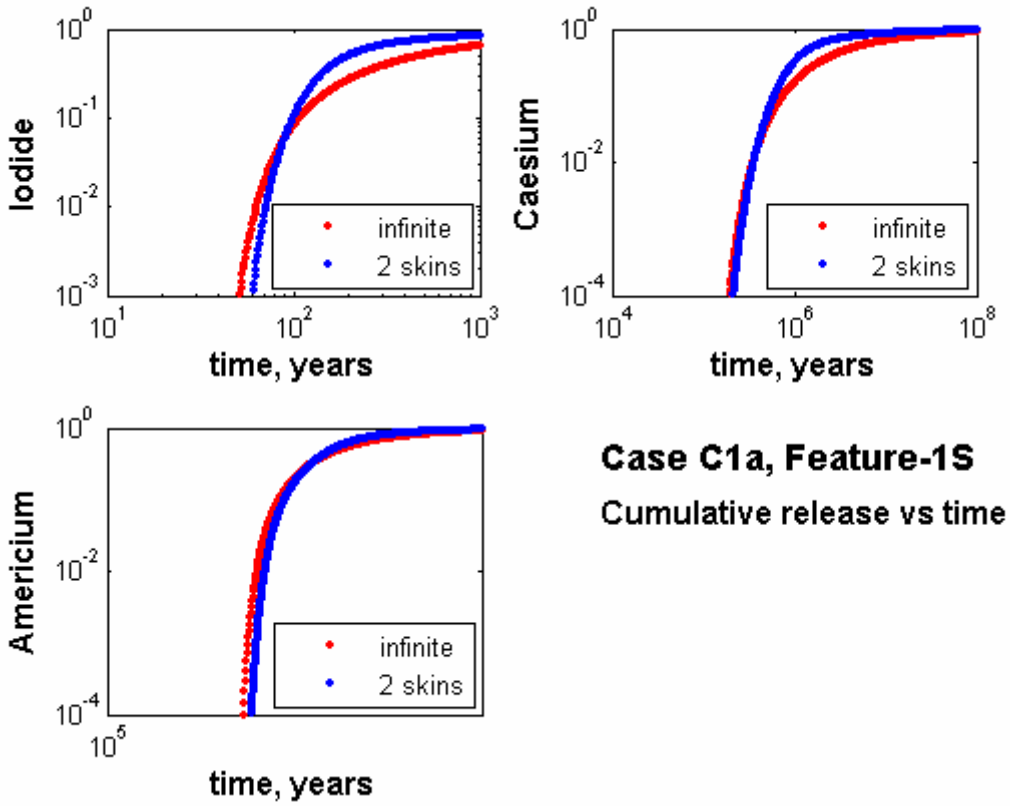

Figure 100. *Breakthrough curves for Case-C1a for an infinite matrix and for a matrix formed for two skin layers and a semi-infinite matrix.*

The results for the Case-C1b are shown in Table 96 and Figure101. In this case the altered zone is also equilibrated with the solute. When the times for recovery of the 50% of the tracer are compared, small differences are found. However, an early arrival of the tracer is observed when diffusion into a complex matrix (two skins and semi-infinite matrix) is considered. This may be due to that equilibrium with the altered zone is not reached initially.

Table 96. Residence times for the Case C1b.

Case-C1b	Iodide	Caesium	Americium
Residence time, infinite matrix, years (Time-1)	195	1.52E+06	3.11E+07
Residence time, two skin layers and infinite matrix, years, (Time-2)	200	1.51E+06	2.63E+07
Ratio Time-1/Time-2	0.975	1.009	1.183

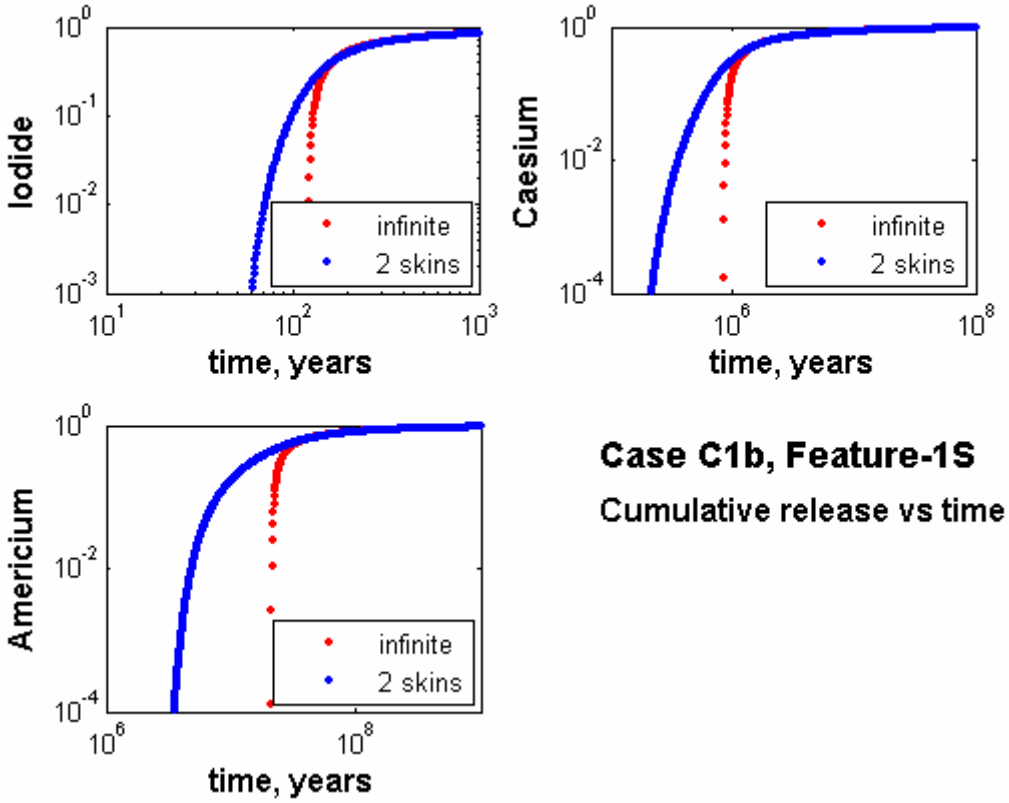

Figure 101. *Breakthrough curves for Case-C1b for an infinite matrix and for a matrix formed for two skin layers and a semi-infinite matrix.*

As may be observed from the results for the Cases C1a and C1b, the recovery/breakthrough times are dependent on the assumptions used. In order to avoid this, the calculations should be done by using a program that may handle diffusion into a matrix formed by several geological materials.

Comparisons for Feature 4S

The results for the Case A2 are shown in Table 97 and Figure 102. In both cases the residence times and the breakthrough curves are similar. The good agreement between the two approach indicates that the coating material reaches equilibrium with the solute in the water in the fracture and that diffusion occurs mainly in the altered zone.

Table 97. Residence times for the Case- A2.

Case-A2	Iodide	Caesium	Americium
Residence time, infinite matrix, years (Time-1)	0.277	1.42E+03	1.04E+04
Residence time, two skin layers and infinite matrix, years, (Time-2)	0.277	1.42E+03	1.04E+04
Ratio Time-1/Time-2	1.00	1.00	1.00

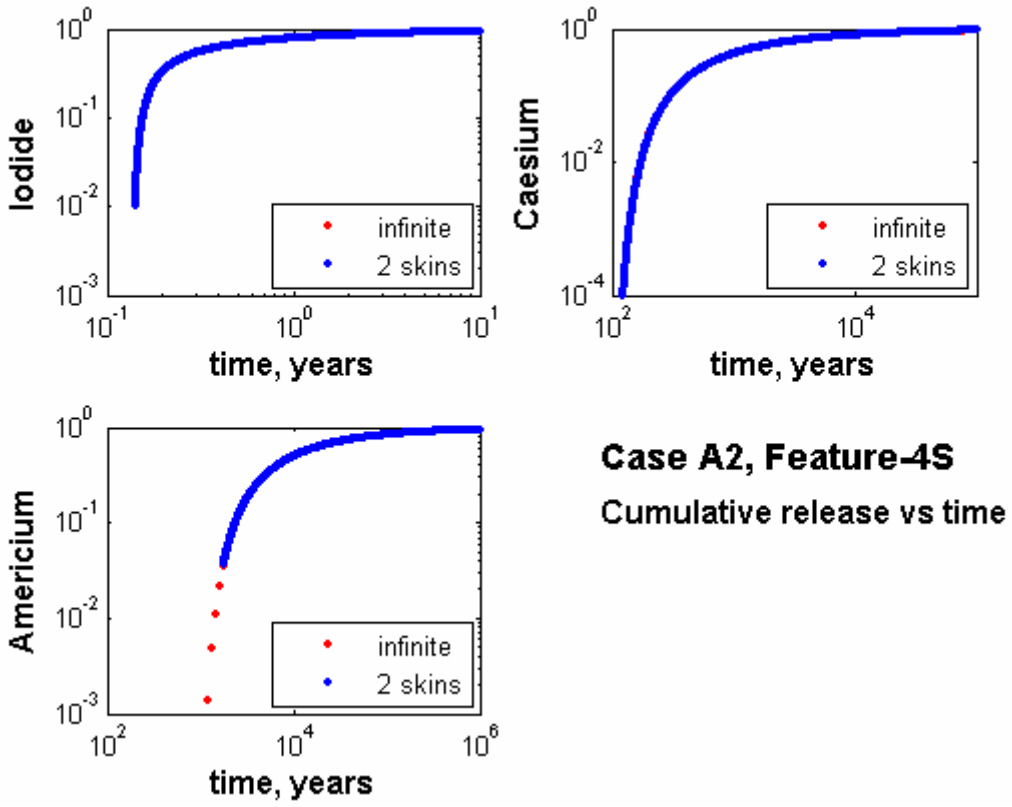

Figure 102. *Breakthrough curves for case A2 for an infinite matrix and for a matrix formed for one skin layer and a semi-infinite matrix.*

The results for the Case-B2 are shown in Table 98 and Figure 103. Small differences are found in the mean residence times. The mean residences times obtained when diffusion into an infinite matrix is considered are somewhat longer. Small differences are observed in the recovery curves.

Table 98. Residence times for the Case-B2.

Case-B2	Iodide	Caesium	Americium
Residence time, infinite matrix, years (Time-1)	15.8	1.34E+05	9.70E+05
Residence time, two skin layers and infinite matrix, years, (Time-2)	14.0	1.16E+05	9.67E+05
Ratio Time-1/Time-2	1.13	1.15	1.00

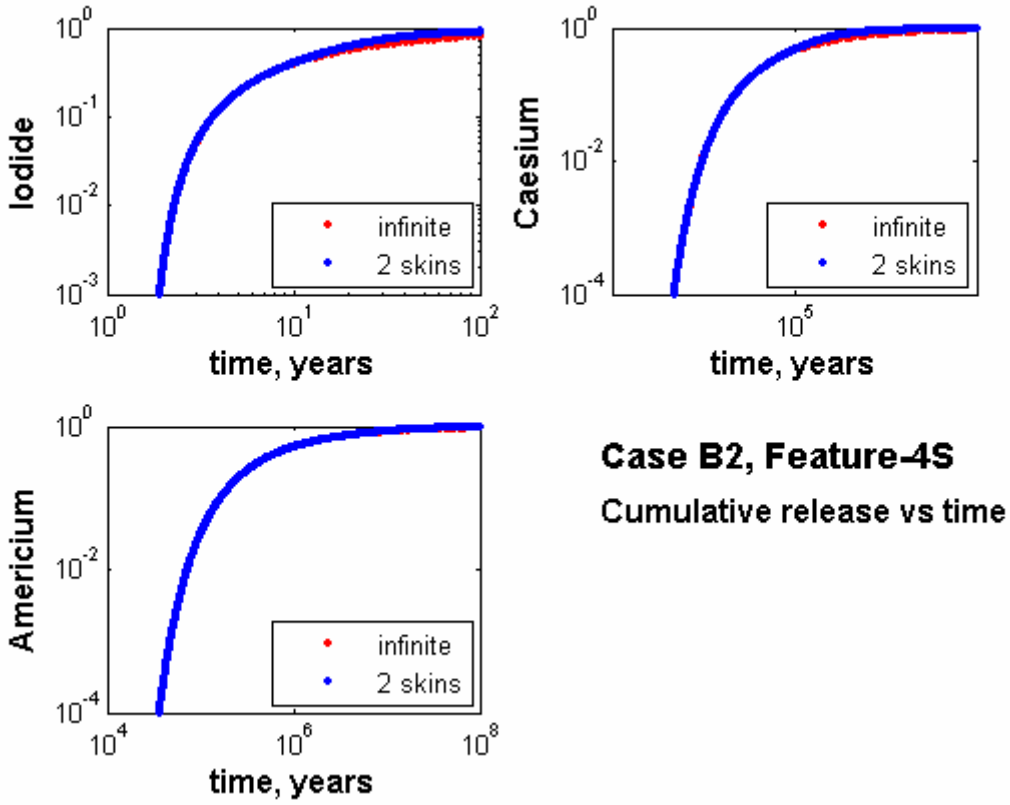

Figure 103. *Breakthrough curves for Case-B2 for an infinite matrix and for a matrix formed for one skin layer and a semi-infinite matrix.*

The results for the Case C2a are shown in Table 99 and Figure 104. For diffusion into a matrix composed of only one geological material with properties similar to those of the altered zone, the residence time is much longer than when all the layers forming the matrix are considered in the model. This is due to that an important part of the diffusion takes place in the intact rock, which has an effective diffusivity lower than that of the altered zone.

Table 99. Residence times for theCcase-C2a.

Case-C2a	Iodide	Caesium	Americium
Residence time, infinite matrix, years (Time-1)	1.46E+03	1.33E+07	9.61E+07
Residence time, two skin layers and infinite matrix, years, (Time-2)	3.94E+02	3.43E+06	5.72E+07
Ratio Time-1/Time-2	3.71	3.88	1.68

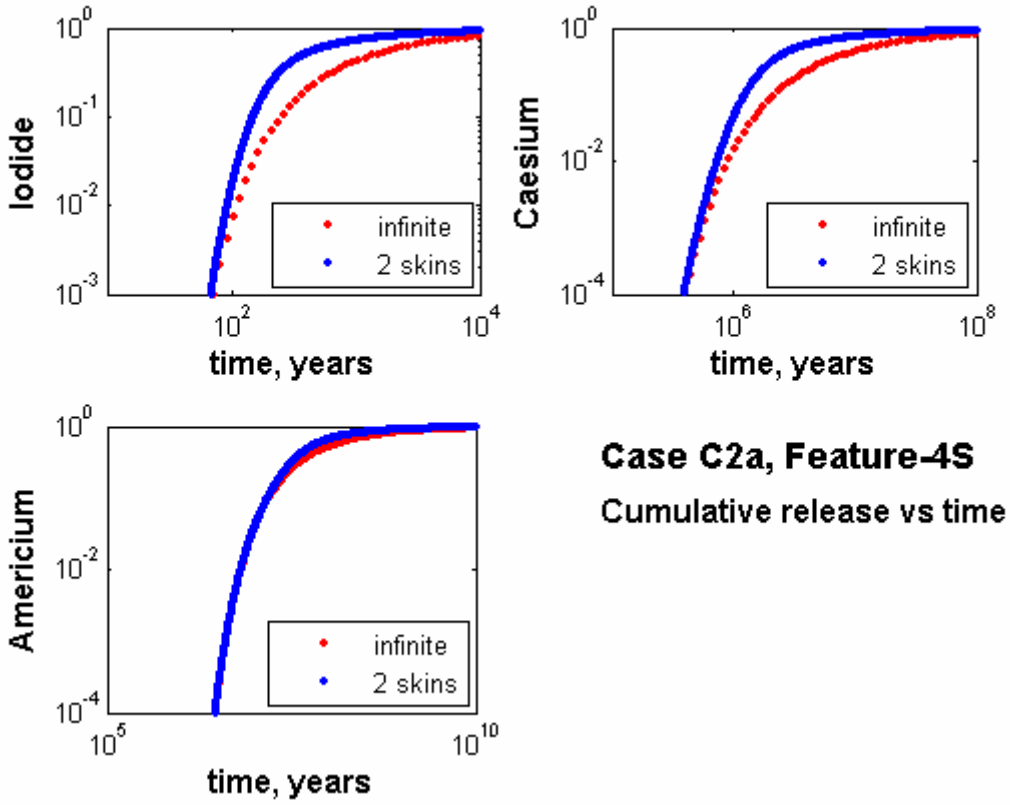

Figure 104. *Breakthrough curves for Case-C2a for an infinite matrix and for a matrix formed for one skin layer and a semi-infinite matrix.*

The results for the Case-C2b are shown in Table 100 and Figure 105. For Caesium and Americium the residences times are significantly shorter when diffusion is modelled as occurring into a matrix formed by only a geological material. This is due to that diffusion in the altered zone is not considered, since equilibrium is assumed.

Table 100. Residence times for the Case-C2b.

Case-C2b	Iodide	Caesium	Americium
Residence time, infinite matrix, years (Time-1)	412	2.27E+06	3.27E+07
Residence time, two skin layers and infinite matrix, years, (Time-2)	394	3.43E+06	5.72E+07
Ratio Time-1/Time-2	1.05	0.66	0.57

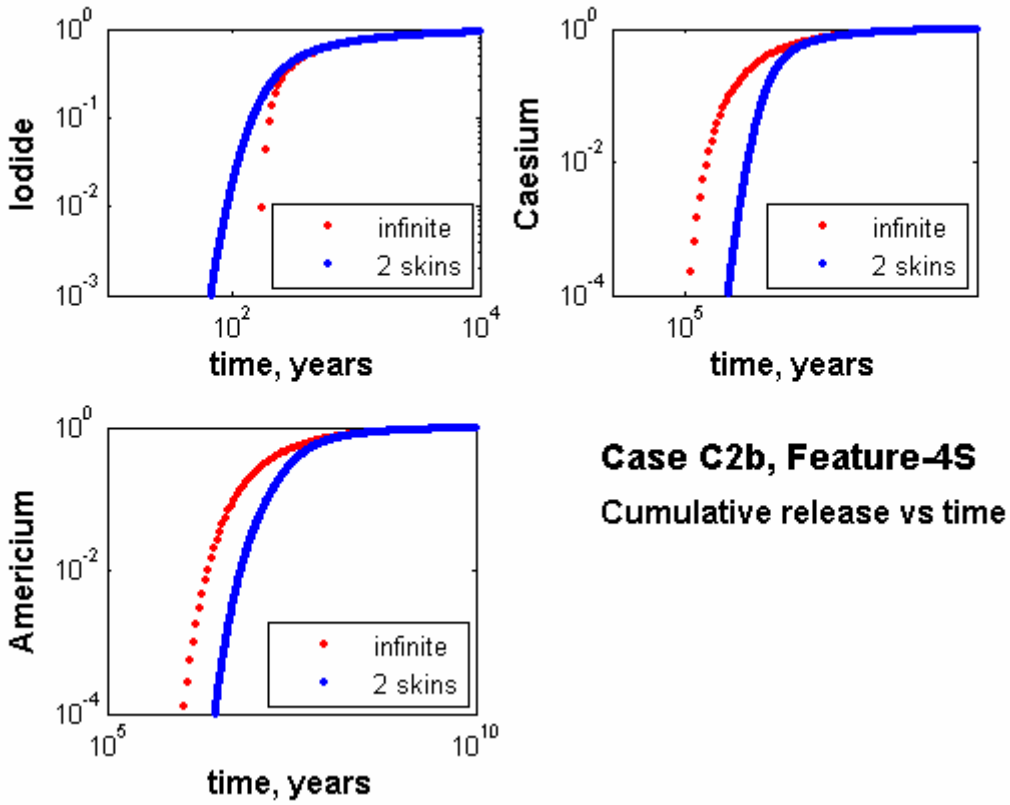

Figure 105. *Breakthrough curves for Case-C2b for an infinite matrix and for a matrix formed for one skin layer and a semi-infinite matrix.*

7.4.2 Factors determining the residence time

As discussed above, the residence time has three components

1. The residence time due to the volume of the channel. This is calculated as the ratio between the volume of the channel and the water flow rate in the channel.
2. The residence time due to equilibrium/instantaneous sorption with the fracture surface and others materials present in the fracture. Material close to the fracture could also be included in the "instantaneous" sorption if the contact times are sufficiently long (i.e., cataclasite for long contact times).
3. The residence time due to diffusion and sorption in the matrix

The fraction of these three components of the residence time will be determined for three radionuclides (Iodide, Caesium, and Americium) under two different hydraulic situations. One is the Case A1, which could be considered as a typical situation for Site Characterisation (SC) and the other is the Case C1, which may be considered as a typical situation for Performance Assessment (PA).

Figure 106 shows the distribution of the residence time in the three components indicated above for the Case A2 (equilibrium sorption with coating and gouge material and diffusion in a matrix with material properties as cataclasite). Notation "water" indicates the residence time determined by the volume of the channel and the water flow rate. The results show that the residence time arising due to the channel volume is only significant for Iodide. For Caesium and Americium the effect of the volume of the channel on the residence time is negligible. The component of the residence time due to equilibrium sorption is about 10-20 %.

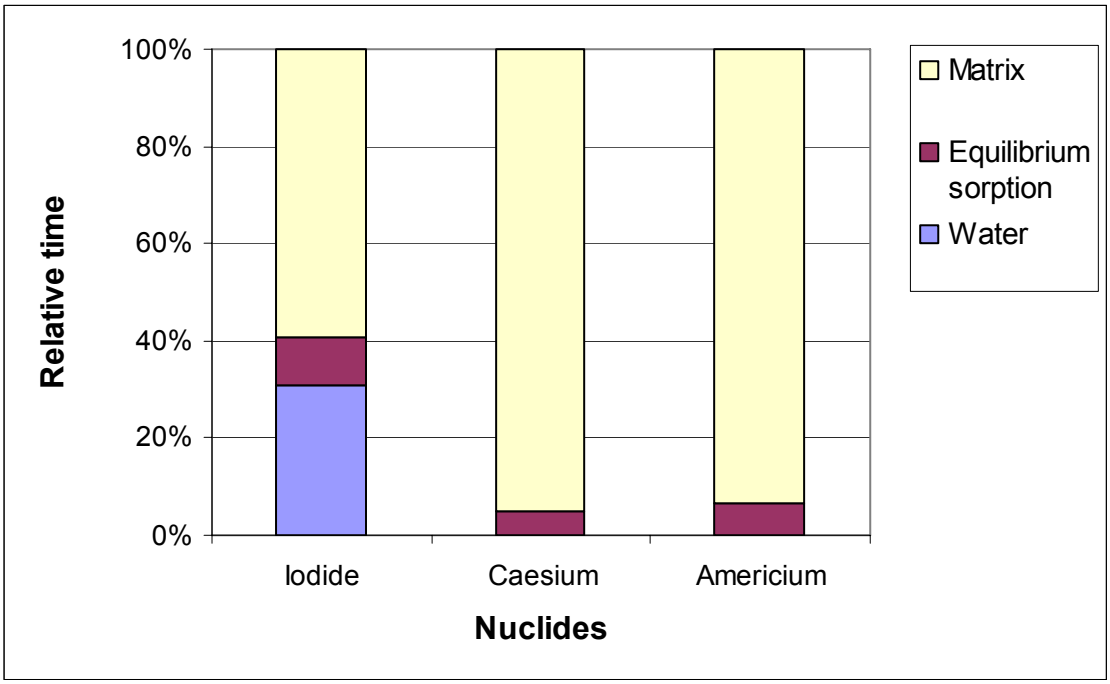

Figure 106. *Relative residence time for the Case A1.*

Figure 107 shows the distribution of the residence time in the three components for the Case C2 (equilibrium sorption with coating, gouge material, and cataclasite and diffusion in a matrix with material properties as altered rock). The results show that the residence time caused by the channel volume is negligible for all radionuclides. The component of the residence time due to equilibrium sorption is only a few percent.

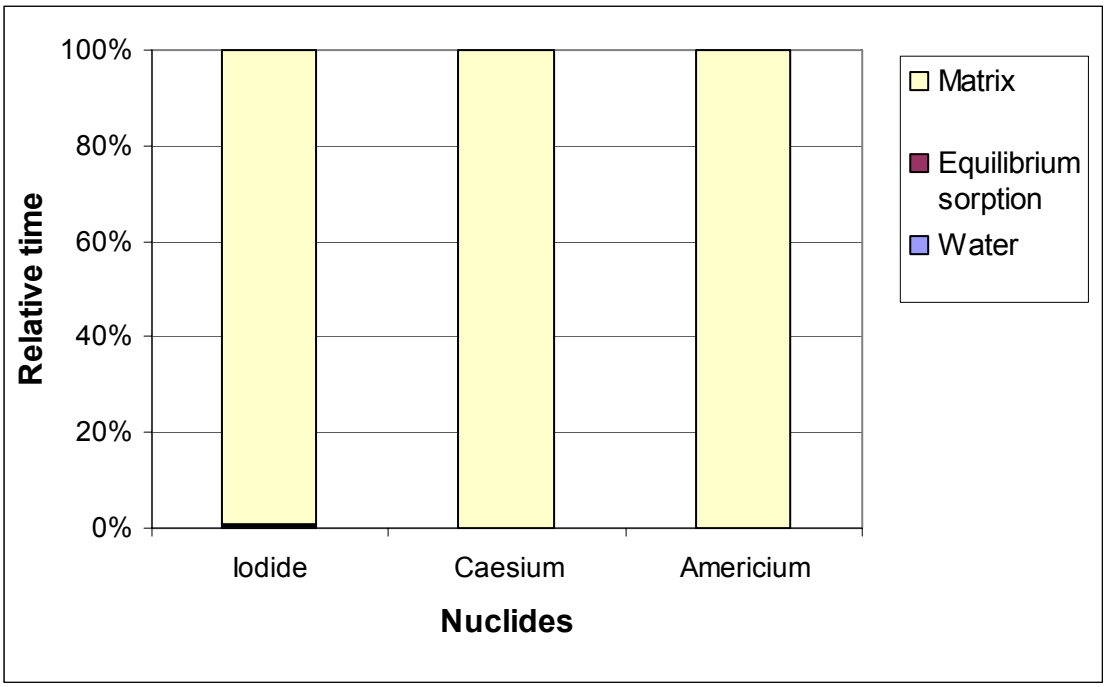

Figure 107. *Relative residence times for the Case C1.*

From these simple calculations, it is found that the volume of the channel is important only for non-sorbing species and under SC (Site Characterisation) conditions. For PA (Performance Assessment) conditions, even for non sorbing species, the volume of the channel has a negligible influence on the residence time of the radionuclides. We conclude that radionuclide transport in SC and PA conditions is controlled by different mechanisms.

Typical tracer tests using non-sorbing tracers have residence times less than 0.1 year. For this reason some runs were done using a hydraulic head difference to obtain water residence time about 0.01 year (three days). In some cases, tracer tests have residence time even less than this. The results of the runs with a water residence time of 0.01 year are shown in Figure 108.

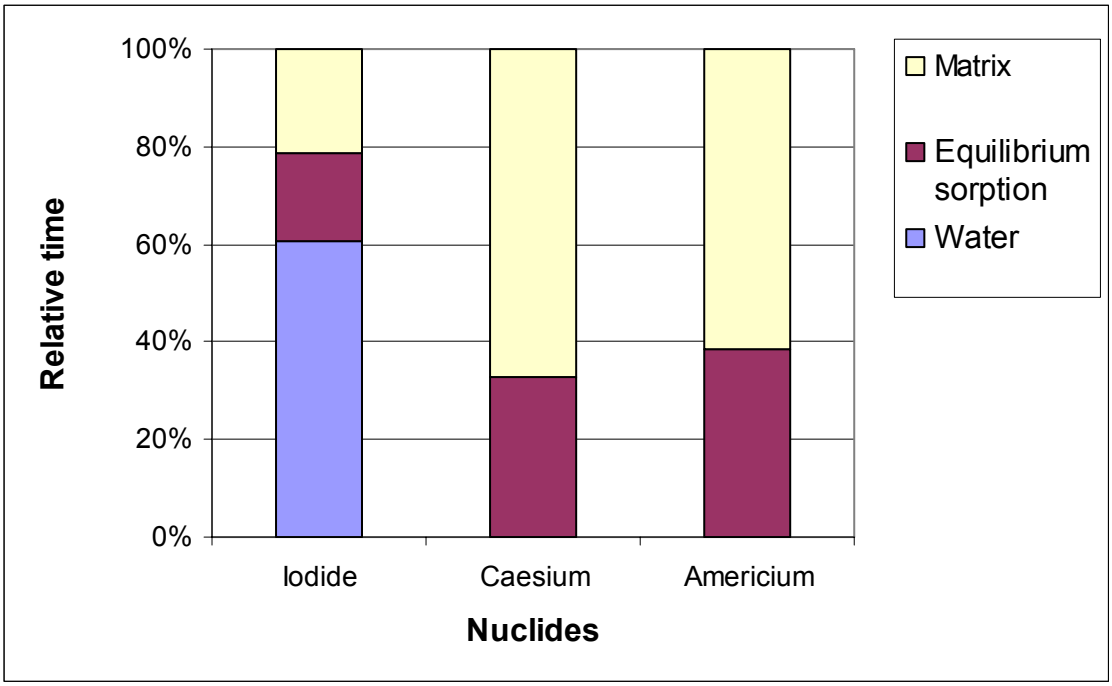

Figure 108. *Relative residence times for tracer tests with a water residence time of 0.01 year.*

One of the main objectives of tracer tests with non-sorbing species and relatively short residence times (on the order of days) is to determine the flow porosity. However, flow porosity, as shown in these results, has no influence on the travel time of radionuclides under PA conditions.

The transport time for a radionuclide from the repository to the biosphere under repository conditions is determined completely by the ratio FWS/Q and the MPG (Material Property Group). The MPG comprises the effective diffusivity, the volume sorption coefficient and the density of the rock matrix.

8 Discussion and conclusions

8.1 Discussion of results

The results from the calibration simulations where flow porosity was adjusted to match the characteristics of the experimental breakthrough data indicate that there is more dispersion along the actual flow paths for tracer transport (i.e., in the field) than can be accounted for in the present model.

Roughly 80% of the injected ^{186}Re (a proxy for ^{131}I) tracer was recovered in tracer test C2. The flow-porosity of the system was estimated by matching the simulated recovery time for 50% of the injected tracer (i.e., t_{50}) with the measured time for recovery of 50% of the recovered tracer. Although the peaks of the experimental and simulated activity-time curves roughly correspond, there is much faster early breakthrough for the tracer in the measurement data than is predicted in the simulations. This indicates a strong channelling effect that has not been captured well using the channel network analogue of the DFN model described in Task 6C.

The tracer recovery data supplied to the modelling groups consisted of "decay-corrected" activity-time curves for the radiotracers. As previously speculated in section 4.2, we believe the tracer cut-off at 500 hours for ^{186}Re relates to the limit of detection of the γ-spectrometric analysis combined with the short half-life of the tracer (90 h) rather than a true cut off for tracer recovery. It would therefore seem that ^{186}Re is a less than ideal choice of tracer for recovery times extending beyond about 500 hours. The ^{47}Ca radiotracer also has a relatively short half-life (108 h) and it is likely that the poor recovery of 29% for this tracer relates as well to the fact that the late arriving tracer has had sufficient time to decay to levels below the limit of detection.

We hypothesize that the broadening of the measured ^{186}Re breakthrough peak in comparison to the relatively narrow breakthrough peak of the simulation is due to a combination of fast channelling with little matrix interaction for the early tracer breakthrough, combined with slower transport flowpaths accompanied by somewhat greater matrix retention for late tracer arrival.

The particle tracking visualizations indicate that there are two principal tracer flowpaths in the simulation model; these have been referred to as the upper and lower flowpaths, respectively. In the stochastic realisations of the channel network representation of the fracture system, there is an average tracer flowpath partitioning of 46/54 between the upper and lower flowpaths. It should be noted that these two flowpaths may not correspond to the physical reality of the TRUE Block Scale rock volume as their existence is contingent upon the existence of DFN structures hypothesized in the Task 6C semi-synthetic hydrostructural model. The DFN features implicated in the modelled tracer transport were identified as 20D, 21D, 22D, 23D, as well as a number of minor, B and C-type background fractures. The stochastically generated background fracture 1925B was found to be particularly important for tracer transport along the upper tracer flowpath.

The simulated mean drawdown was found to be -66 m at the injection node and -343 m at the recovery node. Owing to the high pumping flowrate and the channel network connectivity, however, there is a large change in drawdown over a short distance. The mean drawdown in the 26 nodes lying 1-2 m distant from the recovery borehole is roughly -173 m.

The non-sorbing and poorly sorbing tracer breakthrough curves approximately match the experimental data, although this is purely an artefact of the calibration procedure as matrix diffusion effects are largely absent from these data sets. There is not sufficient data available from the ^{137}Cs data set to draw any specific conclusions, as there are only a few experimental data points available. The first appearance of the tracer at 4000 h, however, is broadly consistent with the first simulated breakthrough and is significantly delayed relative to the first breakthrough of the non-sorbing and poorly sorbing tracers.

8.2 Main conclusions

The simulation results demonstrate that the CHAN3D program can be used to simulate flow and solute transport in a channel network analogue of the discrete fracture network detailed in the Task 6C semi-synthetic hydrostructural model. It has also been shown that a 75 m×75 m×75 m subspace of the 200 m TRUE Block Scale volume is sufficient to model the tracer test C2. We note, however, that the larger 200 m scale model is required initially in order to establish the head boundary conditions for the smaller simulation volume.

The simulated breakthrough data based upon the full Task 6C discrete fracture network (DFN) is relatively consistent from run to run owing to the fact that the fractures are in fixed locations and all other background channels have, for all practical purposes, zero conductance. The only variation arises from channelling effects within the plane of fractures 20D, 21D, 22D, 23D, as well as background fracture 1925B. The channelling effect arises due to the assumed distribution of conductances for channels located within the zone of influence of these fractures. As there was no additional data in the Task 6D data distribution relating to in-fracture channelling, we have assumed a log normal distribution of channel conductances with a standard deviation of $\sigma_c = 1$.

The authors of this report question the usefulness of using the full model containing 5648 fracture features to simulate the tracer test C2, owing to the fact that the bulk of these features are "synthetic" in nature and represent only one stochastic realisation of a DFN. Similar results can be obtained from a model where only the primary "deterministic" features are explicitly considered and where flow and solute transport are allowed to take place in a sparsely distributed set of conductive background channels.

Aside from the apparently broad peak of the experimental breakthrough of ^{186}Re that is suggestive of strong channelling, there is very little constraining power in the experimental data for the tracer tests. Considering the short timescale of the tracer experiment C2, the impact of matrix porosity is also very small and largely dominated by the sorption properties of the fracture coating for the moderately- and strongly-sorbing tracers. For the purposes of Task 6D it may have been more appropriate to stipulate a mean water residence time (t_{w50}) to the modelling groups instead of providing experimental injection and recovery data for tracer test C2, given that one of the primary goals of Task 6D was to provide a common test bed for comparing the different approaches used by the various modelling groups.

Comparison of the CHAN3D simulation results with a well-known stream-tube model that considers hydrodynamic dispersion and matrix interaction effects (Tang, 1981) indicates the importance of allowing for the distribution of the flow-wetted surface to flow ratio (i.e., FWS/Q or the so-called β-factor). In stream-tube modelling approaches the available flow-wetted surface is distributed evenly over the entire flow with dispersion accounted for by assuming a Gaussian mixing process. The multiple flowpaths and channelling effects that arise naturally in the Channel Network model, however, results in a broad distribution of the FWS/Q ratio that strongly influences the retardation of strongly-sorbing tracers. Although both streamtube models and the Channel Network model can be shown to roughly match experimental data in an SC framework, the streamtube approach gives rise to non-conservative results over timescales relevant for PA.

In Task F, it was found that the arrival and residence times depend on the assumptions made to describe equilibrium in the fracture and diffusion into the rock matrix. Different sets of materials may be chosen to be in equilibrium with the nuclides dissolved in the water in the fracture. For diffusion into the matrix, the properties of one of the materials forming the matrix have to be chosen to represent the infinite matrix.

In Task F2, it may be concluded that although the residence time is determined by the same mechanisms in SC and PA, the balance between particular processes that give rise to retardation is fundamentally different. The processes that are most active in SC (water residence time and equilibration with fracture skins and filling materials) have little or not at all influence on the travel time under PA conditions where different processes are likely to dominate (matrix diffusion). Another conclusion is that models that can only handle diffusion into a homogeneous and infinite matrix have a limited ability to model solute transport where consideration is given to the complexity of the matrix. When the solute transport is modelled assuming instantaneous equilibrium with the material in the fracture (coating, gouge, cataclasite) the resultant residence time may be not conservative.

8.3 Lessons learned and implications for Task 6 objectives

The Task 6D modelling work indicates that it is not necessary to explicitly consider the full set of 5648 fracture features to obtain similar breakthrough characteristics for the simulation of tracer test C2. Essentially identical results can be obtained by considering only the major “deterministic” features (the set of 11 D-type features in the data distribution) and assuming a sparse network of conductive background channels. The mean peak breakthrough time for non-sorbing tracer can be altered by adjusting the flow porosity of the system to obtain a rough match with the experimental breakthrough data.

The actual distribution of fractures and flowpaths in the TRUE Block Scale volume is largely unknowable apart from a few strongly conductive flowpaths that can be roughly inferred from borehole hydraulic tests and geophysics. Even in these special cases there is no way of knowing the actual water flowpaths and whether these features can be considered to be planar fractures, or perhaps a loosely defined set of conductive flow channels that roughly follow an inferred fracture plane.

For these reasons, the use of complex representations of fracture geometry such as that detailed in Task 6C may be disingenuous given that we have no way of really testing their applicability. The authors of this report suggest a more non-representational approach with focus upon understanding the statistics of flow-wetted surface proportioning and flow channelling. Different assumptions of flow geometry, for example, made during the construction of conceptual models of the fracture system may give rise to strongly biased SC models. Parameters derived from these SC models could potentially have far-reaching consequences when subsequently used in PA-modelling.

Although it is possible to produce visibly seductive images of tracer transport in sophisticated discrete fracture representations, it is far more important to accurately predict (in a statistical sense) the flow-wetted surface to flow ratio distribution to make predictions of sorbing tracer transport. The actual geometry of fractures and flowpaths is of only minor importance in this respect.

The short timescales inherent in most tracer tests frequently complicates the interpretation of breakthrough data. It is not always a trivial task, for example, to separate out the influence of imperfect tracer injection from channelling phenomena that give rise to the observed breakthrough characteristic for the non-sorbing tracers. For moderately and strongly sorbing tracers, on the other hand, there is frequently poor tracer recovery and most tracer experiments appear to have weak constraining power. In some cases, it appears that stronger than anticipated retardation coupled with short decay times relative to the transport time is responsible for this. Tracer dilution effects, variable hydraulic boundary conditions and hydraulic sinks leading away from the tracer recovery wells also can play a role.

The aim of Task 6 is to bridge the gap between SC and PA-type modelling approaches. A fundamental problem that we try to address is to what extent we can constrain parameters of importance for PA using data derived from SC-modelling?

From the work that has been carried out so far within Task 6, it appears that SC-modelling of tracer tests may not give sufficiently useful information about matrix properties that we can derive meaningful “in-situ” matrix interaction parameters. The time scales of most tracer tests are such that, with the exception of very late tracer arrival, “deep” matrix diffusion can be largely discounted as a significant retardation mechanism. This is of strong importance, however, for PA-timescales where radionuclides will have sufficient time to diffuse to greater depths in the rock matrix.

The penetration depth can be used as a measure of the extent of matrix diffusion. From equation 35 and 36, the penetration depth is seen to be proportional to the square root of the product of apparent diffusivity and the contact time. In an absolute reference frame (for a specified contact time) it is clear that a more strongly sorbing solute will have a shallower depth of penetration than a poorly or non-sorbing solute. For a solute being transported along a flowpath, however, we are most interested in the effective depth of penetration which gives rise to the observed retardation effect in the solute recovery curve. The appropriate contact time in this case would be the actual transport time of the solute (i.e., considering the different residence times of the recovery curve) which is different for solutes with differing sorptive properties.

If the travel time is assumed to be dominated by matrix diffusion effects under PA conditions (as we have found here), the travel time can be shown to be roughly proportional to the product of effective diffusivity and the storage capacity as shown in Equations 44 and 45. The storage capacity is the denominator in equation 35 and 36. If we consider the "effective" depth of penetration which gives rise to the observed solute retardation in the tracer test, the penetration depths for different solutes as estimated by equation 35 or 36 are the same and independent of the sorption properties of the solute. Simply put, a pulse of a more strongly-sorbing solute will have a longer transport time, as compared to a pulse for a less sorbing solute. This additional time will allow the more strongly-sorbing solute, although having lower apparent diffusivity, to penetrate the rock matrix to the same depth as the less sorbing solute.

As the geochemically altered fracture coating is probably only about half a millimetre thick or so, there is some uncertainty about the retardation properties of this part of the rock matrix. We assume the fracture coating (and other materials such as fault gouge) to be substantially weathered and microstructurally altered relative to the bulk of the rock matrix. To account for the contrast between the fracture coating material and the bulk rock matrix, a surface sorption parameter (K_a) is frequently used in transport modelling to replicate the apparent retardation of sorbing species. The estimation of K_a is subject to a large number of assumptions and simplifications and more attention needs to be paid to the influence that uncertainty in this variable has upon other parameters derived from SC modelling. This is particularly the case if breakthrough data is to be used to constrain parameters such as the flow-wetted surface to flow ratio (FWS/Q).

9 References

Andersson, P., Byegård, J., Holmqvist, M., Skålberg, M., Wass, E., and Widestrand, H. (2001) *TRUE Block Scale Tracer Test Stage. Tracer Test, Phase C*, Swedish Nuclear Fuel and Waste Management Company (SKB). Äspö Hard Rock Laboratory. International Progress Report, IPR-01-33.

Andersson, P., Byegård, J., Doe, T., Hermanson, J., Meier, P., Tullborg, E. L. and Winberg, A. (2002a) *TRUE Block Scale Project Final Report – 1. Characterisation and Model Development*, Swedish Nuclear Waste Management Company (SKB), Technical Report TR-02-13.

Andersson, P., Byegård, J., and Winberg, A. (2002b) *TRUE Block Scale Project Final Report – 2. Tracer Tests in the Block Scale*, Swedish Nuclear Fuel and Waste Management Company (SKB), Technical Report TR-02-14.

Benabderrahmane, H., Dershowitz, W., Selroos, J-O., Uchida, M. and Winberg, A. (2000) *Task 6: Performance Assessment Modelling Using Site Characterisation Data (PASC)*. Swedish Nuclear Fuel and Waste Management Company (SKB).

Byegård, J., Albinsson, Y., Skarnemark, G., and Skålberg, M. (1992) "Field and laboratory studies of the reduction and sorption of technetium(VII)", *Radiochimica Acta*, **58/59**, pp. 239-244.

Dershowitz, B., Winberg, A., Hermanson, J., Byegård, J., Tullborg, E. L., Andersson, P. and Mazurek, M. (2003) *Äspö Task Force, Task 6C. A Semi-Synthetic Model of Block Scale Conductive Structures at the Äspö Hard Rock Laboratory*, Swedish Nuclear Fuel and Waste Management Company (SKB), International Progress Report IPR-03-13.

Gylling, B. (1997) *Development and Applications of the Channel Network Model for Simulatuions of Flow and Solute Transport in Fractured Rock*, Ph.D. Thesis, Department of Chemical Engineering and Technology, Royal Institute of Technology, Stockholm, Sweden.

Gylling, B., Birgersson, L., Moreno, L., and Neretnieks, I. Analysis of a long-term pumping and tracer test using the Channel Network Model, Journal of Contaminant Hydrology, Vol 32, 203-222, 1998.

Holmqvist, M., Andersson, P., Trick, T., Fierz, T., Eichinger, L., and Scholtis, A. (2000) *Test of New Possible Non-Reactive Tracers – Experimental Description and Evaluation*, Äspö Hard Rock Laboratory, ITD-00-07.

Lapidus, L. and Amundsen, N. R. (1952) "Mathematics of adsorption in beds", *Journal of Physical Chemistry*, **56**, pp. 984.

Levenspiel, O. (1972) *Chemical Reaction Engineering*, 2 ed., John Wiley and Sons, New York.

Moreno, L., Tsang, Y. W., Tsang, C. F., Hale, F. V. and Neretnieks, I. (1988) "Flow and tracer transport in a single fracture. A stochastic model and its relation to some field observations", *Water Resources Research*, **24**, pp. 20033-3048.

Moreno, L., and Neretnieks, I. (1993) "Fluid flow and solute transport in a network of channels", *Journal of Contaminant Hydrology*, **14**, pp. 163-192.

Moreno, L., B. Gylling, and I. Neretnieks (1997) "Solute transport in fractured media - the important mechanisms for performance assessment"**,** *Journal of Contaminant Hydrology,* **25**, 283-298.

Moreno, L., J. Crawford, and I. Neretnieks Modelling of solute transport using the Channel Network Model. Limited penetration into the rock matrix. In Proceedings of the Second International Symposium, Dynamics of Fluids in Fractured Rock, Berkeley Feb 2004, Ed. B. Faybishenko, 2004 (CD)

Neretnieks, I. (2002) "A stochastic multi-channel model for solute transport – analysis of tracer tests in fractured rock", *Journal of Contaminant Hydrology*, **55**, pp. 175-211.

Robinson, P. C. (1984) *Connectivity, Flow and Transport in Network Models of fractured media*, Ph.D. Thesis, St. Catherine's College, Oxford University, Ref. TP 1072.

Tang, G. H., Frind, E. O., and Sudicky, E. A. (1981) "Contaminant transport in fractured porous media. An analytical solution for a single fracture", *Water Resources Research*, **17**, pp. 555.

Yamashita, R., and Kimura, H., (1990) "Particle-tracking technique for nuclide decay chain transport in fractured porous media", *Journal of Nuclear Science and Technology*, **27**, pp. 1041-1049.

10 Appendix A1 – Estimation of Channel Network Conductances

In the Channel Network model, each channel member is assigned a hydraulic conductance. The conductance is defined by analogy with electrical networks where it is the reciprocal of resistance. The flow in an individual channel (Q_i, m^3/y) may then be expressed as the channel conductance (C_i, m^2/y) multiplied by the hydraulic head difference (ΔH_i, m) between its ends:

$$Q_i = C_i \Delta H_i \qquad \text{(A1-1)}$$

In the Task 6C semi-synthetic hydrostructural model, flow is conceptualised to occur only within the network of discretely connected fracture polygons as depicted in ***Figure 3*** (Section 3.2). To model the system using CHAN3D, it was therefore necessary to convert the discrete fracture network (DFN) data to an equivalent channel network representation. Owing to fundamental differences in the conceptual descriptions of the flow system this can only be done, however, in an approximate sense. The reasons for this will be outlined below.

The hydrologic properties of the fractures comprising the DFN are defined in terms of a hydraulic transmissivity, where Darcy's law describes the relation between flow (Q_f, m^3/y) and transmissivity (T, m^2/y) in the entire fracture:

$$Q_f = T_f W_f \frac{\Delta H_f}{L_f} \qquad \text{(A1-2)}$$

The ratio $\Delta H_f / L_f$ is the hydraulic gradient (m/m) along the direction of flow within the fracture and W_f (m) is the fracture width.

For a fracture discretised into a regular mesh of interconnected channels, the channel network representation could look something like that shown in Figure 109 below:

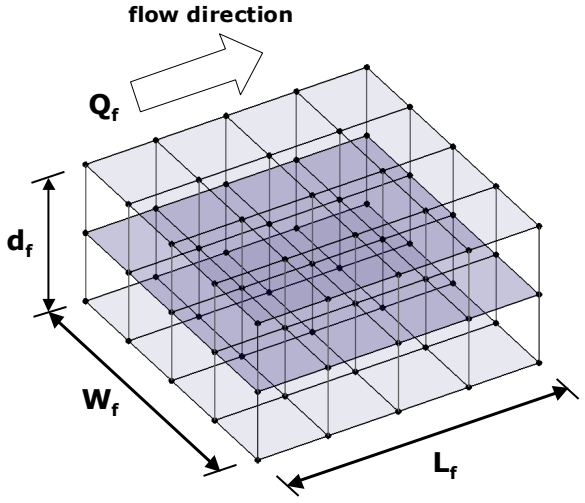

Figure 109. *Schematic diagram showing channel network representation of a discrete fracture (shaded central plane) of width, d_f nominally equal to two channel lengths. The hypothetical fracture is aligned exactly with the background channel network and all dimensions are integer multiples of the individual channel length, L.*

If the channel network and DFN descriptions are equivalent, the total flow in the fracture given by Equation (A1-2) should be equal to the sum of flows in the individual channels across the end planes of the channel network (perpendicular to the direction of flow) as shown above. In the simple example above, there are 15 channels (3×5 end nodes) intersecting the end planes of the hypothetical fracture. If we assume for the moment that the channels are all assigned equal conductances, the flow in each individual channel entering or leaving the control volume must therefore be equal to 1/15 of the total flow calculated by Equation (A1-2).

If the length of an individual channel is denoted as L (m), the flow in the fracture is:

$$Q_f = C_i \left(n_w \times n_d \right) \times L \left(\frac{\Delta H_f}{L_f} \right) \tag{A1-3}$$

In this case, n_w is the number of channels spanning the width of the fracture and n_d is the number of channels spanning the "depth" of the fracture (i.e., channels parallel to the flow direction). It should be noted that the "depth" of the fracture as defined above is purely for heuristic convenience and has no physical relation to the transport aperture (δ) of the fracture. Additionally, a clear distinction must also be made between the overall fracture length, L_f and the individual channel length, L. If the fracture polygon is precisely aligned in the plane of the channel network, the variables n_w and n_d are given by:

$$n_w = \text{Floor}\left[\frac{W_f}{L} \right] + 1 \tag{A1-4}$$

$$n_d = \text{Floor}\left[\frac{d_f}{L} \right] + 1 \tag{A1-5}$$

The "Floor" operator in the above equations indicates that the value of the ratio in the square brackets is rounded down to the nearest integer. In this case, the perfectly aligned fracture with depth 2L and width 4L, gives exactly three parallel planes of interconnected nodes.

If, however, the fracture were to be shifted slightly against the background channel network (by say, a fraction of a channel length in the vertical and horizontal directions, respectively), the value of n_i and n_d would instead be:

$$n_d = \text{Floor}\left[\frac{d_f}{L} \right] \tag{A1-6}$$

$$n_w = \text{Floor}\left[\frac{W_f}{L} \right] \tag{A1-7}$$

This is because in the slightly shifted fracture system, at least one plane of nodes will lie outside the volume of influence of the fracture (See Figure 110 below).

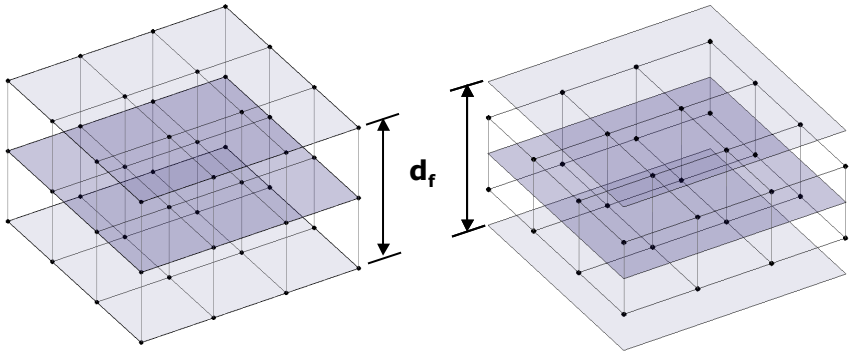

Figure 110. *Schematic diagram showing two alternative channel network representations of a discrete fracture (shaded central plane). The left-hand figure is precisely aligned with the background channel network. The right-hand figure shows the same fracture shifted by half a channel length vertically against the background channel network. The lightly shaded planes delineate the notional bounds of the fracture plane.*

The relation between channel conductance and fracture transmissivity is therefore dependent upon the fracture orientation relative to the channel network. For a fracture that is orthogonally oriented relative to the channel network, the channel conductance-transmissivity relation is bounded by:

$$C_i \geq T_f \times \frac{W_f / L}{\left(\text{Floor}\left[\frac{W_f}{L}\right]+1\right)\left(\text{Floor}\left[\frac{d_f}{L}\right]+1\right)} \qquad \text{(A1-8)}$$

$$C_i \leq T_f \times \frac{W_f / L}{\left(\text{Floor}\left[\frac{W_f}{L}\right]\right)\left(\text{Floor}\left[\frac{d_f}{L}\right]\right)} \qquad \text{(A1-9)}$$

For the fracture depicted in Figure 109, if the fracture width were large compared to the channel length, a small shift of the fracture in the horizontal plane relative to the background channel network would not have a large effect upon the equivalent channel conductance. A small shift in the vertical direction, however, would give only two parallel planes of nodes rather than three comprising the fracture. This would give rise to a 33% discrepancy in the calculated channel conductance between both cases.

An additional complication arises when the fracture plane is rotated in some way relative to the background channel network. If we consider a simple case where the fracture plane is rotated relative to one of the horizontal axes (i.e., x- or y-) by a given angle, the fracture plane and its equivalent channel network representation may appear as shown in Figure 111 below, for various rotational angles:

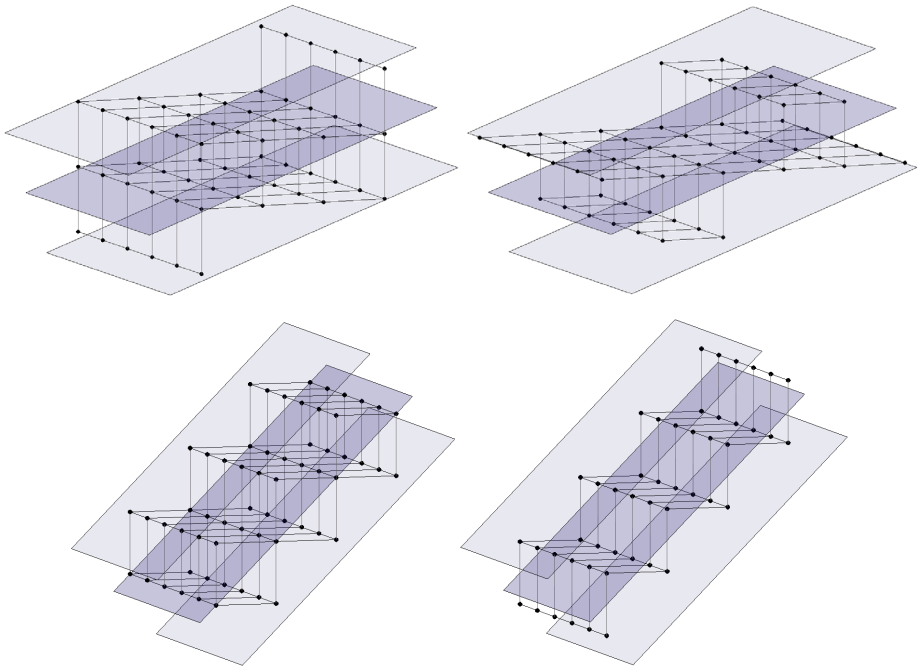

Figure 111. *Schematic diagram showing alternative channel network representations of a discrete fracture (the figures on the right hand side are shifted by half a channel length in the vertical direction), where the fracture is rotated relative to the background channel network. The top row of images is for a rotation of 20° anticlockwise from horizontal and the bottom row corresponds to a rotation of 45°. The lightly shaded planes delineate the notional bounds of the fracture plane.*

Most randomly generated fracture polygons have even more complex channel network representations as they are only occasionally aligned with any given axis (see Figure 112 below).

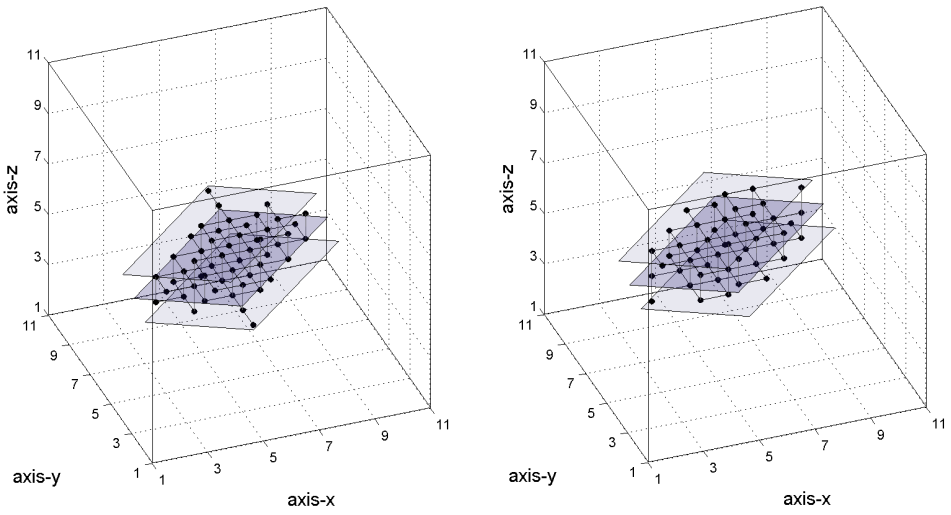

Figure 112. *Schematic diagram showing two alternative channel network representations of a discrete fracture where the fracture is rotated relative to the principal network-axes. As previously, the right-hand figure is shifted by half a channel length in the vertical direction. The lightly shaded planes delineate the notional bounds of the fracture plane.*

It should be noted that randomly generated fracture polygons will, in general, not be well aligned with the background channel network and it is not possible to translate DFN transmissivities to equivalent channel conductances in any simple way.

It was found that a fracture depth of about two channel lengths was the minimum required to give good channel network connectivity in 3D space for randomly oriented fracture polygons. If a fracture depth of less than two channel lengths is used, there is some risk that the channel network representation will be poorly connected or even disconnected in 3D space. This is illustrated in Figure113 below for a fracture depth (d_f) of one channel length. The channel network on the left-hand side of Figure 113 shows poor connectivity with two distinct bottlenecks, while that on the right-hand side is entirely disconnected.

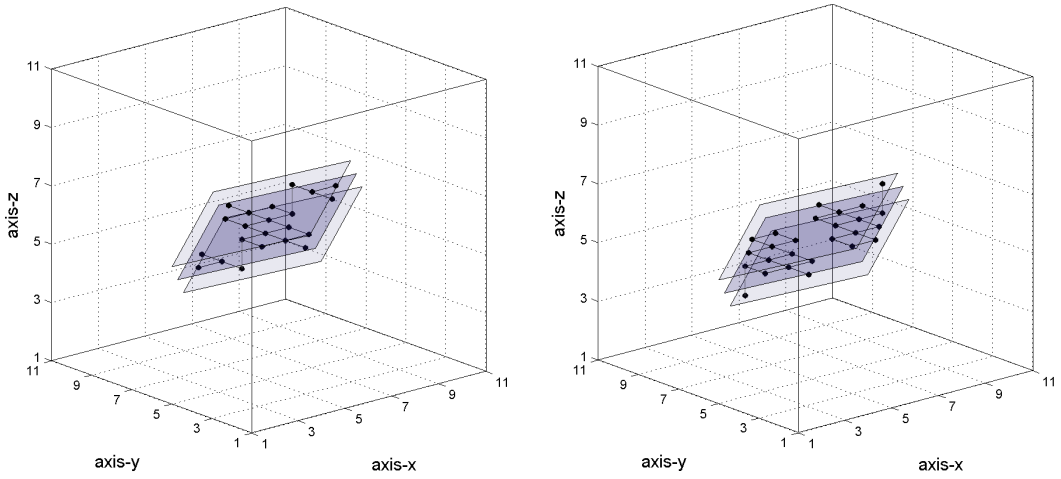

Figure 113. *Schematic diagram showing two alternative channel network representations of a discrete fracture where the fracture is rotated relative to the principal network-axes. In this case, the nominal fracture depth is equal to only one channel length. As previously, the right-hand figure is shifted by half a channel length in the vertical direction. The lightly shaded planes delineate the notional bounds of the fracture plane.*

To obtain a relation between channel conductance and fracture transmissivity, stochastic simulations were performed for 100 randomly generated fracture planes with arbitrary orientation relative to the principal axes of the channel network. In all cases, the fracture depth was taken to be two channel lengths in order to preserve channel connectivity. A typical realisation is visualised in Figure 115 below, where the red- and blue-coloured markers represent nodes where a fixed head boundary condition was applied (i.e., a hydraulic head difference across the fracture end-planes):

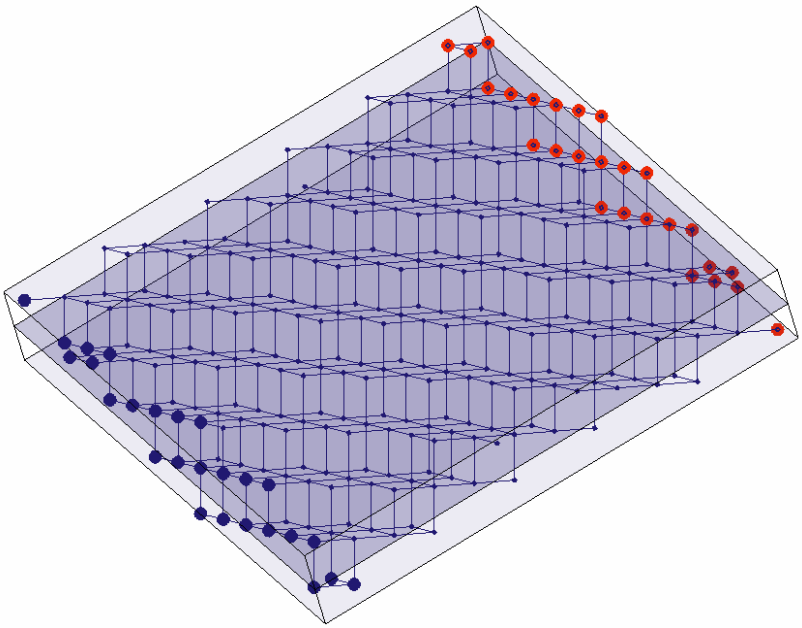

Figure 114. *Typical channel network used to represent a discrete fracture plane. The volume surrounding the shaded plane corresponds to the "zone of influence" of the fracture, which in this case is two channel lengths in depth. All channels lying outside the zone of influence are assigned arbitrarily low conductances. Boundary nodes for a typical flow simulation are visualised as red and blue markers in the figure.*

In each simulation, the total flow entering and leaving the fracture was calculated for an arbitrary set of channel conductances (in this case we chose equal conductances with a zero standard deviation). Given the simulated flow, head difference, and fracture dimensions the equivalent transmissivity was calculated using Equation (A1-2):

$$T_f = W_f \frac{\Delta H_f}{L_f} \Big/ Q_f \qquad \text{(A1-10)}$$

As the channel conductances were already known, this gave an implicit relation between the channel conductance and fracture transmissivity:

$$\alpha = C_i \times W_f \frac{\Delta H_f}{L_f} \Big/ Q_f \qquad \text{(A1-11)}$$

Where,

$$\alpha = \frac{C_i}{T_f} \qquad \text{(A1-12)}$$

Figure 115 below, shows the relation between channel conductance and fracture transmissivity (α) as a function of channel length and fracture dimension:

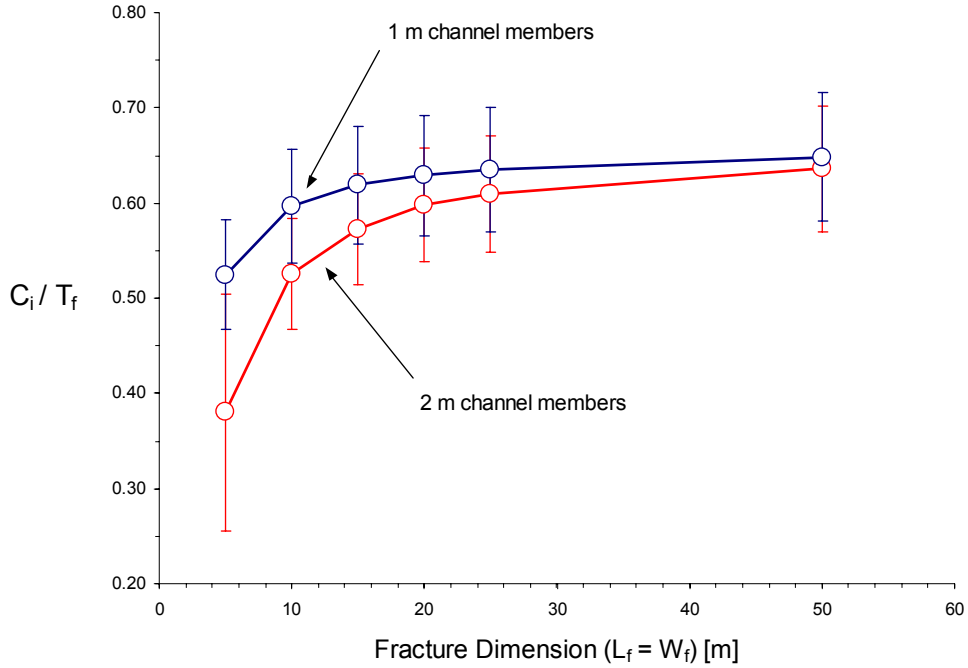

Figure 115. *Relation between channel conductance (C_i) and fracture transmissivity (T_f) for randomly oriented fractures of various dimensions in 3D. Data points and standard error limits (one-sigma) based upon 100 realisations of each fracture dimension.*

The results indicate a large variability for α, particularly for small fractures. This is because small fractures are more strongly influenced by small changes in orientation and dimension than large fractures. For fractures with dimensions on the order of some tens of channel lengths, α converges approximately to a value of 0.65±0.07.

It is worth noting for a fracture that is orthogonally oriented relative to the channel network, we would expect α to be in the range 0.33-0.50 for large fractures (i.e., $W_f / L >> 1$ in Equations (A1-8) and (A1-9). The higher mean value for α in the case of a randomly oriented fracture relates to the fact that randomly placed fractures tend to have less well-connected channel network representations (i.e., they are generally less conductive owing to bottlenecks, etc.).

In the CHAN3D simulations of Task 6D, a value of roughly 0.65 was assumed for the value of α. To convert the fracture transmissivities [m^2/s] in the data distribution to equivalent channel conductances [m^2/y], the following formula was applied:

$$C_i\,[\mathrm{m}^2/\mathrm{y}] = 7.4988 + \log_{10}\left(T_f[\mathrm{m}^2/\mathrm{s}]\right) - \log_{10}\alpha \qquad \text{(A1-13)}$$

To generate the complete channel network analogue of the DFN, all network members were initially given arbitrarily low conductances (in this case, 10^{-12} m^2/y). Using a set of computational geometry routines developed in MATLAB, specific nodes in the channel network were identified as belonging to individual fractures as defined in the DFN data set. This was done by calculating the perpendicular distance between each node and the fracture polygon surface. Nodes lying within one channel length on either side of a fracture polygon were deemed as belonging to that fracture (giving a total fracture depth of two channel lengths). A note was made of each individual fracture associated with a given node owing to the possibility of nodes being shared by two or more closely spaced fractures in the DFN.

As described previously, channel members belonging to each fracture were given conductances based upon the mean value determined for that particular fracture in the DFN data set. In order to allow the possibility of channelling phenomena within individual fractures, the conductance was assigned randomly from a lognormal distribution with the listed mean and an assumed standard deviation. As there were no additional data relating to channelling effects, a standard deviation of unity ($\log_{10}$ units) was assumed for channels residing in all fractures.

If two neighbouring nodes were flagged as belonging to one, or more fractures a conductance (i.e., higher than the default background conductance) was assigned to the channel linking them. If adjacent nodes were flagged as belonging to two (or more) different fractures, the conductance was taken to be the mean of the value given for the fractures involved. If the flagged nodes belonged to the same fracture, then the associated channel was assigned a conductance appropriate for the nominated fracture.

In this way a set of conductive channels was defined, embedded in a background network of essentially non-conductive channels. The mean $\log_{10}$-conductance of individual channels in the active network varied from -1.9 to 2.2. The background channels, on the other hand, were assigned $\log_{10}$-conductances of -12.

The following figures show the channel network connectivity calculated for fracture 21D (Figure 116) and the background fracture 1925B (Figure 117) in the 75 m rock volume defined in the CHAN3D simulation model:

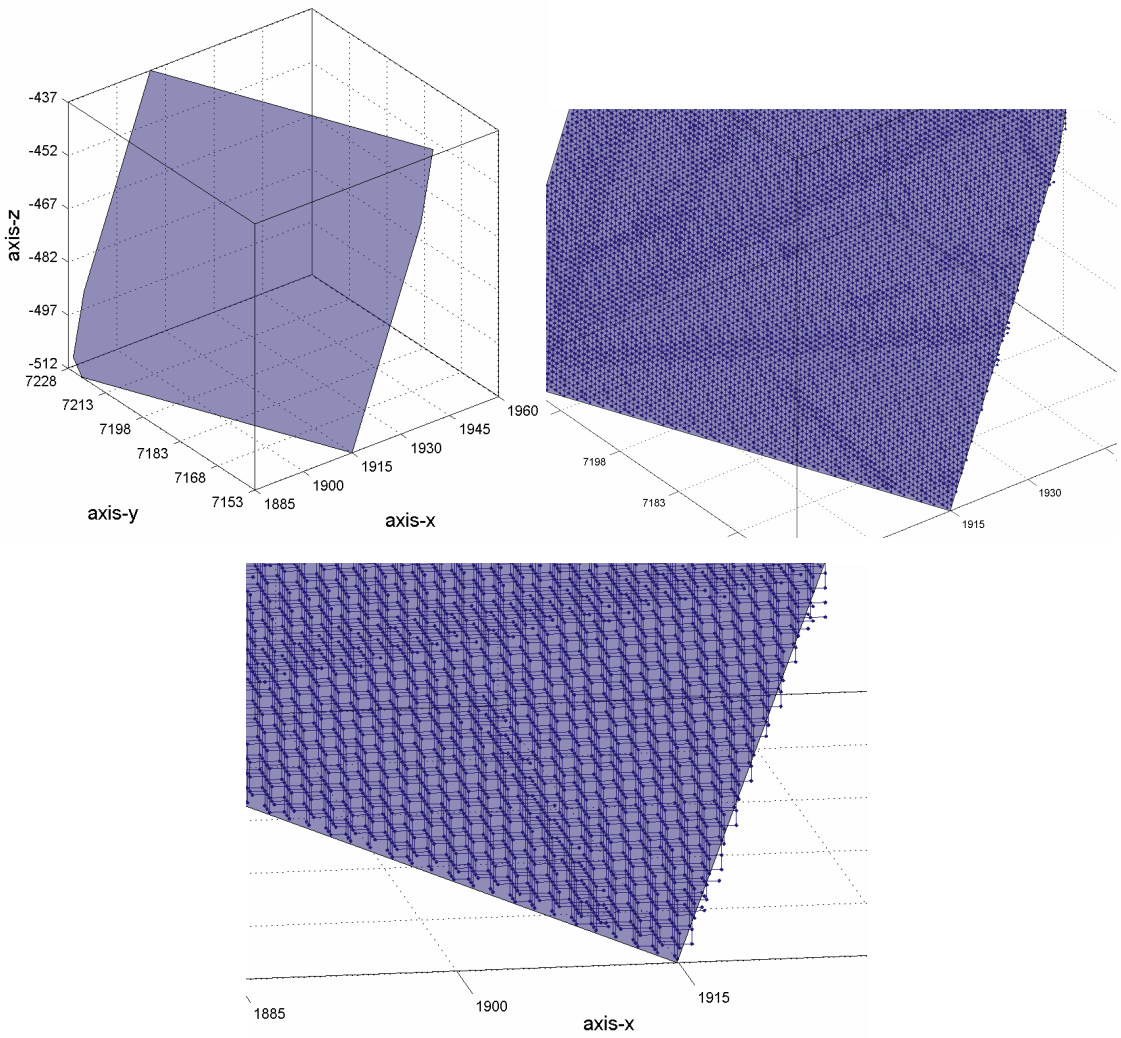

Figure 116. *View of fracture 21B showing fracture polygon (left) and network channels assigned to fracture plane (enlarged detail, right and below centre) for the 75m rock volume. Regions with increased channel density indicate locations where channels are shared with intersecting fractures. This fracture has dimensions of 92 m×87 m (non-truncated).*

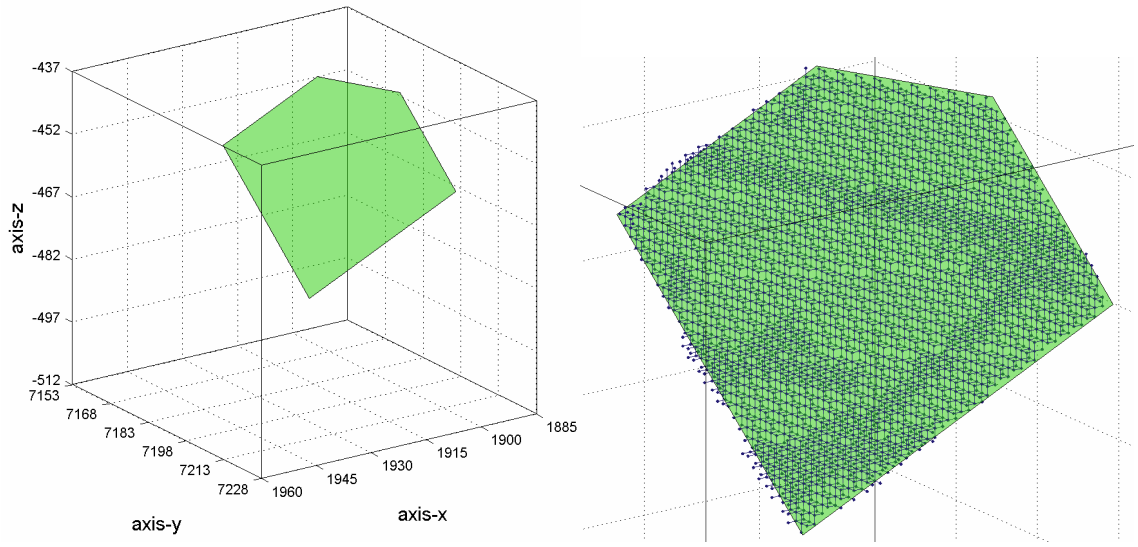

Figure 117. *View of fracture 1925B showing fracture polygon (left) and network channels assigned to fracture plane (enlarged detail, right) for the 75 m rock volume. Regions with increased channel density indicate locations where channels are shared with intersecting fractures. This fracture has dimensions of 43 m×43 m (non-truncated).*

For large fractures, any small discrepancies in the effective conductance owing to fracture geometry are likely to be evened out over the fracture due to the large number of channel members comprising the fracture. For smaller fractures, however, there may be larger discrepancies owing to channel network connectivity issues. Figure 118 below shows the connectivity of one of the smaller background fractures (2004B) in the Task 6C data set:

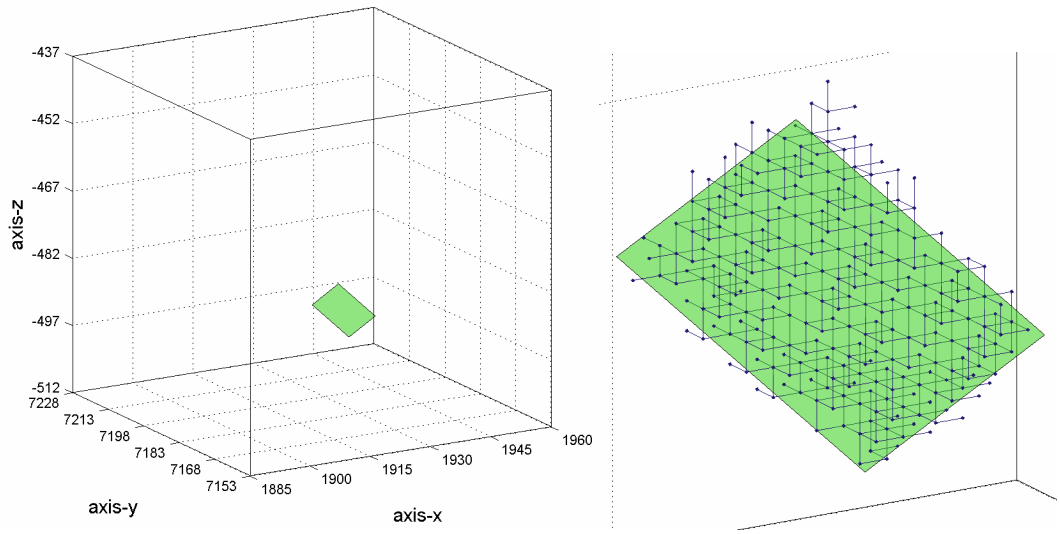

Figure 118. *View of fracture 2004B showing fracture polygon (left) and network channels assigned to fracture plane (enlarged detail, right) for the 75 m rock volume. This fracture has dimensions of 10.62 m×10.62 m.*

For the channel length used in the 75 m simulations (1 m), it appears from Figure 118 that it is still possible to adequately describe the fracture 2004B.

One of the smallest fractures implicated in tracer transport during the CHAN3D simulations of the C2 tracer test is fracture 1067C. This fracture and its accompanying channel network analogue is shown below in Figure 119:

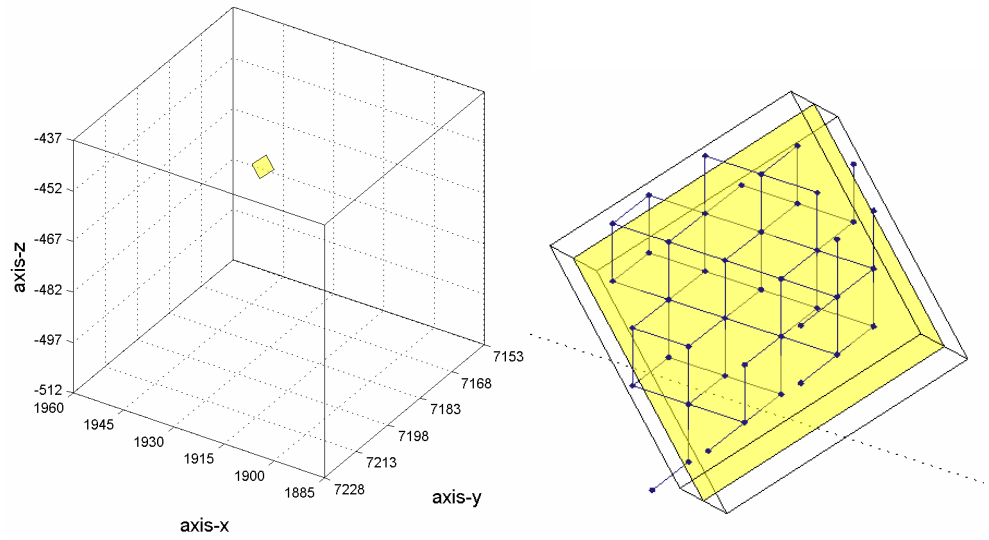

Figure 119. *View of fracture 1067C showing fracture polygon (left) and network channels assigned to fracture plane (enlarged detail, right) for the 75 m rock volume. Approximate limits of node calculation control volume are also indicated in the right-hand image. This fracture has dimensions of 4.38 m×4.38 m.*

Although it appears that the channel network analogue of fracture 1067C describes the fracture reasonably well, the effective conductance of the feature will be influenced by how well it is connected with other fractures comprising the DFN. The same fracture (1067C) is shown in Figure 120 below for the 200 m Block Scale volume and a channel length of 2 m. As can be appreciated from the figure, the channel network analogue of the DFN fracture is less well defined in the 200 m model than it is in the 75 m model.

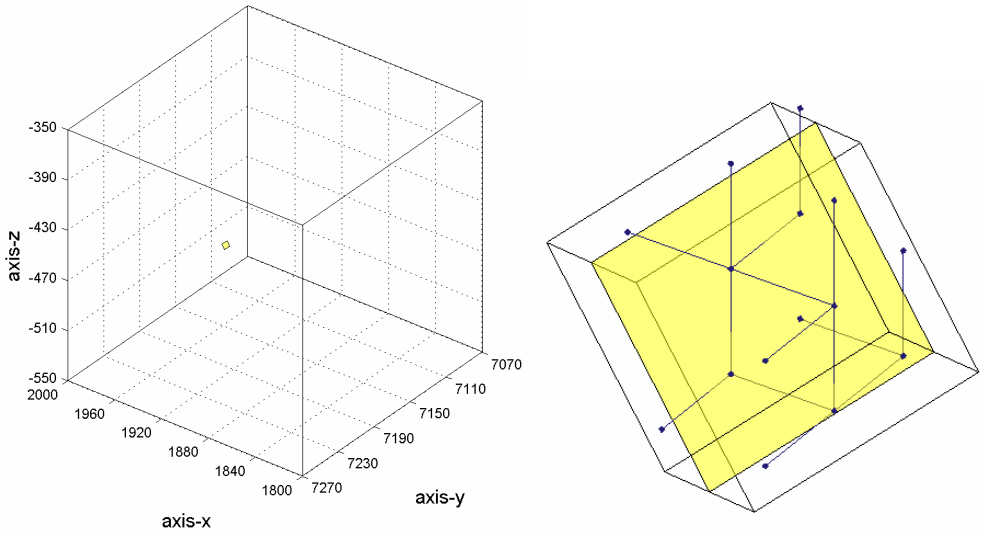

Figure 120. *View of fracture 1067C showing fracture polygon (left) and network channels assigned to fracture plane (enlarged detail, right) for the original 200 m rock volume. Approximate limits of node calculation control volume are also indicated in the right-hand image. This fracture has dimensions of 4.38 m×4.38 m.*

11 Appendix A2. solute transport in a channel with a matrix comprising several layers

A model is developed for solute transport in a single channel including advection, diffusion and sorption in a matrix formed by several layers. The layers have properties different of the matrix proper. In this Appendix, the case for a matrix formed by three layers in addition to the matrix proper is presented.

First, the governing equations are written and then the Laplace transform is applied to this system of PDE. The system of ODE resulting is solved in the Laplace space. Finally, the solution in t is obtained by numerical inversion of thi8s solution (Laplace space).

Figure below shows a schematic picture of the situation for a layer (skin) and the proper matrix. The thickness of the skin is δ_s and the fracture aperture is 2b.

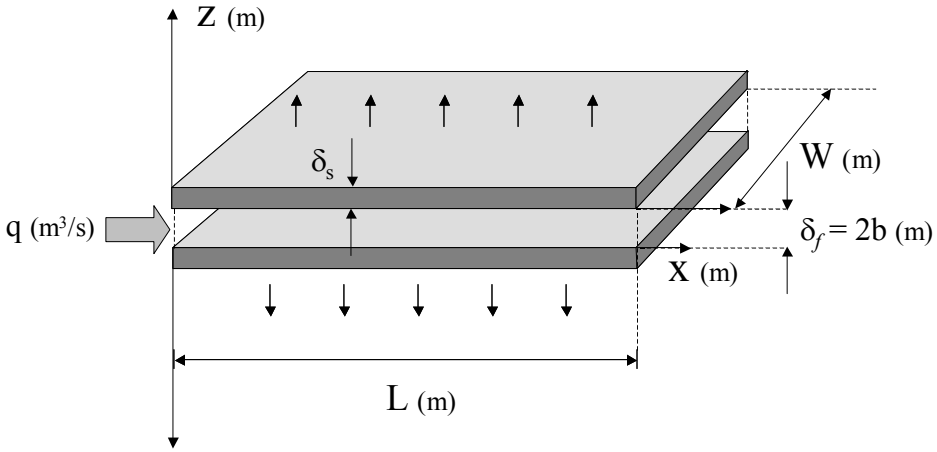

The unsteady, differential mass balance equation for the solute concentration in the channel is given by:

$$\frac{\partial C_f}{\partial t} + \frac{q}{2Wb}\frac{\partial C_f}{\partial x} = \frac{D_{es1}}{b}\frac{\partial C_{ps1}}{\partial z}\bigg|_{z=0} \qquad \text{for } (x > 0,\ t > 0) \qquad \text{(A2-1)}$$

Unsteady diffusion of solute in the rock matrix proper is given by:

$$\left(\varepsilon_{pm} + (1-\varepsilon_{pm})K'_{dm}\rho_{sm}\right)\frac{\partial C_{pm}}{\partial t} = D_{em}\frac{\partial^2 C_{pm}}{\partial z^2} \qquad \text{for } (x > 0,\ z > \delta_{s1} + \delta_{s2} + \delta_{s3},\ t > 0) \qquad \text{(A2-2)}$$

The term on the left-hand side of Equation (A 2) considers accumulation in both the pore water as well as the tracer sorbed in the rock matrix. We define a bulk distribution coefficient (K_{dm}) to implicitly include both the sorbed and the pore water concentrations:

$$\left(\varepsilon_{pm} + \left(1 - \varepsilon_{pm}\right)K'_{dm}\rho_{sm}\right) = K_{dm}\rho_{bm} \tag{A2-3}$$

Then, Equation (A-3) may be written as

$$K_{dm}\rho_{bm}\frac{\partial C_{pm}}{\partial t} = D_{em}\frac{\partial^2 C_{pm}}{\partial z^2} \qquad \text{for } \left(x > 0,\ z > \delta_{s1} + \delta_{s2} + \delta_{s3},\ t > 0\right) \tag{A2-4}$$

For the matrix material nearest the fracture surface that have differing diffusive and sorptive properties than the proper matrix two "surface skins" are defined. The thicknesses are δ_{s1} and for the first and second layer respectively. The corresponding unsteady diffusion equations for the surface skins are:

For the skin-1

$$K_{ds1}\rho_{bs1}\frac{\partial C_{ps1}}{\partial t} = D_{es1}\frac{\partial^2 C_{ps1}}{\partial z^2} \qquad \text{for } \left(x > 0,\ 0 < z < \delta_{s1},\ t > 0\right) \tag{A2-5}$$

For the skin-2

$$K_{ds2}\rho_{bs2}\frac{\partial C_{ps2}}{\partial t} = D_{es2}\frac{\partial^2 C_{ps2}}{\partial z^2} \qquad \text{for } \left(x > 0,\ \delta_{s1} < z < \delta_{s1} + \delta_{s2},\ t > 0\right) \tag{A2-6}$$

For the skin-3

$$K_{ds3}\rho_{bs3}\frac{\partial C_{ps3}}{\partial t} = D_{es3}\frac{\partial^2 C_{ps3}}{\partial z^2} \qquad \text{for } \left(x > 0,\ \delta_{s1} + \delta_{s2} < z < \delta_{s1} + \delta_{s2} + \delta_{s3},\ t > 0\right) \tag{A2-7}$$

Before applying Laplace transform, the Material Property Group for the skins and the matrix are defined:

$$\left(MPG\right)_{s1} = \sqrt{K_{ds1}\rho_{bs1}D_{es1}} \tag{A2-8}$$

$$\left(MPG\right)_{s2} = \sqrt{K_{ds2}\rho_{bs2}D_{es2}} \tag{A2-9}$$

$$\left(MPG\right)_{s3} = \sqrt{K_{ds3}\rho_{bs3}D_{es3}} \tag{A2-10}$$

$$\left(MPG\right)_{m} = \sqrt{K_{dm}\rho_{bm}D_{em}} \tag{A2-11}$$

Moreover, four additional parameters are define, namely A_{s1}, A_{s2}, A_{s3}, and A_m

$$A_{s1} = \sqrt{\frac{K_{ds1}\rho_{bs1}}{D_{es1}}} \tag{A2-12}$$

$$A_{s2} = \sqrt{\frac{K_{ds2}\rho_{bs2}}{D_{es2}}} \tag{A2-13}$$

$$A_{s3} = \sqrt{\frac{K_{ds3}\rho_{bs3}}{D_{es3}}} \tag{A2-14}$$

$$A_{m} = \sqrt{\frac{K_{dm}\rho_{bm}}{D_{em}}} \tag{A2-15}$$

Applying the Laplace transform to Equation (A2-1) gives:

$$-\frac{q}{2Wb}\frac{d\overline{C}_f}{dx}-s\cdot\overline{C}_f+C_{f0}+\frac{D_{es}}{b}\frac{d\overline{C}_{ps}}{dz}\bigg|_{z=0}=0 \qquad \text{(A2-16)}$$

Applying the Laplace transform to Equation (A2-4) gives:

$$\frac{1}{A_m^2}\frac{\partial^2\overline{C}_{pm}}{\partial z^2}-s\cdot\overline{C}_{pm}+C_{pm0}=0 \qquad \text{(A2-17)}$$

Similarly, we can write for the surface skins (Equations A2-5, A2-6, and A2-7):

$$\frac{1}{A_{s1}^2}\frac{\partial^2\overline{C}_{ps1}}{\partial z^2}-s\cdot\overline{C}_{ps1}+C_{ps10}=0 \qquad \text{(A2-18}$$

$$\frac{1}{A_{s2}^2}\frac{\partial^2\overline{C}_{ps2}}{\partial z^2}-s\cdot\overline{C}_{ps2}+C_{ps20}=0 \qquad \text{(A2-19)}$$

$$\frac{1}{A_{s3}^2}\frac{\partial^2\overline{C}_{ps3}}{\partial z^2}-s\cdot\overline{C}_{ps3}+C_{ps30}=0 \qquad \text{(A2-20)}$$

Initial conditions and boundary conditions for a step concentration

The initial conditions of the system are defined to be:

IC1:

$$C_f=C_{f0}=0 \qquad (x>0,\ t=0) \qquad \text{(A2-21)}$$

IC2:

$$C_{pm}=C_{pm0}=0 \qquad (x>0,\ z>\delta_{s1}+\delta_{s2}+\delta_{s3},\ t=0) \qquad \text{(A2-22)}$$

IC3:

$$C_{ps1}=C_{ps10}=0 \qquad (x>0,\ 0<z<\delta_{s1},\ t=0) \qquad \text{(A2-23)}$$

IC4:

$$C_{ps2}=C_{ps20}=0 \qquad (x>0,\ \delta_{s1}<z<\delta_{s1}+\delta_{s2},\ t=0) \qquad \text{(A2-24)}$$

IC5:

$$C_{ps3}=C_{ps30}=0 \qquad (x>0,\ \delta_{s1}+\delta_{s2}<z<\delta_{s1}+\delta_{s2}+\delta_{s3},\ t=0) \qquad \text{(A2-25)}$$

The boundary conditions for a step tracer input are given by:

BC1:

$$C_f = C_0 \qquad (x = 0,\ t > 0) \tag{A2-26}$$

BC2:

$$C_f = 0 \qquad (x = \infty,\ t > 0) \tag{A2-27}$$

BC3:

$$C_{ps1} = C_f \qquad (x > 0,\ z = 0,\ t > 0) \tag{A2-28}$$

BC4:

$$C_{ps1} = C_{ps2} \qquad (x > 0,\ z = \delta_{s1},\ t > 0) \tag{A2-29}$$

BC5:

$$D_{es1} \left.\frac{\partial C_{ps1}}{\partial z}\right|_{z=\delta s1} = D_{es2} \left.\frac{\partial C_{ps2}}{\partial z}\right|_{z=\delta s1} \qquad (x > 0,\ z = \delta_{s1},\ t > 0) \tag{A2-30}$$

BC6:

$$C_{ps2} = C_{ps3} \qquad (x > 0,\ z = \delta_{s1} + \delta_{s2},\ t > 0) \tag{A2-31}$$

BC7:

$$D_{es2} \left.\frac{\partial C_{ps2}}{\partial z}\right|_{z=\delta s1+\delta s2} = D_{es3} \left.\frac{\partial C_{ps3}}{\partial z}\right|_{z=\delta s1+\delta s2} \qquad (x > 0,\ z = \delta_{s1} + \delta_{s2},\ t > 0) \tag{A2-32}$$

BC8:

$$C_{ps3} = C_{pm} \qquad (x > 0,\ z = \delta_{s1} + \delta_{s2} + \delta_{s3},\ t > 0) \tag{A2-33}$$

BC9:

$$D_{es3} \left.\frac{\partial C_{ps3}}{\partial z}\right|_{z=\delta s1+\delta s2+\delta s3} = D_{em} \left.\frac{\partial C_{pm}}{\partial z}\right|_{z=\delta s1+\delta s2+\delta s3} \qquad (x > 0,\ z = \delta_{s2} + \delta_{s2} + \delta_{s3},\ t > 0) \tag{A2-34}$$

BC10:

$$C_{pm} = 0 \qquad (x > 0,\ z = \infty,\ t > 0) \tag{A2-35}$$

The Laplace transforms of the boundary conditions are:

BC1:

$$\overline{C}_f = \frac{C_0}{s} \qquad (x = 0) \tag{A2-36}$$

BC2:

$$\overline{C}_f = 0 \qquad (x = \infty) \tag{A2-37}$$

BC3:

$$\overline{C}_{ps1} = \overline{C}_f \qquad (x > 0,\ z = 0) \tag{A2-38}$$

BC4:

$$\overline{C}_{ps1} = \overline{C}_{ps2} \qquad (x > 0,\ z = \delta_{s1}) \tag{A2-39}$$

BC5:

$$D_{es1} \left.\frac{\partial \overline{C}_{ps1}}{\partial z}\right|_{z=\delta s1} = D_{es2} \left.\frac{\partial \overline{C}_{ps2}}{\partial z}\right|_{z=\delta s1} \qquad (x > 0,\ z = \delta_{s1}) \tag{A2-40}$$

BC6:

$$\overline{C}_{ps2} = \overline{C}_{ps3} \qquad (x > 0,\ z = \delta_{s1} + \delta_{s2}) \tag{A2-41}$$

BC7:

$$D_{es2} \left.\frac{\partial \overline{C}_{ps2}}{\partial z}\right|_{z=\delta s1+\delta s2} = D_{es3} \left.\frac{\partial \overline{C}_{ps3}}{\partial z}\right|_{z=\delta s1+\delta s2} \qquad (x > 0,\ z = \delta_{s1} + \delta_{s2}) \tag{A2-42}$$

BC8:

$$\overline{C}_{ps3} = \overline{C}_{pm} \qquad (x > 0,\ z = \delta_{s1} + \delta_{s2} + \delta_{s3}) \tag{A2-43}$$

BC9:

$$D_{es3} \left.\frac{\partial \overline{C}_{ps3}}{\partial z}\right|_{z=\delta s1+\delta s2+\delta s3} = D_{em} \left.\frac{\partial \overline{C}_{pm}}{\partial z}\right|_{z=\delta s1+\delta s2+\delta s3} \qquad (x > 0,\ z = \delta_{s1} + \delta_{s2} + \delta_{s3}) \tag{A2-44}$$

BC10:

$$\overline{C}_{pm} = 0 \qquad (x > 0,\ z = \infty) \tag{A2-45}$$

The general solution to Equation (A2-17) is:

$$\overline{C}_{pm} = \alpha_1 \cdot \mathrm{Exp}\left(m_1\left(z-\delta_{s1}-\delta_{s2}-\delta_{s3}\right)\right)+\alpha_2 \cdot \mathrm{Exp}\left(m_2\left(z-\delta_{s1}-\delta_{s2}-\delta_{s3}\right)\right) \qquad \left(z > \delta_{s1}+\delta_{s2}+\delta_{s3}\right) \tag{A2-46}$$

Where α_1, α_2 are constants of integration and m_1, m_2 are the roots of the eigenvalue equation:

$$m^2 - s \cdot A_m^2 = 0 \tag{A2-47}$$

the roots of the equation are:

$$m = \pm A_m \sqrt{s} \tag{A2-48}$$

Equation (A2-46) can therefore be written as:

$$\overline{C}_{pm} = \alpha_1 \mathrm{Exp}\left(\left(z-\delta_{s1}-\delta_{s2}-\delta_{s3}\right)A_m\sqrt{s}\right)+\alpha_2 \mathrm{Exp}\left(-\left(z-\delta_{s1}-\delta_{s2}-\delta_{s3}\right)A_m\sqrt{s}\right) \qquad \left(z > \delta_{s1}+\delta_{s2}+\delta_{s3}\right) \tag{A2-49}$$

Similarly, the solution to Equations (A2-18), (A2-19), and (A2-20) can be written directly as:

For skin-1

$$\overline{C}_{ps1} = \alpha_3 \cdot \mathrm{Exp}\left(z\,A_{s1}\sqrt{s}\right)+\alpha_4 \cdot \mathrm{Exp}\left(-z\,A_{s1}\sqrt{s}\right) \qquad \left(0 < z < \delta_{s1}\right) \tag{A2-50}$$

For skin-2

$$\overline{C}_{ps2} = \alpha_5 \mathrm{Exp}\left(\left(z-\delta_{s1}\right)A_{s2}\sqrt{s}\right)+\alpha_6 \mathrm{Exp}\left(-\left(z-\delta_{s1}\right)A_{s2}\sqrt{s}\right) \qquad \left(\delta_{s1} < z < \delta_{s1}+\delta_{s2}\right) \tag{A2-51}$$

For skin-3

$$\overline{C}_{ps3} = \alpha_7 \mathrm{Exp}\left(\left(z-\delta_{s1}-\delta_{s2}\right)A_{s3}\sqrt{s}\right)+\alpha_8 \mathrm{Exp}\left(-\left(z-\delta_{s1}-\delta_{s2}\right)A_{s3}\sqrt{s}\right) \qquad \left(\delta_{s1}+\delta_{s2} < z < \delta_{s1}+\delta_{s2}+\delta_{s3}\right) \tag{A2-52}$$

Using BC10 we can directly see that the constant α_1 in Equation (A2-40) must be zero:

$$\overline{C}_{pm} = \alpha_2 \mathrm{Exp}\left(-\left(z-\delta_{s1}-\delta_{s2}-\delta_{s3}\right)A_m\sqrt{s}\right) \qquad \left(z > \delta_{s1}+\delta_{s2}+\delta_{s3}\right) \tag{A2-53}$$

Determination of the other integration constants

Using the boundary condition BC8 at $z = \delta_{s1} + \delta_{s2} + \delta_{s3}$, we can write:

$$\alpha_2 = \alpha_7 \cdot \mathrm{Exp}\left(\delta_{s3} A_{s3} \sqrt{s}\right) + \alpha_8 \cdot \mathrm{Exp}\left(-\delta_{s3} A_{s3} \sqrt{s}\right) \tag{A2-54}$$

Before applying the BC9, the derivatives of $\overline{C}_{ps3}$ and $\overline{C}_{pm}$ with respect to z are calculated:

$$\frac{\partial \overline{C}_{ps3}}{\partial z} = \alpha_7 A_{s3} \sqrt{s} \cdot \mathrm{Exp}\left(+\left(z - \delta_{s1} - \delta_{s2}\right) A_{s3} \sqrt{s}\right) - \alpha_8 A_{s3} \sqrt{s} \cdot \mathrm{Exp}\left(-\left(z - \delta_{s1} + \delta_{s2}\right) A_{s3} \sqrt{s}\right) \tag{A2-55}$$

$$\frac{\partial \overline{C}_{pm}}{\partial z} = -\alpha_2 A_m \sqrt{s} \cdot \mathrm{Exp}\left(-\left(z - \delta_{s1} - \delta_{s2} - \delta_{s3}\right) A_m \sqrt{s}\right) \tag{A2-56}$$

Equalizing the flux at $z = \delta_{s1} + \delta_{s2} + \delta_{s3}$:

$$\alpha_7 \cdot \mathrm{Exp}\left(\delta_{s3} A_{s3} \sqrt{s}\right) - \alpha_8 \cdot \mathrm{Exp}\left(-\delta_{s3} A_{s3} \sqrt{s}\right) = -\alpha_2 \frac{(\mathrm{MPG})_m}{(\mathrm{MPG})_{s3}} \tag{A2-57}$$

Using the boundary condition BC6 at $z = \delta_{s1} + \delta_{s2}$, we can write:

$$\alpha_5 \cdot \mathrm{Exp}\left(\delta_{s2} A_{s2} \sqrt{s}\right) + \alpha_6 \cdot \mathrm{Exp}\left(-\delta_{s2} A_{s2} \sqrt{s}\right) = \alpha_7 + \alpha_8 \tag{A2-58}$$

Before applying the BC7, the derivatives of $\overline{C}_{ps2}$ and $\overline{C}_{ps3}$ with respect to z are calculated:

$$\frac{\partial \overline{C}_{ps2}}{\partial z} = \alpha_5 A_{s2} \sqrt{s} \cdot \mathrm{Exp}\left(+\left(z - \delta_{s1}\right) A_{s2} \sqrt{s}\right) - \alpha_6 A_{s2} \sqrt{s} \cdot \mathrm{Exp}\left(-\left(z - \delta_{s1}\right) A_{s2} \sqrt{s}\right) \tag{A2-59}$$

$$\frac{\partial \overline{C}_{ps3}}{\partial z} = \alpha_7 A_{s3} \sqrt{s} \cdot \mathrm{Exp}\left(+\left(z - \delta_{s1} - \delta_{s2}\right) A_{s3} \sqrt{s}\right) - \alpha_8 A_{s3} \sqrt{s} \cdot \mathrm{Exp}\left(-\left(z - \delta_{s1} - \delta_{s2}\right) A_{s3} \sqrt{s}\right) \tag{A2-60}$$

Equalizing the flux at $z = \delta_{s1} + \delta_{s2}$:

$$\alpha_5 \cdot \mathrm{Exp}\left(\delta_{s2} A_{s2} \sqrt{s}\right) - \alpha_6 \cdot \mathrm{Exp}\left(-\delta_{s2} A_{s2} \sqrt{s}\right) = \left(\alpha_7 - \alpha_8\right) \frac{(\mathrm{MPG})_{s3}}{(\mathrm{MPG})_{s2}} \tag{A2-61}$$

Using the boundary condition BC4 at $z = \delta_{s1}$, we can write:

$$\alpha_3 \cdot \mathrm{Exp}\left(\delta_{s1} A_{s1} \sqrt{s}\right) + \alpha_4 \cdot \mathrm{Exp}\left(-\delta_{s1} A_{s1} \sqrt{s}\right) = \alpha_5 + \alpha_6 \tag{A2-62}$$

Before applying the BC5, the derivatives of $\overline{C}_{ps1}$ and $\overline{C}_{ps2}$ with respect to z are calculated:

$$\frac{\partial \overline{C}_{ps1}}{\partial z} = \alpha_3 A_{s1}\sqrt{s}\cdot \mathrm{Exp}\left(+ z A_{s1}\sqrt{s}\right) - \alpha_4 A_{s1}\sqrt{s}\cdot \mathrm{Exp}\left(- z A_{s1}\sqrt{s}\right) \tag{A2-63}$$

$$\frac{\partial \overline{C}_{ps2}}{\partial z} = \alpha_5 A_{s2}\sqrt{s}\cdot \mathrm{Exp}\left(+ (z-\delta_{s1}) A_{s2}\sqrt{s}\right) - \alpha_6 A_{s2}\sqrt{s}\cdot \mathrm{Exp}\left(- (z-\delta_{s1}) A_{s2}\sqrt{s}\right) \tag{A2-64}$$

Equalizing the flux at $z = \delta_{s1}$:

$$\alpha_3 \cdot \mathrm{Exp}\left(\delta_{s1} A_{s1}\sqrt{s}\right) - \alpha_4 \cdot \mathrm{Exp}\left(-\delta_{s1} A_{s1}\sqrt{s}\right) = (\alpha_5 - \alpha_6)\frac{(\mathrm{MPG})_{s2}}{(\mathrm{MPG})_{s1}} \tag{A2-65}$$

From BC3 at z=0 and Equation (A2-50), we can write:

$$\overline{C}_f = \alpha_3 + \alpha_4 \tag{A2-66}$$

Using Equations (A2-54), (A2-57), (A2-58), (A2-61), (A2-62), (A2-65), and (A2-66), we can then solve for the unknown integration constants α_2, α_3, α_4, α_5, α_6, α_7, and α_8. As it is shown later, only the value of the integration constant α_3 is needed, this value is:

$$\alpha_3 = \frac{\overline{C}_f}{1 + \mathrm{Expl}\left[\dfrac{\mathrm{MPM} + \mathrm{MMP}\,\mathrm{Exp2} + \mathrm{PMM}\,\mathrm{Exp3} + \mathrm{PPP}\,\mathrm{Exp2}\,\mathrm{Exp3}}{\mathrm{MPP} + \mathrm{MMM}\,\mathrm{Exp2} + \mathrm{PMP}\,\mathrm{Exp3} + \mathrm{PPM}\,\mathrm{Exp2}\,\mathrm{Exp3}}\right]} \tag{A2-67}$$

Where

$$\begin{aligned}
\mathrm{Expl} &= \mathrm{Exp}\left(\delta_{s1} A_{s1}\sqrt{s}\right)\\
\mathrm{Exp2} &= \mathrm{Exp}\left(\delta_{s2} A_{s2}\sqrt{s}\right)\\
\mathrm{Exp3} &= \mathrm{Exp}\left(\delta_{s3} A_{s3}\sqrt{s}\right)
\end{aligned} \tag{A2-68}$$

$$\begin{aligned}
\mathrm{MPM} &= \left(1 - \frac{(\mathrm{MPG})_m}{(\mathrm{MPG})_{s3}}\right)\left(1 + \frac{(\mathrm{MPG})_{s3}}{(\mathrm{MPG})_{s2}}\right)\left(1 - \frac{(\mathrm{MPG})_{s2}}{(\mathrm{MPG})_{s1}}\right)\\
\mathrm{MMP} &= \left(1 - \frac{(\mathrm{MPG})_m}{(\mathrm{MPG})_{s3}}\right)\left(1 - \frac{(\mathrm{MPG})_{s3}}{(\mathrm{MPG})_{s2}}\right)\left(1 + \frac{(\mathrm{MPG})_{s2}}{(\mathrm{MPG})_{s1}}\right)\\
\mathrm{PMM} &= \left(1 + \frac{(\mathrm{MPG})_m}{(\mathrm{MPG})_{s3}}\right)\left(1 - \frac{(\mathrm{MPG})_{s3}}{(\mathrm{MPG})_{s2}}\right)\left(1 - \frac{(\mathrm{MPG})_{s2}}{(\mathrm{MPG})_{s1}}\right)\\
\mathrm{PPP} &= \left(1 + \frac{(\mathrm{MPG})_m}{(\mathrm{MPG})_{s3}}\right)\left(1 + \frac{(\mathrm{MPG})_{s3}}{(\mathrm{MPG})_{s2}}\right)\left(1 + \frac{(\mathrm{MPG})_{s2}}{(\mathrm{MPG})_{s1}}\right)
\end{aligned} \tag{A2-69}$$

$$
\begin{aligned}
\mathrm{MPP} &= \left(1-\frac{(\mathrm{MPG})_m}{(\mathrm{MPG})_{s3}}\right)\left(1+\frac{(\mathrm{MPG})_{s3}}{(\mathrm{MPG})_{s2}}\right)\left(1+\frac{(\mathrm{MPG})_{s2}}{(\mathrm{MPG})_{s1}}\right)\\
\mathrm{MMM} &= \left(1-\frac{(\mathrm{MPG})_m}{(\mathrm{MPG})_{s3}}\right)\left(1-\frac{(\mathrm{MPG})_{s3}}{(\mathrm{MPG})_{s2}}\right)\left(1-\frac{(\mathrm{MPG})_{s2}}{(\mathrm{MPG})_{s1}}\right)\\
\mathrm{PMP} &= \left(1+\frac{(\mathrm{MPG})_m}{(\mathrm{MPG})_{s3}}\right)\left(1-\frac{(\mathrm{MPG})_{s3}}{(\mathrm{MPG})_{s2}}\right)\left(1+\frac{(\mathrm{MPG})_{s2}}{(\mathrm{MPG})_{s1}}\right)\\
\mathrm{PPM} &= \left(1+\frac{(\mathrm{MPG})_m}{(\mathrm{MPG})_{s3}}\right)\left(1+\frac{(\mathrm{MPG})_{s3}}{(\mathrm{MPG})_{s2}}\right)\left(1-\frac{(\mathrm{MPG})_{s2}}{(\mathrm{MPG})_{s1}}\right)
\end{aligned}
\qquad \text{(A2-70)}
$$

Finally

$$\alpha_3 = R\cdot\overline{C}_f \qquad \text{(A2-71)}$$

where

$$R = \frac{1}{1+\mathrm{Expl}\left[\dfrac{\mathrm{MPM}+\mathrm{MMP}\,\mathrm{Exp2}+\mathrm{PMM}\,\mathrm{Exp3}+\mathrm{PPP}\,\mathrm{Exp2}\,\mathrm{Exp3}}{\mathrm{MPP}+\mathrm{MMM}\,\mathrm{Exp2}+\mathrm{PMP}\,\mathrm{Exp3}+\mathrm{PPM}\,\mathrm{Exp2}\,\mathrm{Exp3}}\right]} \qquad \text{(A2-72)}$$

Using the derivative of the concentration in the skin-1 (Equation A2-63) and Equation (A2-66), the flux at the fracture surface may be written as:

$$
\begin{aligned}
\frac{D_{es1}}{b}\frac{\partial\overline{C}_{ps1}}{\partial z}\bigg|_{z=0} &= \frac{D_{es1}}{b}(\alpha_3-\alpha_4)\cdot A_{s1}\sqrt{s} = \frac{(\mathrm{MPG})_{s1}}{b}(2\alpha_3-\overline{C}_f)\sqrt{s}\\
\frac{D_{es1}}{b}\frac{\partial\overline{C}_{ps1}}{\partial z}\bigg|_{z=0} &= \frac{(\mathrm{MPG})_{s1}}{b}\overline{C}_f(2R-1)\sqrt{s}
\end{aligned}
\qquad \text{(A2-73)}
$$

Introducing Equation (A2-73) into Equation (A2-16), it gives

$$-\frac{q}{2Wb}\frac{d\overline{C}_f}{dx} - s\cdot\overline{C}_f + \frac{(\mathrm{MPG})_{s1}}{b}\overline{C}_f(2R-1)\sqrt{s} = 0 \qquad \text{(A2-74)}$$

Regrouping

$$\frac{q}{2Wb}\frac{d\overline{C}_f}{dx} + \overline{C}_f\left[s+\frac{(\mathrm{MPG})_{s1}\overline{C}_f\sqrt{s}}{b}(1-2R)\right] = 0 \qquad \text{(A2-75)}$$

Defining new parameters

$$\frac{1}{S}\frac{d\overline{C}_f}{dx} + T\overline{C}_f = 0$$

where (A2-76)

$$S = \frac{2Wb}{q} \qquad \text{and} \qquad T = \left[s+\frac{(\mathrm{MPG})_{s1}\overline{C}_f\sqrt{s}}{b}(1-2R)\right] = 0$$

Equation (A2-76) is a-variable separable ODE and may be directly integrated. The solution is:

$$\overline{C}_f = A_0 \mathrm{Exp}\left[-STx\right] \tag{A2-77}$$

$$\overline{C}_f = A_0 \mathrm{Exp}\left[-\frac{2Wxb}{q}\left(s+\frac{\sqrt{s}(MPG)_{s1}}{b}(1-2R)\right)\right] \tag{A2-78}$$

Where A_0 is a-constant of integration. Inserting BC1 gives:

$$\overline{C}_f = \frac{C_0}{s}\mathrm{Exp}\left[-\frac{2Wxb}{q}\left(s+\frac{\sqrt{s}(MPG)_{s1}}{b}(1-2R)\right)\right] \tag{A2-79}$$

The above equation may be simplified in terms of the residence time of the water in the channel and the ratio flow wetted surface to flowrate (FWS/Q)

$$t_w = x\frac{2Wb}{q} \qquad \frac{FWS}{q} = \frac{2Wx}{q} \tag{A2-80}$$

Equation (A2-79) can then be written in the form:

$$\overline{C}_f = \frac{C_0}{s}\mathrm{Exp}(-t_w s)\mathrm{Exp}\left(-(MPG)_{s1}\left(\frac{FWS}{q}\right)\sqrt{s}(1-2R)\right) \tag{A2-81}$$

Special cases

Two-skin layer and matrix proper. There are some interesting limiting cases for this equation; for example when skin-2 and skin-3 have the same properties and the total thickness of the skin-2 and skin-3 is set to be δ_{s2}.

The value of the parameter R is then:

$$R = \frac{1}{1+\mathrm{Exp}\left(2\delta_{s1}A_{s1}\sqrt{s}\right)\left[\frac{XMM+XPP\cdot\mathrm{Exp}\left(2\delta_{s2}A_{s2}\sqrt{s}\right)}{XMP+XPM\cdot\mathrm{Exp}\left(2\delta_{s2}A_{s2}\sqrt{s}\right)}\right]} \tag{A2-82}$$

Where

$$\begin{aligned}
XPP &= \left(1+\frac{(MPG)_m}{(MPG)_{s2}}\right)\left(1+\frac{(MPG)_{s2}}{(MPG)_{s1}}\right)\\
XPM &= \left(1+\frac{(MPG)_m}{(MPG)_{s2}}\right)\left(1-\frac{(MPG)_{s2}}{(MPG)_{s1}}\right)\\
XMP &= \left(1-\frac{(MPG)_m}{(MPG)_{s2}}\right)\left(1+\frac{(MPG)_{s2}}{(MPG)_{s1}}\right)\\
XMM &= \left(1-\frac{(MPG)_m}{(MPG)_{s2}}\right)\left(1-\frac{(MPG)_{s2}}{(MPG)_{s1}}\right)
\end{aligned} \tag{A2-83}$$

This R corresponds to the R obtained independently for the case of two skins and matrix proper.

One-skin layer and matrix proper. Another case is when the matrix is formed by a-skin and the matrix proper. In Equation (A2-90), skin-1 and skin-2 have the same properties and the total thickness of the skin-1 and skin-2 is set to be δ_s. The value of R is then

$$R = \frac{1}{1 + \mathrm{Exp}\left(2\delta_s A_s \sqrt{s}\right)\left[\dfrac{1 + \dfrac{(\mathrm{MPG})_m}{(\mathrm{MPG})_s}}{1 - \dfrac{(\mathrm{MPG})_m}{(\mathrm{MPG})_s}}\right]} \tag{A2-84}$$

This R corresponds to the R obtained independently for the case of one skin and matrix proper.

Impervious matrix proper. From the case shown above, another limiting case may be obtained, when the matrix proper has a very small diffusivity (i.e., it is impermeable):

$$\left(\frac{1 + \dfrac{(\mathrm{MPG})_m}{(\mathrm{MPG})_s}}{1 - \dfrac{(\mathrm{MPG})_m}{(\mathrm{MPG})_s}}\right) \Rightarrow 1 \qquad \text{for} \qquad (\mathrm{MPG})_s >> (\mathrm{MPG})_m \tag{A2-85}$$

In this case, Equation (A2-89) can be simplified to:

$$\overline{C}_f = \frac{C_0}{s}\mathrm{Exp}(-t_w s)\mathrm{Exp}\left(-(\mathrm{MPG})_s\left(\frac{FWS}{Q}\right)\sqrt{s}\,\tanh\left[\delta_s A\sqrt{s}\right]\right) \tag{A2-86}$$

This corresponds to the solution for limited matrix connectivity (Frind and Sudicky, 1982)

Implementation

The following parameters are required for calculating the breakthrough curve at outlet.

The omega parameters, defined for the skin-1

$$\omega_{s1} = (\mathrm{MPG})_{s1}\left(\frac{FWS}{Q}\right) = \left(\sqrt{K_{ds1}\rho_{bs1}D_{es1}}\right)\cdot\left(\frac{FWS}{Q}\right) \tag{A2-87}$$

The sigma parameters for the skin-1, skin-2, and skin-3

$$\sigma_{s1} = \delta_{s1}A_{s1} = \delta_{s1}\cdot\sqrt{\frac{K_{ds1}\rho_{bs1}}{D_{es1}}} \tag{A2-88}$$

$$\sigma_{s2} = \delta_{s2}A_{s2} = \delta_{s2}\cdot\sqrt{\frac{K_{ds2}\rho_{bs2}}{D_{es2}}} \tag{A2-89}$$

$$\sigma_{s3} = \delta_{s3} A_{s3} = \delta_{s3} \cdot \sqrt{\frac{K_{ds3}\rho_{bs3}}{D_{es3}}} \tag{A2-90}$$

The ratio between the MPG for the matrix to that for the skin-3

$$RMS3 = \frac{(MPG)_m}{(MPG)_{s3}} = \frac{\sqrt{K_{dm}\rho_{bm}D_{em}}}{\sqrt{K_{ds3}\rho_{bs3}D_{es3}}} \tag{A2-91}$$

The ratio between the MPG for the skin-3 to that for the skin-2

$$RS3S2 = \frac{(MPG)_{s3}}{(MPG)_{s2}} = \frac{\sqrt{K_{ds3}\rho_{bs3}D_{es3}}}{\sqrt{K_{ds2}\rho_{bs2}D_{es2}}} \tag{A2-92}$$

The ratio between the MPG for the skin-2 to that for the skin-1

$$RS2S1 = \frac{(MPG)_{s2}}{(MPG)_{s1}} = \frac{\sqrt{K_{ds2}\rho_{bs2}D_{es2}}}{\sqrt{K_{ds1}\rho_{bs1}D_{es1}}} \tag{A2-93}$$

Introducing these parameters into Equation (A2-81)

$$\overline{C}_f = \frac{C_0}{s} Exp(-t_w s) Exp\left(-\omega_{s1}\sqrt{s}\,(1-2R)\right) \tag{A2-94}$$

Where

$$R = \frac{1}{1 + Exp1\left[\dfrac{MPM + MMP\,Exp2 + PMM\,Exp3 + PPP\,Exp2\,Exp3}{MPP + MMM\,Exp2 + PMP\,Exp3 + PPM\,Exp2\,Exp3}\right]} \tag{A2-95}$$

Where

$$\begin{aligned} Exp1 &= Exp\left(\sigma_{s1}\sqrt{s}\right) \\ Exp2 &= Exp\left(\sigma_{s2}\sqrt{s}\right) \\ Exp3 &= Exp\left(\sigma_{s3}\sqrt{s}\right) \end{aligned} \tag{A2-96}$$

$$\begin{aligned} MPM &= (1-RMS3)(1+RS3S2)(1-RS2S1) \\ MMP &= (1-RMS3)(1-RS3S2)(1+RS2S1) \\ PMM &= (1+RMS3)(1-RS3S2)(1-RS2S1) \\ PPP &= (1+RMS3)(1+RS3S2)(1+RS2S1) \end{aligned} \tag{A2-97}$$

$$\begin{aligned} MPP &= (1-RMS3)(1+RS3S2)(1+RS2S1) \\ MMM &= (1-RMS3)(1-RS3S2)(1-RS2S1) \\ PMP &= (1+RMS3)(1-RS3S2)(1+RS2S1) \\ PPM &= (1+RMS3)(1+RS3S2)(1-RS2S1) \end{aligned} \tag{A2-98}$$